The dissertation committee for Romy Darlene Hanna certifies that this is the approved version of the following dissertation:

CM Murchison: Nebular Formation of Fine-grained Chondrule Rims Followed by Impact Processing on the CM Parent Body

Committee:

Richard A. Ketcham, Supervisor

Victoria E. Hamilton

Jack W. Holt

John C. Lassiter

Michael E. Zolensky

CM Murchison: Nebular Formation Of Fine-Grained Chondrule Rims Followed By Impact Processing On The CM Parent Body

by

Romy Darlene Hanna, B.S. Geo. Sci., M.S.

Dissertation

Presented to the Faculty of the Graduate School of

The University of Texas at Austin

in Partial Fulfillment

of the Requirements

for the Degree of

Doctor of Philosophy

The University Of Texas At Austin

December 2016

Acknowledgements

A large portion of my PhD would not have been possible without the generous support of the NASA Earth and Space Sciences Fellowship (NESSF) program (Grant NNX13AO64H) and I am sincerely grateful to NASA and program manager Dolores Holland for the opportunity it provided me. I am also grateful to the Jackson School of Geosciences for additional support including an Analytical Fees grant that paid for numerous hours of CT scanning. I would like to thank the Smithsonian National Museum of Natural History, curator Tim McCoy, and collection manager Linda Welzenbach for the extended loan of Murchison USNM 5487 and for authorizing and providing new section cuts for my project. Others whose time and help was much appreciated include: James Martinez (JSC) for his help with EBSD sample preparation and tips/techniques, Paula Lindgren (University of Glasgow) who helped introduce me to the meteoritic community, answer my numerous (and likely naïve) questions about CM chondrites, and provided general moral support and friendship, and Jon Friedrich (Fordham University), Martin Lee (University of Glasgow), and Jeff Cuzzi (NASA Ames) who provided encouragement, helpful discussion, and valuable feedback regarding my work and topics related to it.

I would also like to thank my PhD advisor Rich Ketcham and dissertation committee (Mike Zolensky, Vicky Hamilton, Jack Holt, and John Lassiter) for their support and encouragement. I especially appreciate the time Mike gave during my visits to JSC and for helping acquaint me with the field of meteoritics, which was entirely new to me 5 years ago. I'm sure he prevented me from making numerous dumb mistakes. I would like to thank Vicky for her patience while I juggled a dissertation in addition to another project on Mars TIR spectroscopy. Jack and John both helped me expand my

experience in the planetary sciences with the excellent classes they taught and the general help in my work that they provided. And while not on my official committee, a large thanks goes to Whitney Behr, who taught me a lot about microstructural geology, EBSD, and rock deformation outside of any class or formal instruction. Her enthusiasm and interest in my project was much appreciated and I hope we can continue working on structural problems in meteoritics. I also thank Philip Guerrero, graduate coordinator extraordinaire, who helped me navigate graduate school and whose efficiency and enthusiasm in running the graduate program at the Jackson School is unmatched. And last but not least a huge thanks to Rich Ketcham, whose wise advice and very large brain helped guide me through completing a PhD in a field a bit outside both of our previous research experiences. His belief that I could actually pull it off was a huge motivation and his patience while I navigated both a PhD and starting a new family was especially appreciated. Thank you for being a truly extraordinary advisor as well as a friend.

I also owe a huge thanks to everyone in the CTlab – Jessie Maisano, Dave Edey, Matt Colbert, Gary Zuker, Travis Clow, and Zoe Yin. Not only was I generally not available to help much in the lab during the past 5 years, but my new roles as a PhD student and mom were at times very stressful and you got to see the most stressed and overworked version of me during those times. I really appreciate your patience and understanding and I certainly owe you all a few (or perhaps many) beers. Thanks to Travis, Zoe, and additionally Megan Hoffman, for your many hours of menial segmentation in Avizo of chondrules that were essential in establishing error estimates for this work. It was a critical component of my research and I could not have done it without your help. And thank you to the CT research group – Emily Cooperdock, Jordan Hildebrandt, Kylie Wright, Eric Kelly, Rachel Ruthven, and Scott Eckley. It was fun

sharing hours of CT discussion and snacks with you; I learned quite a lot about interesting topics outside of my field. Thank you for the moral support and camaraderie.

And finally, the largest thanks go to my family. To Sam and Charlotte thank you so much for your encouragement and support. Thank you to my parents, brother, and sister who have provided me with a lifetime of love, encouragement, and moral support. Thanks especially to my parents who always encouraged me to follow my heart and passion in life to find work that truly made me happy. Without your financial support and sacrifices to help me go to college in the first place I would not be where I am today, so thank you. Thanks to my beautiful and amazing daughter Evelyn who lights up my world and whom I love dearly. You are going to be an amazing big sister, and I hope that some day you find and do what truly makes you happy. But sincerely, the largest heartfelt gratitude goes to my wonderful husband, John, who is surely the most understanding and supportive spouse in the world. I know that it was extremely difficult and stressful at times, and I sincerely appreciate your help, patience, and support in helping me pursue and realize my dream. Without you, none of this would have been possible.

CM Murchison: Nebular Formation Of Fine-Grained Chondrule Rims Followed By Impact Processing On The CM Parent Body

Romy Darlene Hanna, Ph.D.

The University of Texas at Austin, 2016

Supervisor: Richard A. Ketcham

We examine the primitive carbonaceous chondrite, CM Murchison, to infer details concerning its formation and subsequent processing on the CM parent body. We use X-ray computed tomography (XCT) to measure the 3D morphology and spatial relationship of fine-grained rims (FGRs) of Type I chondrules and find that the relationship between FGR volume and interior core radius is well described by a power law function as proposed for FGR accretion in a turbulent nebula by Cuzzi (2004). We also find evidence that the rimmed chondrules were slightly larger than Kolmogorov-stopping-time nebular particles. Evidence against parent body FGR formation includes a positive correlation between rim thickness and chondrule size and no correlation between interior chondrule roughness (used as a proxy for degree of aqueous alteration) and FGR volume. We find that the chondrules are foliated and that the FGRs are compressed in the direction of maximum stress, resulting in rims that are consistently thicker in the plane of foliation.

After accretion to the CM parent body, the material within Murchison experienced brittle deformation, porosity loss, and aqueous alteration. XCT reveals that partially altered chondrules define a prominent foliation and weak lineation. The

presence of a lineation and evidence for a component of rotational, noncoaxial shear suggest that the deformation was caused by impact. Olivine optical extinction indicates that the sample is classified as shock stage S1 and electron microscopy reveals that plastic deformation was minimal and that brittle deformation was the dominant microstructural strain-accommodating mechanism. Evidence such as serpentine veins parallel to the foliation fabric and crosscutting alteration veins strongly suggest that some aqueous alteration post-dated or was contemporaneous with the deformation and that multiple episodes of fracturing and mineralization occurred. Finally, using the deformed shape of the chondrules we estimate the strain and infer that the original bulk porosity of Murchison before deformation was 32.2 – 53.4%. Our findings suggest that significant porosity loss, deformation, and compaction from impact can occur on chondrite parent bodies whose samples record only a low level of shock, and that significant chondrule deformation can result from brittle processes and does not require plastic deformation of grains.

Table of Contents

List of Tables

List of Figures

Introduction

Carbonaceous chondrites contain primitive material accreted to planetesimals early in solar system history before the nebular dust disk had completely dissipated (Nichols, 2006; Russell et al., 2006). Either due to the small size of the accreted chondrite bodies or to a later accretion time, internal melting and differentiation (largely attributed to heat from short-lived radioisotopes) did not occur (Scott, 2007; Wadhwa et al., 2006). Thus carbonaceous chondrites provide the rare opportunity to study primitive nebular materials and use their characteristics to understand the formation and distribution of nebular materials at this critical time in solar nebula history. However, after accretion to the parent body the material experienced a myriad of secondary processes such as deformation, aqueous alteration, and heating (Bischoff et al., 2006; Brearley, 2006; Huss et al., 2006; Scott, 2007). It is therefore essential to document these effects to understand how they have modified the primitive chondritic material in order to properly intuit early nebular processes. In addition, investigation of the evolution of primitive chondritic asteroids and their regolith since accretion is critical, as various aspects of secondary processing (e.g., source of water and heat for aqueous alteration, origin of deformational petrofabrics) are still debated (e.g., Brearley, 2006; Krot et al., 2006; Rubin, 2012; Zolensky et al., 1997) and the first mission to study and return samples from a primitive carbonaceous asteroid is currently on its way to asteroid Bennu (Lauretta et al., 2015).

The primitive chondrite we selected for study is CM chondrite Murchison. It fell near Murchison, Victoria, Australia in 1969 and it represents the largest recovered mass of CM material to date with recovered mass totaling nearly 100 kg (Fuchs et al., 1973). The CM group chondrites show a particularly wide range of degrees of aqueous alteration and deformation with minimal evidence of heating (Rubin, 2012; Rubin et al., 2007; Zolensky et al., 1997). In addition, the asteroid Bennu has been found on the basis of

visible to near infrared spectral data to be a likely CM or CI type asteroid (Clark et al., 2011; Lauretta et al., 2015). To investigate Murchison we used a combination of well-established (electron microbeam, optical petrography) and more novel (X-ray computed tomography, or XCT) analytical techniques. Our preliminary investigation of a ~44 gram Murchison sample (USNM 5487) with XCT revealed a high proportion of dark (low density) components with a roughly elliptical cross sections when viewed in 2D. Three dimensional fabric analysis revealed that these objects, which were found to be chondrules, appear to have a preferred alignment consistent with a foliation (Hanna et al., 2012). Despite being one of the most extensively studied carbonaceous chondrites since its fall in 1969, foliation in Murchison has never been reported, apart from a microscopic matrix foliation defined by the alignment of the basal plane (001) of serpentine (Fujimura et al., 1983). The initial Murchison report did briefly mention that a few hand samples contained "elongated lenslike shapes that showed a slight lineation pattern" ((Fuchs et al., 1973): page 22), but this was never revisited (e.g. (Rubin, 2012)).

Because XCT is a rapidly developing technique that has only recently begun to be used in the investigation of meteorites and other extraterrestrial materials, and as part of an Invited Review from Associate Editor Klaus Keil at *Chemie der Erde*, we did a survey of the current literature on the application of the technique in the planetary sciences and this is presented as chapter one. An earlier work by Ebel and Rivers (2007) provided a review of meteoritical investigations and applications but focused mainly on synchrotron-based XCT, specifically the XCT beam line at the Advanced Photon Source (APS) at Argonne National Laboratory. We therefore focused our review on laboratory-based polychromatic cone-beam systems, especially since these types of systems are becoming more prevalent in laboratories and museums around the world for research and curatorial purposes. We present a technical overview of the physics of XCT, describe the major components of typical laboratory-based XCT scanners, and provide a guide for how to optimize data collection for planetary materials using such systems. We also discuss data processing, visualization and analysis, including a discussion of common data artifacts

and how to minimize them. We review a variety of recent studies in which XCT has been used to study extraterrestrial materials and/or to address fundamental problems in planetary science. We conclude with a short discussion of anticipated future directions of XCT technology and application.

The second chapter describes our detailed investigation into the deformation and aqueous alteration of the CM Murchison chondrite with sample USNM 5487 from the Smithsonian Institution. We find with further XCT investigation that Murchison displays a prominent foliation fabric as well as a weak lineation defined by deformed, partially altered chondrules. The presence of a lineation and evidence for a component of rotational, noncoaxial shear suggest that the deformation was caused by impact(s). Electron backscatter diffraction (EBSD) and electron microscopy reveal that plastic deformation within the chondrules was minimal and that brittle deformation in the form of fracturing, cataclasis, and grain boundary sliding was the dominant microstructural strain-accommodating mechanism. Textural evidence such as serpentine veins parallel to the foliation fabric and crosscutting alteration veins strongly suggest that some aqueous alteration post-dated or was contemporaneous with the deformation and that multiple episodes of fracturing and mineralization occurred. We also use the deformed shape of the chondrules to estimate the amount of bulk porosity during compaction, and estimate that original bulk porosity of Murchison prior to its deformation was 32.2 – 53.4% and likely at the upper end of this range due to chondrule compressibility.

We then turned our attention to the fine-grained rims (FGRs) that enclose almost all objects within Murchison, and are a feature of many chondrites. There are competing hypotheses as to whether FGRs formed while the chondrules were still freely floating in the solar nebula versus on the parent body surface (e.g., Cuzzi, 2004; Metzler et al., 1992), and so we use higher resolution XCT to examine their 3D morphology in detail. This work is presented as chapter three. We quantify the size, shape, and orientations of the chondrules and their rims and develop a new algorithm to examine the 3D spatial variation in FGR thickness around each chondrule. We find that the FGR volume in

relation to the interior core radius is very well described by a power law function as proposed for accretion of FGRs in a weakly turbulent nebula by Cuzzi (2004) and also find evidence that the rimmed chondrules were slightly larger than Kolmogorov-stopping-time nebular particles. Evidence against parent body FGR formation includes a positive correlation between rim thickness and chondrule size and no correlation between interior chondrule roughness (used as a proxy for degree of aqueous alteration) and FGR volume. We find that the examined chondrules were deformed and foliated by the same impact(s) which deformed CM Murchison and that FGRs were compressed in the direction of maximum stress, resulting in rims which are consistently, slightly thicker in the plane of foliation. Finally, we propose that the highly irregular shape of some chondrules in CM Murchison are a primary feature resulting from chondrule formation, and that high chondrule surface roughness caused larger particles to accrete a relatively larger amount of nebular dust.

Chapter 1: X-ray computed tomography of planetary materials: A primer and review of recent studies[1]

1.1 Introduction

X-ray computed tomography (XCT) has exploded in popularity over the last two decades as a powerful, non-destructive method to characterize objects in three dimensions. Similar to medical CAT scanning in its basic principles and underlying physics, XCT as applied in the physical sciences utilizes higher energies, smaller X-ray focal spot sizes, and/or longer acquisition times to enable higher resolution and superior quality data not attainable in medical settings where dose limitation and subject movement are concerns. In recent years, XCT technology has evolved such that smaller systems are approaching the cost of a high-end scanning electron microscope (SEM) and, thus, more academic and research laboratories are acquiring them to complement other analytical techniques.

The application of X-ray CT for non-medical research purposes began in earnest in the early 1980s after the initial development of medical instruments in the 1960s and 1970s (Hounsfield, 1973, 1976). In the planetary sciences, XCT was applied fairly early as an imaging and qualitative investigation tool for meteorites (Arnold et al., 1983; Hirano et al., 1990; Kondo et al., 1997; Masuda et al., 1986). However, limited access to XCT facilities and expertise prevented its wide application, and it was several years before the first studies aimed at addressing particular planetary problems via the 3D quantification capabilities of XCT appeared (e.g., Gnos et al., 2002; Kuebler et al., 1999; Rubin et al., 2001; Tsuchiyama et al., 2000).

As a non-destructive technique, XCT is particularly useful for documenting and analyzing rare and/or irreplaceable specimens such as meteorites or returned samples

[1] The material presented in this chapter is a modified form of an invited review submitted to Chemie der Erde – Hanna R.D. and R.A. Ketcham (in revision) X-ray computed tomography of planetary materials: A primer and review of recent studies, Manuscript ID CHEMER_2016_62. I wrote the paper in full with some content input and revision editing from Ketcham.

(e.g., Apollo, Stardust, Hayabusa), where sample preservation is of particular concern (Blumenfeld et al., 2015; Flynn et al., 2000; Masuda et al., 1986; Tsuchiyama et al., 2002; Zeigler et al., 2014). Using XCT, the entirety of a sample can be imaged prior to slabbing, sectioning, or distribution to museums and researchers. This not only allows digital curation of the sample but also preserves the 3D context of any subsamples to the original sample and to each other. In addition, the XCT data can be used to characterize macroscale features such as sample heterogeneity, pore structure, and/or petrofabrics that may not be noticeable or measurable with traditional 2D microanalytical techniques (e.g., Benedix et al., 2008; Friedrich and Rivers, 2013; Hanna et al., 2015; Zolensky et al., 2014).

There are several review papers that cover different aspects of XCT as it applies to various geoscientific problems (Cnudde and Boone, 2013; Ebel and Rivers, 2007; Fusseis et al., 2014; Ketcham and Carlson, 2001; Kyle and Ketcham, 2015; Wildenschild and Sheppard, 2013). A recent review by Fusseis et al. (2014) focuses on the application of synchrotron CT to geology and rock mechanics and compiles information on the major synchrotron beamlines available for research around the world, as well as helpful information on how to apply for beam time at these facilities. Wildenschild and Sheppard (2013) focus on the application of XCT to porosity measurement and include a discussion of current and future XCT hardware technology. A more generalized review of XCT in geosciences using both tube-based and synchrotron sources is given by Cnudde and Boone (2013). Ebel and Rivers (2007) provide an informative review of meteoritical investigations and applications, mainly using synchrotron-based XCT, including details on the XCT beam line at the Advanced Photon Source (APS) at Argonne National Laboratory. The present contribution provides an updated overview of XCT investigation of planetary materials with emphasis on more widely used and available lab-based XCT systems.

Our primary goal is to acquaint the general planetary and geochemical science communities with XCT as it applies to extraterrestrial materials, including details on data

acquisition and its optimization for different curatorial and research goals. Because of the proliferation of laboratory-based polychromatic cone-beam XCT instruments (in contrast to more specialized systems with synchrotron sources or helical acquisition geometry), we will focus on the technology, scanning geometry, and data artifacts that are characteristic of these systems, but provide additional details as well as case studies that utilize others. We first give an introduction to the underlying physical principles of XCT, the common components of a laboratory cone-beam scanner, and how scanning parameters are determined and the various trade-offs encountered. We present the numerous ways XCT data can be processed, corrected, visualized, and quantified, with particular emphasis on common data artifacts that are inherent when using polychromatic cone-beam instruments. We then present several recent case studies of how XCT data have been used to address various planetary science problems, and conclude with a short discussion of the future trajectory of XCT. Our intention is that this review serves as a useful primer for planetary scientists to optimize their own XCT data acquisition, be better prepared to interpret and analyze XCT datasets, and be inspired to use this powerful technique to address problems in their own research.

1.2 Principles and physics of XCT

1.2.1 X-ray generation

The easiest way to generate X-rays is to bombard a target material (usually a high-atomic-number metal such as tungsten) with high-energy electrons produced by a heated filament, as in a standard X-ray "tube". A continuum of X-ray energies is produced due to various interactions of the incoming free electrons with bound electrons in the target material. The most dominant interaction produces so-called bremsstrahlung radiation, in which incident electrons decelerate due to interactions with target nuclei (bremsstrahlung arises from the German word *bremsen* for brake). The energy of the resulting radiation depends on the amount of electron kinetic energy transferred by this interaction, and so the X-ray radiation emitted features a broad spectrum of energies up to

the maximum energy of the incident electrons (i.e., it is polychromatic). The maximum energy is generated when an electron actually collides with the nucleus and all of its kinetic energy is converted to X-ray radiation, although the probability of such a collision is low, which is why the majority of the radiation is emitted at lower energies (Fig. 1.1) (Hsieh, 2009). The X-ray tube voltage setting represents the electric potential applied across the chamber that will accelerate electrons up to this maximum energy. For example, if the tube voltage is set to 200 kV, the filament electrons will be accelerated fast enough to generate X-rays up to 200 keV, although the mean X-ray energy is much lower than this (Fig. 1.1). Because the polychromatic nature of this radiation can cause imaging artifacts, a low-attenuation filter can be used to preferentially remove some of these lower energy X-rays (Ketcham and Carlson, 2001). Another source of X-ray radiation is produced when an incident electron ejects an inner-shell electron of a target atom and an outer-shell electron moves inward to fill this hole. Because the outer-shell electron has a higher energy state than the inner-shell electron, its change in energy state gives rise to a characteristic X-ray energy (Fig. 1.1).

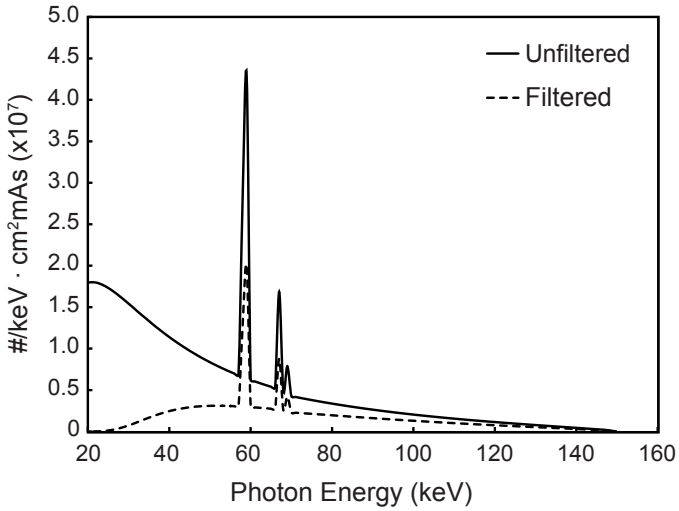

Fig. 1.1 X-ray energy spectrum generated from a tungsten target at 150 keV. *Mean energy of unfiltered beam is 48.2 keV. Filtered spectrum represents same beam after filtering with 10 mm of aluminum. The filtered beam has a higher mean energy of 69 keV due to filtering of low energy X-rays. Graph produced using SpekCalc (Poludniowski et al., 2009).*

The bremsstrahlung and characteristic X-ray radiation actually only represent a small fraction of energy deposited within the target material; the vast majority (>99%) of the incident electron energy is released as heat (Hsieh, 2009). The total X-ray energy output from the target is characterized as the flux (photons/second), although the terms intensity and flux are often used interchangeably (and will be here).

While an X-ray tube system is a relatively cost-effective way to generate X-ray radiation, the limited X-ray flux and polychromatic spectrum can lead to imaging artifacts (Section 1.4). Synchrotron sources provide a way to overcome these limitations, although their specialized setup and high operational cost limit their availability. A synchrotron uses a large storage ring [typically hundreds of meters in circumference (see Table 3.1 in Willmott, 2011)] to accelerate free electrons generated from an electron gun (i.e., a heated filament similar to that used in an X-ray tube) to even higher velocities. This gives electrons up to several GeV of kinetic energy as they are accelerated to very near the velocity of light. X-ray radiation is generated from the electrons as their trajectory is modified, either by using bending magnets (to maintain a circular arc) or by the use of an insertion device (undulator or wiggler) along a straight-line segment in the ring which forces the electrons to slightly oscillate and emit X-ray radiation. The large amount of radiation produced allows the use of beam filtration that can be 'tuned' to a particular X-ray energy while maintaining a high flux to produce a brilliant (i.e., high flux over a small spatial area with minimal beam divergence) monochromatic beam (Willmott, 2011).

1.2.2 X-ray attenuation

A three-dimensional XCT data set represents the attenuation of X-rays at each point within an object. The general attenuation of X-rays in a material is governed by Lambert-Beer's Law

$$I = I_0 \exp(-\mu x) \tag{1}$$

where I is the recorded X-ray intensity, I_0 is the initial X-ray intensity, μ is the linear attenuation coefficient of the material, and x is the path length of the X-ray through the material. Equation (1) only describes a homogenous material which, however, in natural samples is rarely the case. If the object is composed of several different materials, the linear attenuation of each material (u_i) as well as its linear extent (x_i) must be accounted for, resulting in the more general equation

$$I = I_0 \exp\left[\sum(-\mu_i x_i)\right] \quad (2)$$

In the case of a monochromatic beam this equation is sufficient to describe the attenuation of the X-ray beam through a heterogeneous object. However, the more typical laboratory setup employs a polychromatic X-ray beam. Because the linear attenuation coefficient μ is a strong function of X-ray energy, to describe X-ray attenuation of a polychromatic beam through a heterogeneous object requires solving equation (2) over the full X-ray spectrum

$$I = \int I_0(E) \exp\left[\sum(-\mu_i(E) x_i)\right] dE \quad (3)$$

In order to solve equation (3) the full shape of the incident X-ray spectrum is needed, but it is rarely directly measured and depends on several factors, including the target material and type (transmission or directional; Section 1.3.1), accelerating voltage, current, and any beam filters used (Fig. 1.1). These nuances make it difficult to accurately model a polychromatic X-ray beam, and therefore most reconstruction algorithms solve only equation (2), implicitly assuming a single effective energy. As discussed in more detail below, this mathematical simplification can lead to beam hardening artifacts within the reconstructed data.

Within the X-ray energies commonly used for tomography of planetary materials (< ~450 keV), the attenuation of X-rays through a material is the result of three processes whose relative influence varies depending on the incident energy and material properties: photoelectric absorption, incoherent (Compton) scattering, and coherent (Rayleigh) scattering. During photoelectric absorption, an incoming X-ray photon liberates an inner-shell electron (which becomes a photoelectron) leaving the atom ionized. The original X-

ray photon ceases to exist (i.e., it is absorbed). The probability of this effect is heavily dependent on the photon energy (Fig. 1.2) and the atomic number (Z) of the absorbing material, roughly to the fourth power ~Z^4 (Als-Nielson and McMorrow, 2011). In Compton scattering the incident X-ray photon ejects an outer-shell electron (ionization) while retaining some of its energy and, as a result, is scattered as a lower energy photon (i.e., inelastic scattering) (Hsieh, 2009). The probability of this effect is dependent on the electron density of the material (Hsieh, 2009). This causes Compton scattering to be less sensitive to the material composition than the photoelectric effect, especially at lower energies (Fig. 1.2).

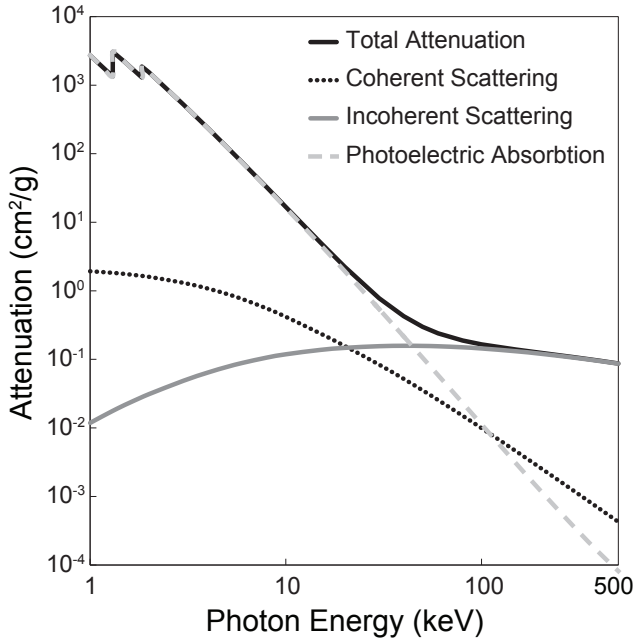

Fig. 1.2 X-ray attenuation of forsterite.
Contribution of various X-ray interactions (coherent scattering, incoherent scattering, and photoelectric absorption) to the total mass attenuation of forsterite (Mg_2SiO_4) for energies up to 500 keV. Attenuation values from the NIST XCOM database (http://www.nist.gov/pml/data/xcom/index.cfm).

The final process, coherent scattering, is an elastic process where the incoming X-ray photon causes an electron to vibrate at the same frequency and emit an X-ray photon of

the same energy. The overall effect is that the incident X-ray is scattered but no energy loss occurs and the affected atom is unchanged (not ionized). The intensity of this effect is roughly proportional to Z^2 (Willmott, 2011) and is most pronounced at lower X-ray energies (Fig. 1.2).

The combination of these effects for different materials can be examined by plotting their total attenuation as a function of X-ray energy. The NIST XCOM database (Berger et al., 2010) compiles the X-ray attenuation coefficients (for scattering and photoelectric absorption, as well as total attenuation) for elements, compounds, and mixtures ($Z \leq 100$). We have created a tool in the form of a Microsoft Excel workbook called MuCalc (http://www.ctlab.geo.utexas.edu/software/) in which the total X-ray attenuations of various terrestrial and meteoritic minerals have been calculated using the NIST XCOM database and can be graphed in order to examine their relative attenuations at various X-ray energies (Fig. 1.3). Further details on this program can be found in Appendix A. The strong dependence of the photoelectric absorption process on Z, coupled with its dominance at lower X-ray energies (Fig. 1.2), makes lower X-ray energies more ideal for distinguishing certain minerals (for example, troilite and fayalite; Fig. 1.3). As the X-ray spectrum produced from a laboratory source is a complex continuum of energies up to the maximum energy (Fig. 1.1), the "effective" X-ray attenuation of the minerals in Fig. 1.3 is an integral of their attenuation coefficients at all energies in this range (Eq. 3).

For the interested reader there are several books that provide more detailed treatments of the various aspects of X-ray computed tomography. A thorough mathematical foundation and detailed explanation of X-ray physics and interactions using both classical and quantum descriptions can be found in Als-Nielson and McMorrow (2011). Hsieh (2009) provides an overview of tube-based laboratory XCT including details on typical XCT scanner components, image reconstruction, and imaging artifacts. Buzug (2008) provides a similar overview but delves into cone-beam system components (albeit in a medical setting) and image reconstruction mathematics in considerably more

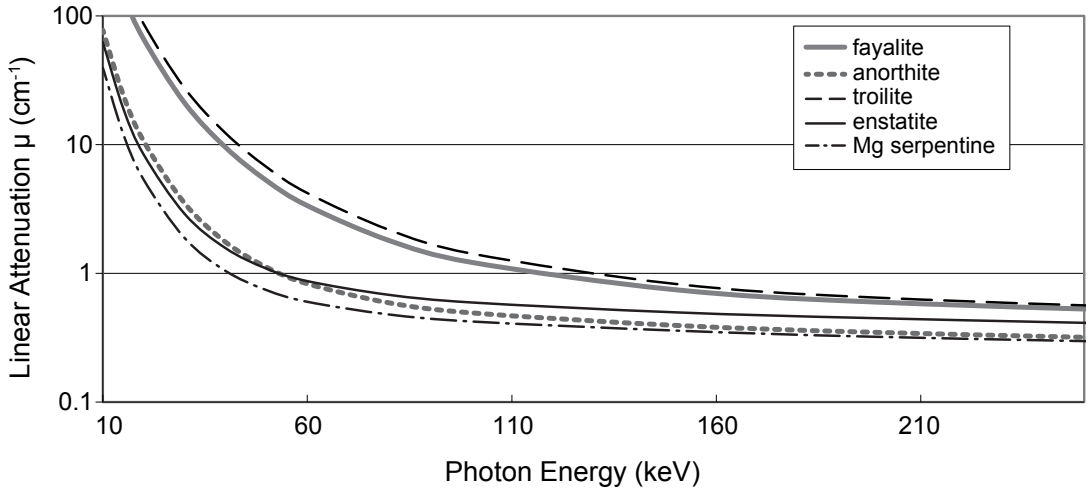

Fig. 1.3 Linear attenuation coefficients for common meteoritic minerals. *Note the increased separation of linear attenuation for anorthite/serpentine and fayalite/troilite at decreased energies, and the change in relative attenuation between anorthite and enstatite. Anorthite is generally less attenuating than enstatite, but at lower energies (< 55 keV) it is slightly more attenuating. At 55 keV they have equal attenuation and would be indistinguishable with XCT. Created with the MuCalc program (Appendix A).*

detail. Those interested in synchrotron facilities for XCT are encouraged to consult Willmott (2011) for in-depth coverage of the capabilities, components, and operation of these systems, including information on additional analytical techniques available using synchrotron radiation.

1.2.3 Really non-destructive?

While XCT is described as non-destructive, X-ray energy is intimately interacting with material at an atomic level, notably by causing ionization and potentially heating. Therefore, some change is occurring at least on a subatomic level and the question arises of whether this interaction is causing a permanent change in material properties that are detectable using other analytical techniques. For meteorites and mission-returned samples where an irreplaceable specimen is often analyzed using a variety of techniques,

potential sample modification from any one technique that could compromise the finding of another is a serious concern. In addition, the interest in using XCT as a general curation tool for planetary samples makes addressing this issue of critical importance to prevent large numbers of samples from being contaminated or modified in any way that potentially hinders future investigation.

For these reasons a few studies have emerged in recent years that aim to identify measurable changes in XCT-scanned samples. Ebel et al. (2009) calculated that the power deposited into 1 cm^2 sample cross section during a synchrotron scan at 10 keV would be ~4.2 x 10^{-4} W, which is many of orders of magnitude lower than the absorbed power from an electron microprobe and corresponds to heating 1 cm^3 of water by 1x10^{-4} degrees/s (~1° in 3 hours). The University of Texas High-Resolution X-ray CT Facility (UTCT) tested for the effects of a routine laboratory XCT scan on the ferromagnetic remanence of two 25-mm-diameter terrestrial igneous (basalt) cores (R. Hanna and R. R. Fu, unpublished data). The two cores were first demagnetized in alternating fields (AF) of 85 mT. These cores were then scanned, one on our FeinFocus II system (180keV, 0.22 mA; 2.21 hour scan) and the other on our Zeiss (formerly Xradia) microXCT system (90 keV, 10 W; 0.98 hour scan). Measurements of the remanent magnetization of the samples were made before and after the XCT scans using the 2G Superconducting Rock Magnetometer at the MIT Paleomagnetism Laboratory. No change in the magnetic moment of the samples was detected after the XCT scans, implying that the change in the magnetization was <1% of the total moment. Reapplication of a 1.5 mT AF revealed no resolvable change in the magnetic moment; the maximum field to which the samples were exposed was therefore <<1.5 mT. We conclude that XCT scanning using the settings indicated above lead to no significant magnetic contamination in our basaltic samples. In regard to organics, Ebel et al. (2009) investigated the effect of a synchrotron scan (beamline 13BM-D at the Advanced Proton Source; 12 keV for ~35 minutes) to polycyclic aromatic hydrocarbon (PAH) residue. No changes were detected in the PAH composition using laser-desorption laser-ionization mass spectrometry. Friedrich et al.

(2016) tested for the modification of amino acids in two samples of the Murchison CM chondrite during conditions slightly harsher than a routine synchrotron XCT scan. They scanned the samples at 46.6 and 48.6 keV with longer beam exposure times (64 and 43 minutes, respectively) than typically used for microtomography imaging experiments and measured no difference in either the amino acid abundance nor the enantiomeric ratios (measured with liquid chromatography-fluorescence detection and time-of-flight mass spectrometry) after X-ray exposure. They estimated that the total dose experienced by two samples was ~1.1 kGy (kilograys) and ~1.2 kGy and also calculated that sample heating was negligible (< 1° C).

However, Sears et al. (2015; 2016) did measure a significant rise in thermoluminescence (TL) in several ordinary chondrites after scanning the samples in a laboratory XCT system. They concluded that XCT-scanned samples experience a radiation dose of 85 ± 5 krad, which is consistent with the XCT dose calculation of Friedrich et al. (2016) (100 krad = 1.0 kGy). This dose is comparable to natural TL measured in Antarctic meteorites (< ~100 krad) that results from a combination of cosmic ray exposure and internal radioactivity (2016; Sears et al., 2013). Because the fall in natural TL during a meteorite's time on Earth is used to calculate its terrestrial residence time (e.g., Sears et al., 2013), XCT scanning could significantly complicate age determinations. Specifically, XCT-scanned samples could be mistaken for freshly fallen meteorites (Sears et al., 2015; 2016).

The confirmation of a measureable radiation dose for an XCT-scanned sample is unsurprising as X-ray radiation is ionizing in nature. It is expected that some molecular change is occurring as a result of this radiation, especially in the case of organics which have been shown to be more sensitive to ionizing radiation than non-organics, especially at lower X-ray energies (Bertrand et al., 2015). Indeed, Moini et al. (2014) examined the effects of synchrotron X-ray radiation on free amino acids [L-cystine, L-asparagine (Asn), and L-aspartic acid (Asp)] and confirmed that several molecular changes including modification (L-cystine; optically visible structure and color change), fragmentation (all),

and racemization (Asp) occurred at low X-ray energies (8 and 22 keV). They found that the degree of damage increased when using a lower X-ray energy or a focused X-ray beam (i.e., beam focused to a smaller cross-sectional size with higher intensity) and for longer irradiation times (up to 1200 seconds). Likewise, the Stardust Team has verified that interstellar candidate grains, particularly organics, show evidence of radiation damage after exposure to synchrotron X-ray radiation experiments [X-ray fluorescence (XRF) and X-ray diffraction (XRD)] which use focused X-ray beams (Bechtel et al., 2014b; Simionovici et al., 2011). However, some damage appears to be the result of the particles being embedded in an insulating medium (Simionovici et al., 2011), and it is also unclear if similar radiation damage would occur from synchrotron X-ray imaging tomography that utilizes unfocused beams. Because the unfocused beam widths are relatively large, the X-ray flux and resulting radiation dose is lower than the nm-scale beams achieved with X-ray focusing lenses (Bechtel et al., 2014a; Friedrich et al., 2016). Qualitatively, the authors and others in our laboratory (UTCT) have personally witnessed visible 'yellowing' of epoxy (for embedded specimens) that has been exposed to (unfocused) polychromatic X-rays (40-420 kV). The color change increases in intensity with repeated XCT scanning.

As a final note, we caution again that X-rays are physically interacting with matter to cause (permanent?) modifications at a subatomic level as a result of ionization and that further investigation, especially in regard to organics modification, is needed. While any changes may not be measureable with most analytical techniques commonly employed today, it is possible, even likely, that as technological advances to characterize material at increasingly smaller scales are developed, changes within matter exposed to routine XCT may become detectable. The potential impact of this scenario is impossible to know, but caution may be warranted when imaging samples at lower X-ray energies or with focused beams (e.g., Tsuchiyama et al., 2013), especially when preservation of organics is of particular concern.

1.3 Acquisition of XCT data

1.3.1 XCT scanner components

There are four primary components common among most non-medical XCT cone-beam systems: 1) an X-ray source that generates X-rays; 2) a rotating stage upon which the sample is mounted; 3) a detector that records the X-ray signal after passing through the sample; and 4) a computer that drives the system and records the collected data. The most critical components of a system are the X-ray source and the detector technology. In traditional turnkey laboratory-based tube XCT systems found today, polychromatic X-rays are generated from a finite point source and diverge to illuminate a sample volume. A cone of the X-ray energy is detected by a 2D planar detector composed of discrete elements, the number of which determines the maximum size of the final image (2048 x 2048 or 4096 x 4096 are common sizes today), although the data can be binned to increase the signal-to-noise ratio (SNR), shorten acquisition time, and/or reduce data volume size. The sample is rotated through 180°(+ fan angle) or 360° on the stage as a sequence of 2D X-ray projections (views) are recorded by the detector. These digital radiographs are recorded, stored, and ultimately reconstructed (Section 1.3.4) to produce a 3D volume of the sample's X-ray attenuation.

In addition to the energy spectrum generated (Fig. 1.1), other important parameters of an X-ray source are the intensity and the focal spot size. The intensity is controlled by the power input of the system and is often quoted as a maximum wattage. The greater the intensity, the better the SNR in the acquired data. The focal spot size is a major factor in determining the maximum spatial resolution that is achievable with a system and the amount of blur that will occur (see Section 1.3.2). In addition, the type of target (directional or transmission) determines the possible spot sizes and flux available. In directional targets the filament electrons hit a thick target material and X-rays are emitted from the target surface at an angle. In transmission targets the filament electrons pass through a thin film of target material and X-rays are emitted on the other side.

Directional targets are capable of a higher flux but also have a larger spot size than transmission targets. Because of their lower flux and smaller focal spot size, transmission targets usually are only used for higher resolution (i.e., smaller object) XCT scanning.

The X-ray source energy, wattage, and focal spot size covary. The total power (wattage) of an X-ray tube is what ultimately governs the volume and type of materials that it can adequately penetrate. Power (P) is related to the energy (voltage V) and current (I) through:

$$P = V\,I \tag{4}$$

The operator can set the voltage (in kV) and current (in mA or μA) to produce the desired power (wattage), up to the maximum allowed on the system[2]. The spot size is sized proportional to the power to prevent damage to the target. For example, if the system is run at a higher total power (wattage), the spot size is enlarged (defocused) to keep the total flux of electrons below a certain threshold, otherwise the target would overheat or crack (although a rotating anode can help limit overheating). Operation at a lower power (reduced voltage and/or amperage) allows for a more focused beam, producing a sharper but noisier image due to the lower intensity. In the end the particular settings used are primarily governed by the size and composition of the sample as well as the imaging objectives.

While a cone-beam source geometry is that most commonly employed today because of its relative efficiency and cost-effectiveness in X-ray generation and collection, its major drawbacks are a parallax effect around the upper and lower edges of the cone that leads to distortion at the edges of the field of view (FOV). This distortion can be minimized by ensuring that the system is geometrically well aligned or through the use of helical scanning, during which the cone beam is vertically translated through the sample during the scan. This has the advantage that all portions of the sample are 'seen' by the nearly perpendicular central rays of the beam and the reconstruction

[2] On some systems the two adjustable parameters are voltage and wattage. In this case the system auto-adjusts the current to supply the intended power.

algorithm can utilize this information to provide a more faithful geometric reconstruction of the object (e.g., Varslot et al., 2011; Yu and Xiaochuan, 2004). Systems capable of helical scanning are primarily limited to non-desktop XCT systems that can house the required gantry system, such as that at UTCT (http://www.ctlab.geo.utexas.edu/the-lab/).

Another way to avoid the common issues associated with a cone-beam geometry is to use a near-parallel beam that can be achieved using a synchrotron source (Ebel and Rivers, 2007; Fusseis et al., 2014; Kyle and Ketcham, 2015). This provides the minimal amount of geometrical distortion, but there may be limits to the FOV available and thus the maximum sample size (Ebel and Rivers, 2007). Yet another beam geometry is a fan beam configuration where the X-rays are collimated to a narrow horizontal beam that is recorded by a linear detector array. Although this requires vertical rastering through the sample (and therefore longer acquisition times), this is an ideal geometry for larger (dm-scale) objects that require higher X-ray energies to penetrate. Because attenuation of higher energy X-rays is dominated by scattering (Fig. 1.2), collimation to a fan beam and the use of a single row of detector elements minimizes associated artifacts (Kyle and Ketcham, 2015). A compromise that can be effective with a flat-panel detector is to collimate the beam and detector so that only a limited number of rows are illuminated, essentially gathering a "flattened cone" of data and eliminating the worst of the scattering.

The other important component of an XCT system that determines its performance is the detector. An X-ray detector is typically made of a scintillating material that produces photons of visible light in response to the absorption of X-ray photons. These flashes of light are counted and recorded by a device that digitizes the signal. Traditionally, charge-coupled devices (CCDs) are used, but these are gradually being replaced by thin film transistor (TFT) arrays (also referred to as flat panel detectors) which are generally regarded as superior technology (e.g., Jaffray et al., 1999; Seibert, 2006). Complementary metal-oxide-semiconductor (CMOS) chips can also be used and are generally lower in cost with faster frame rates but at the expense of image

quality (noise). The quality of a detector for X-ray imaging depends on its size (both individual detector element size and the total number of elements), its efficiency in detecting X-rays (the ideal is 100% sensitivity to all X-ray energies), its ability to minimize cross-talk between detector elements, shadowing (i.e., image persistence or burn-in), and the speed with which it can record signals (i.e., latency). The last is the most limiting factor in how fast an X-ray projection can be acquired and therefore greatly influences the speed of the system. The physical size of the detector element determines how much of the object is subtended by it (i.e., the spatial resolution; Section 1.3.2) and the bit depth of a detector determines the number of different grayscale values it can record (i.e., the contrast in X-ray attenuation; high quality detectors today feature 16- to 32- bit depth).

1.3.2 Spatial resolution

The spatial resolution of a cone-beam XCT scan is a function of several factors, including the scanning geometry, source, detector, and magnification optics if applicable. In the most general sense, the spatial resolution is a function of the width of the beam as it passes from the focal spot through the object to a detector element (Fig. 1.4a). The beam width is a function of the spot size (*s*), detector element size (*d*), the distance between the source and object (*SOD*), and the distance between the source and the detector (*SDD*) (ASTM E1441-11, 2011) (Fig. 1.4a):

$$BW = \frac{\sqrt{d^2+[s(M-1)]^2}}{M} \tag{5}$$

where:

$$M = \frac{SDD}{SOD} \tag{6}$$

Because the X-ray spot has a finite minimum size, each detector element will collect X-rays that have gone through more than one path in the sample (Fig. 1.4a). It is

easy to see from Equation (5) and Fig. 1.4a that as the *s* increases, the width of the beam (*BW)* increases and thus spatial resolution decreases. The physical size of the detector

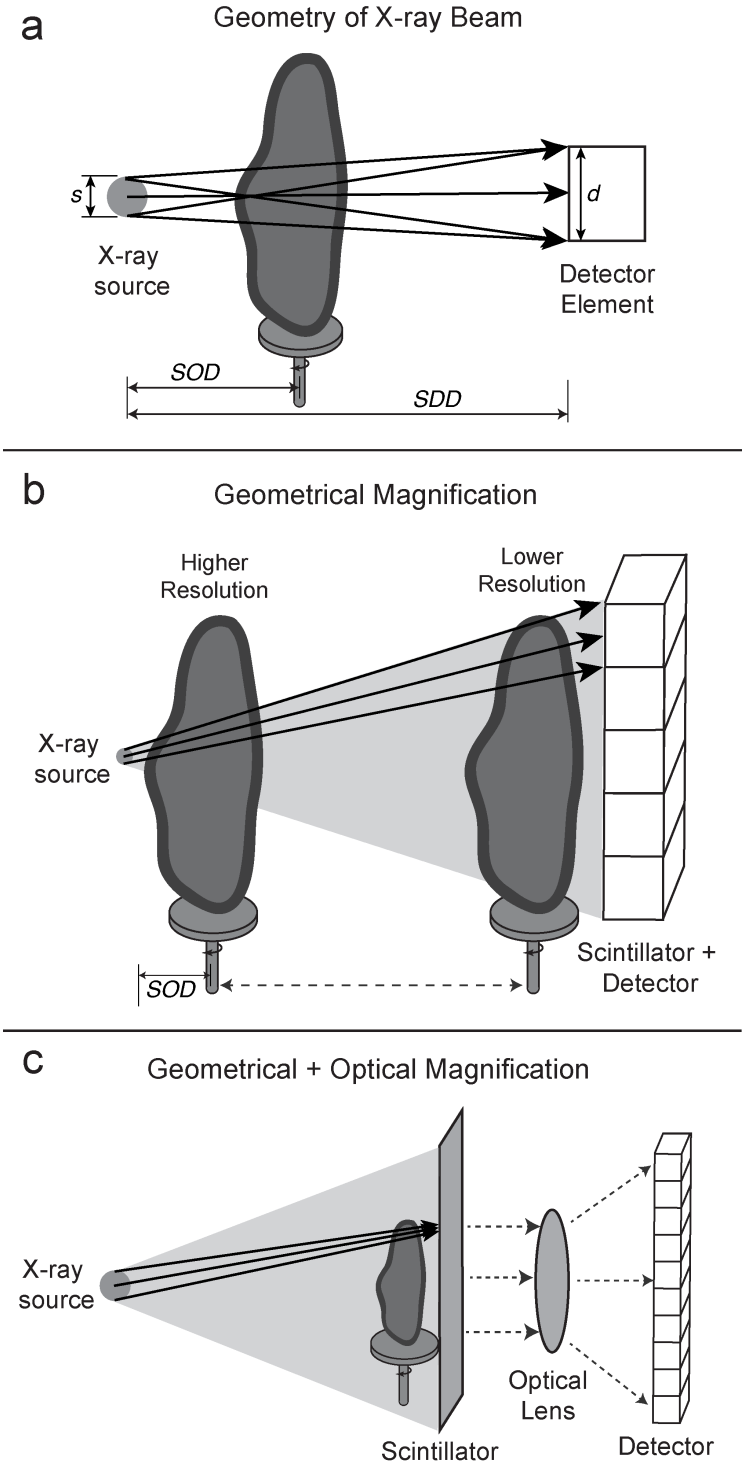

Fig. 1.4 X-ray beam geometry and magnification.

(a) The width of the beam path at the object defines the spatial resolution of a scan and is a function of spot size (s), detector size (d), source-object-distance (SOD) and source-detector-distance (SDD). Refer to Equation (5) in text. (b) In geometrical magnification placing the object close to the source results in higher spatial resolution as SOD, and thus the beam width, is minimized. (c) On some XCT scanners the detector elements are small compared to the source and so the sample is placed close to the scintillator for maximum resolution. Optical magnification is then used to project light from the scintillator onto the detector. Optical magnification is also used in XCT instruments on synchrotron beam lines where a nearly parallel beam precludes geometric magnification unless zone plates are used.

elements also influences spatial resolution, as larger *d* will record more possible paths (larger *BW*). In the majority of scanners *d* is large relative to the *s* and geometric magnification is used to vary spatial resolution by moving the object relative to the source (Fig. 1.4b). The highest resolution is achieved when objects are placed closest to the source and *SOD* (and therefore *BW*) is minimized. However, such an arrangement places the sample into a smaller region of the cone that illuminates the entire detector array, in turn limiting the field of view. Imaging small regions within larger objects is generally limited by the requirement to not place the sample so close to the sources that it hits it.

Conversely, some systems (such as those built by Zeiss, formerly Xradia) use optical magnification in addition to geometrical magnification (Fig. 1.4c). This reduces the dependence of the spatial resolution on the *SOD* and allows for high resolution and also higher magnification of subvolumes within large objects. In these systems the effective detector elements are smaller than the source and therefore objects are placed close to the detector (actually the scintillator; Fig. 1.4c) to maximize geometric magnification. The light from the scintillator is then optically magnified onto the detector to provide further magnification. XCT systems on synchrotron beamlines use optical magnification as well; the beam is nearly parallel, thus geometric magnification is not possible.

In both cases, a reasonable first-order simplification is that resolution in terms of voxel (volume element, or 3D pixel) size is simply the object width, or field of view (FOV) if a sub-region is imaged, divided by the number of elements across the detector array. For example, imaging an object 5 cm in size on a 2048x2048 pixel detector results in a resolution of about 24.4 microns on a voxel edge, assuming the sample fills the entire FOV. However, resolution in terms of feature detection is also a function of the point spread function (PSF) of system (responsible for blur in XCT data (ASTM E1441-11, 2011)) which is a function of a number of factors including beam width, detector

crosstalk, and precision of gantry motions. The PSF is discussed in more detail in Section 1.4.2.

1.3.3 Setting up a scan

The optimal parameters for an XCT experiment are determined primarily by the sample composition and size and the research objectives. The spatial resolution of the data is often the primary concern, as it determines the ability to detect features of interest. In most cases spatial resolution does not directly correspond to feature detection, as it takes a few voxels to discern and measure a feature within an XCT dataset. Exceptions to this include when the material of interest has a markedly higher (e.g., metal) or lower (e.g., pore space) attenuation compared to the surrounding material, or a high aspect ratio (e.g., fractures). In such cases it may be possible to measure features, even on a sub-voxel level, by exploiting the partial volume effect (Kyle and Ketcham, 2015) (Section 1.4.2).

The other important variable in the design of an XCT experiment is the X-ray energy to be used. This also depends on the research objectives, specifically the materials that are present (e.g., minerals, voids) and which of these are important to distinguish in the data. A linear attenuation comparison tool such as MuCalc (Appendix A) can be valuable in determining the optimal energy to maximize the attenuation contrast between phases of interest (Fig. 1.3). While lower-energy X-rays are better able to maximize contrast between most minerals, they are also less penetrating, resulting in potential data contamination by noise or artifacts. The best compromise is to scan at the highest energy that will still allow sufficient attenuation contrast between the phases of interest. If an energy below ~40 keV is required, a lower-atomic-number metal target (such as molybdenum) can produce better results, or a synchrotron source can provide the higher flux needed to avoid excessively noisy data. However, the penetration limitations of these lower energy X-rays will still require a relatively smaller sample and proper

sample preparation. The ideal sample geometry is a cylinder, where the X-rays are passing through a consistent amount of material throughout the rotation.

In some cases, scanning the sample at two different energies (dual energy or absorption edge scanning) may be useful. Because the X-ray attenuation of a material is a well-defined function of its density, atomic number Z, and the X-ray energy (Fig. 1.3), scanning the same material at dual energies allows an estimation of its density and effective (average) Z (Van Geet et al., 2000). This approach requires careful calibration using materials of known composition and density (e.g., Alves et al., 2014) and complications from a polychromatic beam and beam hardening can limit success (Alves et al., 2014; Remeysen and Swennen, 2008; Van Geet et al., 2000). Another form of dual energy scanning (also referred to as absorption edge scanning) involves scanning a material at energies above and below its X-ray K-absorption edge (e.g., Ikeda et al., 2004; Ketcham and Koeberl, 2013; Mayo et al., 2015; Tsuchiyama et al., 2013). Because X-ray attenuation changes markedly on either side of the K edge for certain elements (Fig. 1.5), the large attenuation difference can be used to identify and highlight materials composed of these elements (Ikeda et al., 2004; Mayo et al., 2015), even when using polychromatic sources (Ketcham and Koeberl, 2013). Careful selection of the X-ray energies and proper calibration of the system can also allow calculation of elemental concentrations (Ikeda et al., 2004) and mineralogical compositions (Tsuchiyama et al., 2013), although this requires a monochromatic beam (Section 1.5.4).

After the energy and spatial resolution requirements are determined, the rest of the scanning parameters are selected with the goal of providing sufficient quality data within a reasonable time. The more views (projections) that are collected during a scan the higher the data quality, especially toward the periphery of the FOV. However, higher numbers of views will increase the scan duration, especially on systems with detectors with a significant latency time and increase reconstruction time (Section 1.3.4). Also, there are theoretical limits on the number of views which should be used (i.e., the Nyquist frequency; (Hsieh, 2009)) as well as practical limits to the increase in SNR (Uesugi et al.,

2010). Another parameter is the acquisition time per view, usually expressed in milliseconds. Again, the longer the acquisition time per view the higher the SNR, but at

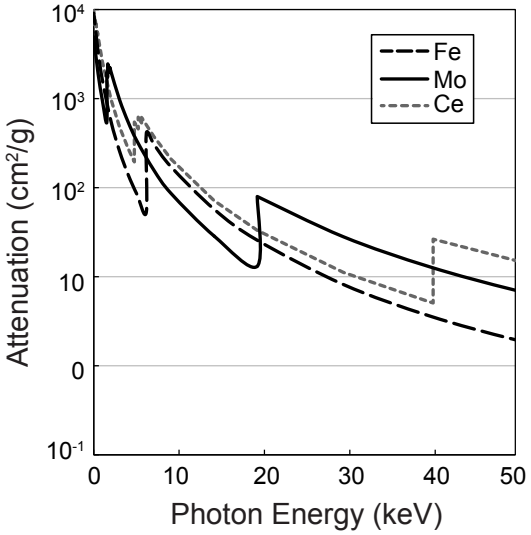

Fig. 1.5 K-absorption edges of Fe, Mo, Ce.
Mass attenuation of iron (Fe), molybdenum (Mo), and cerium (Ce) for energies up to 50 keV showing the K-absorption edges of each element (7.1, 20.0, and 40.4 keV, respectively). The L_I-absorption edges of Mo and Ce are also visible (2.9 and 6.5 keV, respectively). Attenuation values from the NIST XCOM database (http://www.nist.gov/pml/data/xcom/index.cfm).

the cost of a longer scan. Another way to increase SNR is to bin the detector readings (sum signal from adjacent detector elements), usually by 2 or 4, but this also decreases resolution by the same factor. Another scanning option is to pre-filter the beam which will preferentially remove lower energy X-rays to decrease the effects of beam hardening and ring artifacts (Section 1.4.1), but this will also decrease the SNR and possibly degrade material discrimination, so care must be taken to not over-filter. The best choice for all of these parameters will vary depending not only on the composition and size of the sample but also on the particular scanner and, in many cases, the budget (time and/or money). Hands-on scanning experience is the best way to learn the most appropriate settings for various samples and instruments.

Finally, a series of careful calibrations must be performed prior to, during, and/or after the XCT scan to ensure data quality. The two most common are the dark field and bright field calibrations. A dark field calibration (also referred to as an offset) is a projection image taken while the X-ray beam is off. This is usually done only once, either prior to or after the scan, and helps to correct for detector bias present while the X-

rays are off. The bright field calibration (also referred to as a gain) is taken with the X-rays on and the sample outside of the FOV; it is essential to correct for the differential response between detector elements, falloff (due to spherical beam), as well as to account for source drift (change in X-ray intensity over time). The timing of the bright field calibration(s) is generally machine-specific but will also depend on the scan duration (i.e. longer scans can benefit from several bright field calibrations). Another calibration, which varies widely in its implementation among scanners, is the geometrical calibration. This ensures that gantry motions are operating as expected, that the central rotation axis of the sample mount is at a known location with respect to the detector array, that the X-ray source and detector are properly aligned, and that the spatial magnification of the system is properly calibrated. For most turnkey scanners a full geometrical calibration is performed during regular preventative maintenance visits and only a simple central rotation axis shift correction is applied during data processing for a scan. However, for flexible-geometry systems such as the one at UTCT, a geometrical calibration is performed prior to each scan using a phantom (a machined part of known size and geometry).

1.3.4 Reconstruction

During reconstruction the XCT projections are processed and reconstructed into a 3D volume representing X-ray attenuation. The mathematical details of the reconstruction process are beyond the scope of this review, but the most common reconstruction algorithm is filtered back-projection (FBP) in which the data are first convolved with a filter and then the projections are 'stacked' onto a grid through their respective angular positions to gradually build an image of X-ray attenuation (Buzug, 2008; Hsieh, 2009). In its simplest form, FBP is used by systems with a parallel-beam geometry (i.e., synchtrotron sourceFusseis et al., 2014). Cone beam scanners commonly employ the Feldkamp-Davis-Kress (FDK) algorithm, an extension of FBP that accounts for the 3D dispersion of the X-rays from a point source to a 2D detector (Hsieh, 2009).

Reconstruction is a computationally intensive process. Unfortunately, most modern XCT scanners come with their own proprietary reconstruction software that allows little flexibility in data processing/reconstruction and may employ behind-the-scenes algorithms that are not documented, such as noise suppression. Different convolution filters can be used to emphasize particular attenuation contrasts, resulting in improvements in spatial resolution or SNR, but usually as a tradeoff between one and the other (Hsieh, 2009; Ketcham and Carlson, 2001). Because pre-reconstruction data processing can greatly improve data quality (Section 1.4.1) and the computational demands of data reconstruction can create a bottleneck when scanning multiple samples, it is advantageous to use stand-alone reconstruction software that allows greater flexibility in the reconstruction process. Two options currently available are Octopus Reconstruction from Inside Matters (https://insidematters.eu/octopus) and the open source Astra Tomography Toolbox (http://sourceforge.net/p/astra-toolbox/wiki/Home/). A significant hurdle to this approach is translating the data from the scanner-produced format into something the reconstructor can understand.

The result of XCT reconstruction is a 3D image volume, which is typically exported as a series of 2D TIFF files, although other uncompressed image formats (e.g., BMP, DCM) or a 3D-format TIFF file may be used as well. The actual data values within the images are referred to interchangeably as CT values, CT numbers, gray levels, or gray scales, and represent the relative X-ray attenuation of materials within the object (see next section for complicating factors in this assumption). Because there is no standard byte scaling for non-medical XCT data, most reconstruction software allows the user to define minimum and maximum values between which the data are scaled (i.e., the histogram is spread between 0, or black, and 65535, or white, in the case of 16bit data). These can be selected to either encompass all data values (i.e., not saturate or truncate at either the low or high end, which is always the preference for quantitative work), or chosen to emphasize certain attenuation ranges within the dataset. It is not good practice to use byte scaling to eliminate the appearance of scanning artifacts. For example,

scaling the data so that air in the FOV is a uniform black not only removes CT number variation that may alert users to the presence of scanning artifacts, but also shifts the apparent boundary of an object inward, compromising any measurements on the object.

1.4 XCT data

1.4.1 Artifacts

XCT data artifacts are variances in CT number that do reflect a material's actual X-ray attenuation and can significantly hinder data visualization and quantification if not properly accounted for. Some artifacts can be quite subtle and in some cases can significantly influence quantitative measurements, especially when dealing with objects that are small relative to the data resolution.

The most common (and frequently pernicious) artifact in tube-based polychromatic X-ray systems is beam hardening, which causes the CT number of a material to vary depending on its location within the data volume. This occurs because the lower-energy ("soft") X-rays are preferentially filtered out as they pass through an object, thereby "hardening" the beam and increasing its average energy (Fig. 1.1). Because most reconstruction algorithms assume a constant energy (Equation 2 in Section 1.2.2), this manifests as a gradual darkening toward the interior of the object (Fig. 1.6a) and is especially pronounced along the longest X-ray paths (Ketcham and Hanna, 2014).

Beam hardening can be prevented (best option) or corrected in a variety of ways, from the use of scanning calibrations and filters to post-acquisition data processing. XCT systems commonly employ beam filters of various materials to filter out lower-energy X-rays during acquisition of data and calibrations. However, this may lessen the effect without entirely preventing it. In addition, filtering the beam lowers its overall intensity, thus requiring longer scans to achieve a given SNR. Using a phantom of material with similar attenuation properties as the sample material can also help to minimize the effects of beam hardening, but requires unique phantoms for each type and geometry of sample scanned (Edey et al., 2013).

Due to the limitations of these preventative measures, a great deal of research has gone into post-acquisition data processing algorithms to eliminate beam-hardening artifacts. The first and still most commonly employed correction is a simple polynomial

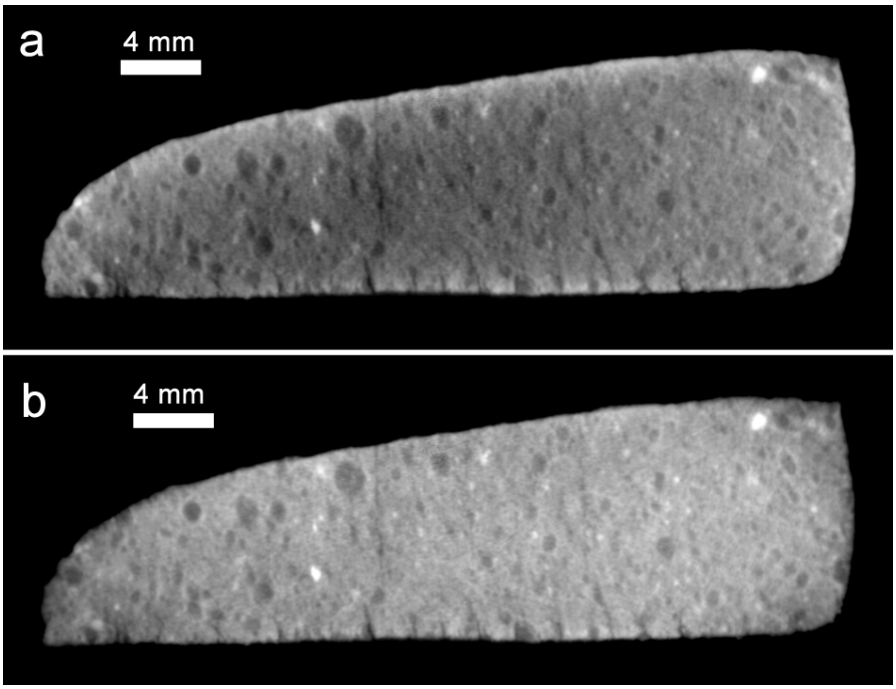

Fig. 1.6 Example of beam hardening correction using Ketcham and Hanna (2014). *(a) CM Murchison XCT slice with beam hardening artifact. Note darker center and brighter edge, especially along top and bottom of sample. (b) Same XCT slice after beam hardening correction. The grey scales of the matrix are more consistent across sample and no central darkening is apparent. XCT data in both (a) and (b) has been corrected for rings (see Fig. 1.6a).*

transform (usually 2^{nd} to 4^{th} degree) that attempts to convert the data from that of a polychromatic to a monochromatic attenuation response, a process referred to as linearization (Herman, 1979). This is the method used by most scanner manufacturers today, as a single or multi-term input in the reconstruction software that is not always straightforward in its implementation and requires trial and error to find the best correction. Some of these shortcomings can be addressed using an iterative optimization process to find an optimal linearization function (Ketcham and Hanna, 2014); a correction using this approach is shown in Fig. 1.6. Another issue with linearization is

that, while it might work well for homogenous materials or less attenuating biological samples, it is often insufficient for denser, heterogeneous objects such as geological specimens. More recent work has attempted to construct a correction based more directly on the physical attenuation process of multiple materials imaged with a polychromatic beam (e.g., Krumm et al., 2008; Kyriakou et al., 2010; Van Gompel et al., 2011). While promising, these algorithms are computationally expensive and remain somewhat limited in their applicability, though they are likely to be more widely available in the future.

Other common XCT artifacts include rings, starbursts, shadows, and streaking, which unlike beam hardening are not limited to polychromatic X-ray sources. Ring artifacts are a result of the differential X-ray response of the discrete detector elements which, when combined with rotational data acquisition, manifest as rings (or partial rings) in 2D slice images (Fig. 1.7a). These can be prevented at acquisition by dithering the stage (as in Zeiss and Bruker XCT systems) or the detector (as in some GE systems) – shifting either by a few microns on X, Y and/or Z from one projection to the next – to average any variation in individual detector elements over adjacent channels.

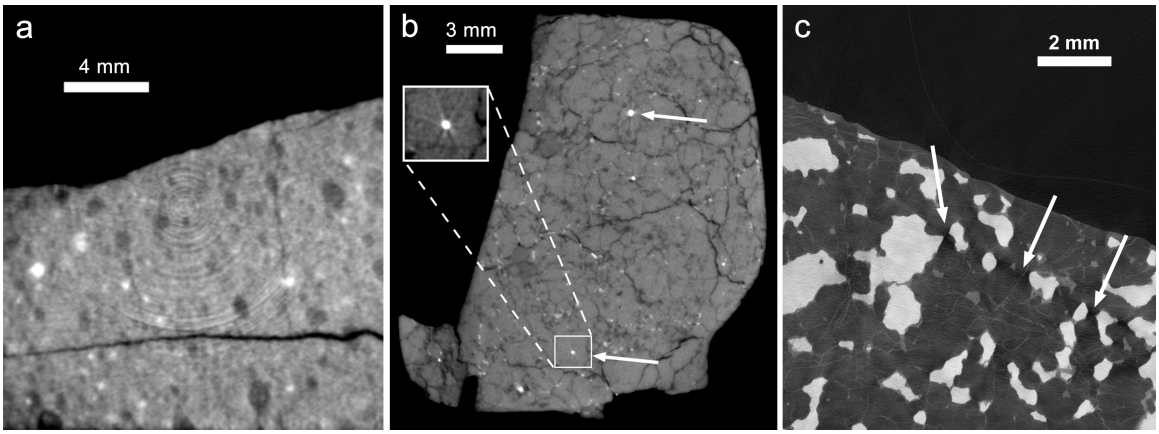

Fig. 1.7 Common XCT data artifacts.
(a) Rings in CM Murchison XCT data. Beam hardening correction has been applied (see Fig. 1.6). (b) Starburst artifact (streaks) from metal inclusions in Almahata Sitta S138. (c) Shadowing from metal in lodranite NWA 2993.

Post-acquisition, rings can be relatively straightforward to correct during data processing using the signals of surrounding detectors to average them out, even in reconstructed

images (Ketcham, 2006b), but this processing can also introduce artifacts by modifying linear features that are tangential to the center of rotation (Kyle and Ketcham, 2015). Another common artifact, starbursts, are caused by highly-attenuating inclusions which leads to bright and dark streaks emanating from the inclusion into the surrounding area (e.g., De Man et al., 1999) (Fig. 1.7b). Shadowing (also referred to as photon starvation) is a similar phenomenon but can be more subtle, where darker areas form in the "shadow" of a highly attenuating material due to the extreme filtering of the beam in these ray paths (Fig. 1.7c). Shadowing can be quite difficult to avoid, even when using relatively high flux synchrotron sources (Ebel and Rivers, 2007). Finally, streaking is caused by very low SNR along long beam paths or the presence of highly attenuating material (Hsieh, 2009). This manifests as pervasive streaks across the reconstructed image [see Fig. 1.7.31 in Hsieh (2009) for an example].

1.4.2 Partial volume effect and blurring

There are two other artifacts inherent in all XCT data that cannot be corrected and must be considered in cases of segmentation or measurement of small features. The first is the partial volume effect (PVE), in which a single voxel contains more than one material and therefore its CT number is an average of the X-ray attenuation of all materials present. Intimately linked with the PVE is the general blur of XCT data, which can be quantified as a point spread function (PSF). The PSF describes the response of the system to an ideal point object and is a complex function of the *BW*, detector response, scanner settings, and reconstruction algorithm (ASTM E1441-11, 2011; Ketcham, 2006a). This blur further complicates quantitative interpretation of CT numbers as it causes each voxel to have contributions from the surrounding voxels. All material boundaries within a heterogeneous specimen will be subject to PVE and blur at some level due to the finite spatial resolution of an XCT scan, but the issue will be most pronounced when the spatial resolution of the dataset approaches the spatial scale of the feature(s) of interest. For example, for a 15-μm thick vein imaged at 5-μm resolution the

majority of voxels intersecting the vein will not reflect pure vein material, but some average of it and the surrounding material. Attempts to measure such features can be subjective and prone to both over- and under-estimation (Ketcham, 2006a). A reasonable solution is to scan at higher resolution (see discussion of spatial versus feature resolution in Section 1.3.3) but this decreases the acquired volume, thus raising the question of whether it is indeed representative. Another solution is to account for this effect when measuring objects near the limit of the spatial resolution of the dataset, as implemented in some software such as Blob3D (Ketcham, 2005a) (Section 1.4.4).

Because the PSF is machine- and scan-dependent, it provides a way to measure and compare different scans among different machines/labs (ASTM E1441-11, 2011). This is useful because, while it has become standard practice to state the voxel size as a measure of precision, for features near the spatial resolution the scan's PSF may significantly affect the accuracy of this measurement (Ketcham and Hildebrandt, 2014). The PSF can be accurately measured using a software tool developed by Ketcham and Hildebrandt (2014) to provide greater confidence in the measurement of features (fractures, inclusions, pores) near the spatial resolution of an XCT dataset.

1.4.3 Visualization

The visual nature of XCT data allows even a novice user to interpret textural information within a scanned sample. The standard format that is most amenable to viewing with a variety of visualization software is a series of 2D images (slices) that can be loaded and 'stacked' into a 3D volume. Table 1.1 lists the most common commercial and freeware used for general visualization of XCT data. The list is by no means exhaustive. Because the determination of particular strengths and weaknesses of a program can be somewhat subjective, we include a few highlights of what we have found or have heard from colleagues to be unique about each program as it applies to XCT data.

The technological advances in XCT systems produce ever-larger datasets and a standard scan can produce a multi-gigabyte (GB) data volume. For this reason it is

important to consider the computational requirements for XCT data visualization and measurement. Although some quantitative analyses require the native 16bit (2^{16}, or 65536 possible grayscale values) data depth that is typically output from the scanner, in

Table 1.1 Visualization software for XCT data.

Name	Commercial / Free	Highlighted Features and Comments
VGStudio	Commercial (Volume Graphics GmbH)	Intuitive graphical user interface and relatively easy to use after a gentle learning curve. One of the more expensive commercial visualization packages available, featuring superior volume rendering, lighting control and animation. Some segmentation tools but limited quantification capabilities.
Avizo	Commercial (FEI Company)	Shorter learning curve for creating simple but impressive visualizations. Superior segmentation tools, including 3D segmentation, separation, and measurement. Extensive user guide and documentation.
PerGeos	Commercial (FEI Company)	Based on Avizo and marketed toward the oil and gas industry. Includes all Avizo capabilities plus a variety of tools specific to rock core analysis including integration with core log data and a pore statistics and modelling module.
Imaris	Commercial (Bitplane)	Visualization and analysis package primarily geared toward the life sciences, but handles all volume datasets including microscopy data formats and 4D data.
Mimics	Commercial (Materialise)	Visualization and basic analysis software for medical data, including XCT. Widely used in the biology and palaeontology communities.
ORS Visual	Commercial (Object Research Systems Incorporated)	Newly developed XCT visualization software primarily used for medical applications.
Octopus	Commercial (Inside Matters BVBA)	Originally developed by Ghent University Centre for X-ray Tomography (UGCT) group. Standard 3D visualization capabilities but notably integrates with additional XCT reconstruction and data analysis modules. Data analysis module (originally Morpho+) has filtering, segmentation, separation, and measurement (including discrete object orientation) capabilities. Standalone visualization module available as freeware.

Table 1.1, cont.

ImageJ	Free (National Institutes of Health)	Excellent, stable analysis and visualization (although primarily 2D) open-source freeware with extensive documentation and very large user base. A must-have program for working with XCT data. A wide variety of specialized plug-ins available. Volume rendering is weakly developed. Segmentation and measurement tools (mostly available as plug-ins) are somewhat limited and rarely operate in 3D.
Fiji	Free (National Institutes of Health)	An ImageJ bundle that includes many of the ImageJ plugins. Targeted at the life sciences.
Drishti	Free (Australian National University)	A more powerful freeware visualization package that includes flexible volume rendering and several other features for making impressive images. No user guide and little documentation make for a steep learning curve and somewhat hidden features.
Slice	Free (SPring-8)	Open-source freeware custom-built for XCT data visualization and analysis. A Unix environment and command line interface allow for building scripts.

most cases the data can be safely downsampled to 8bit (2^8, or 256 possible grayscale values) with a program such as ImageJ (Rasband, 1997-2015) to allow for faster manipulation and processing. It is also important to keep the data in an uncompressed (lossless) format such as TIFF or BMP rather than a compressed (lossy) format such as JPEG, which can significantly degrade data quality if used incautiously.

The basic visualization techniques easily done with a 3D XCT dataset are orthoslicing, isosurfacing, and volume rendering. An orthoslice is a 2D image that is orthogonal to the scanning plane. The original 2D images output by the scanner are the XY orthoslices parallel to the scan plane (vertical axis is Z) and standard 3D visualization software (Table 1.1) can be used to view orthoslices in the other two orthogonal planes (XZ or YZ). Most visualization packages can also reslice the data in any arbitrary orientation within the scan volume, the output of which is usually referred to as an 'oblique slice' or 'nonorthogonal slice' in contrast to 'orthoslice' (Fig. 1.8b). An isosurface is a 3D contour within the data volume. Similar to a 2D topographic map line, an isosurface maps as a threshold a particular CT number (grayscale) value within the dataset and can quickly highlight the exterior of a sample or a specific material or feature within it (Fig. 1.8b). Volume rendering is true 3D visualization, in which every voxel is assigned both a color and an opacity (Fig. 1.8a). Complex and stunning visualizations with false coloring and lighting can be produced using volume rendering, but creating a visualization that is both appealing and informative is an art. Fusseis et al. (2014) provides useful tips for creating visualizations from XCT data (their Section 3.4 and Appendix 4) and visualization textbooks such as Hansen and Johnson (2005) can be consulted for a more in-depth understanding on the various techniques.

1.4.4 Quantification

All of the visualization elements described above can be used to investigate and display the data in illuminating figures and animations, but the real power of XCT data lies in its potential for 3D quantitative analysis. An excellent, short overview of the

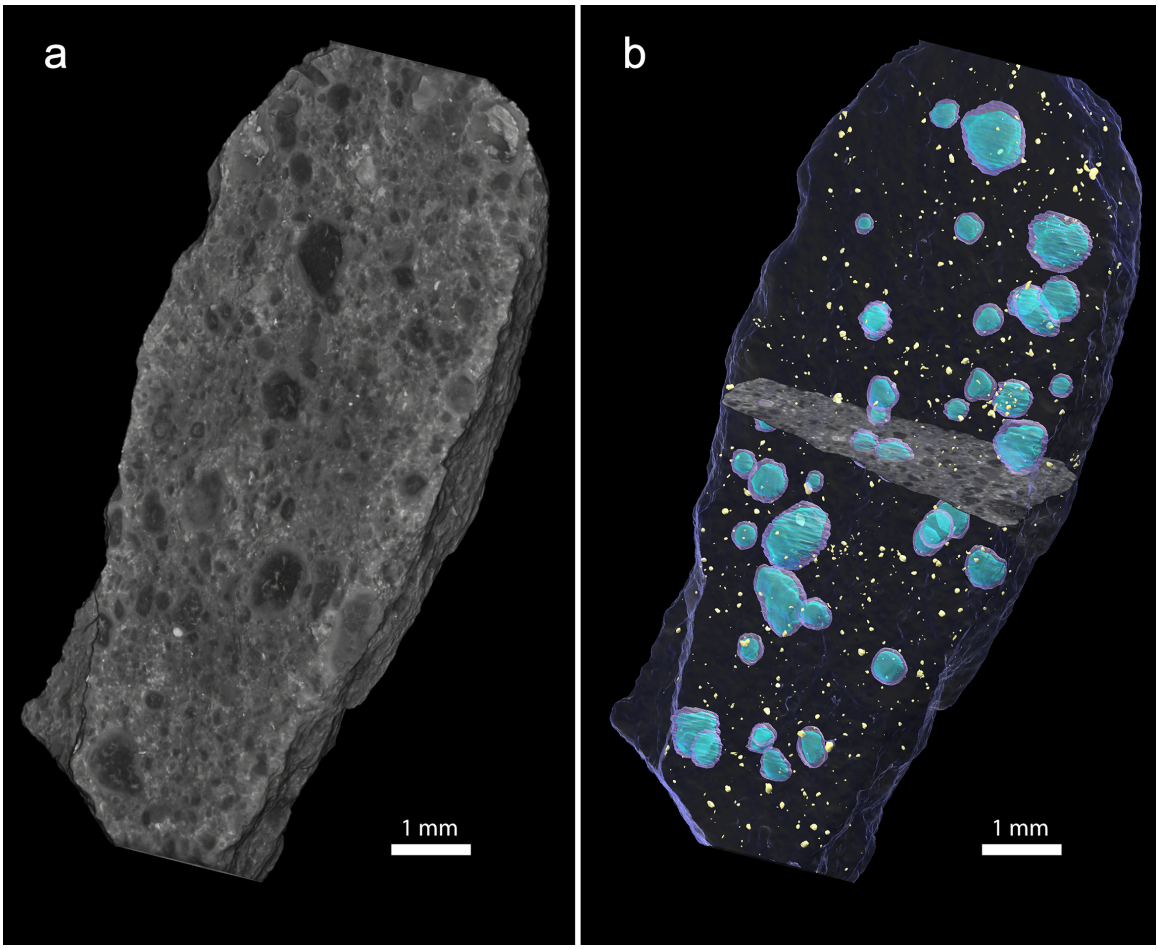

Fig. 1.8 3D visualization of XCT data of CM Murchison.
(a) Grayscale volume rendering of full dataset. (b) Isosurface of sample exterior is rendered as transparent dark blue. Fe sulfides and rare metal grains are rendered as yellow isosurfaces. A set of segmented chondrules (Hanna and Ketcham, 2015) is rendered as semitransparent isosurfaces. Light blue is chondrule interior and purple is surrounding fine-grained rim (FGR). Grayscale nonorthogonal slice is also shown near the center and intersects two segmented chondrules. Renderings were done in Avizo™ (FEI Company).

process of quantification from XCT data is given by Jerram and Higgins (2007). The usual first step in any quantitative analysis is segmentation, in which sets of voxels are designated as particular phases of interest (e.g., minerals, porosity). There are many ways to segment data, and one major difference among different 3D analysis software programs is their segmentation capabilities (Table 1.1). In the simplest case a global

threshold (e.g., all voxels above a given CT number, or between two CT numbers) is used to isolate phases. Complications frequently arise as the CT number of phases can be heterogeneous, overlap with other phases, or be subject to blur, partial volume effects, or other artifacts. There is a rich literature on the development of segmentation algorithms that range from automatic to semi-automatic or user-guided techniques [see Pham et al. (2000) and Milan et al. (2014) for recent reviews]. Additional steps that may be required to facilitate segmentation of phases include pre-segmentation image filtering (e.g., to reduce noise or minimize artifacts), post-segmentation image processing (e.g., to fill holes or remove false detections or 'islands'), and separation to make distinct objects of the same phase that are touching, if individual objects are to be measured.

Chondrules within XCT data of meteorites have proven to be particularly difficult to segment (Ebel and Rivers, 2007). Chondrules are usually polymineralic, with the same phases as the surrounding matrix material, and therefore are typically only distinguished by textural clues such as their large size, spherical shape, and/or differing grain size compared to the matrix (e.g., Griffin et al., 2012; Hanna et al., 2015; Lindgren et al., 2015). One promising technique uses local histograms of intensity to semi-automatically segment large components [including chondrules, Ca,Al-rich inclusions (CAIs), and dark inclusions] from the surrounding matrix (Griffin et al., 2012). This algorithm has been implemented into an open-source ImageJ plugin, PhaseQuant (Elangovan et al., 2012). Another recent technique allows for the segmentation of chondrules using a minimum of three orthogonal planes, enabling rapid segmentation of chondrules while preserving the accuracy of segmentation and measurement (Hanna et al., 2015).

After segmentation and any additional processing is complete, various measurements can be made on the segmented entities using commercial visualization software (Table 1.1) or academically produced quantification freeware (Table 1.2). Among the latter is Blob3D which provides a rich set of object-based measurements including size, shape, surface area, projected area, CT number statistics, contact relationships, and orientation data (Ketcham, 2005a; Ketcham, 2005b). In addition it

Table 1.2 Quantitative measurement freeware for XCT data.[a]

Name	Measurement Capabilities	Other Features	Download
Blob3D	Discrete object measurements: size, shape, projected area, surface area, primitive shape (ellipsoid) approximation, orientation information, CT number statistics, contact relationships	PVE correction, PSF measurement, image processing tools, segmentation and separation utilities	www.ctlab.geo.utexas.edu/software/
Quant3D	3D fabric orientation measurements using fabric tensors	Interactive 3D rose diagrams	www.ctlab.geo.utexas.edu/software/
PhaseQuant	Modal phase abundances and object size distributions	Access to other ImageJ utilities, segmentation module, ground truth tool, and density calibration module	http://geomodeling.uni-koeln.de/Geo-Cosmochemical_Modeling/PhaseQuant.html
Ctsta	Multiscale porosity, percolation and anisotropic permeability, including cluster analysis	Parallelized code can handle very large datasets	Contact developer at liujie86@mail.sysu.edu.cn
Slice	Discrete 3D object measurements: size, primitive shape (ellipsoid) approximation. Also modal analysis of binary data.	Image processing tools, command line interface and scripting	http://www-bl20.spring8.or.jp/slice/

[a] See Table 1.1 for commercial visualization software with more limited quantitative measurement capabilities.

provides a mechanism for accounting for the PVE (Ketcham, 2006a) and characterization of the PSF (Ketcham and Hildebrandt, 2014). Quant3D characterizes pervasive 3D textural fabrics that are defined by distinguishable phases (e.g., minerals, porosity) within the sample (Ketcham, 2005b). PhaseQuant can calculate phase modal abundances (including porosity), object sizes, and provide an interphase distribution measurement, although it is currently optimized only for oxidized CV chondrites (Elangovan et al., 2012; Hezel et al., 2013a). However, PhaseQuant does provide a unique ground truth optimization feature that can estimate the measurement error on the modal phase abundances (Elangovan et al., 2012). Ctsta is a parallelized program that can analyze large segmented volumes to calculate multiscale porosity, percolation, and anisotropic permeability (Liu et al., 2009). Slice is a command-line UNIX-based program that can make discrete object measurements and calculate modal abundances (Nakano et al., 2006). Planetary studies utilizing the capabilities of some of these tools are discussed in the following section.

1.5 Applications in planetary science

We next highlight several recent applications of XCT to the study of planetary materials and analogs. Preceding reviews, including Ebel and Rivers (2007), reported on the earliest XCT investigations of planetary materials, so we will focus on studies published in the last decade or so. This includes an excellent special issue of *Geochimica et Cosmochimica Acta* in 2013 on the 3D imaging of planetary samples (Hezel et al., 2013b) from which several studies are highlighted.

1.5.1 Three-dimensional petrography

As a 3D investigation tool, XCT has enabled a new and powerful type of geological research – 3D petrography. Volumetric data encompass the complete specimen, unlike the limited characterization provided by thin sections, providing more opportunities for key observations. While mineral composition cannot be directly

determined via XCT (except in special cases; Section 1.5.4), the combination of XCT data with traditional 2D microanalytical techniques (e.g., optical petrography, electron microbeam analysis) allows extrapolation to a 3D context. In addition, the unique 3D space of XCT permits the observation and quantification of petrographic textures and relationships only discernible in a 3D context.

One example of the 3D petrographic analysis possible with XCT is the study of two CV Allende and Mokoia chondrites by Hezel et al. (2013a), in which 3D modal abundances of chondrules and CAIs, compound chondrules, matrix, sulfide, metal, and porosity were derived using PhaseQuant with backscattered electron (BSE) images as ground truth data. The authors achieved a relative error of about 10% and, significantly, were able to separate the 3D modal abundances of metal and sulfide between chondrules and matrix. They interpreted the chondrule/matrix modal abundances with previously acquired Mg/Si ratio data to support chondrule-matrix complementarity and their formation from the same nebular reservoir. They were also able to view intrachondrule porosity and opaque-layered chondrules in both chondrites, and in observing a size dichotomy of opaques within chondrules versus the matrix, suggested that the latter were most likely not derived from the former as has been suggested for the CR chondrites (Connolly et al., 2001).

Needham et al. (2013) utilized XCT data to make several key observations of primary and secondary mineralogy as well as fracture networks within the Nakhla Martian meteorite. Unpolished sections from the XCT-scanned sample were used to examine fragile secondary phases (halite, sulfate, iddingsite) with an SEM. Then, after isolating the igneous host minerals of these phases within the XCT data, they were able to examine the 3D fracture network around them that enabled fluid flow for precipitation of the secondary minerals, including a gravitationally enclosed basin which provided a "way up" indicator for the meteorite's original orientation on Mars. They also calculated modal abundances of pyroxene, olivine, feldspar, and opaques on both a 2D slice and 3D volume basis, revealing that mm-scale heterogeneity could significantly influence "whole

rock" geochemical analyses if not properly accounted for. Tomkinson et al. (2015) found similar modal abundance heterogeneity within another nakhlite, NWA 5790, by using XCT data. In this case the heterogeneity could be partially explained by the inhomogeneous distribution of olivine within the sample, easily visible as clusters in the 3D XCT data.

A recent application of XCT to 3D petrographic analysis is the measurement of fine-grained rims (FGRs) in the Murchison CM chondrite (Hanna and Ketcham, 2015). By scanning a small chip (143 mg) at relatively low energy (70 keV) and high spatial resolution (5.5 μm) they were able to discriminate the FGRs around chondrules due to their lower iron content relative to the surrounding matrix (Fig. 1.9a).

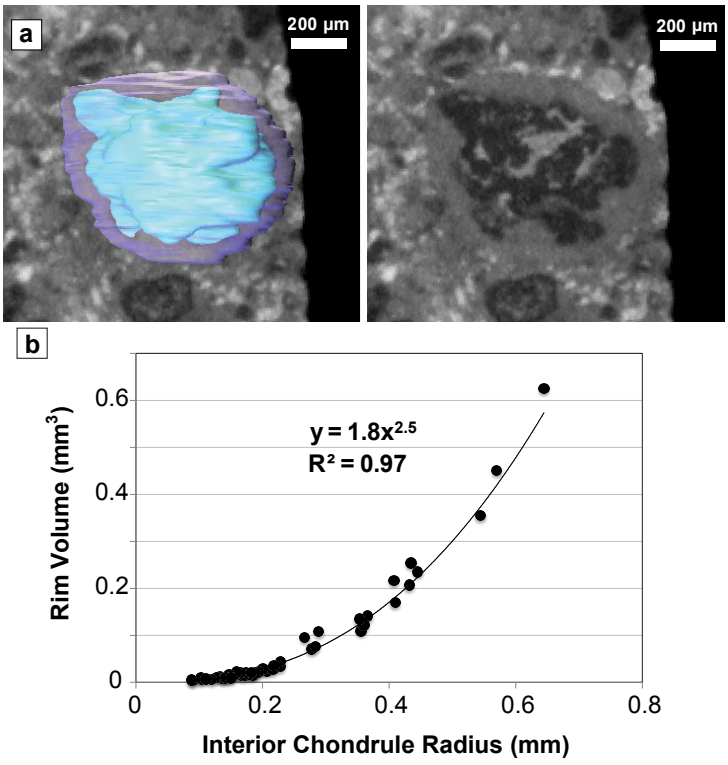

Fig. 1.9 Fine-grained rims (FGRs) in CM Murchison. *(a) Example of a segmented chondrule and FGR. Left image shows whole segmented chondrule with rim (purple) and chondrule interior (blue) bisected by XCT slice and right image shows XCT slice only. Scale bar the same for both images. The chondrule interior has a highly irregular shape but the exterior surface of the rim does not and is smoother. (b) Rim volume versus chondrule interior equivalent spherical radius. The data are well fit by a power law relationship, as proposed by Cuzzi (2004) for chondrules accreting dust rims in the protoplanetary nebula.*

Each chondrule was segmented twice (with and without the FGR), and their analysis showed that FGR volume is related to the interior chondrule equivalent spherical radius

by a power law as proposed by Cuzzi (2004), strongly supporting a nebular formation model of FGRs (Fig. 1.9b). Work is ongoing to measure more chondrules to refine the power law fit and to examine the rim thickness in 3D to determine how the FGR may have been affected by deformation (e.g., Lindgren et al. 2015; Hanna et al., 2015).

Two other unique applications of XCT 3D petrography are an investigation of an interconnected plagioclase network in an H7 chondrite (Tait et al., 2014) and a survey of chromite inclusions among a suite of ordinary chondrites (Alwmark et al., 2011). Tait et al. (2014) demonstrated that large plagioclase crystals that appear isolated within 2D section are actually largely interconnected in 3D (Fig. 1.10). By quantifying the node coordination of the plagioclase using a skeleton diagram they found that over 60% of the nodes have a coordination of 3 or 4 (Fig. 1.10c), strongly suggesting that the plagioclase has pseudomorphed a grain-supported melt network. Alwmark et al. (2011) imaged the interiors of 385 chromite grains from 8 ordinary chondrites with synchrotron XCT to demonstrate that almost two-thirds of chromite grains contain inclusions and that the size and number of the inclusions as well as the size of the host chromite grains vary systematically with petrographic type. Further, the degree of fracturing of the host chromite is correlated with the assigned shock stage of the chondrite. Therefore, study of fossil extraterrestrial chromite grains (the most common mineral to survive long-term weathering on Earth) can provide information on the ancient meteorite flux to Earth.

Friedrich (2008) explored the quantitative possibilities of 3D petrographic observations of XCT data. He tested the use of the gray level co-occurrence matrix (GLCM) (Petrou and Garcia Sevilla, 2006) for the description and classification of chondrites and demonstrated that GLCM descriptors could statistically distinguish between equilibrated L chondrites (Akaba and Castine), an unequilibrated L chondrite (Gunlock), and an oxidized CV (Allende). He also investigated the use of Betti numbers to describe metal morphology in the L chondrites and proposed that they may be a useful

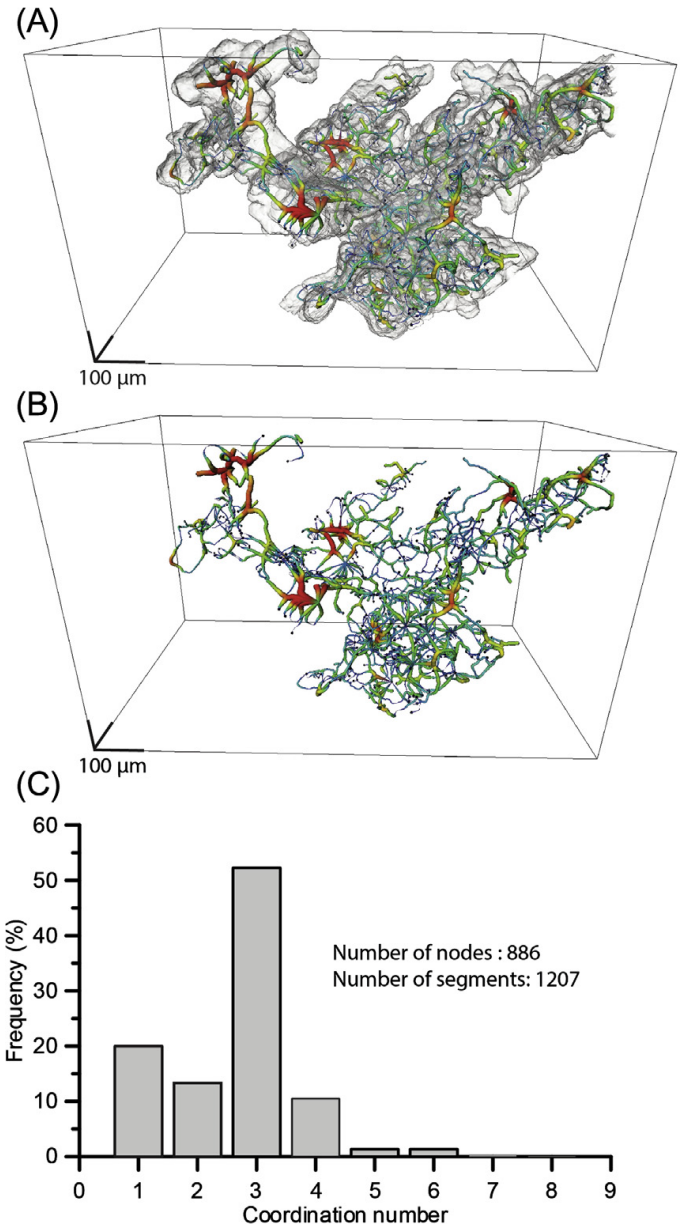

Fig. 1.10 Plagioclase network from XCT data of H7 ordinary chondrite Watson 012. *(a) Plagioclase rendered in grey over colorized skeleton network. (b) Colorized skeleton network where warmer colors emphasize thicker segments (wider plagioclase crystals). (c) Frequency distribution histogram of skeleton network in (b) showing that over 60% of nodes display coordination numbers of 3 or 4, consistent with a melt network in a grain-supported matrix. Figure reprinted from Tait et al. (2014) with permission.*

metric to characterize metal morphological changes that occur with increasing degrees of metamorphism.

Another quantification metric that has been used for petrographic observations of chondrite XCT data is the chondrule convolution index (CVI). Originally proposed as a 2D thin section measurement (ratio of chondrule perimeter to the perimeter of a circle with the same area) by Zanda et al. (2002), later studies expanded the CVI to a 3D measurement using XCT (Ebel et al., 2008; Hertz et al., 2003; Nettles et al., 2006). Hertz et al. (2003) calculated both the 3D CVI and 2D CVI (using orthogonal slices in XCT data) for three Renazzo chondrules and found that neither measurement appeared to be a reliable indicator of the degree of melting or "chemical maturation" of a chondrule, as suggested by Zanda et al. (2002). Nettles et al. (2006) expanded this comparison of 2D to 3D CVI by randomly slicing an XCT-scanned Semarkona chondrule hundreds of times (including non-orthogonal directions) and confirmed that the range in 2D CVI (0.70) for a single chondrule was wider than the range proposed by Zanda et al. (2002) to represent different degrees of chondrule melting (0.69). Ebel et al. (2008) examined eight Renazzo chondrules in detail with XCT and 2D petrographic section. They also found that the 2D CVI measurement was an unreliable indicator but did find that the 3D CVI agrees with the "eye's intuition" of the extent of chondrule melting. They cautioned, however, that the measurement itself is somewhat subjective and could be more informative if combined with 3D metal grain texture and abundance. They illustrated the huge variation in 2D chondrule metal abundance and distribution compared to the true 3D values that are measureable using XCT data, strongly advocating for the use of 3D petrographic observations of chondrules when feasible.

1.5.2 Petrofabrics

Petrofabrics within geological materials provide textural information that can be used to infer deformational history and geologic setting. Terrestrial studies have the advantage of field observations and orientated samples so the structural geology of a

large area can be investigated from field to microscopic scales. For extraterrestrial samples, similar structural studies are limited due to the lack of a larger spatial context and the relative rarity of material which restricts the opportunities for creating the multiple orientated sections that are traditionally required to measure a 3D fabric. As a 3D imaging technique, XCT overcomes the latter limitation and allows for investigation of structural fabrics on at least the hand-sample scale.

Due to their relatively high X-ray attenuation compared to less attenuating silicate minerals, metals can be easily segmented and measured in XCT data. An extensive study by Friedrich et al. (2008b) exploited this characteristic to measure several thousands of metal grains among a large suite of 25 ordinary chondrites using synchrotron XCT. Using Blob3D (Ketcham, 2005a; Ketcham, 2005b) they measured the size and orientation of the grains and found a strong increase in metal grain alignment with increasing shock stage (Fig. 1.11). This direct observation of metal grain alignment complements earlier work that used anisotropy of magnetic susceptibility (AMS) of metal to infer petrofabric development in increasingly impacted ordinary chondrites (Gattacceca et al., 2005).

Since their 2008 study, Friedrich and coworkers have used similar XCT methods to quantify metal grain shape and alignment in many other chondrites to infer their impact histories (Friedrich et al., 2013; Friedrich et al., 2014b; Gattacceca et al., 2014; Jenniskens et al., 2014; Krzesińska et al., 2015; Popova et al., 2013; Zolensky et al., 2010). Friedrich et al. (2014b) demonstrated that an H chondrite breccia experienced multiple impacts of varying intensities. Through XCT and petrographic analysis they identified three separate lithologies within the sample with varying metal petrofabric strengths and orientations. They inferred that at least two impacts occurred on the parent body and that the variably impacted material was mixed together prior to the final impact. In another H chondrite, Kernouvé (H6), Friedrich et al. (2013) established that an early shock event occurred while the host rock was hot (pre- or syn-thermal metamorphism) and resulted in metal vein formation caused by shear stress which accumulated ductile

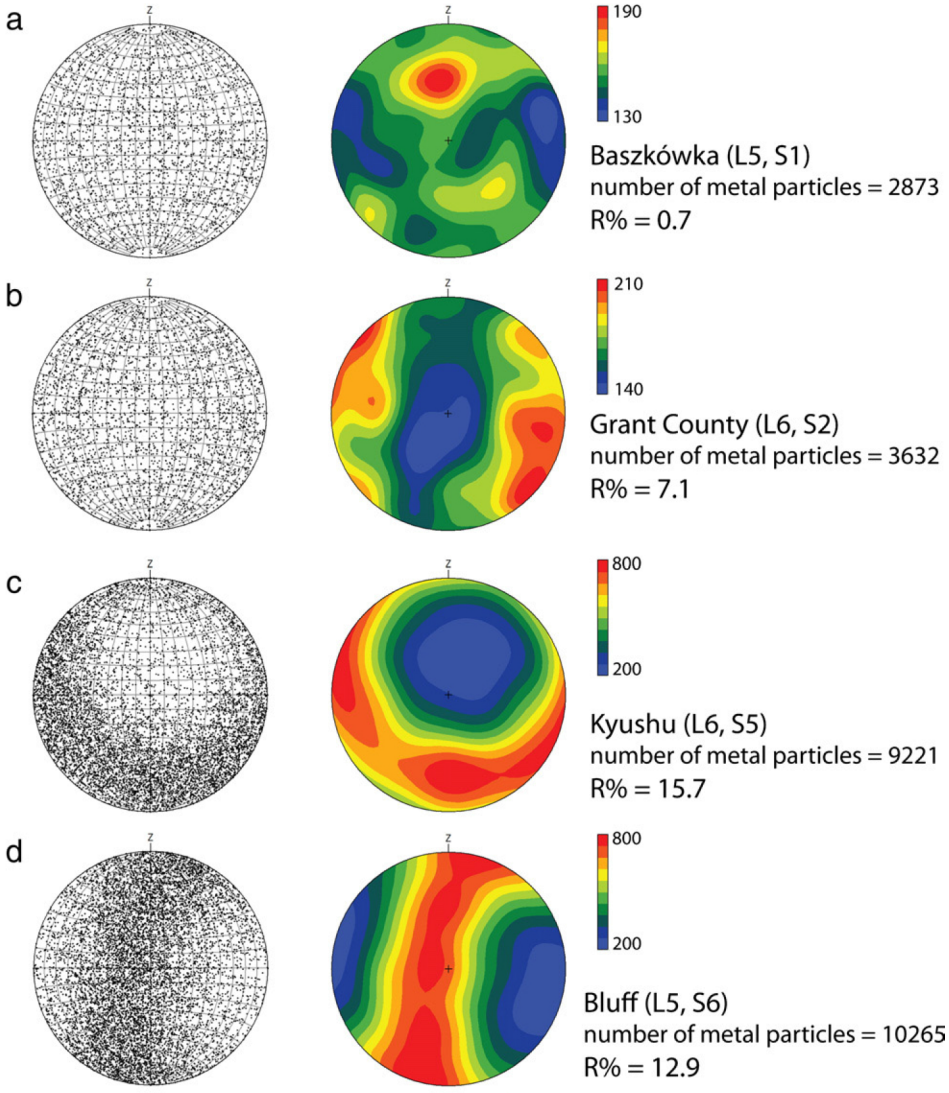

Fig. 1.11 Metal grain orientation in ordinary chondrites.
Metal grain alignment strength is quantified by R% (grain number independent) and generally increases with increasing shock stage for both L5 and L6 chondrites. Figure from Friedrich et al. (2008b) reprinted with permission.

metal grains along shear zones. The absence of a metal grain petrofabric in the chondrite further supported this interpretation, as thermal annealing likely erased any small metal grain alignment that occurred during impact and also reset the shock stage of the sample to S1. Ruzicka et al. (2015) found similar evidence for impact-shear-induced metal vein formation in the L6 chondrite Buck Mountains 005 using XCT. In addition, within the

XCT data they found dextral shear sense indicators in the form of asymmetrical lenses within a metal-poor dike. The probability that these structures would have been found in 2D thin section is low, as it would have required fortuitously oriented sectioning.

Krzesińska et al. (2015) also found evidence for noncoaxial shear from impact using XCT. They surveyed 38 samples of the Pultusk H chondrite and selected three for higher resolution XCT scanning (~4.5-5.2 μm/voxel). The data revealed dark zones of cataclastic matrix with elongated metal nodules and bands that are aligned with shear indicators in the matrix. By comparing the XCT-derived metal modal abundances of the dark (low attenuation) matrix to the surrounding lighter (higher attenuation) clasts (Krzesińska, 2011), they determined that the metal concentrations in the matrix could be attributed to metal migration at the expense of smaller surrounding grains. They found a pervasive metal grain foliation and lineation within the meteorite, and showed that the clastic matrix had a significantly stronger fabric, consistent with the localization of noncoaxial shear strain within these zones.

Benedix et al. (2008) also examined a metal grain fabric, but one that was only indirectly caused by impact. The L chondrite PAT 910501 is an unshocked impact melt with vesicles, metal, and sulfide grains, with the latter frequently in direct contact (Fig. 1.12a). XCT revealed a preferred orientation to both the metal-sulfide contacts and the vesicles, which were both clustered but offset relative to each other (Fig. 1.12b). Because the sample represents a relatively slowly cooled impact melt (Mittlefehldt and Lindstrom, 2001), they interpreted the orientation of the metal-sulfide contacts as an alignment to the local gravitational field as the sheet cooled. Further, the association of the larger vesicles with metal-sulfide intergrowths suggested that the vesicles formed via sulfur vaporization. The offset of the vesicles' long axes orientations to the metal-sulfide contacts was interpreted to result from minor melt turbulence, lateral melt movement that affected the vesicle orientations but not the metal-sulfide contacts, or the differing solidus temperatures of the metal and sulfide compared to the silicate melt which allowed for a gravitational vector change between their respective solidifications. Regardless, the XCT

data provided a rare indication of the gravitational field orientation on the parent asteroid.

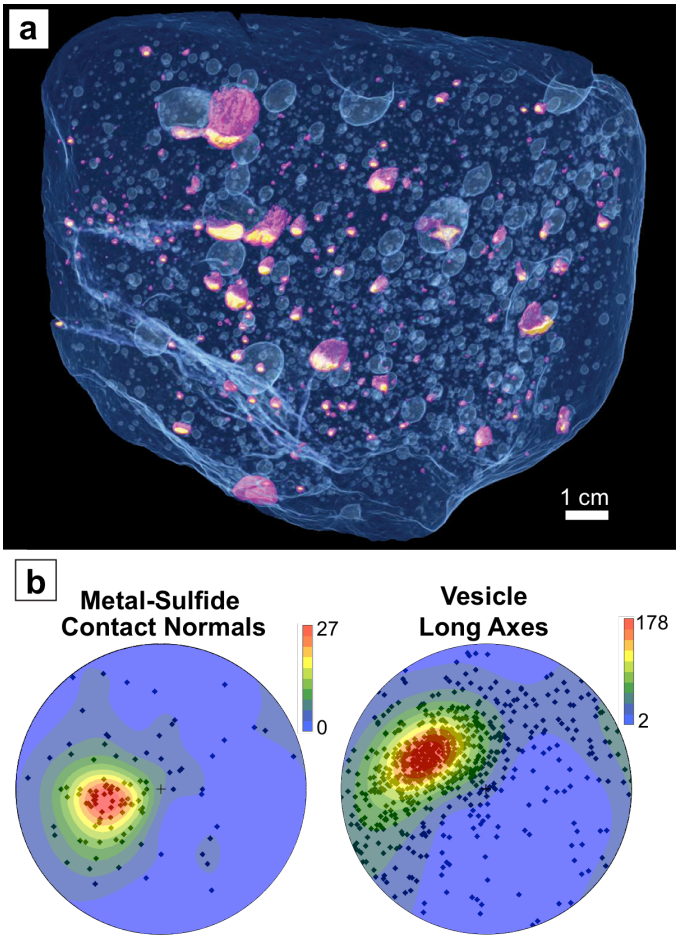

Fig. 1.12 Gravitational orientation of PAT 91501 from XCT.
(a) 3D visualization of XCT data of PAT 91501 from Benedix et al. (2008). Sample exterior and vesicles are rendered transparent blue, metal is yellow and sulfide is magenta. Specimen is orientated in implied crystallization orientation, with sulfide above metal, indicating gravitational orientation on parent body. Note that vesicles are elongated in a direction offset to the metal-sulfide contact (to the left in the image) (b) Stereoplot orientations in PAT 91501 from Benedix et al. (2008). Normals to planes of metal-sulfide contacts (left) and long axes of vesicles (right). Both are clustered indicating a preferred orientation. Orientation of metal-sulfide contact indicates gravitational direction in parent body during solidification of impact metal but the vesicle long axes are offset to this orientation.

In addition to metal grains, chondrules frequently define petrofabrics in chondrites (e.g., Dodd, 1965; Martin and Mills, 1980; Rubin and Swindle, 2011). Because chondrules are typically composed of the same minerals (dominantly ferromagnesian silicates and phyllosilicates) as the matrix, they have similar X-ray attenuation and therefore cannot be as easily segmented as metal grains (Ebel and Rivers, 2007; Hanna et al., 2015). Despite this, a few recent studies have examined chondrule petrofabrics in chondrites using XCT (Almeida et al., 2015; Hanna et al., 2012; Hanna et al., 2015; Lindgren et al., 2015). Almeida et al. (2015) manually segmented chondrules in XCT data of the Leoville CV chondrite and demonstrated that the 2D aspect ratio (measured from random 2D sections) consistently underestimates the 3D strain. The other studies (Hanna et al., 2012; Hanna et al., 2015; Lindgren et al., 2015) used orthogonal segmented sections (Section 1.4.4) to derive the shape and orientation of chondrules in the Murchison CM chondrite, with Lindgren et al. (2015) demonstrating again that the 2D aspect ratio underestimates the 3D strain. Lindgren et al. (2015) also found that the strain orientation indicated by the chondrule foliation differed from that derived by calcite *e*-twin analysis, which they attributed to multiple impacts. Hanna et al. (2015) found evidence for a weak lineation in addition to the foliation defined by deformed chondrules in Murchison. They used the petrofabric orientation measured in the XCT data to cut an oriented thin section from the Murchison sample and found evidence for multiple generations of brittle fracturing and other microtextures aligned with the foliation plane and lineation direction (Fig. 1.13a). They also found that some of the aligned fractures were filled with alteration minerals (serpentine and hydrated sulfide), strongly suggesting that aqueous alteration was contemporaneous with or post-dated the deformation events (Fig. 1.13b). Finally, they used the 3D aspect ratio of the deformed chondrules to estimate the finite strain experienced by Murchison and from this derived an estimate of pre-deformation bulk porosity of 32.2-53.4% [compared to the current Murchison porosity of 22.1% measured by He pycnometry (Macke et al., 2011)].

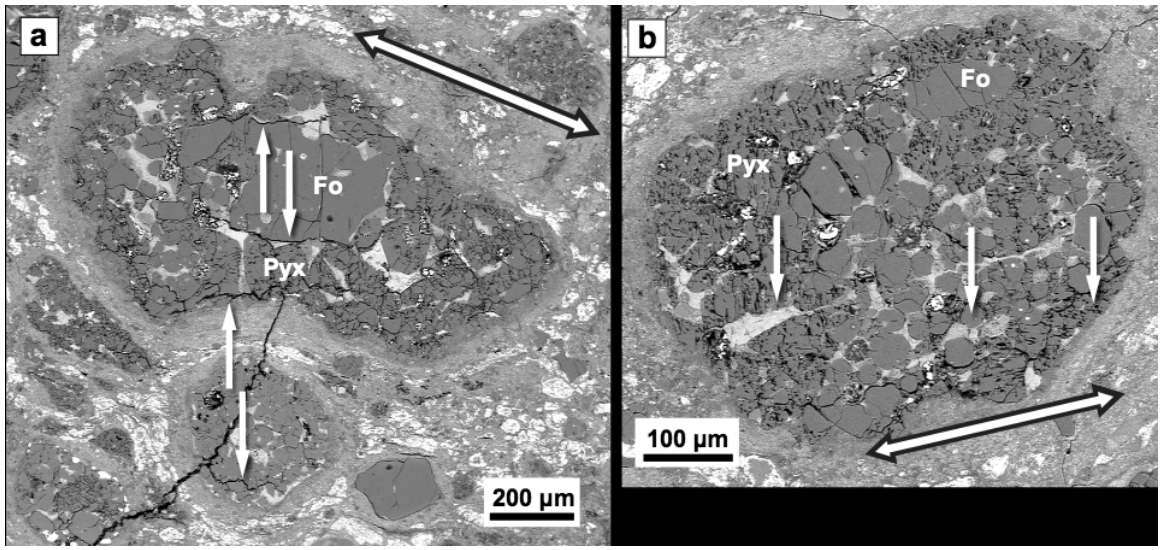

Fig. 1.13 Deformation and alteration textures in CM Murchison.
BSE images of CM Murchison. Large black and white 2-way arrows designate orientation of foliation plane and lineation direction derived from 3D measurement of deformed chondrules in XCT data. Thin section was cut perpendicular to the foliation plane and parallel to the lineation direction. (a) Smaller chondrule is impinging upon the larger chondrule 'above' it and the implied compression direction is approximately perpendicular to the foliation plane. White arrows indicate fractures approximately (sub-) parallel to the petrofabric. (b) Chondrule is flattened in plane of foliation. White arrows indicate large Fe-Mg serpentine vein approximately parallel to the petrofabric. Modified from Fig. 10 of Hanna et al. (2015). Fo = Forsterite, Pyx = Mg pyroxene.

1.5.3 Porosity

Chondrite porosity is most commonly measured using ideal gas pycnometry (e.g., Consolmagno et al., 2008; Macke et al., 2011). However, this measures only bulk porosity and does not provide information on its location or morphology. And while 2D thin sections can be examined to obtain such information, sample preparation can also introduce secondary porosity that can be difficult to discriminate from primary porosity. These issues can be overcome by imaging porosity in-situ and non-destructively with XCT, although there will be a resolution limit below which porosity will not be discernible. Friedrich et al. (2008a) examined a porous (19%) L chondrite (Bsazkówka) using both He pycnometry and XCT and found that on average 64% of the pore space

could be imaged and quantified with XCT at a scan resolution of 16.8 μm. They estimated that only individual pores larger than ~$3x10^{-5}$ mm^3 could be resolved, indicating that nearly two-thirds of the porosity is in the form of large inter- and intra-granular voids, which they interpreted as likely uncompacted, primitive porosity. Sasso et al. (2009) expanded the study to 5 more ordinary chondrites (LL, L, H) but scanned each chondrite twice: one sample at 16.6 μm resolution and a second sample of the same meteorite at 8.3 μm resolution. Unsurprisingly, they found that the higher resolution scan was able to image more of the total porosity (up to 72%) compared to the lower resolution scan (up to 51%) and, similar to Friedrich et al. (2008a), inferred that the majority of XCT-resolvable porosity in these relatively unshocked (S1-S2) chondrites is in the form of original uncompacted porosity, rather than impact-induced porosity (Fig. 1.14). Friedrich et al. (2014a) continued the study still further and found that while all 6

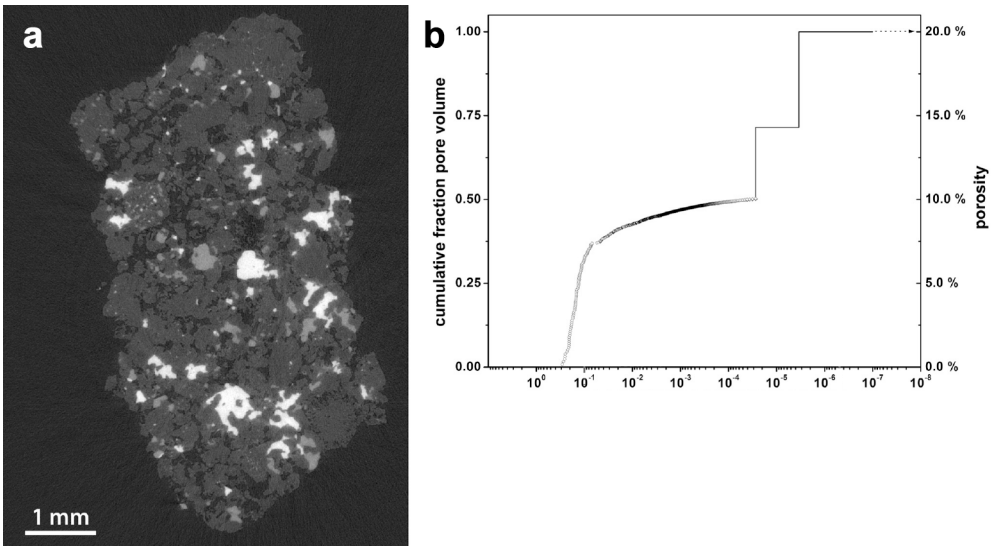

Fig. 1.14 XCT porosity of H5 Miller.
(a) XCT slice of uncompacted ordinary chondrite H5 Miller showing metal (nearly white), FeS (light grey), silicates (dark grey) and pore space (nearly black). Note the abundant large intergranular porosity. (b) Cumulative distribution of porosity in H5 Miller from He pycnometry and XCT. Individual pores were measured in the low-resolution XCT (16.6 μm) scan but not the high-resolution (8.3 μm) scan. Top limit of 20.0% porosity measured by He pycnometry. XCT is able to resolve ~51% and ~72% (low- and high-resolution scans, respectively) of the total porosity. Modified from Figures 1 and 2 of Sasso et al. (2009).

of these ordinary chondrites (OC), plus an additional LL chondrite (MIL 99301), were shock stage S1, they contained relict shock indicators. Based on ^{40}Ar-^{39}Ar dating and additional petrographic evidence of thermal annealing, they concluded that these chondrites experienced mild impacts into already hot material very early in OC parent body history, which produced relatively high shock features in silicates (subsequently annealed) while preserving a significant and rare amount of original, primitive porosity.

Friedrich and Rivers (2013) examined a suite of variously compacted/shocked ordinary chondrites at a resolution of 2.6 μm to determine the structural differences of microporosity among these chondrites. They demonstrated that XCT was able to resolve the vast majority of the microporosity in them (72 -100%) at this scale. They also determined that the structure and location of microporosity has a regular relationship to the degree of compaction. Relatively compacted and shocked samples (Kyushu and Moorleah) retained the majority of their microporosity in the form of fractures and microcracks that are visible as sheet-like structures in the 3D data. In contrast, the microporosity of uncompacted samples (Bsazkówka and ALH A7725) is present as discontinuous intragranular and intergranular voids with little evidence of microcracks or fractures among the grains. This study demonstrated an important difference in the 3D structure of porosity among variably compacted chondrites that would have been impossible to characterize with bulk porosity measurements or more destructive 2D sectioning techniques.

Another unique approach to measuring porosity using XCT was done by Beitz et al. (2013a; 2013b). Rather than directly imaging porosity, these authors inferred its presence (at scales below the scan resolution) in planetary analog materials by calibrating the XCT grayscale values using nonporous material within the data. The first study (Beitz et al., 2013a) observed experimentally produced dust rims around chondrule analogs and derived porosity by examining the grayscale value between that of the pure analog material (zero porosity) and air (100% porosity). They then compared their results to porosity measured using backscattered electron (BSE) imaging of thin sections

and found comparable porosity values between the two methods. Using these techniques, they determined that chondrule analog dust rims formed in a hot environment (1100° C) averaged 60% porosity, whereas rims formed at room temperature (20° C) had a porosity of 75%. They inferred that sintering processes were important in reducing the porosity of the hot accreted rim. They also illustrated their technique on a sample of CM Murchison, measuring a porosity of ~10% in two chondrule rims which is comparable to values reported in the literature. Beitz et al. (2013b) used XCT to estimate the porosities of 25 experimentally impacted analog chondrule(bead)/dust mixtures. As in the (2013a) study, they estimated porosity by calibrating against the expected grayscale value of pure analog material with zero porosity. They found a sizeable range of maximum post-impact porosities, from 1 to 30% (initial porosities of the mixtures were calculated to be 39-70%), and the lowest porosities were achieved when the mixtures were 50/50 beads and dust. They also used the porosities of their impacted samples to calculate the pressures reached during compaction and inferred that the more porous CM chondrites were compacted and lithified at lower pressures than the less porous CV chondrites, confirming that the CMs are generally less shocked than the CVs.

1.5.4 Chemical composition and ultra-small particles

As discussed in Section 1.2, the linear attenuation coefficient (LAC) of a material is largely dependent on X-ray energy (Fig. 1.3) and therefore artifacts arise when reconstruction algorithms assume a single energy attenuation for data acquired using polychromatic sources. This severely complicates any attempt to use reconstructed CT numbers to derive the linear attenuation coefficient of a material (and thus the composition and/or density of the material itself). However, synchrotron sources can provide monochromatic X-rays that prevent these artifacts, allowing a quantitative relationship between CT number and theoretical LAC to be defined, especially for coarser grained material. Derivation of theoretical LAC values using fine-grained material will be more difficult as it does not account for variations in microporosity or

grain boundary networks, which will also directly affect CT number. Still, Tsuchiyama et al. (2005) succeeded in this effort using the SP-μCT system at the SPring-8 synchrotron facility. By imaging a set of standards of known composition, they determined an empirical relationship between CT number and theoretical LAC and confirmed that the relationship held for several minerals in a garnet schist rock.

Although specific to the SP-μCT system, this equation is independent of the material being imaged and has been successfully applied to the investigation of several meteorites. Uesugi et al. (2010) imaged a variety of meteorites (ordinary chondrites, CV3, CO3, shergottite, ureilite, and an iron meteorite) and demonstrated that the Fe content of olivine can be obtained and is comparable to the value obtained by SEM-EDS. They also demonstrated that subtle Fe/Mg zoning in an olivine phenocryst can be quantified using their LAC relationship (Fig. 1.15). They do point out that at the energies

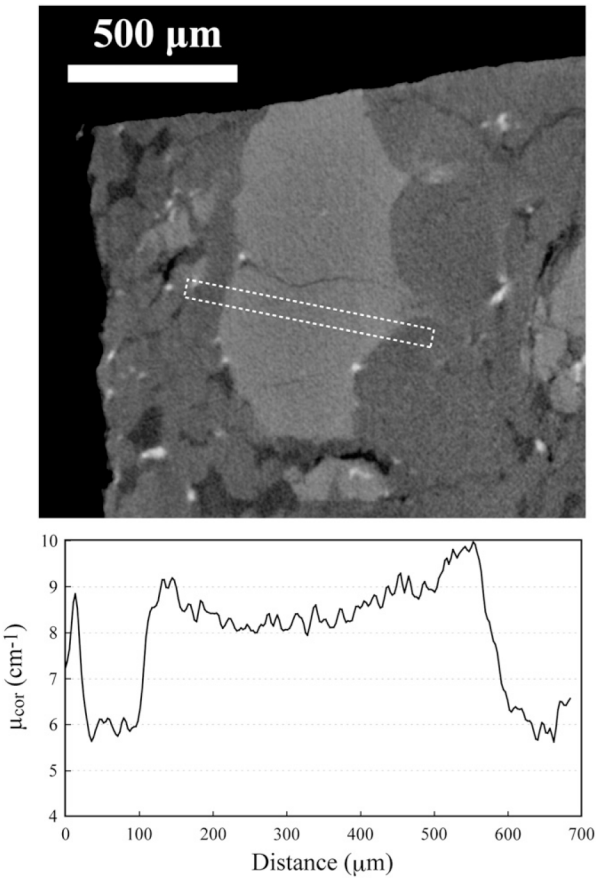

Fig. 1.15 Zoning in olivine phenocryst using LAC.
(top) XCT slice of shergottite DaG 476 with olivine phenocryst. White dotted box shows location of LAC line profile (bottom). Plotted values are averaged perpendicular to the long side of the rectangle. Zoning in olivine is evidenced by its LAC variation from 8.1 to 10.0 cm^{-1} (center to rim), which is equivalent to Fa29-39. Figure from Uesugi et al. (2010) reprinted with permission.

(≥ 30 keV) required to avoid noise-related artifacts in these 4-5 mm sized silicate and metal-bearing samples, the LAC values of some minerals overlap and thus textural observations are required to determine the mineral phase. However, with this information, chemical compositions of major minerals in meteorites can be determined, and general classification of meteorite samples is possible by using histograms of the LAC values present in an XCT dataset. Uesugi et al. (2013) applied the LAC method to a large suite of carbonaceous chondrites to further investigate the use of the LAC histograms to determine the chemical compositions of chondrules and matrix. They demonstrated that the peak LACs of both are correlated, indicating a compositional complementarity between them. They also extracted low-Fe inclusions (representing mainly chondrules, but also CAIs, amoeboid olivine aggregates (AOAs), and low-Fe silicate grains) and analyzed their size distributions, finding that they are unique among the different chondrite classes. Both of these findings supported localized formation of chondrites without large mixing in the nebula.

Motivated by the ambiguity of chemical composition in the LAC approach outlined above, Tsuchiyama et al. (2013) explored the use of analytical dual-energy XCT to more accurately determine mineral composition. This method was first introduced for the investigation of Hayabusa particles (Nakamura et al., 2011; Tsuchiyama et al., 2011) but a detailed description of the method is presented in Tsuchiyama et al. (2013). This method utilizes the LAC approach of Tsuchiyama et al. (2005) but scans the sample twice at different energies, 7 and 8 keV, which are on either side of the Fe K-absorption edge (Fig. 1.5). For Fe-bearing minerals, the LAC value will vary significantly between the two scans, and the signature of this variation will be unique among different minerals (including Fe-bearing solid solutions), allowing more precise determination of the mineral phase and chemical composition. Fig. 1.16 shows an example of the dual-energy method on a heterogeneous Hayabusa particle. After imaging the particle, Tsuchiyama et al. (2013) mounted and polished the sample for SEM analysis and verified that the Mg# of olivine and low-Ca pyroxene matched EPMA results to within ~5% error. Due to the

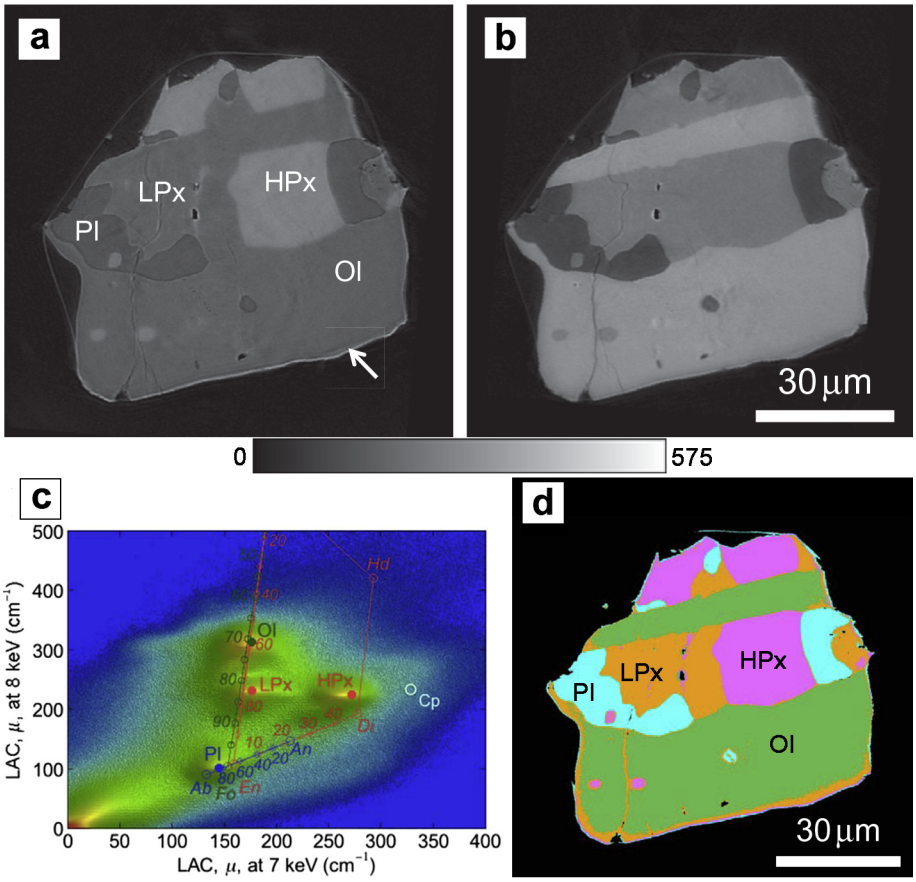

Fig. 1.16 Composition of Hayabusa particle from XCT.
Hayabusa particle RA-QD02-0024. (a) XCT LAC of particle at 7 keV. Arrow points to X-ray refraction artifact (phase contrast) at particle edge. (b) XCT LAC of particle at 8 keV. (a) and (b) have same scale and the greyscale bar indicates the LAC values of the images. (c) 2D histogram of LAC values at 7 and 8 keV; logarithmic density of the histogram is mapped to a rainbow color scale (bright blue is zero, red is maximum). Graph shows detail of silicate mineral LACs; metal and oxides plot outside this space. Numbers along the forsterite (Fo)–fayalite, enstatite (En)–ferrosilite, enstatite (En)–diopside (Di), and albite (Ab)–anorthite (An) lines are the forsterite, enstatite, wollastonite and albite contents (in mol.%), respectively. Ferrosilite and fayalite end members are just outside the plot area (above 500 cm^{-1} on the 8 keV axis). Large solid circles show LAC values calculated from the mean chemical composition of the minerals within the particle. (d) Mineral phase map determined by LAC analysis. Misidentifications are present at some surfaces, phase boundaries, and fractures. Ab: albite, An: anorthite, CP: Ca phosphate (F-apatite), Di: diopside, En: enstatite, Fo: forsterite, Hd: hedenbergite, HPx: high-Ca pyroxene, LPx: low-Ca pyroxene, Ol: olivine, Pl: plagioclase. Modified from Figures 2, 4, and 5 of Tsuchiyama et al. (2013).

low energies (≤ 8 keV), however, there is a size limit of around 100 microns to the grains that can be analyzed using this technique (for imaging at the Fe K-absorption edge; if another element absorption edge is desired, the scan energies and thus maximum particle sizes will change).

Because of the small sizes of the imaged particles, the dual-energy XCT technique requires higher scan resolution (submicron) than is typical of standard XCT systems (>1 μm/voxel), even when using a synchrotron source (Wildenschild and Sheppard, 2013). To achieve this, an X-ray magnification optics system utilizing a Fresnel zone plate (FZP) was installed on a beamline at the SPring-8 facility (Uesugi et al., 2006). This system has been successfully used to image a variety of ultra-small particles at nanometer resolution (Section 1.6), including Hayabusa (Ebihara et al., 2015; Nakamura et al., 2011; 2013; Tsuchiyama et al., 2011) and Stardust (Nakamura et al., 2008a; 2008b) particles as well as organic nanoglobules from the C2 chondrite Tagish Lake (Matsumoto et al., 2013). Nakamura et al. (2008a; 2008b) achieved up to 43 nm resolution using the FZP setup to image several Stardust particles at 8 keV and examine the structure of both crystalline and amorphous particles. Nakamura et al. (2008b) also used the LAC relationship established by Tsuchiyama et al. (2005) to measure the Mg# of olivine in the crystalline particles and found that they were largely forsteritic (≥ 78 Mg#). Ebihara et al. (2015) measured the Mg# of olivine in Hayabusa particles using LAC analysis (84-96 nm resolution) and found that they are consistent with a composition of Fo68-Fo71. Matsumoto et al. (2013) imaged a particle of the C2 Tagish Lake meteorite at 42 nm and identified 38 organic nanoglobules (≤ 1 μm in size). They were not able to determine unambiguously whether they were hollow or fluid-filled, but they were able to confirm that none of them contained silicate (mineral grain) cores.

1.6 Future directions

The evolution of XCT is largely driven by advances in source and detector technologies that allow higher resolution and/or faster acquisition, or that provide new,

complementary data modalities. In detectors, increased efficiency (in both speed and sensitivity) can significantly decrease measurement time per frame and facilitate time-resolved XCT experiments that can image dynamic processes in as little as one millisecond per projection, although the high brilliance of a synchrotron source is required (e.g., Armstrong et al., 2014; Mokso et al., 2011). Decreased detector element size and increased number of detector elements will also continue to see incremental upgrades. One of the latest innovations in detector technology is a hybrid pixel array detector (HPAD, also known as a photon counter) (Broennimann et al., 2006; Willmott, 2011). Unlike traditional CCD detectors, which accumulate a charge and then convert this into a digital signal, HPADs directly detect every single X-ray photon above a set energy, leading to a large reduction in background noise and thus greatly increasing SNR (Willmott, 2011). This new type of detector has already been installed at several synchrotron beam lines[3].

Another active area of detector technology research is the development of X-ray detectors that can record the energy of the incoming X-ray photons, enabling chemical characterization (e.g., Egan et al., 2015). Currently there are two types of energy-sensitive detectors: 1) multispectral detectors that count single photon energies within each pixel and divide the detections into 5-10 energy bins; and 2) hyperspectral detectors that measure the energy accumulated in each pixel during an exposure time (frame) and subsequently reconstruct the pixel energy spectrum (Boone et al., 2014; Egan et al., 2015). The latter has the advantage of much greater spectral resolution but at a cost of measurement and processing time. Both of these detectors require a polychromatic X-ray beam and thus are well suited to laboratory-based XCT machines, although the detector technology has not yet been incorporated into commercial systems. However, Egan et al. (2015) demonstrated the potential for chemical characterization of a mineralized ore sample by replacing the standard flat panel detector in a commercially available laboratory-based XCT system with a HEXITEC hyperspectral detector (Fig. 1.17). As

[3] https://www.dectris.com/references_list.html, accessed December 15, 2015.

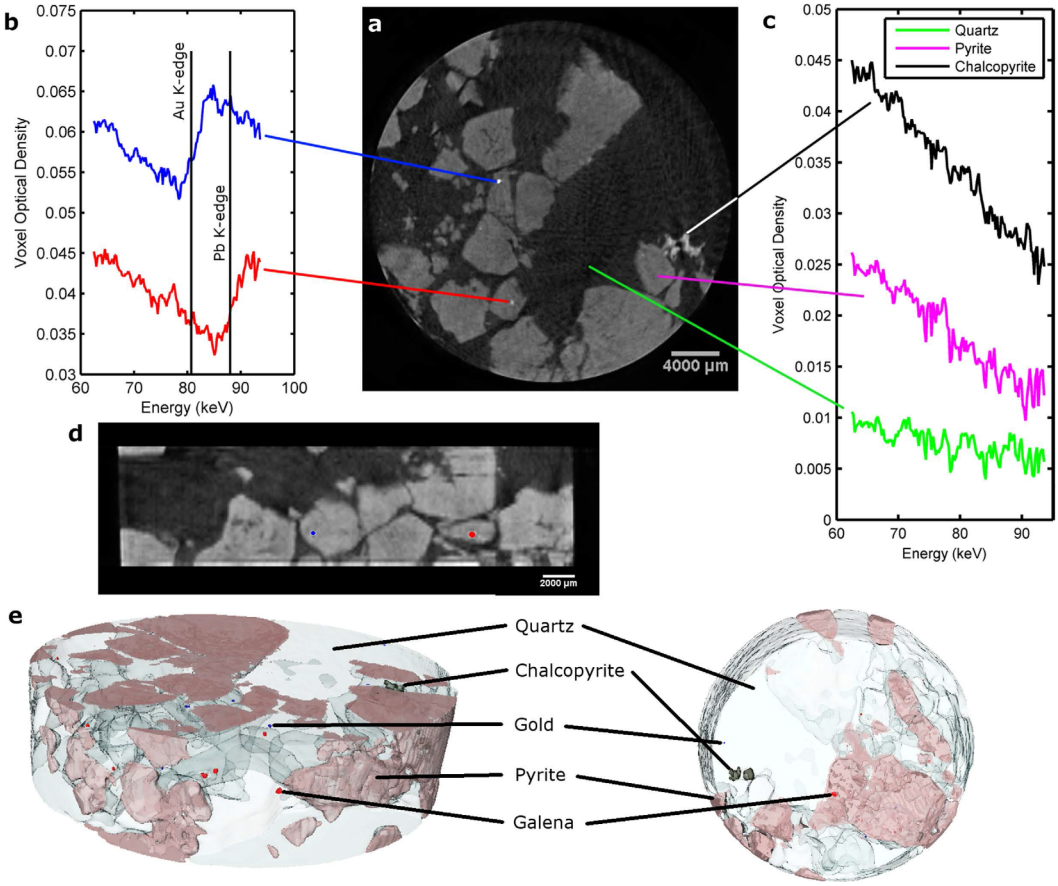

Fig. 1.17 XCT scan using hyperspectral X-ray detector of gold-bearing ore core. *(a) 2D grayscale XCT slice of core. Grayscales represent integrated attenuation over full spectral range. (b) Single voxel spectra of two particles showing gold and lead K-edges. (c) Single voxel spectra of quartz, pyrite, and chalcopyrite. (d) 2D grayscale XCT reslicing perpendicular to scan plane, highlighting segmented particles of gold (blue) and lead (red). (e) 3D visualization of core showing distribution of the various minerals. Figure from Egan et al. (2015) reprinted with permission.*

this detector technology matures it is anticipated that it will be added to commercially available XCT systems, opening up a myriad of avenues to explore 3D chemical composition in a laboratory setting.

Another way to derive 3D composition is to combine XCT with another analytical technique that can provide elemental or crystallographic information such as X-ray fluorescence (XRF) or X-ray diffraction (XRD) (e.g., Bleuet et al., 2010; Lemelle et al., 2004; Poulsen, 2004; Uesugi et al., 2013). The technique of combining XRF with XCT

is further along but still limited in application as XRF tomography requires pencil beam rastering across the sample during each projection image resulting in significant acquisition times (Bleuet et al., 2010; Wildenschild and Sheppard, 2013). However, recent investigations utilizing position-sensitive X-ray spectrometers distributed around the sample stage have aimed to improve imaging speed (Meng et al., 2011). Still, fluorescence X-rays are prone to self-absorption and therefore typically only the outer few millimeters of a sample can be imaged (Wildenschild and Sheppard, 2013). In contrast, XRD has a penetration depth comparable to normal X-ray attenuation (Section 1.2.2), so combining XRD with XCT is more straightforward. In its most basic implementation, a pencil (focused) beam is rastered over the sample for each projection, but this necessarily leads to long acquisition times (e.g., Grant et al., 1994; Uesugi et al., 2013). For example, using XRD-CT, Uesugi et al. (2013) were able to image the distribution of olivine, serpentine, and pentlandite in a CM Murchison particle but only reconstructed a single slice due to the long experimental time (2 hours for 1 slice). Much research has been done to create a true 3D tomographic XRD system that can map grain orientations in 3D using a non-focused, full-field beam (e.g., Grant et al., 1994; Herbig et al., 2011; Johnson et al., 2008; King et al., 2014; Ludwig et al., 2007; Poulsen, 2004). There are several variants of implementation, but X-ray diffraction contrast tomography (DCT) is unique in that simultaneous acquisition of diffraction data and absorption (XCT) are possible (Johnson et al., 2008). Further, DCT can be done using a polychromatic X-ray tube source, enabling 3D crystallographic orientation mapping without the requirement of a synchrotron source (King et al., 2013) and is very recently available as an option on Zeiss Versa systems (Feser et al., 2015; McDonald et al., 2015).

There are several new developments in both laboratory and synchrotron X-ray sources that aim to increase flux, decrease spot size, and/or reduce heat on the target. For standard X-ray tubes, the latest advancement is the replacement of the solid metal target with a continuous liquid metal jet as the anode (e.g., Espes et al., 2014; Hemberg et al., 2003; Larsson et al., 2011). This allows increased power output (flux) even at smaller

focal spots, as thermal damage or melting of the target material is not a concern (see Section 1.3.1). For synchrotron sources, development of the next (fourth) generation is mainly focused on increasing the brilliance of the beam either through the use of an Energy Recovery Linac (ERL) or a Free Electron Laser (FEL), although the latter produces a destructive beam (Sham and Rivers, 2002; Willmott, 2011). There is also active research intro shrinking the size of synchrotron sources to bring the brilliance of synchrotron radiation to a standard laboratory setting [i.e., Compact Light Source (CLS)] (Wildenschild and Sheppard, 2013; Willmott, 2011). These will not be as brilliant as current third-generation synchrotron sources, but will supply a flux somewhere between that of an X-ray tube and a storage ring beamline (Willmott, 2011). These are still in the development stage, although the first tomographic data utilizing a CLS have recently been acquired (Eggl et al., 2015).

Nanoscale XCT imaging (nanoCT), achievable at synchrotron sources for a couple of decades (e.g., Nakamura et al., 2008b; Sakdinawat and Attwood, 2010), is now possible with laboratory-based sources. The first implementations utilized SEMs; directing the electron beam on a metal target produces an X-ray beam that can be used for full-field tomographic imaging of small samples (Vonlanthen et al., 2015). Although a theoretical resolution of ~50-60 nm is reported, this requires specialized software corrections that are not widely implemented on commercial systems (Brownlow et al., 2006; Mayo et al., 2005). Actual implementations on commercial laboratory SEMs report resolutions an order of magnitude larger than this (~500-600 nm) (Mayo et al., 2007; Russell and Howard, 2013; Vonlanthen et al., 2015). Russell and Howard (2013) imaged an unmelted CAI from the Allende CV3 chondrite at 550 nm resolution. The XCT data revealed that the CAI is a complex, porous network of rounded nodules, suggesting that it formed by condensation from a gas rather than from crystallization of a melt. Vonlanthen et al. (2015) imaged small volcanic ash particles also using an SEM-based XCT system. They included a detailed analysis and discussion of the actual spatial resolutions possible and concluded that, while the projection images have a resolution of

~650 nm, mechanical instability, electron beam drift, and data processing can introduce significant blur into reconstructed images, making the practical spatial resolution (see Section 1.3.3) somewhat lower than this. These resolution limitations combined with long acquisition times [~17-36 hours; (Vonlanthen et al., 2015)] make their use somewhat limited, although future improvements in electron beam drift and mechanical stability should improve resolution (Mayo et al., 2007). For now, several commercial cone-beam laboratory scanners can acquire data with similar resolution and faster acquisition times [see Fig. 1 in Maire and Withers (2014)].

The only true nanoCT (< 100 nm resolution) laboratory systems commercially available today are the 800 or 810 Ultra systems sold by Zeiss. These systems utilize a high efficiency condenser lens and a Fresnel zone plate (FZP) to achieve a maximum spatial resolution around 50 nm (Tkachuk et al., 2007). They are also equipped with an annular phase ring that can be optionally inserted to produce Zernike phase contrast within the tomographic volume (Eastwood et al., 2014; Tkachuk et al., 2007). Phase contrast tomography is based on the refraction, as opposed to absorption, of X-rays at interfaces and so can highlight interior boundaries and edges (Eastwood et al., 2014; Wilkins et al., 1996; Withers, 2007). In fact, phase contrast effects are almost always present to some extent in XCT data from synchrotron sources due to the highly coherent beam (Cloetens et al., 2002; Fusseis et al., 2014).

Finally, ever-increasing advances in computational capabilities are driving development of XCT, mainly in the areas of data processing and reconstruction software. For example, the general evolution of more powerful computers is enabling the development of more complex and/or automated XCT data segmentation algorithms such as Object Based Image Analysis (e.g., Leitner et al., 2014) and Iterative Local Thresholding (e.g., Deng et al., 2016). Increased processing speeds and the implementation of XCT reconstruction on GPUs (e.g., Fang and Klaus, 2007) are facilitating the use of iterative reconstruction (IR) algorithms, which are more accurate but computationally more expensive than filtered back projection (FBP) (De Witte et al.,

2010; Hsieh, 2009). While FBP filters and projects the data only once, IR converges on a solution through repetition, requiring more computational resources (Beister et al., 2012). There is a myriad of types of IR algorithms and the recent review article by Beister et al. (2012) gives an informative overview of the major variants and recent developments.

These algorithms also enable reconstruction approaches that can produce high quality data from specialized XCT techniques such as discrete tomography and sparse imaging (Batenburg and Sijbers, 2011; Maire and Withers, 2014; Sidky et al., 2006). Discrete tomography aims to combine image reconstruction and segmentation in a single step, where the output of the reconstruction is a segmented data volume (e.g., Batenburg and Sijbers, 2011). This works well in situations where a few known homogenous materials are present and greatly simplifies the reconstruction iterations as the number of possible grayscales is limited (Batenburg and Sijbers, 2011). In addition, Myers et al. (2011) demonstrated how the simplified reconstruction of discrete tomography can enable time-resolved tomographic imaging of dynamic processes using two-phase fluid flow as an example. In sparse (or under-sampled) imaging, only a limited number of views are collected and IR algorithms have been shown to produce data superior to FBP in these situations (Chen et al., 2008; LaRoque et al., 2008). Sparse imaging is a particularly promising approach for XCT of dynamic processes in the laboratory where lower X-ray flux precludes the fast data acquisition possible with a synchrotron source (e.g., Mokso et al., 2011). Reconstruction with limited views would allow for faster data acquisition, perhaps on a timescale of some dynamic processes, although this has yet to be demonstrated (Maire and Withers, 2014).

1.7 Summary

X-ray computed tomography is an essential tool for 3D imaging at a wide range of spatial scales, with increasing improvements in technology enabling nanometer-scale resolutions and time-resolved experiments even in a laboratory setting. It has been applied with great success to address many problems in planetary science and the

expectation is that its use will only grow as the technique becomes more widely available and adopted. Its exceptional capabilities for 3D visualization and quantification have been amply demonstrated, and future developments, most notably the integration of XCT with other techniques that can be used to determine chemistry and/or mineralogy, will greatly expand its utility. Certainly, XCT is quickly earning its place among the standard analytical techniques available today to study planetary materials.

Chapter 2: Impact-induced brittle deformation, porosity loss, and aqueous alteration in the Murchison CM chondrite[4]

2.1 Introduction

CM chondrites contain undifferentiated solar system material that is generally considered primitive, but detailed study has demonstrated that many chondrites have been heavily processed by deformation (impacts/burial), aqueous alteration, and brecciation (Biscoff et al., 2006; Brearley, 2006; Bunch and Chang, 1980; Stoffler et al., 1988). Unraveling these effects is important for understanding the alteration processes taking place on asteroids—for example, the cause and timing of aqueous alteration (Brearley, 2006; Krot et al., 2006). Additionally, identifying and 'seeing through' the effects of post-accretion alteration and deformation will help better constrain models of formation of the primitive components (e.g., chondrules) as well as models of planetary accretion (e.g., location and conditions of parent body formation within the solar nebula).

Deformed chondrules and aligned, textural petrofabrics are not uncommon among chondrites (Cain et al., 1986; Dodd, 1965; Martin and Mills, 1980; Martin et al., 1975; Rubin and Swindle, 2011; Scott et al., 1992; Sneyd et al., 1988; Zolensky et al., 1997). Deformation textures have variously been attributed to burial (Cain et al., 1986; Zolensky et al., 1997) or impact (Lindgren et al., 2015; Rubin, 2012; Rubin and Swindle, 2011; Scott et al., 1992; Sneyd et al., 1988), and have been proposed to have a positive correlation with aqueous alteration among the CM chondrites (Rubin, 2012). Chondrule deformation due to impact is emerging as the favored mechanism, as several studies demonstrate a correlation between deformation and other impact-induced features such as shock level and anisotropic magnetic susceptibility (Gattacceca et al., 2005; Nakamura et al., 1992; Scott et al., 1992; Sneyd et al., 1988). In addition, experimental studies of

[4] The material presented in this chapter is a modified version of the Geochimica et Cosmochimica Acta publication - Hanna R. D., Ketcham R. A., Zolensky M. and Behr W. (2015) Impact-induced brittle deformation, porosity loss, and aqueous alteration in the Murchison CM chondrite. *Geochim. Cosmoch. Acta* **171**, 256-282. I performed all data collection and analysis and wrote the paper in its entirety. Coauthors provided minor data interpretation support and revision editing.

impact compaction of chondrites show that chondrules will deform and foliate in response to impact stress (Nakamura et al., 1995; Nakamura et al., 2000; Tomeoka et al., 1999). It has been hypothesized that chondrule deformation during impact is due to matrix pore collapse and the chondrule 'squeezing' into the surrounding pore space (Nakamura et al., 1995; Scott et al., 1992). However, the microstructural mechanisms that allow the chondrules to change shape in such a marked degree have not been investigated in much detail. Nakamura et al. (1992) examined olivine and pyroxene in the strongly foliated Leoville CV chondrite and suggested that impact shock plastically deformed the chondrules, resulting in high dislocation densities and undulose extinction of olivine leading to its shock stage classification of S3 (Scott et al., 1992). Scott et al. (1992) found that other CVs with prominent petrofabrics also display a high shock stage (≥ S3), indicating that some plastic deformation occurred during the impact that foliated the chondrules. Based on these correlations between shock stage and petrofabric, plastic deformation of silicates within the chondrules is often assumed to be the primary strain-accommodating mechanism (Bland et al., 2014; Cain et al., 1986), but there has been no direct investigation as to whether plastic deformation is actually the mechanism by which the chondrules change shape.

Several CM chondrites also show foliated chondrules but the mechanism behind these is puzzling as CMs consistently have a low shock stage (S1-S2), suggesting that plastic deformation of the silicates within chondrules should be insignificant (Scott et al., 1992). The Murchison CM chondrite classified as S1-S2, in particular, was noted early on to have a "lineated fabric" on several stones (Fuchs et al., 1973), and Fujimura et al. (1983) found a preferred alignment of phyllosilicate basal planes (001) in their Murchison sample by using X-ray pole goniometry. More recently X-ray computed tomography (XCT) has been used to show that chondrules in Murchison are deformed and show a moderate foliation (Hanna et al., 2012; Lindgren et al., 2015). Lindgren et al. (2015) explained this apparent anomaly by proposing that Murchison, along with most

other CMs, has experienced multiple mild-intensity impacts which foliated the chondrules but left the ferromagnesian silicates relatively unshocked.

Another process that has been intimately linked with impact-induced foliation fabrics in chondrites is porosity loss. An inverse correlation between porosity and impact-induced petrofabrics (anisotropy of magnetic susceptibility) has been found in ordinary chondrites (Gattacceca et al., 2005; Sugiura and Strangway, 1983) and Martin and Mills (1980) made the more general observation that less friable (presumably, less porous) chondrites display stronger preferred alignments of deformed chondrules. Impact experiments into the Allende CV chondrite verified that progressively stronger impacts increasingly reduced the porosity while increasing the 2D aspect ratio of deformed chondrules (Nakamura et al., 2000). All of these observations lend strong support to the idea that chondrules are deforming from impact as pore collapse in the matrix (i.e. porosity loss) is occurring (Nakamura et al., 1995; Scott et al., 1992). Therefore, quantifying the amount that chondrules have been deformed from an initial state could also provide the amount of matrix porosity loss that the chondrite has experienced.

Porosity is an important material property that greatly affects a wide range of physical processes. Porosity significantly influences cratering mechanics; not only does it contribute to the attenuation of impact shock waves but it also determines the amount and distribution of waste heat generated (Melosh, 1989; Sharp et al., 2006). Porosity affects permeability and the movement of water through an object, controlling the extent and type (e.g., open- vs. closed-system) of aqueous alteration. Porosity also influences a material's thermal conductivity and therefore its thermal inertia (Zimbelman, 1986), which has implications for the movement of heat and energy on an asteroid. Meteorites, being samples of asteroids, are expected to exhibit physical characteristics, including porosity, similar to them. However, measurement of meteorite porosity and comparison with the estimated porosity of asteroids based on remote observations has shown that asteroids are significantly more porous than their meteorite analogs. The average

porosity of CM chondrites is ~24.7% (Macke et al., 2011) whereas C-type asteroids (generally interpreted to represent CM chondrite material) have an average porosity of ~38% with values up to 80% (Britt et al., 2002).

Typically this porosity difference is attributed to macroporosity in asteroids that is larger than the scale of our meteorite samples (Britt and Consolmagno, 2000). High macroporosities can have significant implications for the internal coherency and structure of an asteroid, leading to the interpretation of an asteroid as a 'rubble-pile' (Britt and Consolmagno, 2000). But there is also surely a sampling bias, as highly porous, friable carbonaceous chondrites are unlikely to survive ejection from the parent asteroid (Scott et al., 1992) or Earth entry and landing (Baldwin and Sheaffer, 1971; Consolmagno et al., 2008). Indeed, carbonaceous chondrites comprise less than ~2% of our meteorite collection but spectral data indicate that low-albedo carbonaceous asteroids dominate (> 75%) the main belt asteroid population (Chapman, 1999; McSween, 1999). Therefore, our chondrite collection may not provide an accurate representation of actual asteroid microporosities.

We have two primary objectives with this work. First, we investigate the fabric of the deformed chondrules in Murchison to determine its origin and to quantify the strain the sample has undergone. We then use this information to derive an estimate of pre-deformation porosity. Second, we use a range of microanalytical techniques to determine the microphysical mechanisms (brittle vs. plastic) and the strain-accommodating phases that allowed the chondrules in Murchison to change shape from their initial state. This will enable us to determine the cause and conditions of deformation in the Murchison sample and explore the implications and consequences of such deformation in the larger picture of secondary processing on the CM parent body.

2.2 Analytical methods

2.2.1 X-ray computed tomography

We used X-ray computed tomography (XCT) to create digital three-dimensional (3D) datasets of Murchison sample USNM 5487 (44 g). XCT is a non-destructive imaging technique that produces a series of two-dimensional (2D) images (slices) where the gray scales in each image represent X-ray attenuation, which is to first order dependent on the density and mean atomic number (Z) of the material (Ketcham and Carlson, 2001). It is nearly non-destructive [no sample preparation required and the instrument does not heat or alter the sample apart from possible organics modification (Bertrand et al., 2015; Moini et al., 2014)] and provides a full 3D context to textural and/or petrographic observations. For more details on and geological applications of XCT refer to Ketcham and Carlson (2001) and Ebel and Rivers (2007).

We scanned the sample both in its entirety and within two smaller sub-volumes at higher resolution (Fig. 2.1). The full-volume and sub-volume #1 scans were done on the ACTIS scanner Feinfocus subsystem (microfocal X-ray source and image intensifier detector) at the University of Texas High Resolution X-ray CT Facility (UTCT) with intensity control off and in high power mode. The full-volume scan settings were 120 kV, 0.25 mA, 1800 views, 2 samples per view, inter-slice spacing 58.16 μm and inter-pixel spacing 53.71 μm. The sub-volume scan settings were 180 kV, 0.22 mA, 2400 views, 2 samples per view, inter-slice spacing 32.05 μm, and inter-pixel spacing 29.30 μm. The specimen was mounted in a plexiglass cylinder, and the X-ray signal was calibrated by measuring the signal through the empty cylinder. Sinograms were corrected for ring artifacts, streaks, and beam hardening using in-house IDL-based software. For the full-volume scan the beam hardening correction method described in Ketcham and Hanna (2014) was used and parameters included two-material mode, reducing image resolution by 4x during optimization runs, and 5 points for the linearization function. The sub-volume scan had less beam hardening, due to its simpler

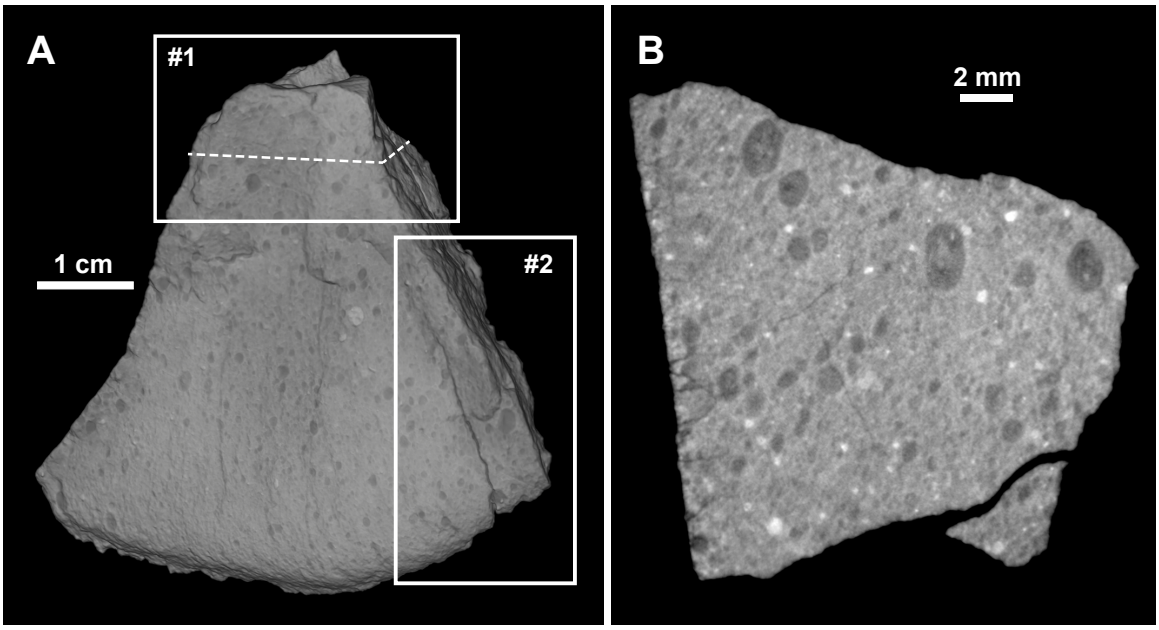

Fig. 2.1 Murchison XCT subvolume locations and example data.
(a) *3D volume rendering of USNM 5487 using XCT data of full-volume scan. White boxes indicate sub-volume scan areas and dashed line shows location of b.* ***(b)*** *XCT slice #211 from sub-volume scan #1.*

geometry and the higher X-ray energy used, so a standard polynomial correction was applied. Slices were reconstructed using a customized version of the standard BIR reconstruction software to produce 16bit TIFF images. A post-reconstruction rotation correction was applied to the full-volume scan to correct for stage rotation errors between slice acquisition sets. A post-reconstruction ring correction (Ketcham, 2006b) was applied to the sub-volume TIFFs to eliminate remaining rings, and for both scans duplicate slices in overlapping sets were deleted.

We scanned the second sub-volume on the Xradia microXCT instrument at the UTCT facility. The sub-volume was scanned at 100 kV and 10W with a 1 second acquisition time per view (1081 views) using the LFOV objective. The detector-object distance was 43.5 mm and the source-object distance was 66.0 mm. The detector pixels were binned by a factor of 2 to increase the signal-to-noise ratio and a 1 mm CaF_2 pre-filter used to decrease beam-hardening artifacts. Instrument stage dithering prevented

ring artifacts and all other reconstruction parameters (center shift, beam-hardening correction, byte scaling and kernel smoothing) were applied in the Xradia instrument software. The final reconstructed data set has a voxel size of 40.54 μm.

2.2.2 XCT fabric measurement

XCT data from the full-volume and sub-volume #1 scans are shown in Fig. 2.1. The brightest greyscales in the images represent the most attenuating material (i.e. the phases with the highest density and/or mean atomic number) and the darkest greyscales the least attenuating material. We defined two components based on greyscale and morphology: a volumetrically minor bright component and a relatively more abundant dark component that is almost always manifested as an elliptical object in 2D (Fig. 2.1b). We segmented the bright objects (isolated from the XCT volume) using an automatic thresholding algorithm in Blob3D (Ketcham, 2005a; Ketcham, 2005b).

The dark objects required more specialized processing, as their greyscale range overlapped with that of the surrounding matrix. The only reliable means of delineating them accurately was manual segmentation in Avizo™ software, principally "brush" tools that allow one to paint the regions in the data. Hand-painting all voxels encompassing a given chondrule is very labor intensive, however, and a more efficient alternative was developed. Starting in Avizo™, one or more representative cross sections in each orthogonal plane were manually segmented for each chondrule. These data were then exported to Blob3D, and an ellipsoid was fitted to their outer margins using a specialized merit function. This partial segmentation method was tested and found to provide an accurate representation of orientation and degree of anisotropy of the object compared to the traditional full segmentation approach in Blob3D (Ketcham, 2005a). To get an accurate shape and orientation measurement, only dark objects without visible fractures were segmented for analysis.

After segmentation the size, location, and orientation information of each object was calculated using Blob3D (Ketcham, 2005a; Ketcham, 2005b). Orientation

information is derived by fitting an ellipsoid to the segmented component (using either the full object or orthogonal sections) and exporting the magnitude and orientation of the three axes of the ellipsoid. These ellipsoid orientations are plotted on stereonets in lower hemisphere projection using the Stereo32 software (Roeller and Trepmann, 2010). Because the scan geometries of the two sub volumes were different from the full volume scan, the orientation measurements from the sub volumes were rotated to match the full volume scan orientation (procedure described in Appendix B).

Stereo32 is also used to test whether a set of object (ellipsoid) orientations are non-random and define a petrofabric using the spherical statistics parameters defined by Woodcock and Naylor (1983). These authors define two parameters, K and C, which describe the shape and strength respectively of a fabric defined by a set of vector orientations (in our case, the set of ellipsoid axes). For a set of orientations, the three eigenvectors are calculated and the eigenvalues (i.e. magnitude of the eigenvectors) are defined as S_1, S_2, and S_3. The petrofabric shape is characterized by the shape parameter

$$K = \ln\left(\frac{S_1}{S_2}\right)/\ln\left(\frac{S_2}{S_3}\right) \quad (1)$$

which ranges from zero (girdle or 'great circle' distribution on a stereonet; $K < 1$) to infinite (cluster distribution; $K > 1$) (Woodcock and Naylor, 1983). The strength of the fabric is characterized by the strength parameter

$$C = \ln\left(\frac{S_1}{S_3}\right) \quad (2)$$

where a weak fabric has C close to zero and a strong fabric has C around 4 or above (Woodcock and Naylor, 1983).

Because the calculated eigenvectors represent the three dominant, orthogonal directions in a set of individual orientations, they also uniquely describe the fabric orientation of each scan volume. For example, the primary (longest) ellipsoid axes of uniformly flattened objects that define a foliation fabric will lie in a girdle (shape parameter $K < 1$) when plotted on a stereonet (Turner and Weiss, 1963). The first and second calculated eigenvectors of these primary axes will lie on this great circle and the

third eigenvector will be orthogonal to these, i.e. it will represent the pole to the foliation plane. For a lineation fabric, the primary ellipsoid axes will lie in a cluster (shape parameter $K > 1$) on the stereonet and therefore the first eigenvector (strongest dominant direction) of this cluster will represent the lineation direction. Hence, in this work we define the orientation of the lineation and foliation direction in each scan volume as the orientation of the first and third eigenvectors, respectively, of the primary ellipsoid axes.

To determine the error in derived orientations of objects and fabrics using the partial orthogonal section method we tested this method on an XCT dataset of a garnet-kyanite schist that had been previously measured using the full segmentation method in Blob3D (Ketcham, 2005b). We segmented the garnets using both methods (partial orthogonal sections and full segmentation) and compared the derived orientations between them. Based on our results we estimate that measurement errors in absolute axial orientations for individual objects using best-fit ellipsoids to orthogonal sections will be up to 9° and slightly higher (10-12°) when using only 3 orthogonal planes to represent the object. However, as multiple measurements are combined to derive a fabric orientation, moderate to strong fabrics ($C > 2.0$) will have only about 4° of measurement error in fabric orientation (depending on the sample size and number of planes used). Weaker fabrics ($C < 2.0$) will have larger errors in fabric orientation, up to 11°.

2.2.3 Optical and electron microscopy

We used the derived foliation plane and lineation direction orientations of dark-toned XCT objects in the full-volume scan to cut a thin section from the sample approximately perpendicular to the foliation and parallel to the lineation. Comparison of the actual cut thin section to the XCT data indicates that the thin section was cut approximately 101.9° to the foliation plane and 7.4° off of the lineation direction. The polished section was examined using an optical microscope and a JEOL JSM-64900 LV SEM in the Electron Microbeam Analysis Laboratory in the Jackson School of Geosciences at the University of Texas at Austin. The section was carbon-coated for the

SEM and all images and data were collected at 15 kV in high vacuum mode. The working distance was 10 mm and the spot size setting varied between 50 and 62 (unitless as it determines both the beam diameter and illumination current on this model). The smaller spot size was used for backscattered electron (BSE) imaging, as the large difference in atomic number Z in the sample caused image saturation at larger spot sizes. The larger spot sizes were used for energy dispersive X-ray spectroscopy (EDS) for more efficient spectrum collection and greater accuracy in peak identification. For all EDS spectra the EDAX Genesis software was used for automatic peak identification, but all identified peaks were manually verified. EDS spectra were used for qualitative phase identification where possible and for qualitative elemental composition otherwise. EDS X-ray elemental maps were collected using the automated collection algorithm provided by the EDAX Genesis software using major element Kα peaks.

2.2.4 Electron backscatter diffraction

After general petrography and phase identification was complete we removed the carbon coating and further polished the section for electron backscatter diffraction (EBSD). Carbon removal and polishing consisted of the following steps (section cleaned and rinsed between steps): 1) removal of carbon with 1 micron diamond polish, 2) polishing with colloidal silica, 3) 1 micron diamond polish, 4) 0.3 micron alumina polish, and 5) final polishing with colloidal silica. We performed EBSD on an FEI XL 30 ESEM equipped with an HKL Nordlys EBSD detector at the Electron Microbeam Analysis Laboratory in the Jackson School of Geosciences at the University of Texas at Austin. Section was mounted at a 70° tilt and all patterns were acquired at 25 or 30 kV with varying spot size 6.0-7.0 and working distance 11.0-17.9 mm. H_2O gas was used to keep constant pressure between 0.1 and 0.3 Torr (varied per session). Step sizes for automated mapping varied between 0.1 and 1.2 microns per pixel. Pattern acquisition and indexing was done in Oxford AZtec 2.2 software and we used the HKL Channel 5 software suite for post-processing and analysis.

2.3 Results

2.3.1 XCT petrofabric

Using auto-segmentation in Blob3D, we segmented light-toned objects from each of the three XCT scan data sets. To eliminate orientation biasing that can occur when an object subtends only a few voxels, any objects with a tertiary (short) ellipsoid axis less than 3 voxels in length were removed (Ketcham, 2005b). A summary of results is presented in Table 2.1 and the orientations of the primary and tertiary axes of the best-fit ellipsoids to the light-toned objects are presented in Fig. 2.2. Overall the orientations of both axes in all volumes are widely distributed, but contouring (calculated using cosine sums in the Stereo32 software) and a 99% confidence interval for a non-random distribution suggests that a preferred orientation may be present in the full-volume and sub-volume #1 data. However, not only are the calculated *C* strength parameters low ($C \leq 1.1$), but also the shape factor *K* is different for each dataset. The full-volume primary and tertiary axes display a weak girdle distribution ($K=0.9$ and $K=0.8$, respectively) while sub-volume #1 axes both indicate a cluster distribution ($K=2.0$ and $K=1.3$). This fabric inconsistency between scan volumes, combined with the complete lack of fabric in the sub-volume #2 dataset, suggests that no significant fabric is present among the light-toned inclusions and they are generally randomly orientated within the Murchison sample. We checked for evidence of a stronger fabric among subsets of inclusions in the full-volume data by limiting analysis to objects with the largest volume, highest aspect ratio (primary/tertiary axis lengths), or highest elongation (primary/secondary axis lengths), but found none.

A total of 475 dark-toned objects were segmented and measured among the three scan volumes and a summary of results is presented in Table 2.2. Fitted ellipsoid shapes of the dark-toned objects, plotted on a ternary diagram using the TRI-PLOT software (Graham and Midgley, 2000), show that the majority of the objects (66% total) depart from a compact (spherical) shape and that all three scan volumes show the same spread in

Table 2.1 Light-toned XCT object best-fit ellipsoid measurements

	Full-Volume (n=389)				Sub-Volume #1 (n=263)				Sub-Volume #2 (n=82)			
	Min	**Max**	**Mean**	**Std[4]**	**Min**	**Max**	**Mean**	**Std[4]**	**Min**	**Max**	**Mean**	**Std[4]**
Primary Axis Length (μm)	210	1000	370	110	120	760	230	100	150	740	260	100
Secondary Axis Length (μm)	180	900	300	100	100	580	190	80	140	730	210	80
Tertiary Axis Length (μm)	170	660	250	80	100	550	160	70	120	630	180	70
Aspect Ratio[1]	1.10	2.66	1.48	0.24	1.07	4.39	1.48	0.33	1.08	2.25	1.49	0.28
Elongation[2]	1.02	1.73	1.23	0.15	1.01	2.64	1.23	0.18	1.02	1.74	1.24	0.17
Flatness[3]	1.00	1.81	1.21	0.15	1.01	2.05	1.21	0.16	1.01	1.72	1.21	0.16
Volume (mm^3)	0.03	1.90	0.16	0.20	0.00*	0.99	0.05	0.11	0.01	1.43	0.06	0.16

[1]Primary axis length/Tertiary axis length [2]Primary axis length/Secondary axis length [3]Secondary axis length/Tertiary axis length [4]1σ standard deviation *Minimum volume = 0.0047 mm

Table 2.2 Dark-toned XCT object best-fit ellipsoid measurements

	Full-Volume (n=187)				Sub-Volume #1 (n=155)				Sub-Volume #2 (n=142)			
	Min	**Max**	**Mean**	**Std[4]**	**Min**	**Max**	**Mean**	**Std[4]**	**Min**	**Max**	**Mean**	**Std[4]**
Primary Axis Length (μm)	310	1880	690	270	150	1450	470	180	190	950	390	140
Secondary Axis Length (μm)	210	1460	560	220	120	1090	370	140	170	760	320	110
Tertiary Axis Length (μm)	150	1170	450	170	100	800	300	110	120	570	260	80
Aspect Ratio[1]	1.22	2.38	1.54	0.22	1.13	2.33	1.58	0.23	1.10	2.09	1.50	0.24
Elongation[2]	1.02	1.78	1.23	0.14	1.02	1.77	1.27	0.16	1.01	1.71	1.22	0.15
Flatness[3]	1.01	1.81	1.26	0.13	1.02	1.83	1.25	0.14	1.01	1.83	1.23	0.14
Volume (mm^3)	0.04	10.69	1.11	1.70	0.01	5.32	0.32	0.60	0.02	1.75	0.19	0.22

[1]Primary axis length/Tertiary axis length [2]Primary axis length/Secondary axis length [3]Secondary axis length/Tertiary axis length [4]1σ standard deviation

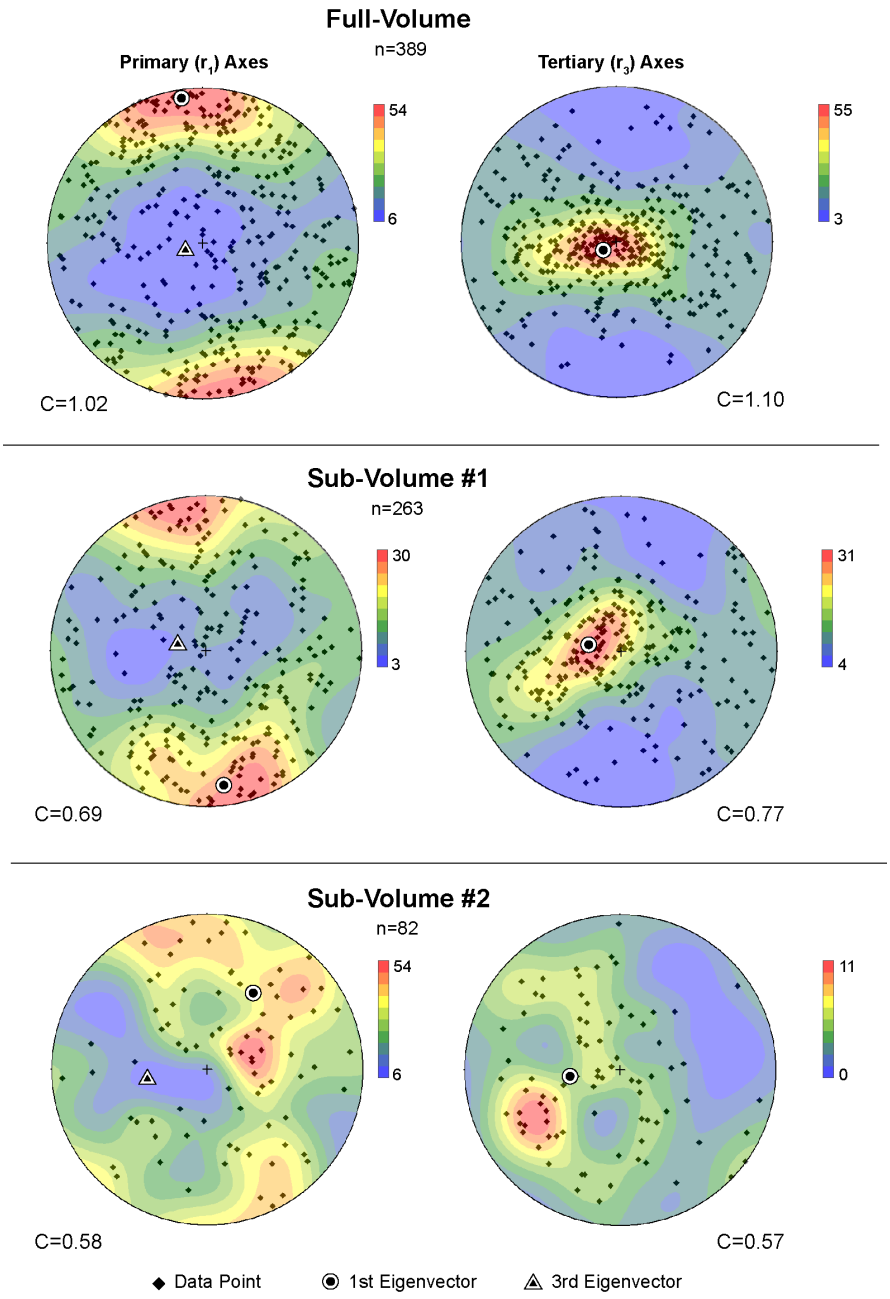

Fig. 2.2 Light-toned XCT object fitted ellipsoid orientations for three scan volumes. *N is number of extracted objects per volume and C is the fabric strength defined by each set of axes. Color bars show density contour values. A weak fabric is suggested by the contours for the full-volume and sub-volume #1 scans but the low C values do not confirm the presence of a fabric. No fabric is evident in sub-volume #2.*

shape distribution with a heavier trend (39% of all objects) toward an elongate (rod-like) shape (Fig. 2.3). Figure 2.4 plots the orientations of the ellipsoids (primary and tertiary axes) and a prominent non-random fabric is apparent, with all three scan volumes showing a preferred orientation of the object primary axes along a great circle girdle and a strong clustering of the tertiary axes, indicating that the dark-toned objects define a foliation fabric (Turner and Weiss, 1963). The *K* shape parameter supports these interpretations, confirming a girdle distribution for the primary axes (whole *K*=0.6; sub-volume #1 *K*=0.4; sub-volume #2 *K*=0.2) and a cluster distribution for the tertiary axes (whole *K*=3.4; sub-volume #1 *K*=2.5; sub-volume #2 *K*=5.6). All six distributions are found to be non-random at the 99% confidence interval (Woodcock, 1977; Woodcock and Naylor, 1983). In addition, there is a weak clustering of the primary axes (suggested by contouring and supported by a slightly larger *K* (0.6) for the whole volume), suggesting a subtle lineation in addition to the foliation (Turner and Weiss, 1963).

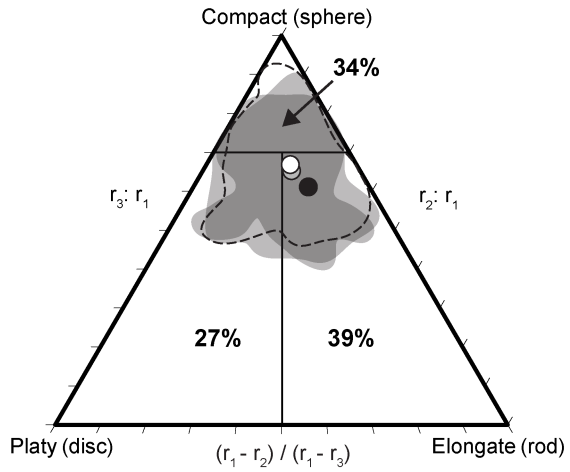

Fig. 2.3 Dark-toned XCT object fitted ellipsoid shapes for three scan volumes. *R is ellipsoid axis lengths where 1, 2, and 3 represent the primary, secondary, and tertiary axes respectively. Dark grey area shows extent of full volume shapes, light grey shows extent of sub-volume #1 shapes, and black dashed outline shows extent of sub-volume #2 shapes. Dots show average fitted ellipsoid shape (full-volume black, sub-volume #1 grey, sub-volume #2 white). Object shapes from all three data sets overlap and the majority of objects (39%) have an elongate shape.*

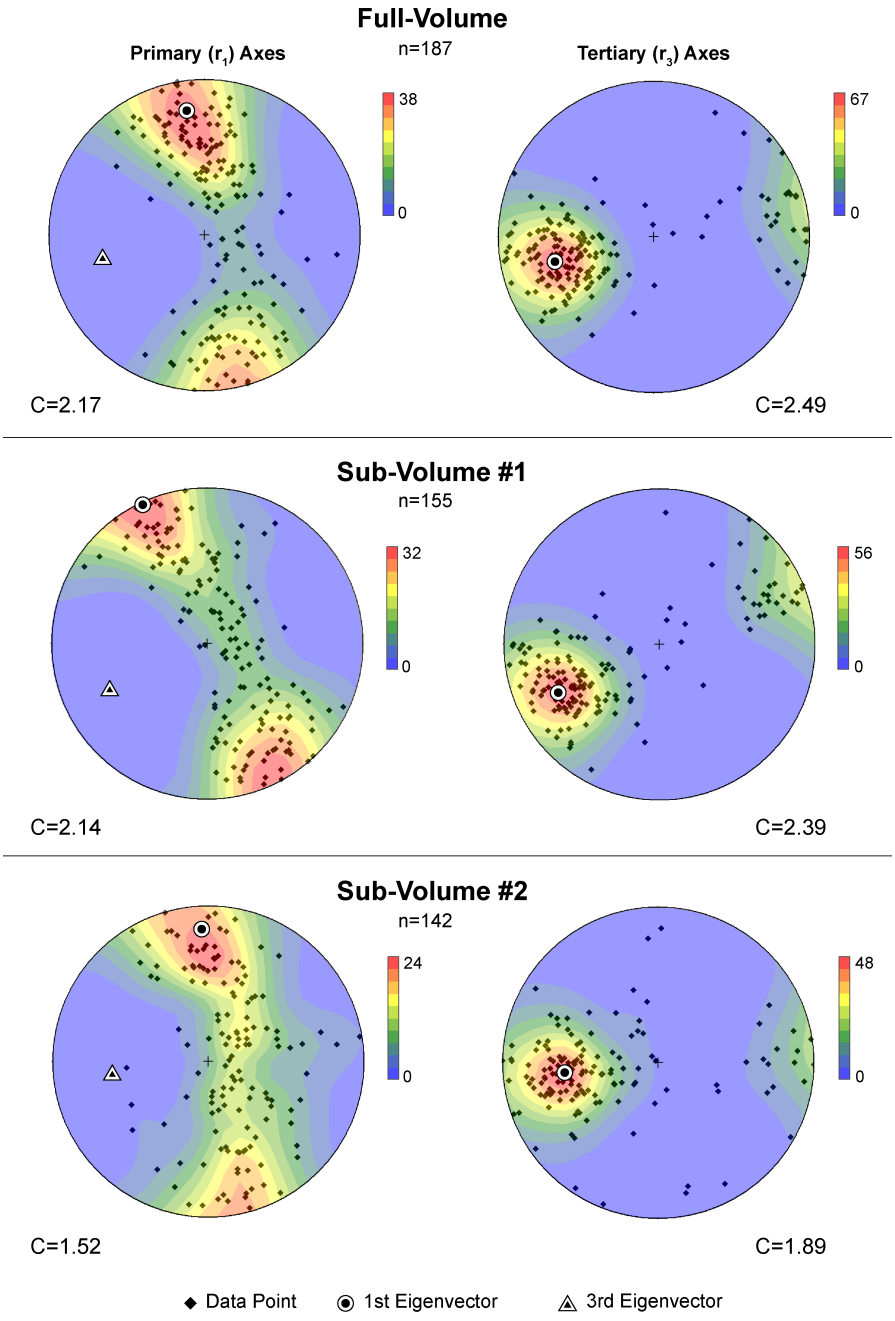

Fig. 2.4 Dark-toned XCT object fitted ellipsoid orientations for three scan volumes. *N is number of extracted objects per volume and C is the fabric strength defined by each set of axes. Color bars show density contour values. Note moderately strong foliation fabric and weak lineation fabric (slight clustering of primary axes).*

The primary and secondary ellipsoid axis lengths of full-volume dark-toned objects are plotted in Fig. 2.5. A linear regression line through the zero intercept with a high correlation (0.91) and slope of 1.22 indicates consistent object shape elongation of about 22% in the long axis direction, further supporting the presence of a weak lineation in the Murchison sample.

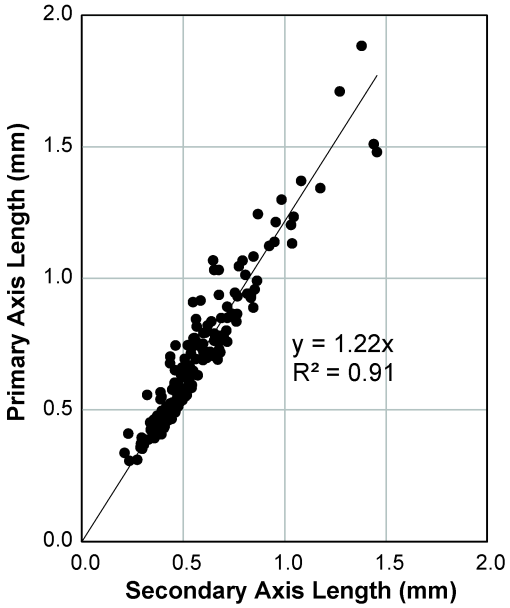

Fig. 2.5 Primary versus secondary axes lengths of full-volume scan dark-toned XCT objects.
A high correlation (R^2) of a linear regression line with a slope of 1.22 suggests a consistent object elongation of 22%.

Among the three scan volumes there do appear to be differences in the derived fabric strengths and orientations. Both the full-volume and sub-volume #1 have a moderate foliation strength with C=2.17 (whole) and C=2.14 (sub-volume #1). Sub-volume #2 has a lower C value of 1.52 corresponding to a relatively weaker fabric. The differences in these fabric strengths are also readily visible in Fig. 2.3, with sub-volume #2 displaying a more diffuse distribution of points around the great circle girdle. Figure 2.3 also suggests that the foliation orientation among the three volumes slightly differ and this is quantified in Table 2.3. The orientation differences between the full-volume and sub-volume #1 is 11.3° (foliation) and 20.2° (lineation). Both volumes have moderate fabric strengths ($C > 2.0$) so the estimated measurement error is 4°, suggesting that a

Table 2.3 Departures in derived fabric orientation between scan volumes

	Sub-Volume #1 ↔ Full-Volume	Sub-Volume #2 ↔ Full-Volume	Sub-Volume #2 ↔ Sub-Volume #1
Lineation Direction[1]	20.2°	6.0°	23.4°
Pole to Foliation Plane[2]	11.3°	6.6°	17.3°

[1]First eigenvector of primary axes [2] Third eigenvector of primary axes

subtle orientation change may be present. Sub-volume #2 shows a lower orientation difference from the full-volume (6.0° for the lineation and 6.6° for the foliation), and due to its weaker fabric ($C < 2.0$) this falls within the expected measurement error (11°). However, when compared directly to sub-volume #1, sub-volume #2 shows a much higher orientation change, suggesting again that sub-volume #1 may have a subtle but real orientation difference compared to the rest of the sample. Finally, we checked to see if the differences in fabric strength and orientation among the data sets might result from systematic bias due to the different scanners and settings used but found no evidence of this (Appendix C).

We also plotted the size frequency distribution of the dark-toned objects segmented within each volume (Fig. 2.6) to investigate whether the different fabric orientations and strengths among the volumes correlated with the size of the segmented objects. Because the full-volume scan has the lowest spatial resolution, the objects segmented in this volume are biased towards larger sizes with the last bin including objects up to 10.7 mm^3 in size. The full-volume size frequency distribution is still an approximate normal distribution similar to the sub-volume scans with a peak around 0.3 mm^3 (equivalent spherical radius ~415 microns). More significantly however, the two sub-volume scans which showed marked departures in orientation (sub-volume #1) and fabric strength (sub-volume #2) from the full-volume scan have similar size frequency distributions, suggesting that these fabric differences are independent of the size

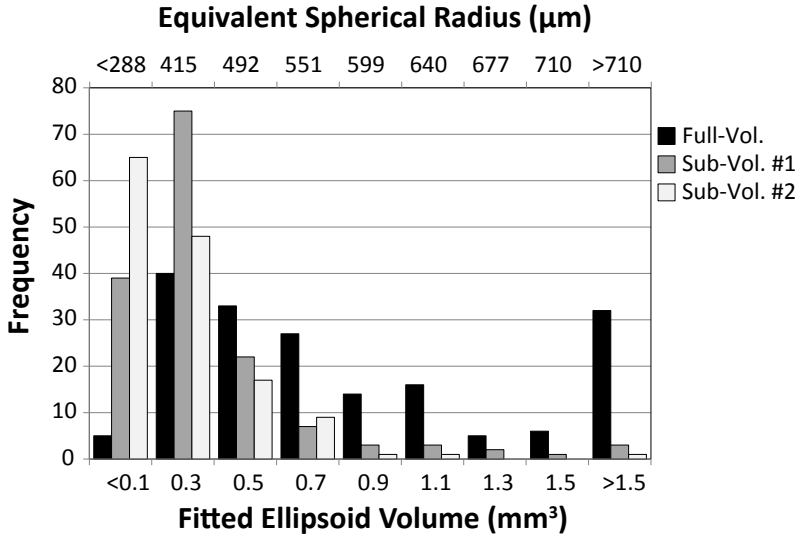

Fig. 2.6 Size frequency distribution of dark-toned XCT objects in each scan volume. *Peak at objects >1.5 mm^3 in whole volume scan is due to inclusion of objects up to 10.7 mm^3.*

distributions of the segmented objects. We do note that sub-volume #2 does include the greatest number of objects smaller than 0.1 mm^3 in size and this may contribute to a weaker measured fabric as discussed in more detail below. Finally, we found no correlation between the degree of elongation or aspect ratio and the size of the object in any of the three scan volumes.

2.3.2 Identification of XCT objects

To identify the mineralogy and rheology of the dark- and light-toned XCT objects we examined and compared the thin section cut from the scanned sample with matching XCT data. A BSE image and EDS map of a portion of the section compared to the co-located XCT data are shown in Figure 2.7. X-ray attenuation is a strong positive function of the atomic number Z of a material (Ketcham and Carlson, 2001), and since backscattered electrons are also strongly proportional to Z (Reed, 2005), is expected that the relative grayscales between the two datasets will be similar as is shown in Fig. 2.7.

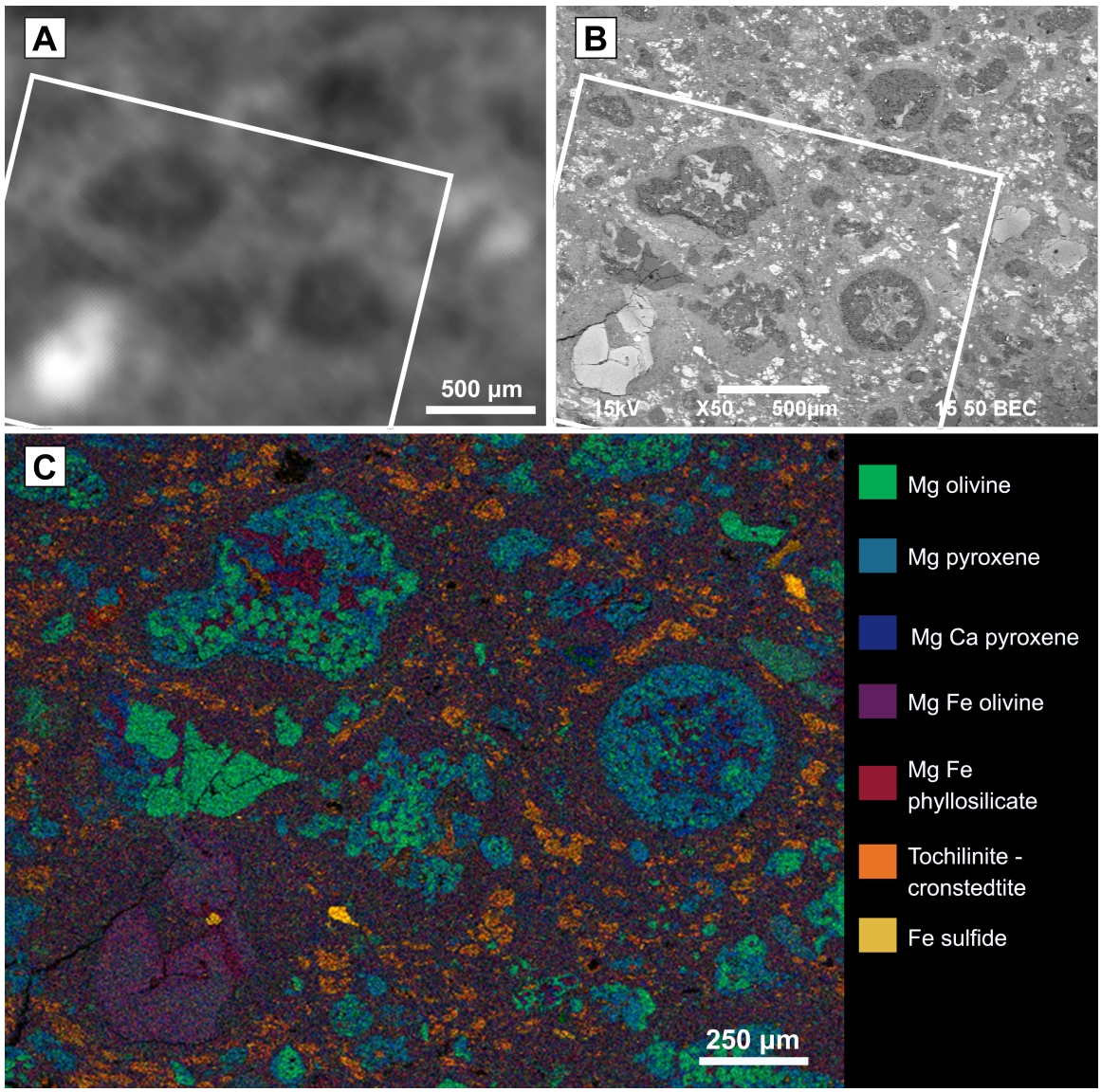

Fig. 2.7 BSE image and EDS map of Murchison section compared to co-located XCT data.

a) XCT data from sub-volume #1 have been interpolated and smoothed to facilitate comparison to BSE image in b. b) BSE image of approximately same region shown in a showing finer detail but generally the same relative greyscales as in the XCT data. ***c)*** *EDS X-ray elemental false color map of portion of area in (a) and (b) (white outlines) highlighting the various phases. Fe is red, Mg is green, Si is blue, and S is yellow.*

However, the significantly higher resolution of the BSE image (2 μm/pixel) reveals finer scale compositional heterogeneity that is concealed by the lower resolution (~30 μm/pixel) XCT data.

Seven light-toned and ten dark-toned XCT objects were examined in the section using optical petrography, BSE imaging, and EDS to determine the dominant phases composing the two populations. Six of the seven light-toned XCT objects are Fe-bearing olivine crystal fragments or porphyritic Fe-bearing olivine chondrules (Fig. 2.7). The other light-toned object identified is an 800-micron altered CAI containing 1-10 micron spinels rimmed with Fe-bearing serpentine. The ten dark-toned XCT objects were all Mg-pyroxene and Mg-olivine porphyritic (POP) chondrules, or fragments of POP chondrules, with minor low-Ca pyroxene and Fe-bearing phyllosilicate (Fig. 2.7). In several cases the Fe-bearing phyllosilicate is visible in the XCT data as bright spots within the dark-toned object interiors (Fig. 2.7a). The matrix, which appears brighter in XCT relative to the dark-toned objects, is relatively higher in Fe due to the presence of Fe-bearing phyllosilicate and clumps of tochilinite/cronstedtite (Fig. 2.7c). In summary, the dominant factor separating light and dark components in the XCT data appears to be the presence of iron, with the dark-toned porphyritic chondrules being dominated by pure Mg silicates.

We note that the fine-grained rims (FGRs) present around many of the chondrules in Murchison are characterized by an absence of tochilinite/cronstedtite as has been documented in other CMs (Trigo-Rodriguez et al., 2006) and therefore will appear dark in the XCT data relative to the surrounding matrix (Fig. 2.7c). At the scan resolution of this study (30-60 μm per voxel) the FGRs are not resolvable and therefore segmentation of the dark-toned XCT objects and subsequent size and orientation analysis includes this rim. However, Fig. 2.7 suggests that the shape and orientation of a chondrule may differ with and without the FGR. This 3D shape departure is currently being investigated with higher resolution XCT data as a separate study (Hanna and Ketcham, 2015).

We examined the three XCT data sets in detail for additional textural or petrographic features such as lithic clasts, veins, and fractures. We did not find any evidence of clasts or veins but fracturing is common, and in particular we found a set of 5 pervasive fracture planes running sub-parallel to the foliation plane defined by the deformed chondrules. However, some of these fracture planes emanate from desiccation cracks in the fusion crust suggesting their origin is related to heating and fragmentation during atmospheric entry. In searching for other deformation textures, we found one clear example of a dark-toned XCT object deforming around a light-toned object and confirmed that the direction of flattening suggested by the deformation is normal to the foliation plane (Fig. 2.8). Therefore, this texture is likely the result of the same deformation event that caused foliation of the Mg-silicate porphyritic chondrules, and also suggests the bright and dark-toned XCT objects differ not only in composition (Fe) but in rheology as well.

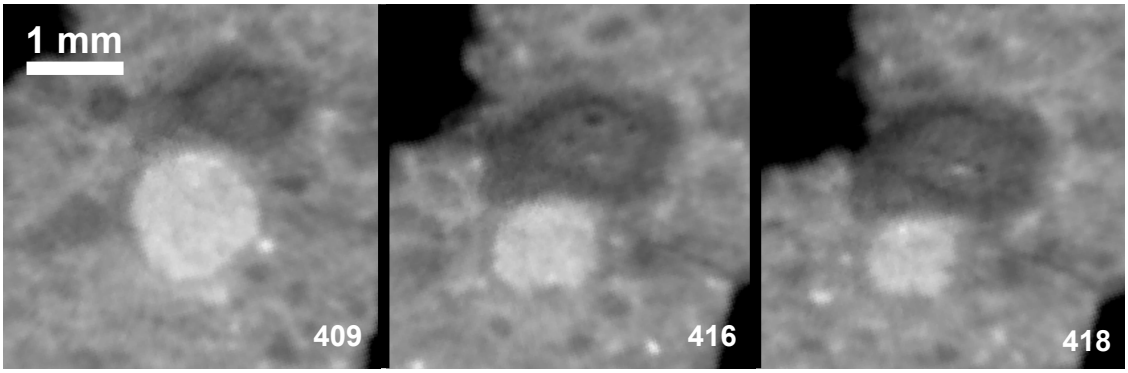

Fig. 2.8 XCT slices from sub-volume #1 showing dark-toned XCT object deformation.
Slice number is indicated in lower right corner and the scale is the same for all images. The dark-toned XCT object appears to be deforming around the light-toned XCT object suggesting they have markedly different rheologies. The foliation plane is horizontal to image.

2.3.3 Detailed petrology and microstructures

We investigated the thin section optically and examined olivines, both in chondrules and in the matrix, for undulose extinction that might be indicative of shock. Out of 42 olivine grains 50 microns or larger, only six grains displayed undulose extinction and the remaining grains exhibited sharp optical extinction. Using the shock stage classification scheme of Scott et al. (1992), this classifies our Murchison sample as S1, which is consistent with other studies that have assigned Murchison as shock stage S1 to S1/S2 (Rubin, 2012; Scott et al., 1992; Tomeoka et al., 1999). Some of the chondrule pyroxene is clearly twinned and pyroxene also commonly poikilitically encloses smaller olivines (Fig. 2.9). Much of the pyroxene has a mottled appearance under crossed polars, but it is unclear at the optical scale whether this is undulose or mosaic extinction or is due

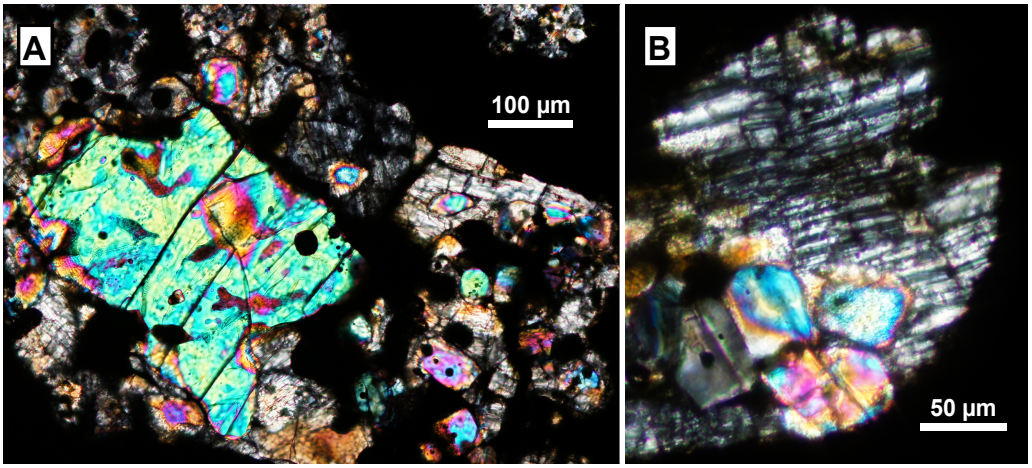

Fig. 2.9 Cross-polarized transmitted light photomicrographs of USNM 5487. *(a) Large fractured olivine surrounded by pyroxene, some with faint twins, with smaller poikilitic olivine. The large fractured olivine shows no evidence of alteration products within the fractures and has sharp optical extinction. (b) Large twinned pyroxene with smaller olivine grains (different chondrule).*

to very fine twinning. Brittle crystalline fracturing is pervasive in olivine and pyroxene, both in chondrules and in the matrix (Fig. 2.9). In some instances these fractures appear to be filled with alteration products (serpentine) but in most cases extensively fractured olivine shows no evidence of internal alteration along fractures (Fig. 2.9-2.10).

We examined fifteen chondrules in thin section that were also measured in the XCT data to investigate mineral phases, microtextures, and alteration features, and relate them to their 3D shape and orientation derived from XCT. Using BSE images, we mapped the distribution and proportion of olivine, Mg pyroxene, low Ca pyroxene, serpentine (or other serpentine group phase), and other phases (sulfide and oxide). While the phase mapping and proportion estimation was necessarily done in 2D thin section, we avoided any chondrules that crossed the section on their outer edges. We tested for possible correlations between amounts of the various phases with the 3D aspect ratio (i.e. amount of flattening) or 3D elongation index (i.e. amount of lengthening) of the chondrules but found none, suggesting that the relationship between chondrule shape and phase abundance is random.

Fracturing and other brittle microtextures within and around the chondrules often show systematic relationships with the foliation plane and/or lineation direction. Fractures are commonly parallel to foliation (white arrows in Fig. 2.10a-c), and we found several instances where these fractures have been filled with alteration products such as Mg-Fe serpentine (white arrows in Fig. 2.10c) with some veins displaying central pores indicating that the mineralization did not fill the void space completely or that the vein was still opening as secondary phases were being precipitated (black arrows in Fig. 2.10e). As is seen in the XCT data, textures consistent with compression perpendicular to the foliation plane are also common (Fig. 2.10b). Brittle fracturing of the anhydrous silicates is abundant, leading to a cataclasis-like texture in which the interior portions of the chondrules look 'crunched' (Fig. 2.10c-d). We did find a few cases where chondrules show evidence of less deformation and in some isolated areas preserve the texture of original mesostasis. Figure 2.11 displays images of a chondrule with a lower 3D aspect ratio (1.29 compared to 1.67 for the chondrule shown in Fig. 2.10c-f) that shows relatively less brittle fracturing of the anhydrous silicates and preserves the original texture of mesostasis in several areas. This suggests that deformation of chondrules to form a foliation was accommodated mainly by brittle fracturing and comminution,

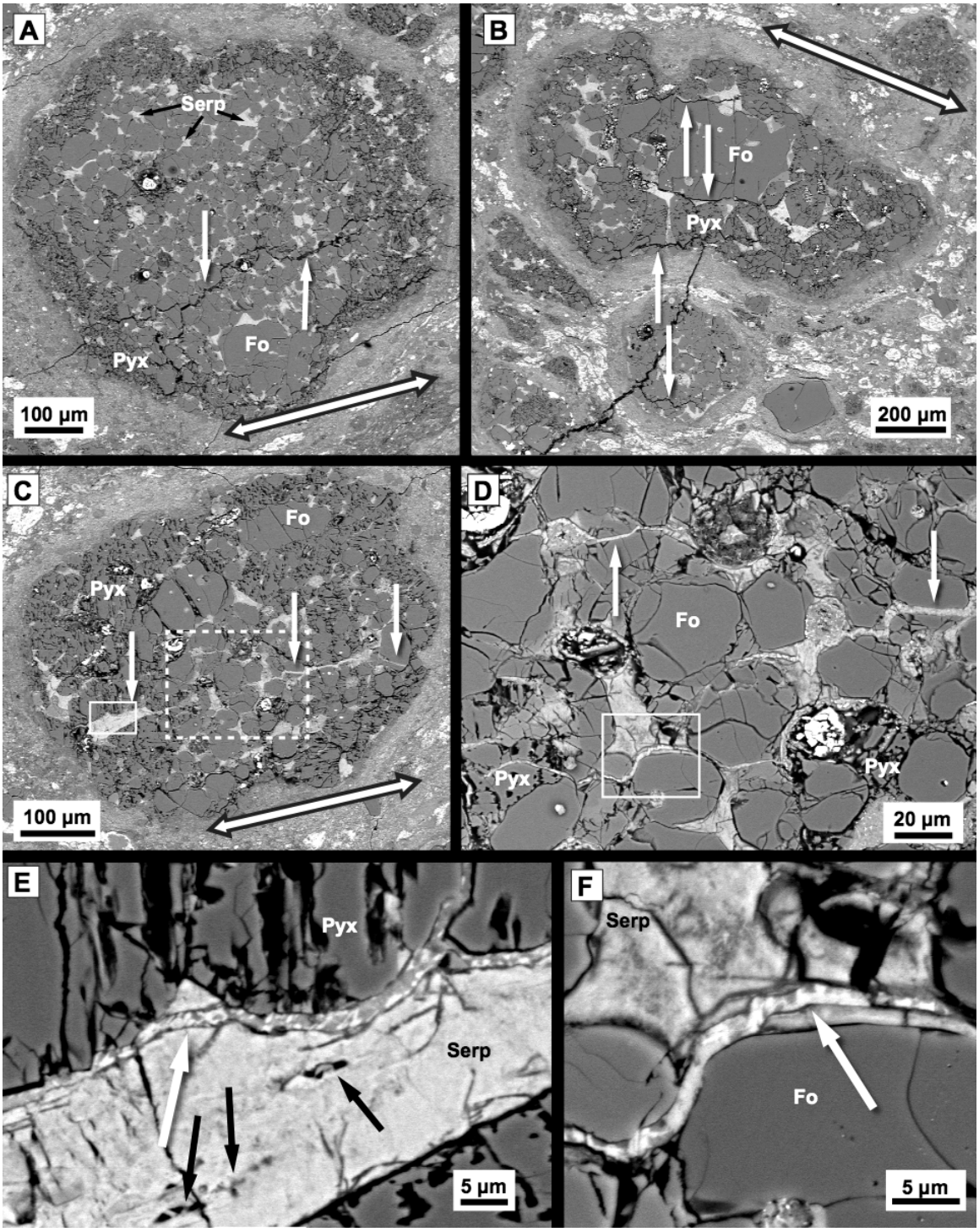

Fig. 2.10 BSE images of 3 POP chondrules.

Fig. 2.10, cont.
Foliation plane and lineation direction indicated by large black and white arrow. Foliation plane approximately perpendicular to image plane in all BSE images. Foliation plane orientation in d-f same as in c. (a) Major chondrule fracture (white arrows) approximately parallel to foliation plane and lineation direction. Smaller silicate fractures also present. (b) Smaller chondrule appears to be impinging into larger chondrule 'above' it. Compression direction inferred by texture matches that from foliation plane (sub-vertical). Silicate fracturing is common in both chondrules and some larger fractures (white arrows) are parallel to the foliation plane. Larger chondrule is also shown in Fig. 2.9a, the labeled forsterite is the large green crystal in that image. (c) Large vein approximately parallel to foliation plane and lineation direction filled with Mg-Fe serpentine (white arrows). Chondrule flattened in plane of foliation. Large dashed box shows location of d, small white box shows location of e. (d) Higher resolution area showing intensely fractured forsterite and pyroxene, alteration veins, and areas of massive serpentine. White arrows indicate fractured forsterites which have been crosscut by serpentine veins. White box shows location of f. (e) Higher resolution image of large vein shows that it has been crosscut by a second, S- and Fe-bearing vein likely containing tochilinite (white arrow). Larger massive vein is serpentine only (no S detected). Black arrows point to pores in central part of vein suggesting mineralization did not go to completion. (f) High resolution image of vein in b showing crosscutting relationship of smaller vein (white arrow) with surrounding massive serpentine. Vein contains higher S and Fe than surrounding serpentine suggesting it contains tochilinite. Fo = Forsterite, Pyx = Mg pyroxene, Serp = Mg-Fe serpentine.

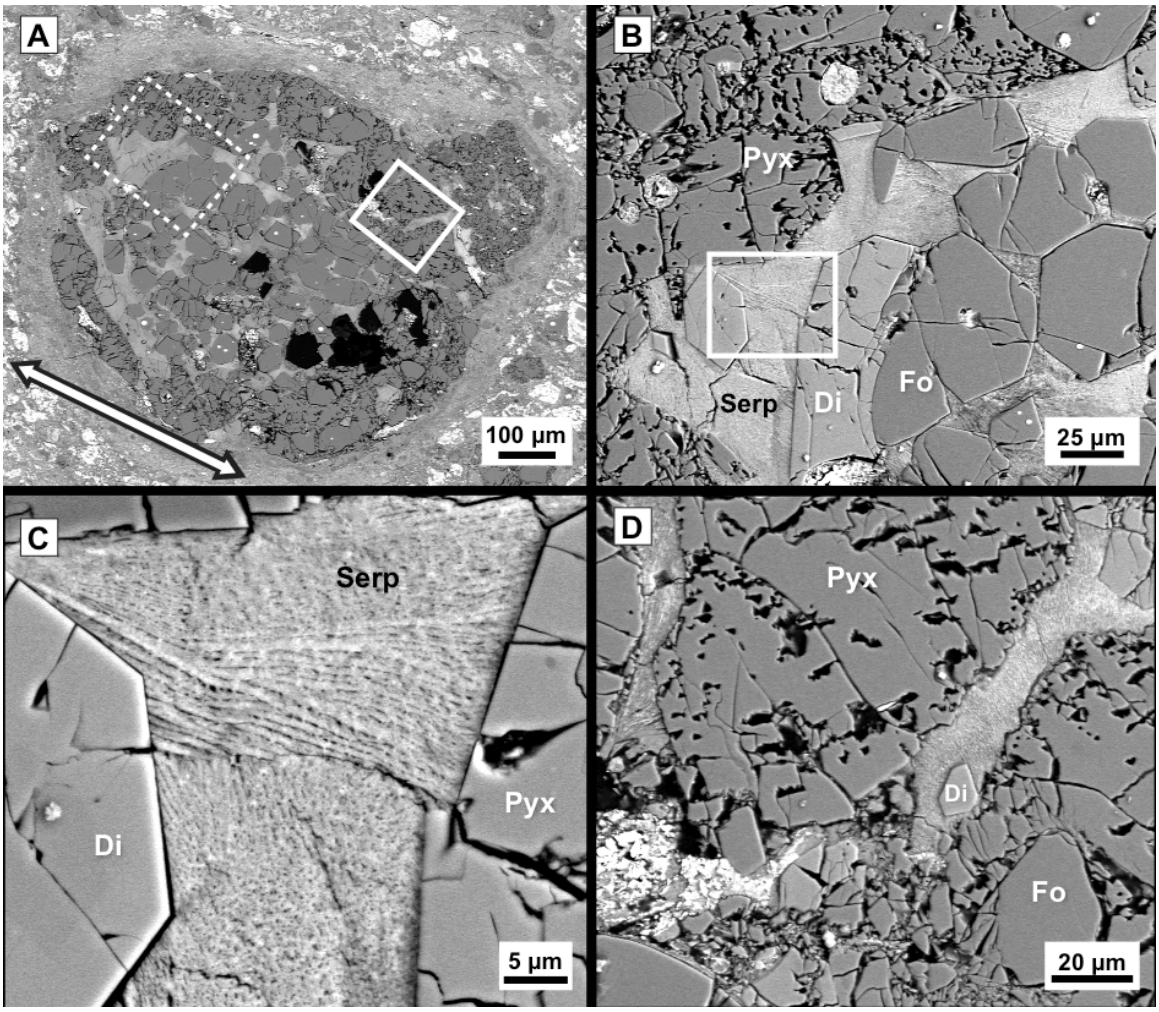

Fig. 2.11 BSE images of single POP chondrule.
(a) Foliation plane and lineation direction indicated by large black and white arrow. Chondrule flattened in plane of foliation. Black areas were plucked during thin section preparation. Dashed box shows location of b, solid box shows location of d. (b) Interior with areas of mesostasis replaced by serpentine but preserving original texture. Several silicates (forsterite and diopside) have euhedral faces with less fracturing compared to silicates in Fig. 2.12. Box shows location of c. (c) Preserved original mesostasis texture. (d) Another area where original texture of mesostasis has been partially preserved (upper right and upper left) but destroyed and comminuted in lower left region of image. Fo = Forsterite, Pyx = Mg pyroxene, Serp = Mg-Fe serpentine, Di = Diopside.

perhaps preferentially in mesostasis where the chondrule rheology was weakest. The more compressed and fractured chondrule (Figure 2.10) has lost all of this original mesostasis texture. Figure 2.12 highlights another deformed chondrule with little evidence of original mesostasis texture that instead exhibits a complex assemblage of alteration minerals, anhydrous silicate fragments, and mineralized areas in between larger fractured olivine and pyroxene crystals.

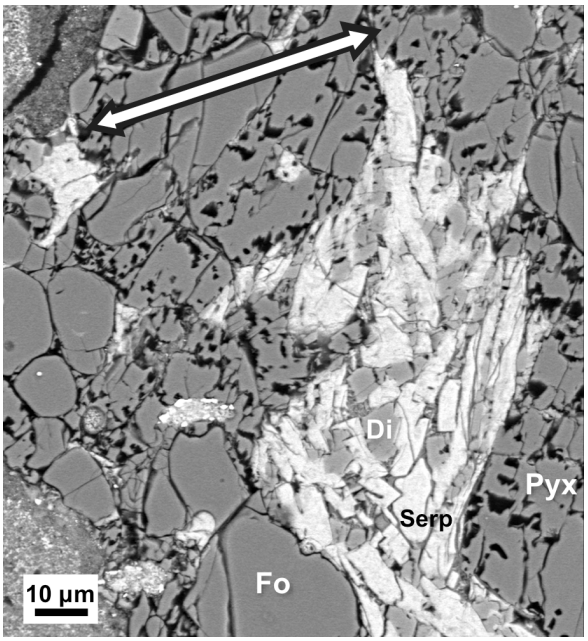

Fig. 2.12 Typical mesostasis texture between olivine and pyroxene silicates. *BSE image. No original mesostasis texture is visible but rather angular fragments of pyroxenes are surrounded by massive serpentine (compare to Fig. 2.13). Foliation plane and lineation direction indicated by large black and white arrow. Fo = Forsterite, Pyx = Mg pyroxene, Serp = Mg-Fe serpentine, Di = Diopside.*

It is also apparent from the alteration textures that some aqueous alteration post-dated the deformation event and that there was more than one episode of fracturing and mineralization. The largest alteration vein in the chondrule in Fig. 2.10c (white arrows) is parallel to the foliation plane and lineation direction, strongly implying that it is genetically related to the fabric-causing event. The presence of interior pores in the central portions of the vein indicates (Fig. 2.10e) that it was opened and then filled with alteration products (in this case Mg-Fe serpentine). Further, the vein also bisects two large olivine grains (Fig. 2.10c-d), suggesting that they were energetically fractured and then filled with an alteration mineral. At higher resolution it becomes apparent that the

large serpentine vein has been crosscut by another vein (white arrow in Fig. 2.10e), implying that the massive serpentine vein was present during the formation of the second, smaller vein. This second vein is relatively brighter in the BSE images due to a higher amount of iron (white arrow in Fig. 2.10f). The higher iron content, along with the presence of sulfur, indicates that the smaller vein likely contains tochilinite or perhaps very fine-grained pyrrhotite. In contrast the first, more massive vein does not contain any evidence of sulfur, suggesting that it is dominated solely by Mg-Fe serpentine. We found several other cases of cross-cutting mineralized veins within chondrule interiors suggesting multiple episodes of fracturing and mineralization, and usually at least one of the veins is parallel to the foliation and lineation direction suggesting they are related to the deformation event which foliated and lineated the chondrules. While it is possible that reflections and refractions from a single impact event could cause crosscutting fractures, it is unclear whether the aqueous fluid composition could evolve during the same time frame and therefore it seems more likely that the multiple fracture sets occurred during discrete deformation events.

We also see evidence of relative movement aligned with the lineation direction, and evidence that aqueous alteration postdated the movement. Figure 2.13a-b shows a fragmented Fe-bearing olivine chondrule in which the movement of a major fragment is largely in the direction of the lineation. In the area between the fragments numerous needle-like fibers of serpentine have grown in all directions, including perpendicular to the compression direction indicated by the foliation plane. The absence of deformation of the serpentine needles and the fact that they have not been dehydrated suggests that little deformation or thermal metamorphism has taken place since their emplacement. Another fragmented Fe-bearing olivine chondrule is shown in Fig. 2.13c-f. Again, apparent movement is parallel to the lineation direction, and the movement of the fragments as well as the v-pull-apart fractures (white arrows in 2.13c) indicate a sinistral sense of shear (Hippertt, 1993). The v-pull-apart fracture in the smaller fragment has

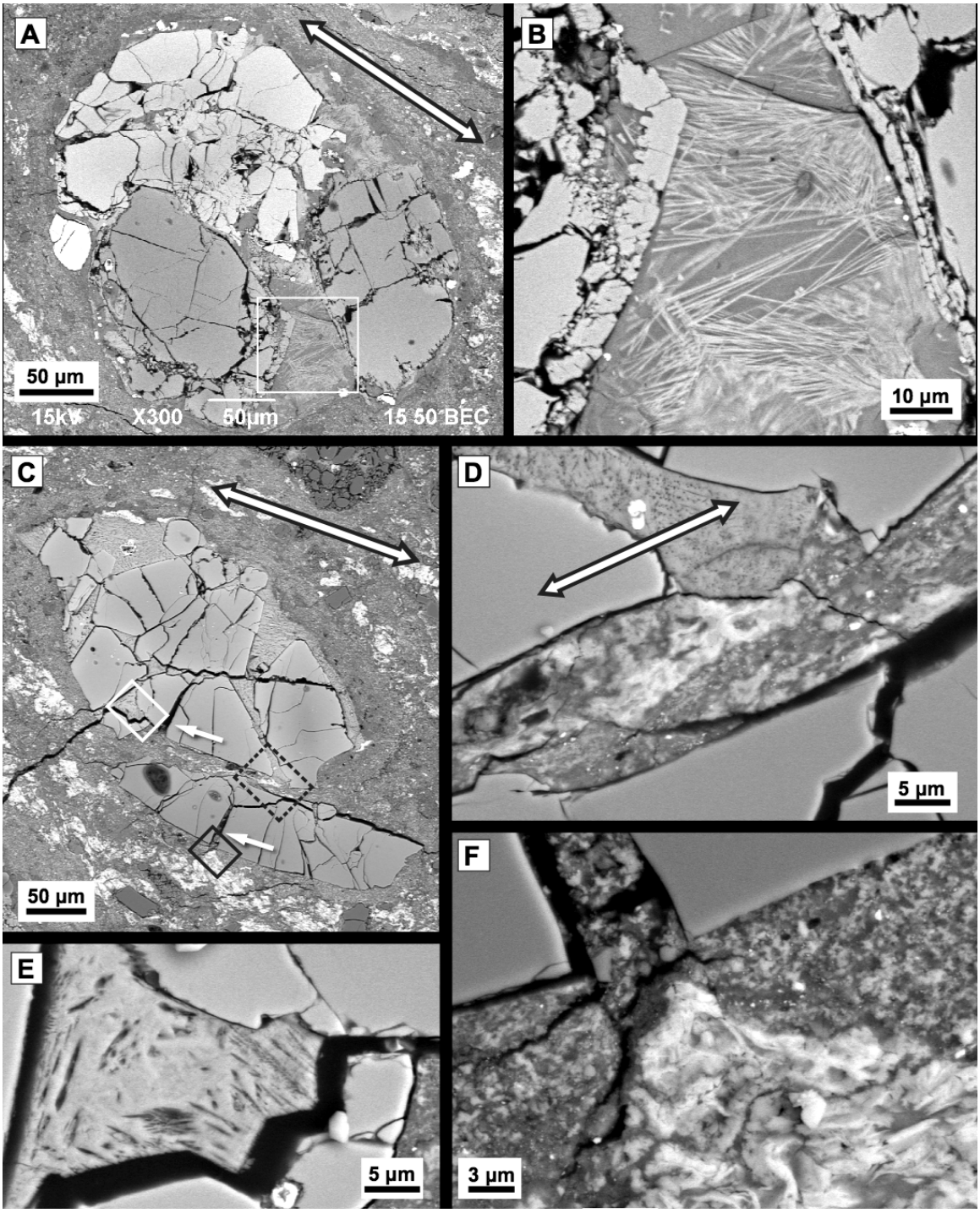

Fig. 2.13 Relative movement and alteration in Fe-bearing olivine chondrules.

Fig. 2.13, cont.
BSE images. (a) Foliation plane and lineation direction indicated by large black and white arrow; same orientation for b. Relative motion of the smaller fragment is in line with the lineation direction. White box shows location of b. (b) Area between fragments has been infilled with alteration material including fine serpentine fibers some of which have grown approximately perpendicular to the foliation plane. No subsequent deformation or dehydration of the fibers is apparent. (c) Foliation plane and lineation direction indicated by large black and white arrow. Relative motion of the smaller fragment is in line with the lineation direction. Black dashed box shows location of d. White solid box shows location of e and black solid box shows location of f. (d) Foliation plane and lineation direction indicated by large black and white arrow; same orientation for d and f. Tochilinite has formed in the space created by the two chondrule fragments. (e) Mesostasis replaced by serpentine preserves dendrite pseudomorphs in the form of pore space. (f) Tochilinite forms in the space created by the V-pull-apart fracture (bottom white arrow in c) in the smaller fragment.

made pore space in the fine-grained rim for the formation of tochilinite (Fig. 2.13f). Additional evidence of post-deformation aqueous alteration is the deposition of tochilinite between the two chondrule fragments (Fig. 2.13d), although in this case the tochilinite lens is elongated parallel to the foliation and lineation direction. This could be an inherited fabric or could indicate that it was deformed during or after emplacement.

2.3.4 EBSD and plastic deformation

While clinopyroxene twinning can be the result of impact shock (Leroux, 2001; Rubin et al., 1997), it can also occur as a result of inversion from protoenstatite during chondrule cooling (Buseck et al., 1980). To help distinguish between the two scenarios it is necessary to determine the twinning plane and to confirm that the pyroxene is in the monoclinic form (clinoenstatite for the pure Mg pyroxene in our sample).

We have found using EBSD that not only is the majority of the Mg pyroxene in the form of clinoenstatite (CLEN), but that all of the 23 grains we examined are twinned on the {100} plane, regardless of their crystallographic orientation (Fig. 2.14a-b). In addition, the observed twins are much larger than typical {100} clinopyroxene shock twins (~5 nm) and no {001} shock twins were observed (Leroux, 2001). We also mapped 29 diopside grains, and while growth twins on the {100} plane were found in several grains, no shock twins were observed. Growth twins can be distinguished from shock twins in diopside by their larger size and limitation to one or two units (Raleigh and Talbot, 1967). Element zoning patterns where visible further supported the interpretation of growth, rather than shock, twinning in diopside. For these reasons it is most likely that the pervasive CLEN twinning found in Murchison chondrules formed from inversion of protoenstatite during chondrule cooling and are not the result of shock.

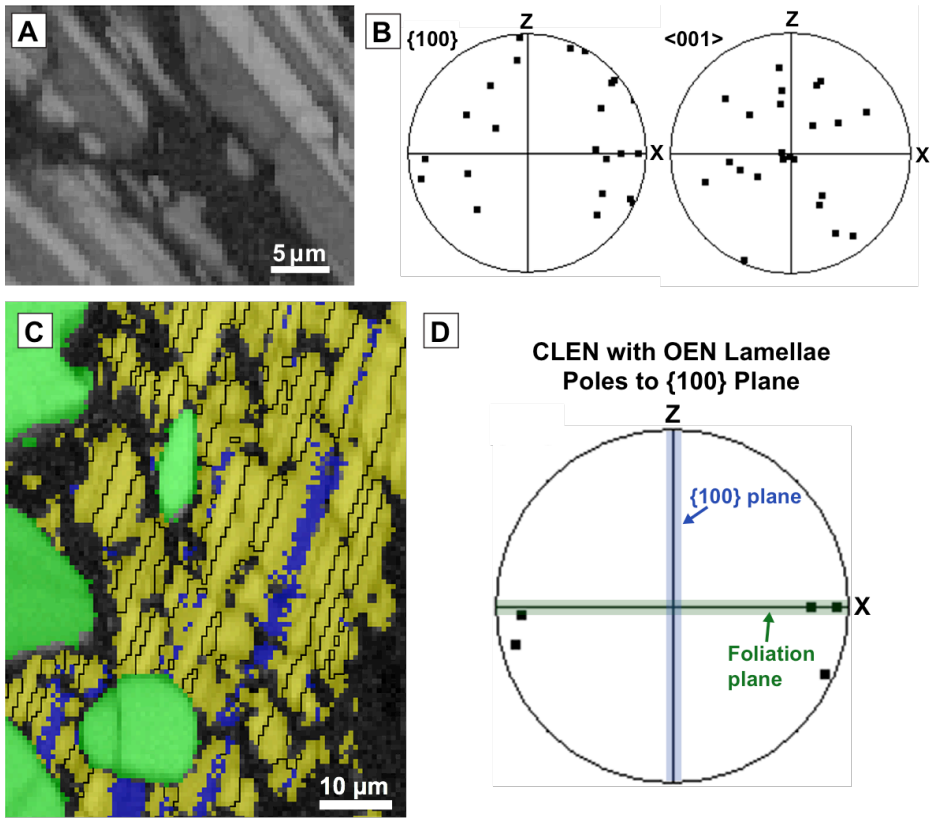

Fig. 2.14 Twinned clinoenstatite.
(a) EBSD band contrast map highlighting CLEN twins. (b) Pole figures showing the orientation of 23 CLEN grains in 9 different chondrules. Plot on left are poles to the {100} crystallographic plane and the plot on the right shows the <001> axis directions of the same grains. In both plots the horizontal X axis is the foliation plane and lineation direction. No preferred orientation of the twinned CLEN grains is evident. (c) EBSD phase map showing OEN lamellae (blue) within twinned CLEN (yellow). Green is forsterite. (d) Poles to {100} plane of 5 CLEN grains with OEN lamellae in 5 different chondrules. All grains are orientated with their {100} crystallographic planes approximately perpendicular to the foliation plane.

However, within the twinned CLEN grains we found a weak but intriguing trend. About 20% of the twinned CLEN grains displayed prominent orthoenstatite (OEN) lamellae and these five grains, located in five different chondrules, have a preferred orientation where their {100} crystallographic planes are approximately perpendicular to the foliation plane (i.e. direction of maximum stress) (Fig. 2.14c-d). While the sample

size is low, stress-induced orthopyroxene lamellae have been previously reported in ureilite pigeonite (Mori and Takeda, 1988). Further, it has been well-documented that CLEN lamellae form in terrestrial orthoenstatite in the presence of shear stress (Coe and Kirby, 1975) and shock-induced CLEN lamellae have been observed in the enstatite chondrites (Rubin et al., 1997), although it is unclear if this process can occur in the reverse direction. OEN can also form from inversion of protoenstatite during cooling although it is kinetically unfavored (Buseck et al., 1980) and indeed TEM-scale intergrowths of OEN and CLEN have been observed in some enstatite chondrites (Folco and Mellini, 2000) as well as within Murchison (Martin and Lindgren, in review). However, in this case the OEN is in the form of thick (> 1 μm) lamellae and there appears to be a preferred orientation to grains that contain them, suggesting that their presence is related to the stress the chondrules have undergone rather than their cooling history.

We also used EBSD data to quantify the strain present in olivine and pyroxene in twelve chondrules to determine if they have been plastically deformed during the event(s) that foliated and lineated them. Plastic deformation in a crystal is manifested by an abundance of low-degree misorientations (<10°) within the crystal lattice that are indicative of dislocations resulting from stress (Brewer et al., 2009). However, very low misorientations can be at the limit of the instrument resolution, which depends on several factors including hardware and operating conditions (Humphreys, 2001; Prior, 1999). In interpreting correlated misorientations mapped within grains, we conservatively ignored misorientations of less than 3°, although including them does not change our results. Overall we found very limited low-angle misorientations within olivine and pyroxene, but did find that pyroxene displayed a slightly higher amount of misorientation per surface area (Fig. 2.15). This combined with the commonly sharp optical extinction of olivine and absence of shock twinning in clinopyroxene indicates that plastic deformation within chondrules was minimal and that their deformation was accommodated primarily through brittle processes.

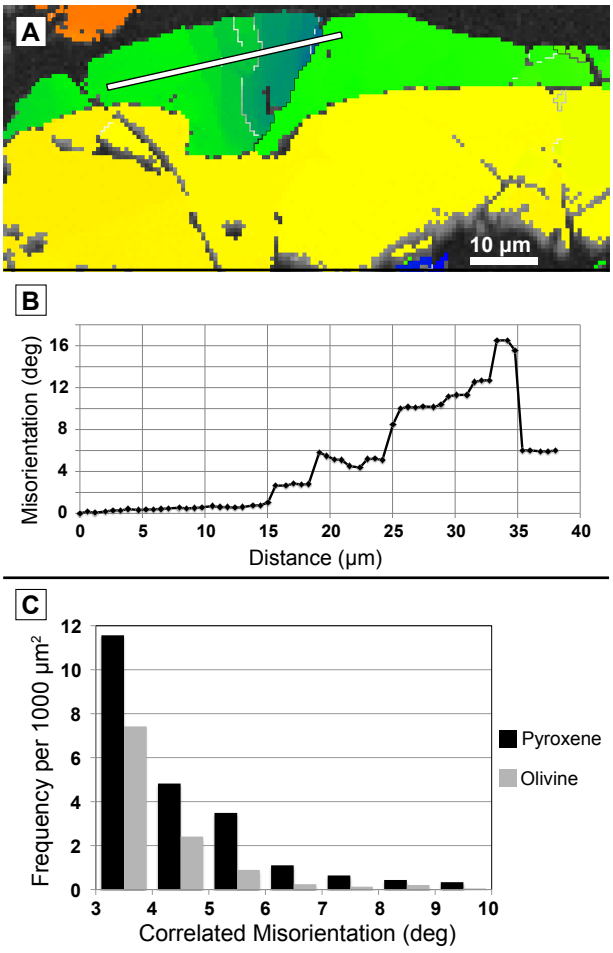

Fig. 2.15 Pyroxene and olivine lattice misorientations.
(a) EBSD Euler 1 Orientation Map. Top diopside (green-bluish) grain shows 16° of gradual misorientation across white line until lattice slip/fracture. Olivine (yellow) displays less than 4° of misorientation across full length. (b) Misorientation profile (relative to first point) along white line in diopside in a. (c) Correlated misorientations normalized for area within olivine and pyroxene (CLEN and diopside) grains among 12 chondrules. Misorientations less than 3° are below the instrument resolution. Total surface area mapped for olivine and pyroxene was 122,781 and 133,480 µm2, respectively.

2.3.5 Porosity loss estimate

Assuming that the chondrules were initially spherical and incompressible and that the strain is entirely uniaxial (coaxial, non-rotational deformation), the amount of strain or uniaxial shortening (ε) can be estimated by examining the degree to which the chondrules have changed shape from a sphere to a uniformly flattened ellipsoid (Fig. 2.16a). After strain ε (between 0 (no shortening) and 1), the tertiary (short) axis r_3 of the deformed ellipsoid is related to the original sphere radius R by

$$r_3 = R(1 - \varepsilon) \quad (3)$$

If the chondrule is incompressible then the volume remains the same requiring that

$$R^3 = r_3 {r_1}^2 \quad (4)$$

where r_1 is the primary (long) axis of the deformed ellipsoid. The aspect ratio a of the ellipsoid is defined by the ratio of the longest to shortest axes

$$a = {r_1}/{r_3} \quad (5)$$

Rearranging (3) and (5) to substitute for R and r_1 in equation (4) and simplifying leads to

$$\varepsilon = 1 - a^{-2/3} \quad (6)$$

so the total strain ε can be derived from the average aspect ratio a of the deformed chondrules. Porosity (P) of a material is defined as

$$P = \left(1 - \frac{V_g}{V_b}\right) x\ 100\% \quad (7)$$

where V_g is the grain volume (i.e. solid material that is not pore space) and V_b is the bulk volume (including pore space) of the meteorite.

Because observational and experimental evidence suggests that deformation of chondrules through impact accompanies porosity loss in the surrounding matrix (Gattacceca et al., 2005; Martin and Mills, 1980; Nakamura et al., 2000; Sugiura and Strangway, 1983), we can use the strain derived using the deformed chondrules in Murchison to calculate the amount of porosity that was removed in the matrix during deformation. The form of this matrix porosity could be intergranular microporosity or fracture porosity; both would likely be removed during collapse of the matrix (pore space created from fracturing during impact is addressed in Section 2.4.3). If deformation of the surrounding matrix is accommodated completely by collapse of this pore space, then V_g remains constant and after deformation the bulk volume V_b is reduced by a factor of (1- ε).

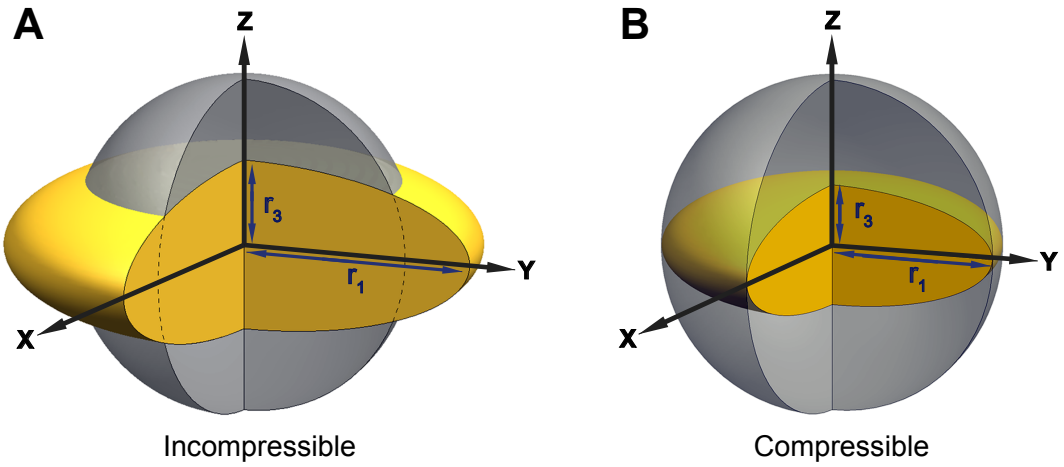

Fig. 2.16 Idealized spherical chondrule (grey) deformed to uniformly flattened (r_1=r_2) ellipsoid (yellow).
r_1 is the primary axis of the deformed chondrule and r_3 is the tertiary axis. Deformed chondrules in a and b have the same aspect ratio (r_1/r_3) but different axes lengths. (a) Chondrule is incompressible and strain occurs in X and Y equally. (b) Chondrule is completely compressible and therefore all strain is accommodated in Z. For a compressible chondrule more strain is required to produce the same aspect ratio of the final deformed chondrule.

Using equation (7) we can define the current (post-deformation) meteorite porosity P_1 as

$$P_1 = \left(1 - \frac{V_g}{(1-\varepsilon)V_b}\right) x\ 100\% \quad (8)$$

and the pre-compaction porosity (P_0) can be determined by rearranging (8) and substituting for V_g into another equation (7) for P_0

$$P_0 = \left[1 - (1-\varepsilon)\left(1 - \frac{P_1}{100}\right)\right] x\ 100\% \quad (9)$$

Therefore, the pre-deformation porosity P_0 can be determined using the total strain ε and current meteorite porosity P_1.

For the full-volume XCT data set with 187 segmented chondrules, the mean aspect ratio is 1.54 with a standard deviation of 0.22 (Table 2.2). Using equation (6), uniaxial shortening is then 0.25, and using the average Murchison bulk porosity of 22.1%

(Macke et al., 2011) this suggests a pre-compaction porosity of 41.6% (equation (9)). Using the standard deviation of 0.22 as a proxy for the measurement and calculation error, this expands the range of uniaxial shortening to 0.17-0.31 and the pre-compaction porosity to 35.3%-46.6%. The highest chondrite bulk porosity measured to date is 43% for C2 Tagish Lake (Hildebrand et al., 2006), suggesting that this porosity range is reasonable for coherent chondrite rock, but is still well below the hypothesized ~60-75% bulk porosity of original accreted material (Beitz et al., 2013a; Ormel et al., 2008).

Pure uniaxial compression (non-rotational deformation) would result in a foliation fabric with uniformly flattened objects. However we do see a weak lineation in the primary axes of our chondrule best-fit ellipsoids (Fig. 2.4). Further, the chondrules have an elongated shape (Fig. 2.3) that is manifest as a consistent ~22% elongation in the long axis compared to the intermediate axis of the chondrules (Fig. 2.5) and we see limited evidence for a sense of shear with some component of rotation (Fig. 2.13c). All of this is strong evidence for an impact, rather than burial compaction, origin for the deformation of the chondrules as the latter scenario produces pure uniaxial stress only. It is unclear how a shear component of the stress from impact would influence the porosity loss, but a conservative approach is to subtract the degree of elongation (0.22) from the calculated average aspect ratio (which assumes an isotropic shape by ignoring the secondary axis) to derive an estimate of the aspect ratio (1.32) attributed to pure uniaxial strain. This aspect ratio is equal to the lower end of our error estimate and therefore does not change the range of our porosity loss estimate. Accounting for error could lower this estimate further, but we believe this is compensated by the fact that the chondrules were at least partially compressible, as discussed below. Therefore our minimum estimate of pre-deformation porosity remains 35.3%.

Another key assumption of our calculation is that the chondrules were initially spherical, which is commonly assumed in similar calculations but difficult to know for certain as these chondrules are aggregate and granular in texture (Fig. 2.10-2.11), and some chondrules are obviously fragments of originally larger chondrules (refer to Fig. 2.7

and 2.13). One test of original sphericity prior to deformation is an ellipticity plot which collates the primary and tertiary axis of each deformed object and tests for a linear fit (Ramsey and Huber, 1983). Assuming the objects were spherical and had the same rheological response to a uniaxial force, they would all plot along a line with a slope equal to their aspect ratio. Randomly orientated non-spherical shapes exposed to uniaxial compression would result in objects with a large range of aspect ratios and thus a significant amount of scatter about a linear trend. Figure 2.17 shows the ellipticity for 187 chondrules from the full-volume scan. Linear regression through zero intercept with a high correlation (R^2=0.86) and slope (1.52) near the mean aspect ratio (1.54) is support for nearly, but not absolutely, spherical chondrules prior to deformation (Ramsey and Huber, 1983). Some scatter is surely introduced by including an unknown quantity of fragmented chondrules and by the differences in rheological response among the chondrules (for example, the amount or arrangement of original mesostasis). Despite these factors the deformed chondrule shapes still show a relatively small spread in aspect ratio, suggesting that the assumption of a nearly spherical shape is reasonable.

Our calculation also assumes that the chondrules are completely incompressible and that strain occurs in 3 dimensions (contraction in Z and expansion in X and Y) to produce a uniformly flattened chondrule with a constant volume. However, if the chondrules are completely compressible (i.e. contain pore space, like the matrix), strain is limited to one dimension (Z), requiring a greater amount of strain in Z to produce the same aspect ratio (Fig. 2.16b). In this case the deformed chondrule has a primary ellipsoid axis r_1 equal to the initial spherical radius R. Using R for r_1 and equation (3) for r_3 in equation (5) and rearranging yields

$$\varepsilon = 1 - a^{-1} \tag{10}$$

Using the aspect ratio of 1.54 ± 0.22, ε = 0.24-0.43 and results in a pre-deformation porosity of 41.0 - 55.7% (equation (9)).

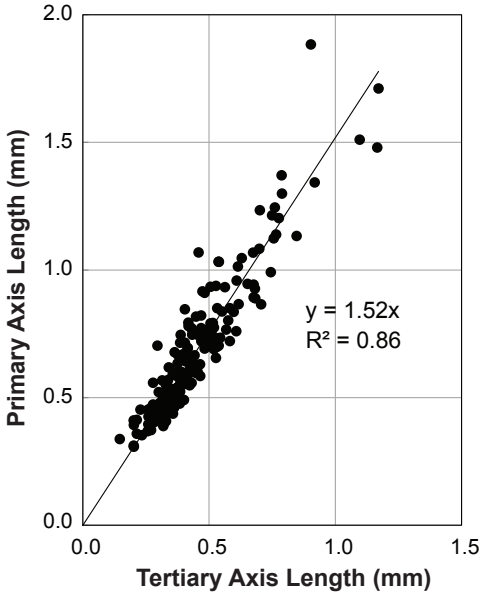

Fig. 2.17 Ellipticity analysis of full-volume chondrules.
Primary (r_1) versus tertiary (r_3) axis lengths of fitted ellipsoids to full-volume chondrules. Linear regression through zero intercept with high correlation (R^2 = 0.86) and slope (1.52) near the mean aspect ratio (1.54) is support for nearly spherical chondrules prior to deformation.

Finally, we note that the equations describing our model of porosity collapse exclude potential complicating effects of water, notably the possible presence of ice in the pre-deformed material, and post-deformation aqueous alteration. The former concern is probably a secondary issue if we assign the ice to the pore fraction and make the simplifying assumption that it is either sparse or can be considered fully compressible due to escape during melting or vaporization. Aqueous alteration will tend to increase phase volume, and if some of this volume increase is accommodated by expansion into pore space then it may represent an additional component of porosity loss. In our model this would mean that the present-day porosity we are using is too low, and using a higher post-deformation porosity would in turn increase the inferred pre-deformation porosity.

2.4 Discussion

2.4.1 Brittle deformation via impact

Murchison is considered a regolith breccia and therefore different regions could have experienced different deformation and alteration histories as has been seen for other

CMs (Zolensky et al., 2014). We do see evidence of a subtle but real change in foliation direction and strength among the sub-volumes analyzed (Fig. 2.3 and Table 2.3) but the departures are not large enough to represent different clasts with markedly different histories (Friedrich et al., 2014b; Zolensky et al., 2014). Overall the entire sample seems to have undergone the same deformation history resulting in a foliation signature that is relatively consistent on a cm-scale. Therefore, we interpret the foliation and lineation fabric found in our sample as resulting from in-situ deformation.

However, the subtle change in foliation and lineation orientation between sub-volume #1 and the other two scan volumes may represent a difference in in-situ finite strain within the sample. A component of rotational shear strain in Murchison is suggested by rare shear-sense indicators (Fig. 2.13c) and may also explain the difference in foliation and lineation orientation between the scan volumes. In the full-volume scan we found that the dark objects were consistently elongated by 22%, but if we apply this same technique to sub-volume #1 we find the objects are elongated slightly more, by ~25% ($R^2 = 0.87$). Further, subtracting this from the sub-volume #1 average aspect ratio (Table 2.2) results in almost the same estimate of flattening (1.33 compared to 1.32 for the full-volume). This suggests that while the uniaxial strain between the volumes is the same, there exists a small difference in rotational strain, just as there exists a small difference in the foliation plane orientation and lineation direction between the two volumes (Table 2.3). This correlation between rotational strain and foliation orientation is consistent with some component of noncoaxial shear, because during noncoaxial shear, the foliation plane rotates progressively toward the shear plane (Passchier and Trouw, 2005). For coaxial, or pure shear deformation, the foliation should remain the same orientation regardless of finite strain magnitude. The cause of the difference in finite strain is difficult to determine, but is most likely the result of rheological differences on a cm-scale within the sample, related to the number or size of chondrules, proportion of matrix, or the amount of original porosity (which is likely also related to the first two properties).

Consequently, we interpret the lineation fabric defined by the Murchison chondrules to result from a component of noncoaxial shear from impact. Lineation fabrics in chondrites have also been interpreted as an intersection fabric formed from multiple impacts (Smith et al., 2006; Sugiura and Strangway, 1983) and because we see evidence for multiple deformation events this could apply to our Murchison sample as well. However, the correlation between the foliation orientation and degree of rotational strain argues in favor of impact-induced rotational shear. Evidence for impact-induced noncoaxial shear has also been found in the Pultusk H chondrite in the form of shear fractures in silicates and deformed metal grains. Unlike for the Pultusk H chondrite however, we do not see abundant shear sense indicators nor evidence of frictional melting in localized shear zones (Krzesińska et al., 2015). Therefore, we believe that the dominant strain leading to chondrule deformation was coaxial (pure shear) compression with a minor component of noncoaxial (rotational, or simple) shear. Noncoaxial strain does occur in impact settings but the magnitude of this strain in comparison to the coaxial component (i.e. the vorticity) is unclear and is also dependent on the location within the impact structure (Melosh, 1989; Trepmann, 2008).

While the indication of noncoaxial strain is a strong argument against overburden due to burial compaction as the deformation mechanism, there is another tectonic setting other than impact that could cause simple shear. For a chondrite parent body that is partially differentiated with an overlying primitive chondritic crust (Elkins-Tanton et al., 2011; Weiss and Elkins-Tanton, 2013), it is expected that a cooling core would causing compressional thrust faulting in the overlying undifferentiated chondritic crust (Elkins-Tanton, 2015) much like has been seen on Mercury (Byrne et al., 2014). While the absence of a strong impact shock signature (S1 in Murchison) could be an argument against an impact origin, there are other reasons (discussed below) why impact(s) may not impart a shock signature to chondrule silicates. The strain rate of deformation (higher for impact, lower for tectonic faulting) could be a more reliable indicator of the

deformation mechanism, although this is complicated by the fact that tectonic faulting can also occur during the modification stage of sufficiently large impacts (Melosh, 1989).

In a previous study, Lindgren et al. (2015) measured a foliation fabric defined by dark-toned XCT objects (chondrules) in a smaller, separate Murchison sample using the method described here. The foliation fabric strength for that sample was weaker (C=1.46) and the average aspect ratio higher (1.75 ± 0.39) than for this sample. Unfortunately the samples are not orientated to each other so fabric orientations cannot be compared. Because we see small differences in fabric strength and average aspect ratio among sub volumes in this study that we interpret as evidence of differences of finite strain within the bulk meteorite, it is likely that the same explanation applies to the fabric difference with the other Murchison sample as well. However, because the other scan had a much higher resolution (7.4 μm), dark-toned objects as small as ~60 μm in cross-section were included in the analysis making it more likely that some of these objects were crystal (fragments) with low X-ray attenuation (forsterite, calcite) rather than chondrules (Lindgren et al., 2015). In contrast, the smallest objects segmented for this study are ~120 μm in cross-section, making it less likely that this analysis includes crystal fragments. Still, sub-volume #2 does include the greatest proportion of these smallest objects (Fig. 2.6) and also has a much weaker fabric than the other two scan volumes (Fig. 2.4) so it is possible that this population includes some large crystal fragments. Indeed, when we consider only the 77 largest objects in this scan volume, the *C* strength of the foliation fabric increases to 1.63 (primary axes) and 2.04 (tertiary axes).

Our textural observations, most significantly a lineation and evidence for noncoaxial shear, are most consistent with impact rather than burial compaction as the deformation mechanism, in agreement with several studies that have also attributed foliation (Lindgren et al., 2015; Rubin, 2012; Scott et al., 1992; Sneyd et al., 1988) as well as lineation (Krzesińska et al., 2015) in chondrites to impact. The major outstanding question, however, is how exactly are the chondrules changing shape? Is it a plastic or brittle process? Our findings strongly suggest that plastic deformation within crystalline

silicates has been minimal (Fig. 2.15), despite the large shape change evidenced by the foliation fabric and chondrule shapes (Fig. 2.3-2.5). This is consistent with Martin and Lindgren (in review) who examined forsterite in a Murchison chondrule using TEM and found no evidence for subgrain boundaries or other defects, also indicating that plastic deformation did not occur. Despite this, we see evidence that the majority of chondrules initially had a nearly spherical shape (Fig. 2.17) and so significant deformation within the chondrules has taken place. Therefore, we find that the majority of this strain was accommodated by brittle processes, both in the form of micro-fracturing of silicates (Fig. 2.9-2.13) as well as complete fracturing of chondrules (Fig. 2.13). Some grain boundary sliding and structural rearrangement is certainly taking place along with fracturing, and indeed we see clear evidence of relative movement between large fragments (Fig. 2.13).

However, we believe the largest movement and compression is most likely taking place between the crystal silicates in the mesostasis. Chondrule mesostasis, being glass and crystallites (or aqueously altered versions of them), would be the most structurally weak material within a chondrule and would preferentially experience the most strain. We believe we see evidence of this preferential deformation of mesostasis, as preserved original mesostasis texture is rare in our Murchison sample. Most commonly between the larger olivines and pyroxene crystals we see massive, texture-less serpentine sometimes with angular fragments of pyroxene that do not have the euhedral appearance of late stage crystallization (Fig. 2.10-2.12). We interpret the massive serpentine found within and around the olivine and pyroxene as the comminuted, altered remnants of mesostasis glass. In addition, where we do see heavily fractured and fragmented silicates within or around massive serpentine, it is more commonly pyroxene than olivine (Fig. 2.12). This is perhaps not surprising as the pyroxene shows a degraded texture with pore space that makes it stand out relative to the olivine in BSE images despite their similar greyscale (Fig. 2.10-2.12). This degraded texture and pore space would make pyroxene weaker relative to olivine, and indeed this degraded, porous texture in pyroxene is seen in several CMs, including relatively unaltered ones, suggesting that it is present very early

in CM chondrite alteration history (Hanowski and Brearley, 2001; Lindgren and Lee, 2015; Martin and Lindgren, in review). Previous workers have interpreted the preferential cracking and pore creation in CLEN to be a result of the inversion process from protoenstatite to CLEN upon chondrule cooling (Hanowski and Brearley, 2001; Yasuda et al., 1983), further suggesting that this pyroxene pore space is likely present at the time of deformation.

We therefore hypothesize that the majority of the overall shape change of the chondrule is being accommodating by fracturing, cataclasis, and perhaps collapse, firstly of the mesostasis and secondarily of pyroxene. Fracturing and cataclasis would lead to general communition of the mesostasis material and enable easier movement of it relative to the fractured, but still coherent, silicate grains. And the preferentially fragmented pyroxene would also contribute some movement and reorganization of the chondrule interior. We also see evidence for multiple episodes of fracturing and alteration, so the earliest alteration phases may also be preferentially accommodating some deformation (Fig. 2.13c-d) and allowing easier relative movement between grains (Fig. 2.12). Finally, some compression (volume change) may be also taking place within the chondrules if micropores are present within the mesostasis or pyroxene and being crushed out similar to void space removal in the matrix. We do see evidence of voids within altered mesostasis (Fig. 2.18) and pores have been found in altered mesostasis in another CM (Lindgren and Lee, 2015). We note that this implies that the chondrules are not completely incompressible as initially assumed, driving the pre-deformation porosity to higher values (section 2.3.5).

A natural question following this line of reasoning is why are the chondrules deforming only brittlely in Murchison, and not plastically, as impact shock is known to cause plastic deformation in silicates and this is commonly seen in other foliated chondrites (Nakamura et al., 1992; Scott et al., 1992)? It is possible that Murchison may have seen higher shock levels, but that the most highly deformed minerals have been preferentially destroyed by subsequent aqueous alteration. However, this would imply

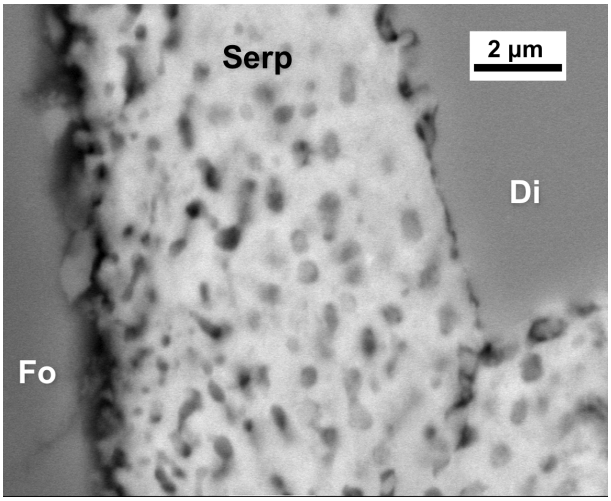

Fig. 2.18 Altered mesostasis texture showing void space.
Fo = Forsterite, Serp = Mg-Fe serpentine, Di = Diopside.

that the most deformed chondrules (i.e. with a higher aspect ratio or more elongation) would have a higher proportion of alteration products, and we do not see this correlation. Lindgren et al. (2015) addressed this paradox in Murchison by proposing that it experienced multiple, mild impacts, and our evidence of primarily brittle chondrule deformation with multiple fracturing events supports this interpretation as well. However, recent impact modeling of chondrule/matrix mixtures also suggests that the high initial porosity of the matrix leads to heterogeneous shock effects where the matrix experiences the highest shock pressures and temperatures while the chondrules remain relatively 'cold' (Bland et al., 2014). Therefore, the mild impact signature recorded by the Murchison chondrules could be at least partially the result of inherent material properties (i.e. porosity) and not a true reflection of the absolute impact intensity (impact velocity, pressure) experienced by the chondrite body.

Regardless, in Murchison, a relatively porous CM chondrite, impact force resulted in significant deformation of chondrules in a brittle manner and a record of high intensity impact leading to large amounts of plastic deformation is not found. While it is possible that annealing could have taken place after deformation and erased evidence of plastic deformation, we do not see evidence of this such as 120° triple junctions between grains. In addition, the high abundance of undehydrated serpentine and tochilinite strongly

suggests that Murchison was never heated to the higher temperatures required for annealing. Regardless, we do see evidence of some limited plastic deformation, mainly in clinopyroxene, which may indicate that clinopyroxene is weaker than olivine at high stresses (Raterron and Jaoul, 1991). The higher amount of plastic deformation within pyroxene could also be the result of lattice dislocations caused during the inversion from protoenstatite (Ruzicka, 1990), however this process cannot account for the higher amount of misorientations that we also see in diopside relative to olivine (Fig. 2.15). Regardless, the most significant portion of deformation and foliation of the chondrules is accommodated by brittle mechanisms, including some collapse of the chondrule porosity. Future models of chondrite deformation, especially when attempting to reproduce foliated or deformed chondrules, should account for this behavior instead of or in addition to plastic deformation of crystalline silicates to account for the change in shape of the chondrules (e.g. Bland et al., 2014).

Finally, we consider the implications of our observation that predominantly pyroxene and mesostasis within the Murchison chondrules are allowing the chondrules to change shape in response to the impact stress. This suggests that chondrules with a higher initial amount of these phases might allow for a larger amount of strain and shape change. As previously stated we did check for a positive correlation between amount of pyroxene or serpentine (altered mesostasis) and the shape of the chondrules and found none. However, if chondrule porosity collapses during the deformation, volume change will occur preferentially for these phases, erasing the evidence of their higher initial proportions and essentially 'normalizing out' the relative proportions of these phases among chondrules. Further, if certain chondrite classes have higher proportions of POP chondrules with abundant pyroxene and mesostasis, this might pre-disposition them to flatten and foliate in response to the presence of impact stress. In other words, the differences in petrofabric degree or strength between the different chondrite classes or within the classes themselves may not only reflect differences in impact intensity or conditions, but depend also on the initial rheology of the chondrules within them.

2.4.2 Relative timing of aqueous alteration

Our observations of microtextures involving alteration strongly suggest that some aqueous alteration post-dated or was contemporaneous with the impact events that foliated the chondrules. Several fractures parallel to the foliation fabric are filled with alteration products (Fig. 2.10c) with incomplete mineralization in some cases (Fig. 2.10e), and there is also evidence of serpentine and tochilinite precipitation after movement of chondrule fragments where the movement is also aligned with the macroscopic deformation fabric (Fig. 2.13). From a relative timing perspective, this seems to support the Rubin (2012) hypothesis that impacts facilitated some aqueous alteration of the CM chondrites by opening fractures within the chondrite body to allow for fluid flow. While Murchison has a relatively low degree of aqueous alteration (2.5 according to Rubin et al. (2007)) and a moderately strong foliation fabric (this work), Rubin (2012) generally found among the CMs a positive correlation between degree of aqueous alteration and petrofabric. Our Murchison sample suggests that while this direct correlation trend may not be valid for all CMs, there is evidence of impact facilitation of aqueous alteration in even the least altered CM chondrites such as Murchison. Further, we find evidence that there were multiple episodes of fracturing and aqueous alteration, and that later alteration involved formation of tochilinite (or pyrrhotite) while earlier alteration did not (Fig. 2.10d-f).

We can also surmise that no significant deformation or heating occurred after the latest phase of aqueous alteration. First, as is common for most CMs, the presence of tochilinite and serpentine argue against significant post-formation heating as both phases dehydrate at relatively low temperature (~245°C for tochilinite and ~400°C for serpentine, depending on composition) (Fuchs et al., 1973; Tonui et al., 2014). In addition, Murchison shock experiments have shown that by 10 GPa, Mg-Fe serpentine begins to decompose and tochilinite has completely decomposed (Tomioka et al., 2007). We see abundant fibrous tochilinite, and in one clear example, delicate serpentine fibers up to 40 microns long have remained undeformed and undehydrated after their

emplacement following the major deformation event (Fig. 2.13). If any significant deformation or shock equivalent to what had originally ruptured the iron-bearing olivine chondrule had occurred, the serpentine fibers would have been destroyed as sheet silicates are among the first silicates to break down in the presence of shock (Horz and Quaide, 1973). This is consistent with other work using bulk H, C, and N abundances and isotopic compositions which also indicated that Murchison has not been heated since aqueous alteration (Alexander et al., 2013).

While some aqueous alteration certainly post-dated the impact event(s), what remains unclear is whether any aqueous alteration also pre-dated it, especially in regards to hydration of chondrule glassy mesostasis or the matrix. It is possible, although we don't see any clear evidence for it, that glassy mesostasis was hydrated prior to the impact event(s). If the chondrule mesostasis was altered prior to deformation, it would have caused some mesostasis to be microporous as the crystallites preferentially leached out (Lindgren and Lee, 2015). This would result in greater compressibility of the mesostasis and the chondrule in general, and also allow for easier grain rearrangement (grain boundary sliding) within the chondrule due to the lubricating nature of the phyllosilcates. Since hydration of glassy mesostasis represents one of the very first stages of alteration among the CMs (Rubin et al., 2007) and unaltered, glassy mesostasis is rare even in the least altered CMs (Lindgren and Lee, 2015), we favor the interpretation that mesostasis was hydrated early, if not before the first deformational event then shortly thereafter and therefore provided some degree of chondrule compressibility during later deformation event(s).

2.4.3 Strain estimate and porosity loss

Using X-ray pole figure goniometry to determine the alignment of matrix serpentine basal planes, Fujimura (1983) estimated that Murchison had experienced ~9% uniaxial strain. While this is slightly lower than our minimum estimate of uniaxial strain (17%) using deformed chondrules, it is likely that their strain measurement is not directly

comparable to ours. First as we have found within our single Murchison sample, different regions of Murchison may have experienced different finite amounts of strain. Second, other work has suggested that the strain measurement derived using phyllosilicate grain foliation may not reflect the overall strain experienced by the sample and is therefore not directly comparable to strain estimates using other sample characteristics (Etheridge and Oertel, 1979; Oertel, 1983).

As mentioned in section 2.3.5, a key assumption of our strain estimate is that the chondrules were initially spherical. The ellipticity analysis of the deformed chondrules (Fig. 2.17) suggests that the chondrule were nearly, but not perfectly, spherical. We note that with this method initial sphericity is indistinguishable from a situation in which all objects have the same non-spherical, ellipsoidal shape and have a uniform orientation. This could be the result from an earlier deformation event but it would be impossible to distinguish this from the latest deformation and therefore our strain estimate remains the same and represents the total, finite strain. The other possibility is that the chondrules were initially non-spherical and accreted with a fabric on the parent body. Perhaps a foliated texture could be produced by accretion onto the parent body but a lineated texture (Fig. 2.4) would be hard to explain using current models of accretion of chondrule-sized objects that predict clumping under self gravity in a weakly turbulent nebula (e.g., Cuzzi et al., 2008). Regardless, we hypothesize that although initial sphericity of chondrules is a sufficient first-order approximation for our strain calculation, the original, pre-deformation shape of POP chondrules found in Murchison was most likely not perfectly spherical and XCT study of an unbrecciated and undeformed CM (e.g., Yamato 791198 (Metzler et al., 1992)) would be required to investigate original POP chondrule shape.

We calculate that our Murchison sample had a pre-deformation bulk porosity of 35.3 to 55.7%, depending on the influence of shear strain on pore compaction and the compressibility of the chondrules. The latter factor in particular is an important consideration, as we see evidence (pyroxene and mesostasis pore space) for some degree

of chondrule compressibility, which means the pre-deformation porosity is likely at the higher end of this range. Regardless of these factors, however, our estimate represents a significant loss in bulk porosity on the CM parent body as a result of impact, consistent with experimental and modeling studies (Bland et al., 2014; Nakamura et al., 2000). However, impacts are also hypothesized to create porosity in the form of open fractures and granular microcracks, which might be important in facilitating aqueous alteration of CM chondrites (DeCarli et al., 2001; Rubin, 2012). Indeed, we see abundant evidence of microcracks and fractures within chondrules (Fig. 2.10-2.13). Therefore, obviously some porosity is being created during deformation and this is leading to a localized increase in porosity. However, an unknown portion of this porosity is later filled by aqueous alteration products (e.g., Fig. 2.10), complicating the estimate of porosity increase through fracturing. Therefore the remaining unfilled porosity that is created from the result of impact deformation is unknown. One study which examined the nature of porosity in ordinary chondrites using XCT found that the most compacted samples had the majority of their porosity in the form of intragranular cracks and larger fractures as a result of impact shock rather than original intergranular porosity (Friedrich and Rivers, 2013). Using the average porosity of these compacted samples (3.9%) as an estimate of post-deformation porosity created via impact, this suggests that 18.3% of the total 22.2% current porosity of Murchison (Macke et al., 2011) is in the form of uncompacted porosity, resulting in a revised estimate of 32.2 – 53.4% for initial bulk porosity. Therefore, at a minimum the initial bulk porosity of Murchison was 32.2% prior to the deformation that foliated the chondrules within it, although evidence of chondrule compressibility suggests that the initial porosity was at the higher end of this range.

2.5 Conclusions

We have found that foliated and lineated chondrules within CM Murchison were deformed by impact and that primarily brittle, rather than plastic, mechanisms allowed for the deformation of the chondrules. Pyroxene and chondrule mesostasis were the

primary phases accommodating the strain within chondrules, and there is evidence to suggest that the chondrules were not completely incompressible and that some pore collapse occurred within them in addition to in the surrounding microporous matrix during impact. Aqueous alteration post-dated, or was perhaps contemporaneous with the deformation, and there were multiple episodes of fracturing and mineralization. We estimate that the strain experienced by our Murchison sample was 0.17 to 0.43 and likely the upper limit of this as the chondrules were compressible along with the matrix. This composes the first estimate of pre-deformation bulk porosity for a chondrite, 32.2 – 53.4%, perhaps providing a glimpse of primary, accretionary porosity for chondrite parent bodies.

Chapter 3: Evidence for accretion of fine-grained rims in a turbulent nebula for CM Murchison

3.1 Introduction

Fine-grained rims (FGRs) are dust-sized material that surrounds chondrules, calcium-aluminum inclusions (CAIs), and other inclusions in chondritic meteorites. They are present in unequilibrated chondrites and are usually distinguishable from the surrounding matrix in optical and scanning electron microscopy images on the basis of their differing texture and/or composition (Lauretta et al., 2006). Among the different chondrite groups FGR characteristics differ, most notably in that the carbonaceous chondrites have significantly thicker rims compared to the ordinary chondrites as well as hydrated phases (e.g., serpentines, smectites) which are absent in the rims of ordinary chondrites (Metzler and Bischoff, 1996; Zolensky et al., 1993). Among the carbonaceous chondrites the thickest and perhaps best developed FGRs are found in CMs and as a result these have been the most extensively studied (e.g., Metzler and Bischoff, 1996; Metzler et al., 1992; Trigo-Rodriguez et al., 2006). In some CM chondrites, FGRs surround all macroscopic components and dominate the proportion of fine-grained material in the rock with only minor interstitial matrix (Metzler et al., 1992). Although the term implies a specific genetic origin for the FGRs, chondrites with this texture have been termed "primary accretionary rock" (Metzler et al., 1992).

The exact origin and formation of FGRs in CMs is still intensely debated however and formation in both nebular (Brearley et al., 1999; Bunch and Chang, 1984; Greshake et al., 2005; Hua et al., 2002; Metzler et al., 1992; Zega and Buseck, 2003) and parent body (Sears et al., 1993; Takayama and Tomeoka, 2012; Trigo-Rodriguez et al., 2006) settings have been argued (Fig. 3.1). Proposed FGR formation in the nebula involves accretion of unequilibrated nebular dust to chondrule surfaces (e.g., Metzler et al., 1992).

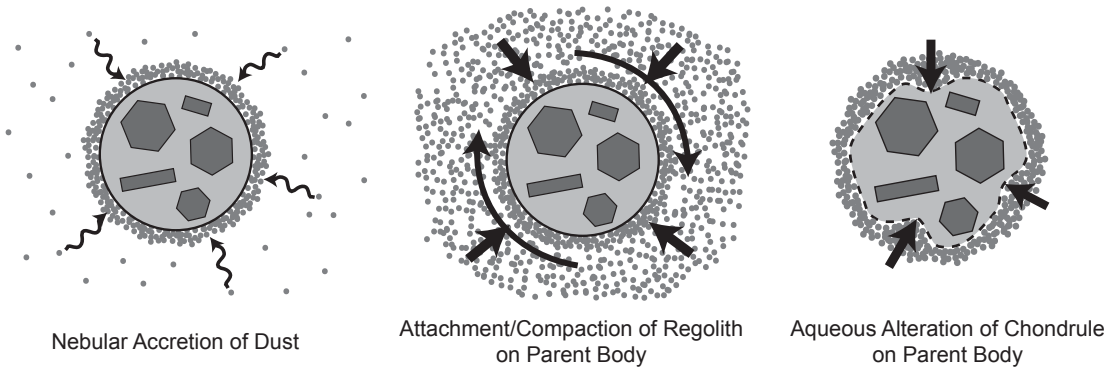

Fig. 3.1 Three proposed formation scenarios for FGRs in CM chondrites.

Mechanisms of FGR formation in a parent body setting involves one of two processes (or some combination thereof): 1) formation in the parent body regolith through attachment and/or compaction of fine-grained material onto the chondrule surface (Sears et al., 1993; Takayama and Tomeoka, 2012; Trigo-Rodriguez et al., 2006) or 2) formation via aqueous alteration of the chondrule while it resides on the parent body (Sears et al., 1993; Takayama and Tomeoka, 2012). Arguments for the differing formation locations have been made on the basis of textural and mineralogical evidence. Evidence cited for nebular formation includes hydrated phases in the rim in direct contact with chondrule glass (Metzler et al., 1992) and sedimentary rim textures such as layering and grain-size coarsening (Brearley et al., 1999). Parent body formation evidence includes alteration textures along the chondrule/rim boundary indicating some areas of the rim formed through alteration of the chondrule (Takayama and Tomeoka, 2012) and low rim porosity compared to the matrix which may have arisen due to preferential compaction of material next to the chondrules (Trigo-Rodriguez et al., 2006). A final FGR formation mechanism not depicted in Figure 3.1 is impact-generated accretionary lapilli (King and King, 1981). However, this formation process has not been discussed in detail and has been mostly discounted in recent literature in favor of nebular or other parent body processes (e.g., Metzler et al., 1992).

Another observation taken as evidence for nebular formation of FGRs in CMs is a positive correlation between rim thickness and the size of the interior chondrule (Greshake et al., 2005; Metzler et al., 1992). Conversely, Trigo-Rodriguez et al. (2006) did not find strong evidence for a such a correlation in the CMs they examined and argued that this was evidence against nebular formation and instead proposed that the rims were formed in a parent body setting. All of these studies used uncorrected measurements made in 2D thin section, which gives only apparent chondrule size and rim thickness unless the appropriate measurement corrections are applied (e.g., Sahagian and Proussevitch, 1998). Another complicating factor is that many CMs show evidence of deformation that has significantly altered the shape of the chondrules and their rims (Hanna et al., 2015; Lindgren et al., 2015; Rubin, 2012; Zolensky et al., 1997). In addition, although astrophysical arguments have been made for the positive linear correlation between rim thickness and interior chondrule radius (Morfill et al., 1998), this theory has since been refined on the basis of other evidence that the solar nebula was likely weakly turbulent (Cuzzi et al., 1996; Cuzzi et al., 2001). Specifically, dust accretion around chondrules in a weakly turbulent nebula results in a specific power law relationship between the FGR volume and interior chondrule radius (Cuzzi, 2004; Cuzzi and Hogan, 2003).

Accurate measurement of FGR thickness and volume requires three-dimensional (3D) data of the chondrules and their rims, which the previously used techniques cannot provide. X-ray computed tomography (XCT) allows non-destructive measurement of textures and components in situ and preserves their 3D spatial context (e.g., Hanna and Ketcham, in review; Ketcham and Carlson, 2001). Spatial context is particularly important for samples that have undergone deformation that has resulted in a petrofabric. Previous XCT studies found CM Murchison to have a moderately strong foliation as well as a weak lineation (Hanna et al., 2015; Lindgren et al., 2015), likely due to impact(s) which also resulted in porosity loss and aqueous alteration (Hanna et al., 2015). If FGRs in CMs are produced via aqueous alteration on the parent body (Sears et al., 1993;

Takayama and Tomeoka, 2012), it is possible that we may see evidence for this in the form of greater FGR volume with increased degree of alteration among chondrules.

The goal of our study is to nondestructively examine the 3D morphology of FGRs in CM Murchison for which we have previously quantified the deformational strain and documented the resulting aqueous alteration (Hanna et al., 2015). Using 3D measurement of the FGRs, we will determine if there is a positive correlation between the thickness or volume of the rim and the size of the interior chondrule in order to establish if there is evidence for nebular FGR formation and whether the nebular environment was laminar or turbulent, which should result is slightly different FGR/chondrule size relationships (Cuzzi, 2004; Morfill et al., 1998). We will also look for evidence of FGR deformation that may have occurred during the impact(s) such as preferential compaction of the rims in the direction of maximum stress (i.e. perpendicular to the foliation plane) and determine if there is evidence for parent body FGR formation via aqueous alteration of the chondrules.

3.2 Analytical methods

3.2.1 X-ray computed tomography

We scanned six small chips (0.143 – 3.63 g; some embedded in epoxy) from the CM Murchison USNM 5487 sample that was previously measured by Hanna et al. (2015) (Table 3.1). All scanning was done at the University of Texas High-Resolution X-ray Computed Tomography Facility (UTCT) at 70 or 90 kV X-ray energy and the reconstructed voxel (3D pixel) size ranged from 5.5 to 9.9 microns (Table 3.1). XCT produces a 3D volume of the X-ray attenuation of an object where the values are referred to as CT numbers and are mapped to grayscale values for viewing. Because X-ray attenuation is a function of the atomic number and density of a material, the relative CT numbers are a proxy for different compositions within the sample (although some compositions overlap in their X-ray attenuation) (e.g., Hanna and Ketcham, in review).

Table 3.1 Physical characteristics and scanning parameters of six chips of USNM 5487 examined for this study

Data Name	USNM Sample #	Weight (g)	Embedded in Epoxy?	Location in original USNM 5487 main mass[a]	UTCT System Used	Energy (kV)	Scan Time (hours)	Voxel Size (μm)
Chip A[b]	5487[c]	0.143	No	Sub-Volume #2	Xradia	70	6.08	5.50
Chip A_HR[d]	-	-	-	-	Xradia	70	11.55	3.00
Chip 1	5487-1	3.63	Yes	Sub-Volume #1	NSI	90	2.50	9.99
Chip 3-1	5487-3-1	0.87	Yes	Sub-Volume #2	NSI	90	2.50	9.99
Chip 3-3	5487-3-3	1.22	Yes	Sub-Volume #2	NSI	70	3.03	9.49
Chip 3-5	5487-3-5	1.32	Yes	Sub-Volume #2	NSI	90	2.50	9.99
Chip 3-6	5487-3-6	0.77	Yes	Sub-Volume #2	NSI	70	3.03	9.49

[a]See Hanna et al. (2015) Figure 1 [b]Scanned in two parts [c]Unlabeled portion of main mass [d]Higher-resolution subvolume scan of Chip A

In a typical XCT image, the lowest CT numbers (darkest grayscales) represent the least X-ray attenuating materials while relatively higher CT numbers (brighter grayscales) are materials that are relatively more attenuating to X-rays.

Samples were scanned on two of the XCT systems at UTCT (Table 3.1). The samples were scanned at varying data resolutions to provide a statistically significant number of measureable chondrules at a range of sizes. Relatively low energies (70-90 kV) were used to enhance the contrast between iron-bearing phases and helped to more clearly distinguish the rims that are lower in iron content than the surrounding matrix (Section 3.3.1). The first sample is an unlabeled chip of the USNM 5487 main mass and was scanned twice on the Xradia (now Zeiss) microXCT 400 system using a 0.35 mm SiO_2 filter to reduce beam hardening artifacts. For the first scan (Chip A) the chip was imaged in two parts and then combined. The final reconstructed voxel size was 5.50 μm. The second scan (Chip A_HR) targeted a subvolume of the sample at higher resolution (3.00 μm). This higher-resolution scan was used to investigate the different object types and their accompanying FGRs in more detail. Two more individual scans of 5 larger-mass samples were done on the NSI system at lower resolution to measure additional larger chondrules ($\geq$ 300 μm in radius). The first NSI scan was of 5487-3-3 and 5487-3-6 and the second scan of 5487-1, 5487-3-1, and 5487-3-5. Both scans utilized the FeinFocus source and Perkin Elmer detector with no beam filtering. The final reconstructed voxel sizes for these scans were 9.49 μm (Chips 3-3 and 3-6) and 9.99 μm (Chips 1, 3-1, and 3-5).

3.2.2 XCT measurement of chondrules and FGRs

Chondrules within the six XCT datasets were manually segmented in the Avizo™ program. Each chondrule was segmented twice (with and without FGR) and added to different label (segmentation data) fields. Specifically, we used the brush tool to outline the exterior of the chondrule and then used the fill command to complete the segmentation. This was done for every other XCT slice across the chondrule in one

orthogonal plane (segmentation plane varied across chondrules to minimize systematic measurement bias) and then the interpolate tool was used to fill in the remaining slices. After the entire chondrule was segmented, smoothing was applied once in each of the other two orthogonal planes (in Avizo™ selection smooth operates only in 2D) to minimize jagged edges that resulted from manual segmentation and interpolation in a single plane. Only whole chondrules with clearly defined rims were segmented and we avoided any chondrules that were on the sample edge, crossed by a visible fracture, or impinged by another chondrule.

Segmentation data was exported into the Blob3D software (Ketcham, 2005a; Ketcham, 2005b) and chondrule size and orientation measured with (whole chondrule) and without (interior chondrule) the FGR. Orientations were derived from best-fit ellipsoids to the whole and interior chondrule exteriors (both with and without the FGR). Orientations were plotted on stereonets using the Stereo32 software (Roeller and Trepmann, 2010). This software was also used to calculate the strength of fabrics defined by the chondrule orientations and is reported as the C parameter. Lower values of C represent a weaker fabric and relatively higher values represent a relatively stronger fabric. Further details on this fabric strength parameter calculation can be found in Hanna et al. (2015). Reported aspect ratios are the ratios of the long axis to the short axis of the fitted ellipsoids. The reported whole and interior chondrule radii are spherical volume equivalent radii using the respective XCT measured chondrule volumes. The FGR volume was determined by subtraction of the two measured volumes (measurement with and without the FGR). To determine the average FGR thickness for each chondrule the interior chondrule radius was subtracted from the whole chondrule radius. The measurement of the actual 3D FGR thickness around each chondrule is described in Section 3.2.4. A summary of our estimated measurement errors for all reported parameters are listed in Table 3.2 and described in detail in Appendix D.

Table 3.2 Measurement errors for parameters reported in this study[a]

	Relative %
Interior Chondrule Volume	3.9%
Whole Chondrule Volume	1.7%
FGR Volume[b]	4.1%
FGR % Volume[c]	3.1%
Interior Chondrule Radius[d]	1.3%
Whole Chondrule Radius[d]	0.6%
Average FGR Thickness[e]	4.1%
FGR % Thickness[f]	4.1%
Interior Chondrule Aspect Ratio	0.5%
Whole Chondrule Aspect Ratio	1.4%
Interior Chondrule CVI	1.3%
Whole Chondrule CVI	1.0%
Interior Chondrule Ellipticity	0.1%
Whole Chondrule Ellipticity	0.2%
Interior Chondrule Roughness	1.4%
Whole Chondrule Roughness	1.0%

[a]See Appendix A for derivation details
[b]Derived from measured volumes of whole and interior chondrules
[c]Normalized to whole chondrule volume
[d]Equivalent spherical radius
[e]Derived from equivalent spherical radii of whole and interior chondrules
[f]Normalized to maximum radius of best-fit ellipsoid to whole chondrule

3.2.3 Shape measurement

To quantify the shape irregularity (departure from an idealized sphere or ellipsoid) of the chondrules we used three indices. The first is the Convolution Index (CVI), which is the ratio of the chondrule surface area to the surface area of a sphere of equivalent volume (Hertz et al., 2003; Zanda et al., 2002).

$$\text{CVI} = \frac{\text{surface area}_{chondrule}}{\text{surface area}_{sphere}} \quad (1)$$

This is the inverse of the more commonly used particle shape measurement sphericity (Blott and Pye, 2008). A CVI value of one indicates that the chondrule is a perfect sphere and higher values indicate higher degrees of departure in shape from a sphere (Fig. 3.2). One ambiguity with this index is that it cannot distinguish between a smooth ellipsoid and a spherical but rough surface, as both will increase the surface area of the chondrule relative to an equivalent volume sphere. Because our previous work had shown that Murchison chondrules are deformed into ellipsoids (Hanna et al., 2015), we deconvolved the CVI into two new indices which quantify ellipticity and roughness separately. The ellipticity index is defined as

$$\text{Ellipticity} = \frac{\text{surface area}_{best-fit\ ellipsoid}}{\text{surface area}_{sphere}} \quad (2)$$

where the best-fit ellipsoid is that found for the chondrule by Blob3D (Section 3.2.2), normalized in size to the volume of the chondrule. An ellipticity value of 1 indicates that the chondrule is a perfect sphere and higher values indicate a more ellipsoidal shape (Fig. 3.2). The roughness index is defined as

$$\text{Roughness} = \frac{\text{surface area}_{chondrule}}{\text{surface area}_{best-fit\ ellipsoid}} \quad (3)$$

where the best-fit ellipsoid is the same as in Equation (2). A value of 1 indicates that the chondrule has a smooth surface and higher values indicate increasing degrees of surface roughness (Fig. 3.2). Estimated measurement errors for these indices are listed in Table 3.2 and described in detail in Appendix D.

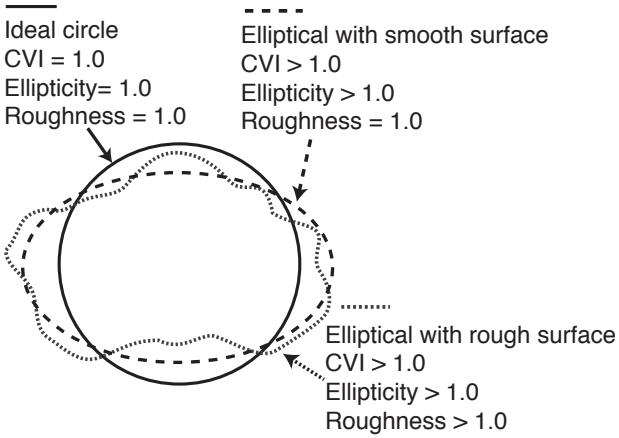

Fig. 3.2 Chondrule shape measurements (idealized in 2D).
A perfect circle (sphere) has a CVI, ellipticity, and roughness of 1.0. Higher degrees of irregularity lead to a larger amount of surface area compared to a perfect sphere and a CVI > 1.0. CVI is deconvolved into ellipticity and surface roughness. Chondrules with a more ellipsoidal shape will have ellipticity > 1.0 and chondrules with a rough surface (whether the chondrule is ellipsoidal or not) with have roughness > 1.0.

3.2.4 3D FGR thickness measurement

To determine the actual 3D thickness of the FGR around each chondrule a new algorithm was implemented in Blob3D (Appendix E). For each rimmed chondrule, the algorithm "looks outward" from the chondrule center along a set of 3D traverses evenly covering a unit sphere and measures the thickness of the rim along each vector (Fig. 3.3). The chondrule center is defined as the center (average vertex) of the surface (set of vertices) that defines the outer extent of the rimmed chondrule. Because the FGR thickness was found to vary systematically with chondrule size, the thickness measurements were normalized by the maximum diameter of the chondrule and are reported as FGR percent thickness. To ensure a more random sampling of vectors for FGR measurement that sufficiently covered 3D space, several sets of uniform vectors were generated using the method of Ketcham and Ryan (2004); each set was randomly rotated and then collated to create a list of 2065 vectors. Each chondrule FGR shell was measured with this set of vectors and then the average percent FGR thickness among all

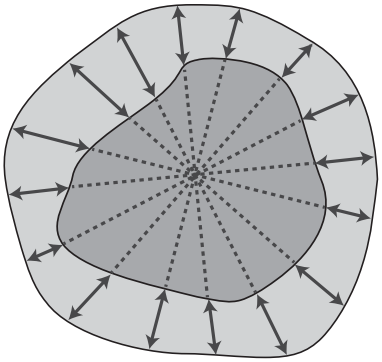

Fig. 3.3 Blob3D rim thickness measurement (idealized in 2D). *Algorithm looks outward from chondrule center to measure FGR thickness along each vector.*

chondrules was calculated for each vector. These data were inspected for spatial coherence using stereoplots. Note that the average *percent* FGR thickness reported in these plots is different from the average FGR thickness calculated by subtracting the volume equivalent spherical radii of the whole and interior chondrules (Section 3.2.2; reported in Table 3.3). The latter is an average FGR thickness for each chondrule, while the former is an average percent FGR thickness among all chondrules in each measured orientation.

3.3 Results

3.3.1 General observations

The XCT data of all samples are similar in appearance and highlight differences in X-ray attenuation primarily due to the presence of iron. Figure 3.4 shows an example XCT slice of the Chip A sample. Overall it bears a striking resemblance to a low-resolution backscattered electron (BSE) image, which is unsurprising as both XCT and BSE imaging are sensitive to elemental composition (Hanna and Ketcham, in review; Reed, 2005). We identify phases based on our previous work utilizing optical and

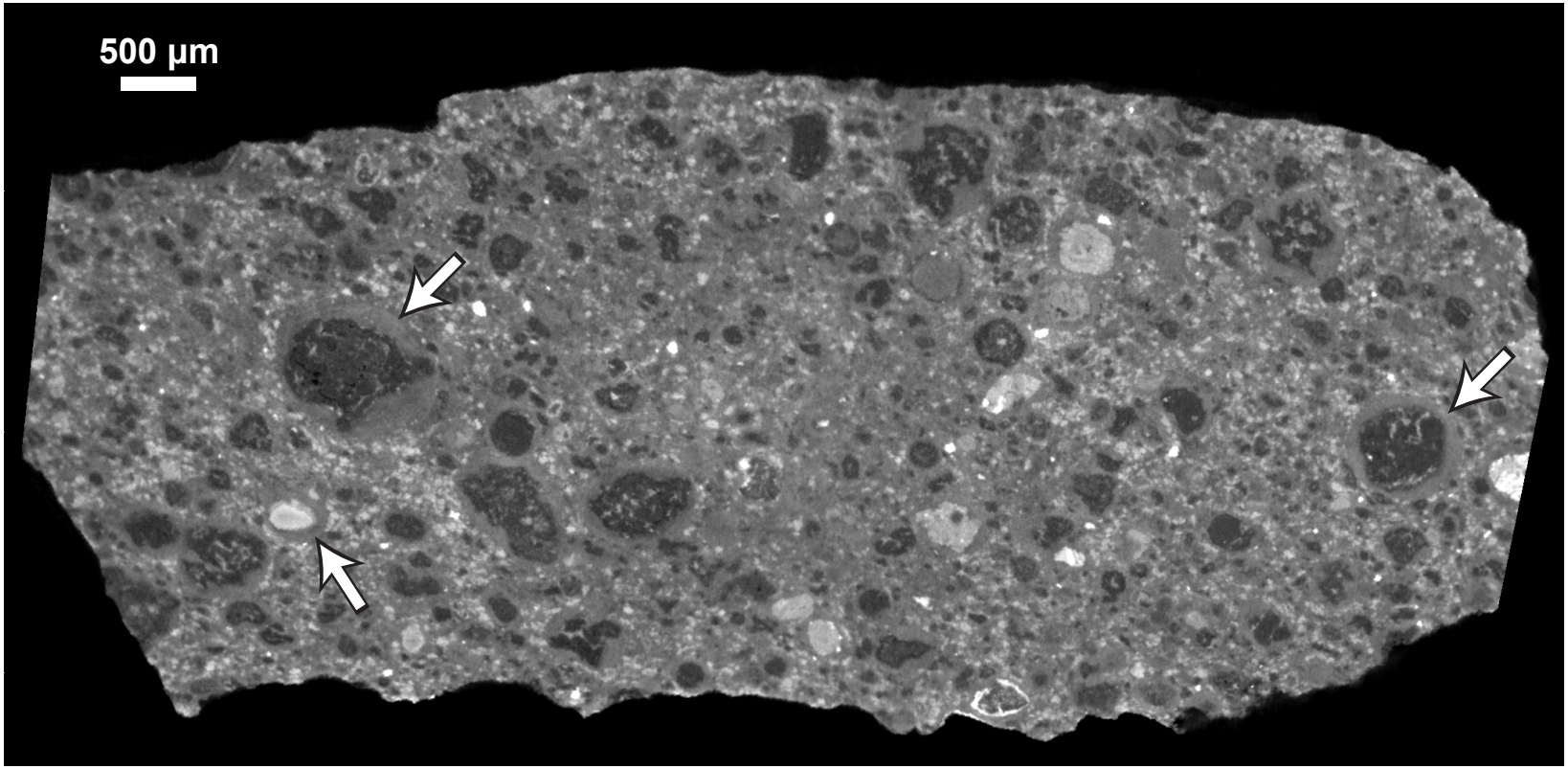

Fig. 3.4 XCT slice 529 along XZ axis of Chip A.
Greyscale (e.g., X-ray attenuation) variations are primarily due to differing amounts of iron. Dark objects are Type I chondrules dominated by Mg olivine and pyroxene and brighter objects are Type II chondrules (Fe-bearing olivine), Fe-bearing olivine crystal fragments, Fe serpentine, and Fe sulfides. FGRs appear as a moderate grayscale rim around most objects. White and black arrows point out three examples of prominent FGRs.

electron microscopy to support XCT examination of Murchison (Hanna et al., 2015). The darkest, or least attenuating objects, are Type I chondrules dominated by pure Mg silicates (olivine and pyroxene). The minor bright phases visible within the Type I chondrules are low Ca pyroxene and Fe-Mg serpentine and sulfide. The largest bright, highly attenuating objects in Fig. 3.4 are Type II chondrules (dominated by Fe-bearing olivine), Fe olivine crystal fragments, and Fe sulfide. Fe sulfide appears brightest within the image due to its higher iron content. The smaller, more dispersed bright phases are clumps of tochilinite, cronstedtite, and serpentine [TCS, sometimes referred to in the literature as PCP, or poorly/partly characterized phases (Fuchs et al., 1973; Nakamura and Nakamuta, 1996)]. FGRs surrounding chondrules and other objects appear as a medium grayscale within the XCT data and are primarily distinguished by the absence of the bright TCS clumps that are common in the surrounding matrix (Fig. 3.4; see also Figs. 3.5 and 3.7). The absence of TCS clumps in FGRs has been noted previously for other CMs (Trigo-Rodriguez et al., 2006).

Many of the discrete objects (not including TCS clumps) within the XCT data have distinguishable FGRs. Figure 3.5 highlights several different object types with FGRs found within the samples. The first (Fig. 3.5A) is an example of a Type II chondrule with an FGR located on the edge of Chip 3-3. The olivines are clearly zoned and a thick FGR is distinguishable around the entire portion of the chondrule that is present. Figure 3.5B shows a rimmed CAI from Chip 3-6. Note the pores and highly irregular boundary of the interior portion in contrast to the smoother FGR. An object approximately 400 microns in diameter with an FGR from Chip A_HR is shown in Figure 3.5C. It is also visible in the Chip A XCT data at lower resolution. Because it has minimal internal structure and an angular shape we interpret the object to be a lithic clast. We searched for but did not find any other apparent lithic clasts among the XCT datasets. The object shown in Fig. 3.5D is an unknown object from the Chip A_HR XCT dataset, with a very diffuse and irregular boundary with large interior pores and cracks. It is unclear if the lighter-toned rim around the object is a true FGR or is part of the object

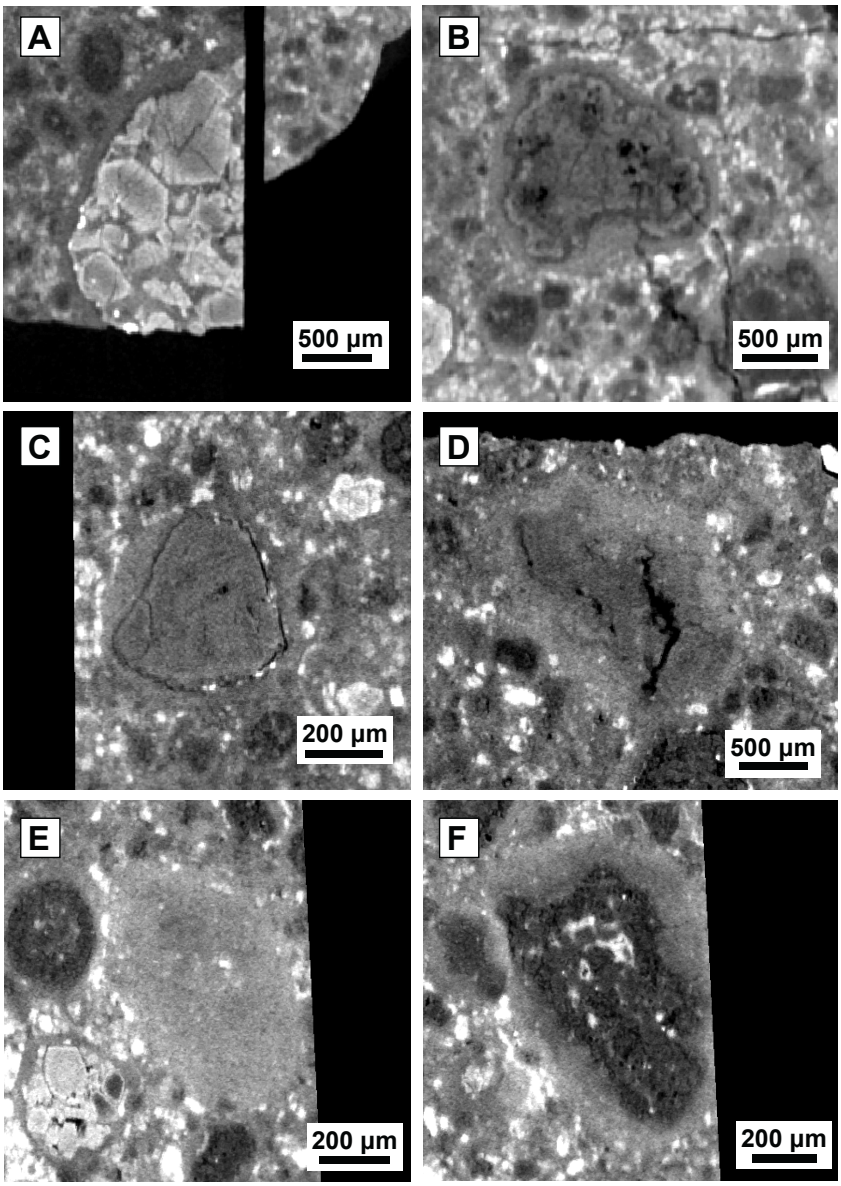

Fig. 3.5 Various rimmed objects in the XCT data.
(A) Portion of Type II chondrule in Chip 3-3. XZ slice 609. Note zoned olivines. (B) CAI with FGR in chip 3-6. XZ slice 894. The CAI has interior pores and a highly irregular boundary that is not reflected in the outer boundary of the FGR, which is much more smooth. (C) Presumed lithic clast in Chip A_HR. YZ slice 239. FGR is difficult to discern in places but completely encases object. (D) Unidentified object that appears to have a faint, but discernable FGR in Chip A_HR. YZ slice 443. (E) In YZ slice 630 of Chip A_HR, the edge of an FGR appears as if it is an isolated clast of FGR material with no interior object. (F) However, YZ slice 665 reveals that the FGR does indeed enclose a Type I chondrule.

itself (i.e., an alteration rind of some kind). We found two other smaller objects with a similar appearance within the Chip A_HR dataset. Like the object in Figure 3.5C, they also appeared to have a rim. We searched for but did not find objects of this type in the other sample datasets.

One object type that we actively searched for was clasts of FGR material with no interior object, as have been reported in other CMs (Trigo-Rodriguez et al., 2006). It is possible that the unknown objects like those in Figure 3.5C are clasts of this type, but we do not favor this interpretation because they clearly show a rim. When looking through the XCT slices it is very common to see what looks like an isolated clast of FGR material with no interior object but nearby slices confirm that this is merely the edge an FGR-enclosed object (Fig. 3.5E-F). We also searched in all datasets for groups of chondrules or other inclusions that are all enclosed by a single FGR but did not find any.

Although many types of objects were found to have FGRs only Type I chondrules were measured for this study. Testing formation theories based on chondrule and FGR sizes requires a statistically significant number of objects and Type I chondrules are much more abundant than other object types in CM Murchison. In addition, it is hypothesized that other object types, such as refractory inclusions, may have different rimming properties in a nebular formation setting due to their larger size and/or different densities (Cuzzi, 2004). A total of 61 Type I chondrules among the 6 samples were segmented and measured (Table 3.3).

3.3.2 Chondrule and FGR sizes and shapes

Table 3.3 lists the XCT measurements of 61 chondrules segmented for this study, including the range of chondrule sizes and FGR properties. Measured chondrule sizes ranged from 176.2 to 1503.6 μm in equivalent spherical diameter. Average FGR thickness among the chondrules ranged from 27.8 to 102.5 μm. The best-fit line to the interior chondrule radius and the average FGR thickness for each chondrule (Fig. 3.6A), including uncertainty in FGR volume (4.1%; Table 3.2), has a slope of 0.11 ± 0.004 (2-

Table 3.3 XCT measurements of 61 chondrules with FGR among 6 samples.

	Num.	IC[a] Volume (mm^3)	FGR Volume (mm^3)	IC Radius (μm)	Average FGR Thickness (μm)	IC Aspect Ratio	WC[b] Aspect Ratio	IC CVI	WC CVI	IC Ellipticity	WC Ellipticity	IC Roughness	WC Roughness
Chip A	1	0.027	0.019	185.3	36.1	1.43	1.38	1.20	1.21	1.02	1.02	1.17	1.19
	2	0.019	0.015	166.6	34.5	1.76	1.54	1.22	1.20	1.05	1.03	1.16	1.17
	3	0.089	0.071	277.3	59.5	1.42	1.31	1.53	1.25	1.02	1.01	1.51	1.23
	4	0.016	0.017	157.3	42.2	1.71	1.51	1.28	1.26	1.04	1.02	1.24	1.24
	5	0.015	0.014	151.8	37.6	1.78	1.68	1.38	1.29	1.04	1.04	1.32	1.25
	6	0.005	0.007	103.4	37.0	1.55	1.37	1.24	1.17	1.03	1.01	1.21	1.16
	7	0.010	0.012	132.7	40.2	2.02	1.70	1.37	1.27	1.07	1.04	1.28	1.22
	8	0.026	0.016	184.8	31.2	1.17	1.17	1.18	1.16	1.00	1.00	1.17	1.16
	9	0.095	0.076	283.5	61.3	1.89	1.58	1.54	1.24	1.05	1.03	1.47	1.20
	10	0.021	0.015	172.1	33.9	1.65	1.46	1.24	1.20	1.03	1.02	1.20	1.18
	11	0.196	0.122	360.5	63.0	1.92	1.71	1.42	1.24	1.06	1.04	1.34	1.20
	12	0.011	0.009	135.9	30.2	1.12	1.23	1.15	1.18	1.00	1.01	1.14	1.17
	13	0.037	0.025	206.8	38.5	1.42	1.37	1.31	1.19	1.02	1.01	1.28	1.18
	14	0.017	0.020	159.5	47.6	1.23	1.32	1.25	1.20	1.01	1.01	1.24	1.18
	15	0.024	0.017	179.3	35.6	1.33	1.29	1.20	1.19	1.01	1.01	1.19	1.18
	16	0.034	0.028	200.9	44.6	1.49	1.57	1.26	1.22	1.02	1.03	1.23	1.19
	17	0.031	0.022	193.9	39.1	1.23	1.25	1.21	1.21	1.01	1.01	1.20	1.20
	18	0.009	0.010	127.2	38.3	1.35	1.27	1.15	1.17	1.01	1.01	1.13	1.16

Table 3.3, cont.

19	0.003	0.004	89.9	30.3	1.39	1.36	1.15	1.18	1.02	1.02	1.13	1.16
20	0.050	0.034	228.3	43.5	1.64	1.49	1.22	1.20	1.03	1.02	1.18	1.18
21	0.022	0.020	173.9	42.3	1.85	1.66	1.33	1.31	1.05	1.04	1.26	1.26
22	0.013	0.016	146.1	44.0	1.41	1.42	1.31	1.20	1.02	1.02	1.29	1.18
23	0.080	0.096	266.8	80.2	1.43	1.32	1.49	1.17	1.02	1.01	1.46	1.16
24	0.005	0.009	103.0	44.8	1.36	1.24	1.15	1.19	1.02	1.01	1.13	1.18
25	0.028	0.020	188.2	36.9	1.90	1.64	1.27	1.21	1.05	1.03	1.21	1.17
26	0.007	0.006	119.4	28.5	1.35	1.36	1.16	1.18	1.01	1.01	1.15	1.17
27	0.043	0.027	216.8	38.9	1.55	1.48	1.28	1.23	1.03	1.02	1.25	1.20
28	0.012	0.009	140.9	30.3	1.58	1.45	1.25	1.22	1.03	1.02	1.21	1.19
29	0.006	0.008	110.9	36.3	1.16	1.11	1.20	1.16	1.00	1.00	1.19	1.16
30	0.019	0.021	165.0	46.7	1.71	1.50	1.39	1.24	1.04	1.02	1.34	1.21
31	0.017	0.022	158.9	51.2	1.44	1.47	1.32	1.21	1.02	1.02	1.29	1.19
32	0.013	0.017	147.6	45.6	1.56	1.48	1.26	1.16	1.03	1.02	1.22	1.14
33	0.050	0.045	228.7	54.0	2.01	1.75	1.39	1.26	1.07	1.05	1.30	1.20
34	0.025	0.020	182.1	39.6	1.55	1.40	1.42	1.19	1.03	1.02	1.38	1.17
35	0.043	0.036	217.9	48.5	1.20	1.20	1.48	1.19	1.00	1.01	1.47	1.18
36	0.003	0.005	88.1	34.0	1.14	1.21	1.13	1.14	1.00	1.01	1.13	1.13
37	0.101	0.108	288.9	79.4	1.73	1.55	1.53	1.25	1.04	1.03	1.47	1.22
38	0.012	0.010	142.6	32.1	1.22	1.23	1.30	1.17	1.01	1.01	1.29	1.17
39	0.185	0.134	353.5	70.6	1.39	1.38	1.24	1.20	1.02	1.01	1.22	1.19

Table 3.3, cont.

	40	0.014	0.009	150.1	27.8	1.32	1.40	1.22	1.21	1.01	1.02	1.20	1.19
Chip 1	1	0.408	0.248	460.2	78.9	2.29	2.14	1.54	1.25	1.10	1.08	1.40	1.15
	2	0.963	0.392	612.7	73.8	1.51	1.53	1.19	1.17	1.02	1.03	1.16	1.14
Chip 3-1	1	0.164	0.149	339.6	81.6	2.12	1.97	1.40	1.22	1.08	1.06	1.30	1.15
	2	0.382	0.165	450.0	57.3	2.18	2.01	1.30	1.25	1.10	1.08	1.18	1.15
	3	0.531	0.210	502.4	58.9	1.65	1.56	1.31	1.22	1.03	1.03	1.27	1.18
	4	0.256	0.145	394.1	63.6	1.62	1.57	1.24	1.20	1.04	1.04	1.20	1.16
	5	0.192	0.108	357.8	57.5	1.26	1.17	1.16	1.16	1.01	1.00	1.15	1.16
Chip 3-3	1	1.123	0.625	644.8	102.5	1.57	1.42	1.42	1.22	1.03	1.02	1.38	1.20
	2	0.775	0.450	569.9	94.0	1.50	1.49	1.29	1.19	1.02	1.02	1.26	1.16
	3	0.288	0.170	409.9	68.4	1.20	1.25	1.15	1.15	1.00	1.01	1.14	1.14
	4	0.337	0.207	431.8	74.7	1.44	1.42	1.20	1.18	1.02	1.02	1.18	1.15
	5	0.205	0.141	365.8	69.8	1.49	1.45	1.23	1.17	1.02	1.02	1.21	1.15
	6	0.285	0.217	408.0	84.9	1.53	1.52	1.27	1.21	1.02	1.02	1.24	1.18
Chip 3-5	1	1.780	0.588	751.8	75.0	1.56	1.53	1.20	1.18	1.03	1.02	1.17	1.15
	2	0.332	0.196	429.5	71.8	1.49	1.37	1.26	1.18	1.03	1.01	1.23	1.17
	3	0.411	0.238	461.4	75.9	1.79	1.77	1.35	1.22	1.05	1.05	1.29	1.16
	4	0.288	0.187	409.5	74.3	1.42	1.35	1.34	1.17	1.02	1.01	1.31	1.16
Chip 3-6	1	0.676	0.356	544.3	82.5	1.19	1.25	1.18	1.16	1.00	1.01	1.18	1.15
	2	0.370	0.235	445.3	79.4	1.19	1.23	1.14	1.16	1.01	1.01	1.13	1.15
	3	0.188	0.110	355.7	58.8	1.19	1.19	1.19	1.16	1.00	1.00	1.19	1.16

Table 3.3, cont.

	4	0.343	0.254	434.3	88.0	1.89	1.74	1.46	1.22	1.07	1.05	1.37	1.17
Minimum		0.003	0.004	88.1	27.8	1.12	1.11	1.13	1.14	1.00	1.00	1.13	1.13
Maximum		1.780	0.625	751.8	102.5	2.29	2.14	1.54	1.31	1.10	1.08	1.51	1.26
Mean (*n*=61)		0.192	0.108	279.8	54.2	1.53	1.46	1.29	1.20	1.03	1.02	1.25	1.18

[a]IC = interior chondrule [b]WC = whole chondrule

sigma uncertainty in fit) and a moderately strong correlation ($R^2 = 0.73$). This is consistent with Metzler et al. (1992) who also reported a positive correlation between chondrule size and FGR thickness and which has been argued as evidence for nebular accretion of the rims (Metzler et al., 1992; Morfill et al., 1998). However, Cuzzi (2004) suggested that nebular formation of FGRs may manifest more precisely as a power law relationship between the interior chondrule radius and the FGR volume. To determine this relationship while including the uncertainty in FGR volume (4.1%; Table 3.2) we used the Levenberg-Marquardt method to determine a non-linear least squares fit to the data (Press, 2007). When analyzed this way the data shows a much stronger fit ($R^2 = 0.98$; Fig. 3.6B) with a power law exponent of 2.50 ± 0.02 (2-sigma uncertainty in fit).

In regard to chondrule shape, we first examine the relationships of the CVI, ellipticity, and roughness indices for the interior chondrules. In Figure 3.6C it is apparent that ellipticity and roughness are uncorrelated and thus well separated indices that are independently quantifying the ellipticity and surface roughness of the chondrules. Figures 3.6D-E show that the CVI measurement (which is a mixture of both the ellipticity and surface roughness indices) is more strongly influenced by the chondrule roughness than the chondrule ellipticity, to which is only weakly correlated. Similar results are obtained when examining the relationships between the CVI, ellipticity, and roughness of the whole chondrules, although the CVI shows a slightly stronger correlation with ellipticity ($R^2 = 0.39$) and a relatively weaker correlation (compared to the interior chondrules) with roughness ($R^2 = 0.69$) (not shown).

When comparing the shapes of the interior chondrule to that of the whole chondrule (including FGR), it is apparent that the interior chondrule has both a larger aspect ratio and a more irregular shape than the whole chondrule (Table 3.3 and Fig. 3.6F-H). Figures 3.6F-G show that the interior chondrule aspect ratio and ellipticity are consistently, slightly larger than that of the whole chondrule ($R^2 = 0.90$ for both). This is most likely a natural consequence of the interior chondrule plus outer rim structure, which is explained in more detail in Appendix F. The surface roughness of the interior

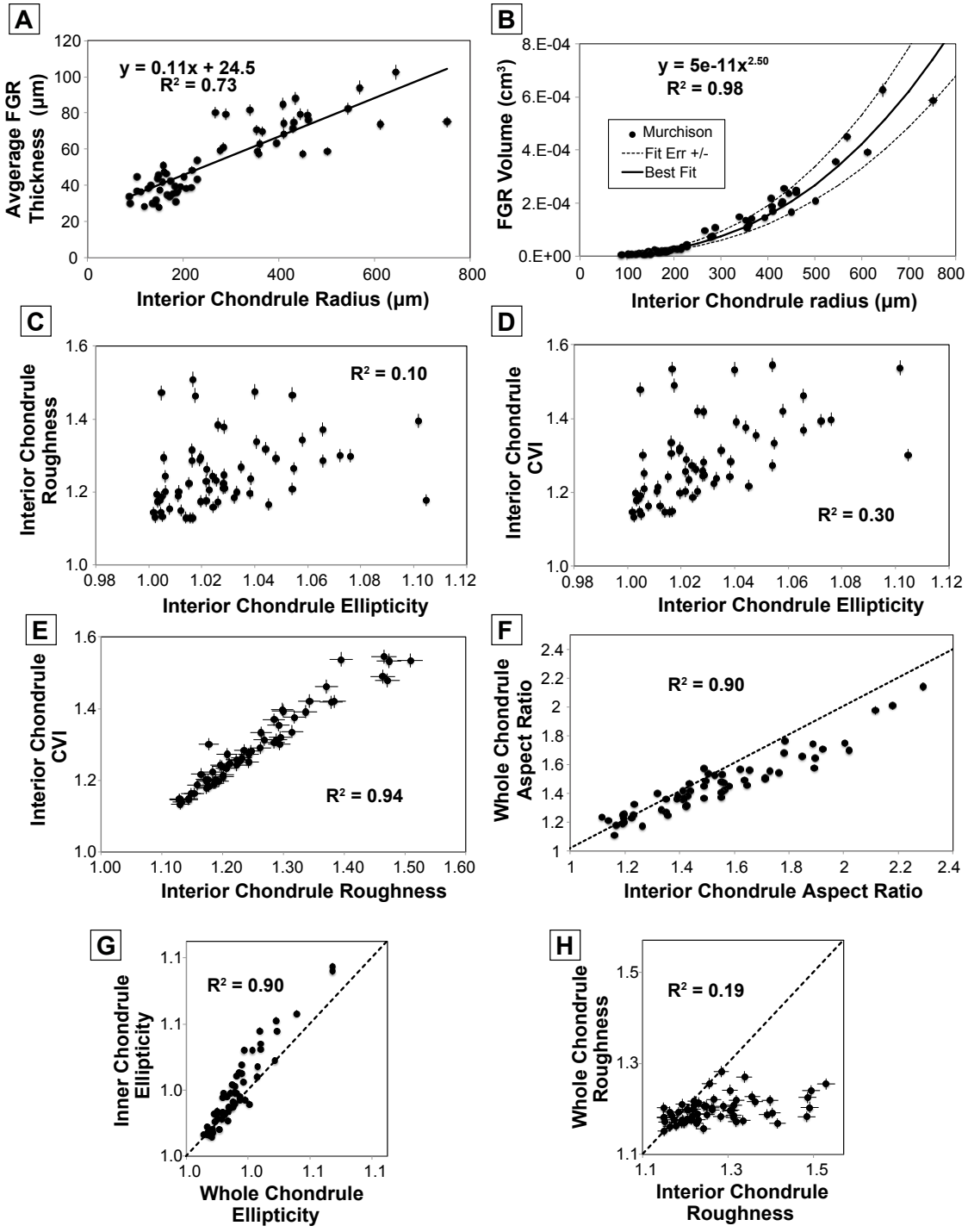

Fig. 3.6 Size and shape relationships between interior chondrules and FGRs.

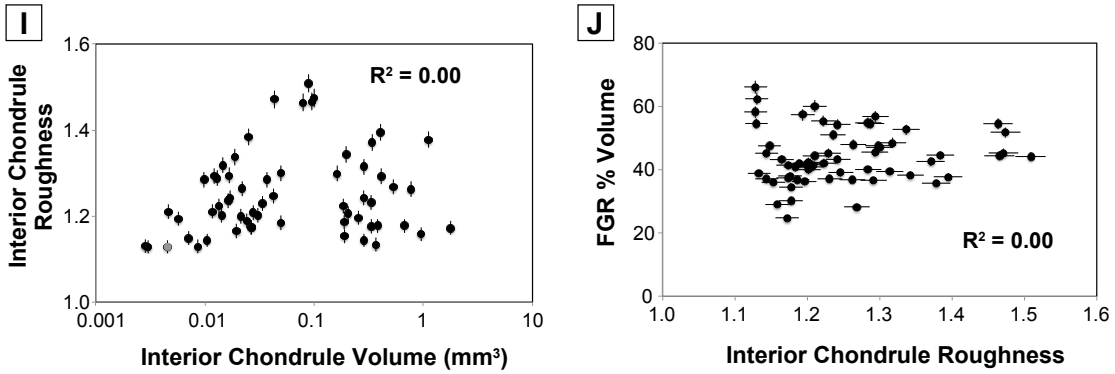

Fig. 3.6, cont.

(A) Average FGR thickness and interior chondrule radius are moderately positively correlated. Interior chondrule radius measurement error (1.3%) is about the size of the symbols. (B) FGR volume and interior chondrule radius are very well fit using a power law relationship with exponent 2.50. Data is less well fit with a simple linear regression ($R^2 = 0.89$). Interior chondrule radius measurement error (1.3%) is about the size of the symbols. (C) Interior chondrule roughness and ellipticity are uncorrelated, indicating that they are well-separated indices. Measurement error of ellipticity is about the size of the symbols. (D) There is a very weak correlation between the interior chondrule CVI and ellipticity, indicating that the CVI measurement is not strongly influenced by the ellipticity of the chondrule. (E) In contrast, there is a strong correlation between the interior chondrule CVI and roughness, indicating that the CVI is strongly influenced by the surface roughness of the particle. (F) Interior and whole chondrule aspect ratios are strongly correlated and the interior chondrule aspect ratio is consistently, slightly larger than that of the whole chondrule. Measurement errors of both are about the size of the symbols. (G) Interior chondrules tend to be slightly more elliptical in shape than whole chondrules. Measurement errors of both are about the size of the symbols. (H) The surfaces of interior chondrules are usually rougher than the whole chondrule (rim) surface and display a much wider range in surface roughness (1.13 – 1.51) compared to the whole chondrules (1.13-1.26). (I) There is no correlation between interior chondrule surface roughness and volume. The smallest chondrules appear to be limited in roughness but this may be the result of selection bias (Fig. 3.8). Grey dot is referenced in Fig. 3.8 and text. Measurement errors of interior chondrule volume is about the size of the symbols. There is no correlation between surface roughness and the FGR volume, suggesting that a significant portion of FGR volume was not formed via alteration of the chondrule.

the interior chondrules display a much wider range in surface roughness (1.13 – 1.51) compared to the whole chondrules (1.13-1.26) (Table 3.3). Finally, interior chondrule chondrule is also usually larger than that of the whole chondrule surface (Fig. 3.6H), and roughness does not show any systematic correlation with chondrule size, including the interior chondrule volume or relative FGR volume (Fig. 3.6I-J).

Visual examples of chondrules with relatively high and low surface roughness are shown in Figure 3.7. The first chondrule (Fig. 3.7A-B) has a relatively high roughness (1.47; interior chondrule) that is evident in its segmented shape. The exterior of this

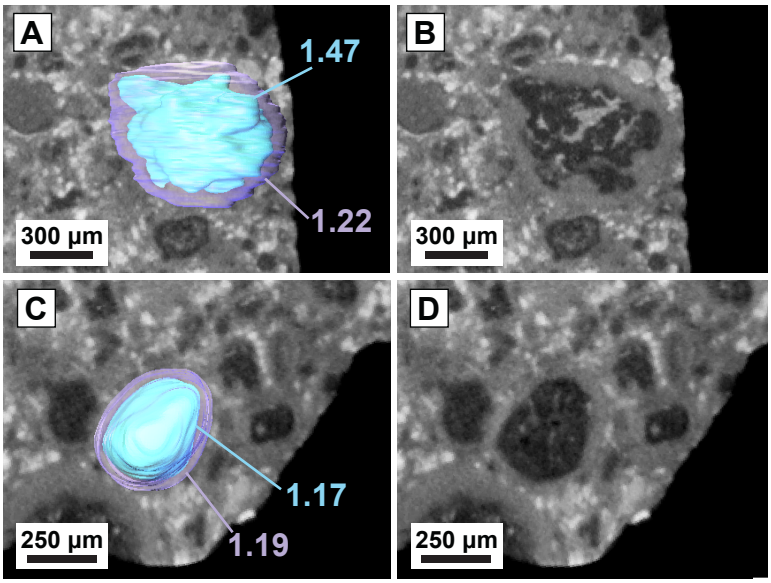

Fig. 3.7 Examples of chondrules with high (A-B) and low (C-D) roughness. (A) Segmented FGR (purple) and interior chondrule (blue) bisected by XCT YZ slice 181. The interior chondrule has a higher roughness (1.47) than the whole chondrule (1.22) (B) XCT YZ slice 181 only showing irregular 2D expression of interior chondrule compared to exterior FGR. (C) Segmented FGR (purple) and interior chondrule (blue) bisected by XCT XY slice 198. The interior chondrule has a slightly lower roughness (1.17) than the whole chondrule (1.19). This interior chondrule has a much smoother surface than the chondrule in Fig 7A-B which is reflected in its lower roughness value. (D) XCT XY slice 198 only showing smoother 2D expression of interior chondrule and whole chondrule compared to chondrule in Fig. 3.7A-B.

chondrule with the FGR is much smoother with a lower roughness (1.22). In contrast, the segmented shape of the other chondrule interior (Fig. 3.7C-D) is much smoother and its

roughness index correspondingly lower (1.17). The whole chondrule roughness (1.19) of this chondrule is similar to the other chondrule (Fig. 3.7A-B). It is intriguing that for the smoother chondrule shown in Figure 3.7C-D the interior chondrule is just slightly less rough (1.17) than the whole chondrule (1.19), however they overlap in roughness when the measurement error is considered (Table 3.2). Still, Figure 3.6I suggests that the smallest interior chondrules may have a limit to their surface roughness and so we examined the XCT data to determine if this was true. While only a qualitative examination, we did find examples of small chondrules with an apparent volume approximately equivalent to one of the smallest chondrules (grey dot in Fig. 3.6I) with an apparent high surface roughness (Fig. 3.8). Therefore this upper limit on surface roughness for small chondrules (Fig. 3.6I) appears to not be a universal trend and is most likely due to selection bias.

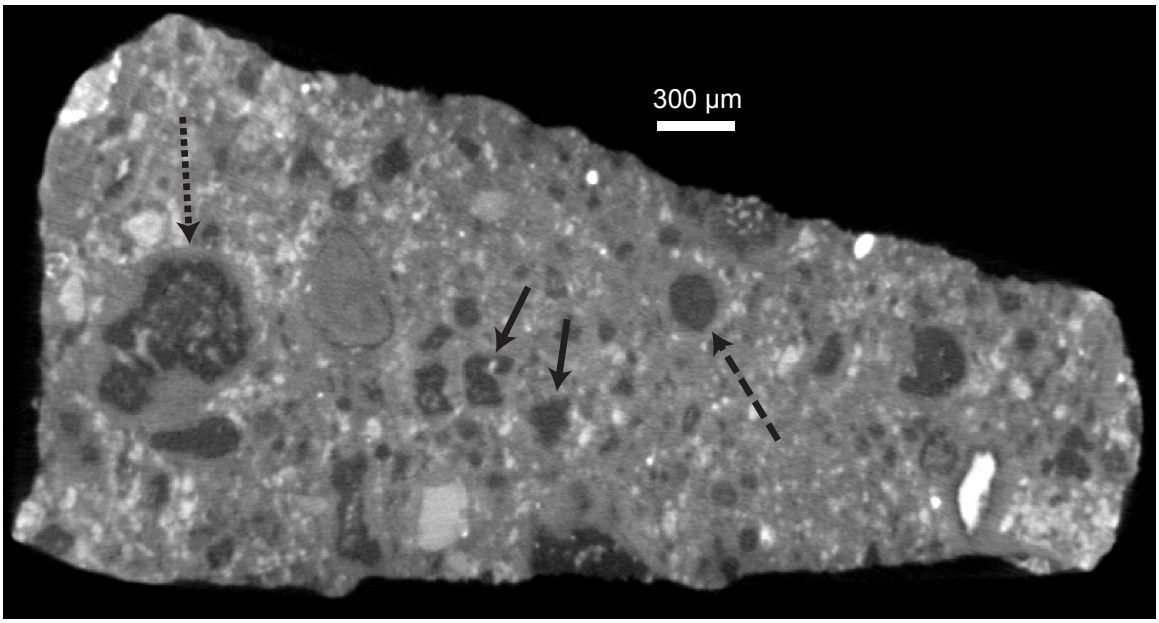

Fig. 3.8 XCT slice showing small chondrules with various roughness.
XY slice 1002 showing small, smooth chondrule with low roughness (1.13; far right, dashed arrow) compared to larger chondrule with higher roughness (1.46; far left, dotted arrow). Solid black arrows highlight smaller chondrules that appear to have a similar volume to the smaller smooth chondrule (dashed arrow) but with a more irregular shape, suggesting that not all smaller chondrules have a low roughness. Smooth chondrule (dashed arrow) is plotted as grey dot in Figure 3.6I.

3.3.3 Chondrule and FGR thickness orientations

The orientations of the 61 segmented chondrules are plotted on lower-projection stereonets in Figure 3.9. The chondrules display evidence of a foliation fabric with primary (long) axes along a great circle girdle and tertiary (short) axes in a cluster (e.g., Turner and Weiss, 1963). This fabric, as well as its orientation, matches that of the foliation fabric previously found in the entire Murchison sample (Hanna et al., 2015). The chondrule orientations measured in this study also show evidence of a very weak lineation (clustering of primary (long) axes), similar to the entire Murchison sample, and the direction (1st eigenvector of the primary axes) of the lineation is similar to that of the whole Murchison sample. However, the strength of the measured fabric in this study is weaker (C=1.43-2.13) compared to the entire Murchison sample (C=2.17-2.49), which is most likely the result of the lower number (n=61 compared to n=187). In addition, the strength of the fabric defined by the interior chondrules only (C=1.43-1.48) is weaker than that of the whole chondrules when including the FGR (C=1.69-2.13), probably due to the more irregular shape of the interior chondrules compared to the whole chondrule (Table 3.3 and Figs. 3.6-3.7) which causes increased variability in their long and short axes orientations (Fig. 3.9).

The variability of FGR thickness around the chondrules also shows a consistent spatial relationship with the foliation plane orientation in Murchison (Fig. 3.10). Figures 3.10A-B display the average FGR percent thickness of the maximum chondrule length thickness among all 61 chondrules in both the upper and lower projections. These plots show that the variability of FGR thickness is nearly symmetrical around the chondrules and that the FGRs are thicker by up to 3.8% in a planar distribution (i.e., great circle girdle). Further, the orientation of this plane appears to match that of the foliation fabric defined by the deformed chondrules (Fig. 3.9). Because the variability of FGR thickness around the chondrules is nearly symmetric, we also combined the upper and lower projection plots into a single (lower) projection plot to reduce noise and enable easier

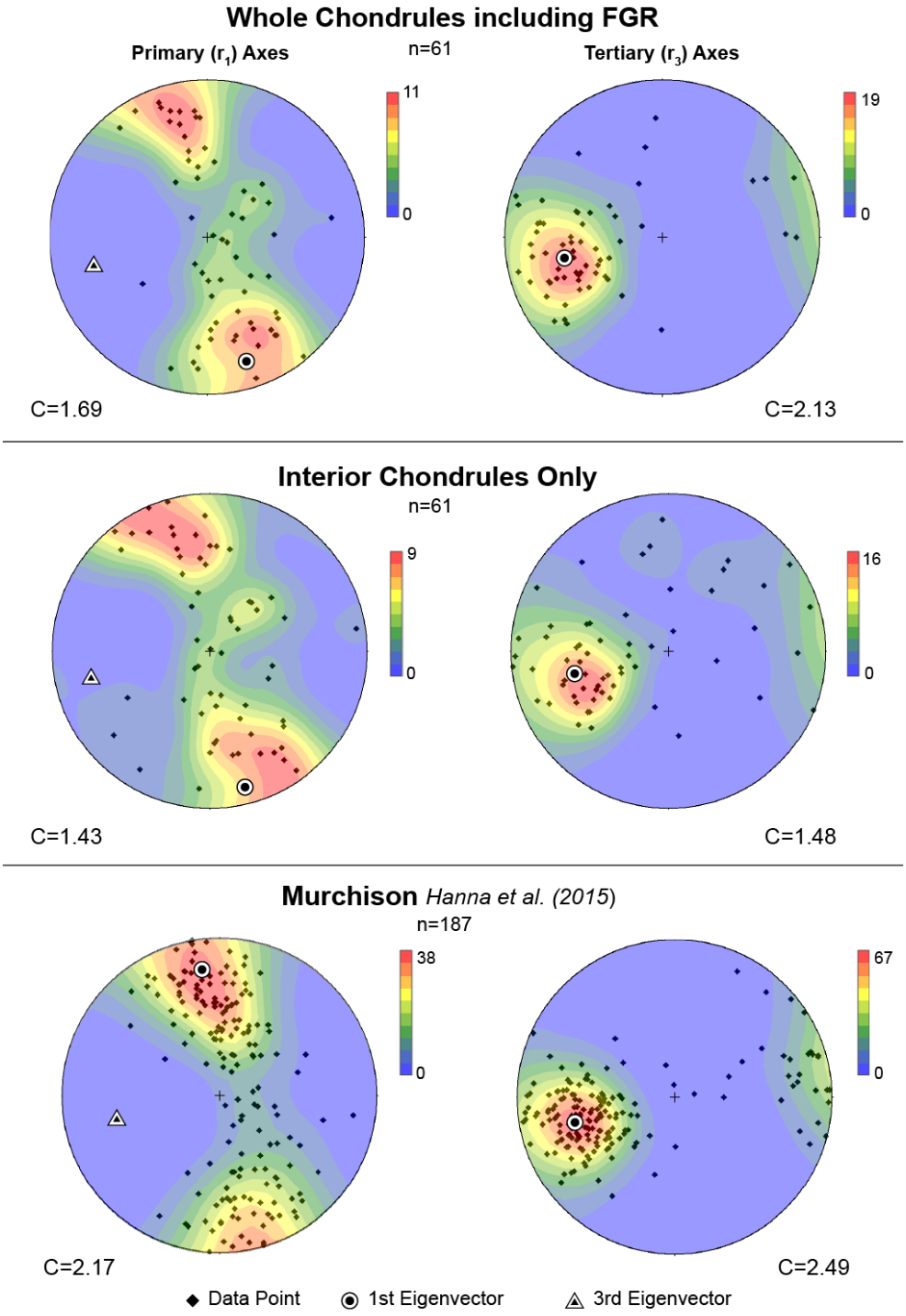

Fig. 3.9 Chondrule orientations.

Fig. 3.9, cont.
Chondrule orientations using primary (long) and tertiary (short) axes of best-fit ellipsoids to chondrules with (top plots) and without (center plots) the FGR. The bottom plots show the orientation of chondrules from the whole Murchison sample from Hanna et al. (2015). All lower projection plots. Chondrules measured in this study display the same foliation fabric orientation as the whole Murchison sample from Hanna et al. (2015). Interior chondrules show weaker fabric (C=1.43 and 1.48 versus 1.69 and 2.13 for whole chondrules with FGR) which is most likely a result of their more irregular shape compared to the FGR exterior (Table 3.3 and Figs. 3.6-3.7).

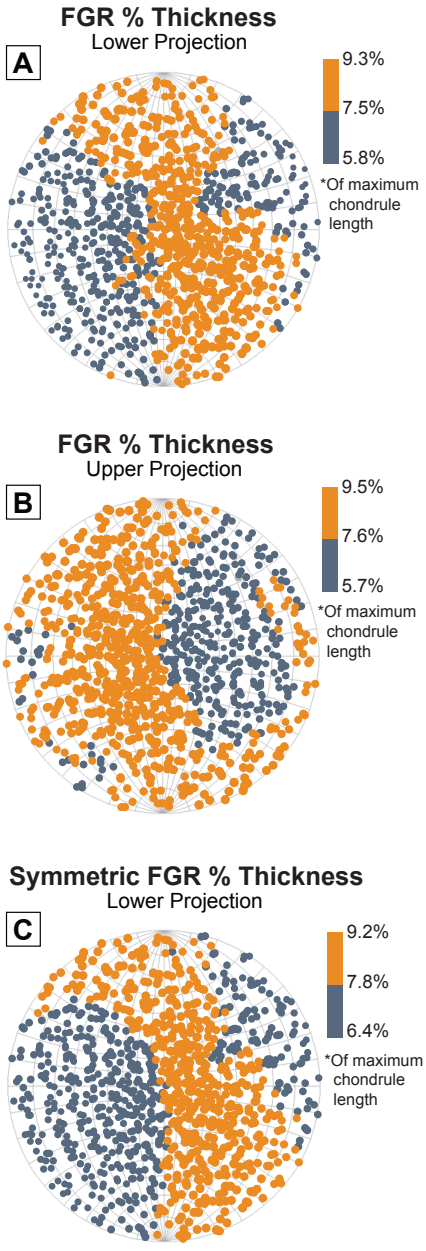

Fig. 3.10 Average 3D FGR % thickness *(A-B) Average FGR percent thickness of maximum chondrule length among the 61 measured chondrules in directions indicated. In these plots each dot represents a directional measurement, not a discrete chondrule. Upper and lower projection plots indicate that the FGRs are consistently thicker approximately in a plane. (C) Average symmetric FGR percent thickness of maximum chondrule length among the 61 chondrules in directions indicated. FGRs are consistently thicker in the plane of foliation.*

comparison to the lower projection plot of the foliated chondrule orientations (Fig. 3.10C). For each directional measurement, we averaged both the upper and lower projection FGR percent thickness for each chondrule. The average of these measurements among all chondrules for each direction were then plotted (Fig. 3.10C).

Figure 3.10C more clearly shows that the FGRs are consistently, slightly (up to 2.8% of maximum chondrule length) thicker in the plane of foliation defined by the deformed chondrules. A schematic illustration of this FGR thickening in the foliation plane is shown in Figure 3.11. While 2.8% represents a very small difference in actual FGR thickness (i.e., for the average chondrule diameter of ~560 μm (Table 3.3) this translates to a difference in FGR thickness of ~15.7 μm) and is actually below our estimated measurement error of 4.1% (Table 3.2; although the actual error is likely lower, see Appendix D for details), their spatial consistency and correspondence to the deformed chondrule foliation orientation gives us confidence that the measured differences are real. Overall, this result strongly suggests that the FGRs were in place at the time of chondrule deformation which has been interpreted to result from impact(s) and which also predated or was contemporaneous with aqueous alteration of Murchison (Hanna et al., 2015).

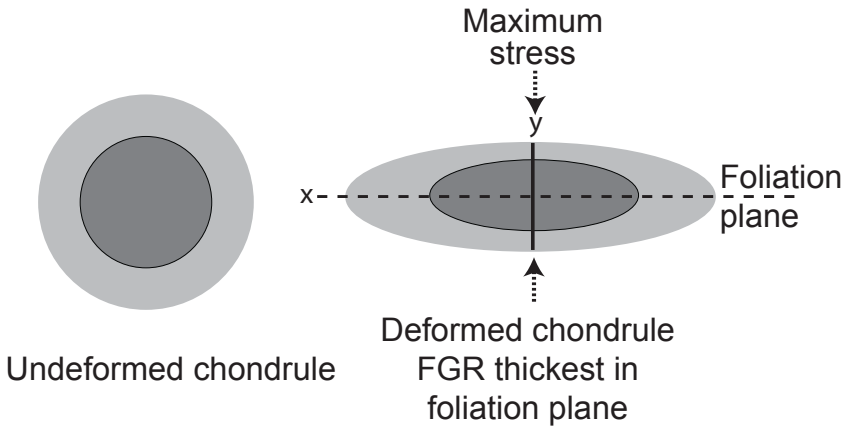

Fig. 3.11 Schematic of deformed chondrule with thicker FGR in plane of foliation. *Schematic illustration of an initially spherical chondrule (left) with an FGR that is thicker in the plane of foliation (x) after deformation (right). Direction of maximum stress (y) is perpendicular to foliation plane.*

3.4 Discussion

3.4.1 Nebular formation of FGRs

The results presented here strongly support a nebular formation environment for FGRs around chondrules in CM Murchison. First, the FGR volume and interior chondrule radius data are extremely well fit by a power law function as suggested by Cuzzi (2004) (Fig. 3.6B). Neither of the parent body formation scenarios proposed to date, regolith compaction and aqueous alteration, predicts any such relationship. If the FGR formed through aqueous alteration of the chondrule surface inward (Sears et al., 1993; Takayama and Tomeoka, 2012), there is no reason this would result in a correlation between rim thickness and chondrule size (Fig. 3.6A). The same reasoning applies to a regolith compaction origin, as such a chaotic and likely haphazard process would not result in a systematic correlation between FGR volume and chondrule size.

There is additional evidence against a parent body aqueous alteration origin for FGRs. If they are formed through alteration of chondrules, it is expected that we would see examples of completely altered chondrules that result in FGR 'clasts'. We actively searched all of our XCT datasets for such objects but did not find them. In addition, aqueous alteration of chondrules would likely result in an FGR composition that is dependent on the initial composition of the chondrule. And while several studies have documented compositional and chemical variation among FGRs in CMs, including Murchison (Brearley and Geiger, 1993; Brearley and Geiger, 1991; Metzler et al., 1992), we compared average FGR CT grayscales (which are a function of composition) of various object types (several Type I, several Type II, and the lithic clast in Figure 3.5C) and found no significant differences correlated with object type. Further evidence against a parent body aqueous alteration origin for the FGRs is that there is no correlation between the shape irregularity of the interior chondrule and the relative FGR volume (Fig. 3.6J). While it is possible that aqueous alteration proceeds equally along the entire chondrule surface and therefore does not produce an irregular inner chondrule shape, we

do not favor this interpretation because 1) Type I chondrules in Murchison are heterogeneous in composition and texture (e.g., Fuchs et al., 1973; Hanna et al., 2015) which would result in uneven alteration around the exterior and 2) in other CMs where aqueous alteration has taken place along the chondrule exterior, irregular degrees of alteration and embayments are seen (Takayama and Tomeoka, 2012). We do not preclude the possibility that some aqueous alteration might have increased the FGR volume, but the proportion of FGR volume created this way must have been limited enough that it did not significantly affect the FGR volume/chondrule radius power law relationship caused by the nebular formation setting (Fig. 3.6B).

Other evidence for pre-accretionary formation of FGRs is that the FGRs were deformed during the impact(s) that foliated the chondrules, resulting in thicker rims in the plane of the foliated chondrules (Figs. 3.9-3.10). This requires that the FGRs are already formed and in place before the deformation event on the parent body. While this does not necessarily discount formation of the FGRs on the parent body (i.e., they could have formed prior to the deformation), it is more consistent with a pre-accretionary (nebular) origin. If the FGRs were formed on the CM parent body, they had to form prior to significant impact deformation and aqueous alteration (Hanna et al., 2015). In particular, if FGRs were formed through parent body aqueous alteration, the aqueous alteration that accompanied the impact would have further increased the volume of the FGRs and erased the power law relationship between FGR volume and interior chondrule radius, which we do not observe.

The power law relationship between rim volume and interior chondrule radius proposed by Cuzzi (2004) is for the formation of FGRs in a weakly turbulent nebula. He showed that this nonlinear relationship is a direct consequence of the particle-size dependent gas-relative velocity of the particle as it moves through the gas (and the dust that is coupled to it) (Cuzzi, 2004; Cuzzi and Hogan, 2003). This size-dependent velocity in turn leads to a size-dependent accumulation of dust around the chondrule as larger chondrules encounter a higher amount of dust in the same amount of time relative to

smaller chondrules. Specifically, he derived an expression (Eq. (11); (Cuzzi, 2004)) for the volume of the rim produced as a function of the interior chondrule radius and showed that this expression is also dependent on whether the nebula was turbulent or laminar and the Stokes number of the particles. The latter two variables are encapsulated in the variable *p* in Equation (11) of this work. The Stokes number describes the aerodynamic behavior of a particle and is defined as the ratio of a particle's stopping time to the overturn time of some characteristic eddy (Cuzzi and Hogan, 2003). Stopping time refers to the timescale it takes a particle to equilibrate with changes in nebular gas flow – smaller particles are better coupled to the gas and equilibrate more quickly (Cuzzi and Weidenschilling, 2006). Nebular turbulence is characterized by an inertial range of lengthscales, from the largest (commonly regarded as the local orbital period) to the smallest, or Kolmogorov, scale (Cuzzi and Hogan, 2003). Therefore particles with a stopping time on the smallest length scale of turbulence have a Kolmogorov stopping time.

The rim volume predictions using Equation (11) of Cuzzi (2004) for a range of *p* values are plotted in Fig. 3.12. Note that different *p* values inform on the nebular turbulence scales and not the absolute sizes of the particles. A *p* value of 1 indicates that the nebula was laminar or, if turbulent, that the particles were sized 'smaller' *relative* to the Kolmogorov stopping time which is dependent on the size of the smallest eddy (Cuzzi, 2004). Lower values of *p* apply only to a turbulent nebula, and various *p* values correspond to particles sized differently relative to the Kolmogorov stopping time. A *p* value of 0.75 is predicted to correspond to particles that are sized such that their stopping time is exactly the Kolmogorov stopping time in the nebula (Cuzzi, 2004; Cuzzi and Hogan, 2003). Particles that are sized 'smaller' relative to the Kolmogorov-stopping-time size have *p* values between 0.75 and 1.0, and particles sized slightly larger relative to this smallest nebular eddy have *p* values below 0.75 (Cuzzi, 2004; Cuzzi and Hogan, 2003). Therefore, examination of where the Murchison data fall within these predicted rim volume/chondrule radius relationships could shed light on whether the nebula was

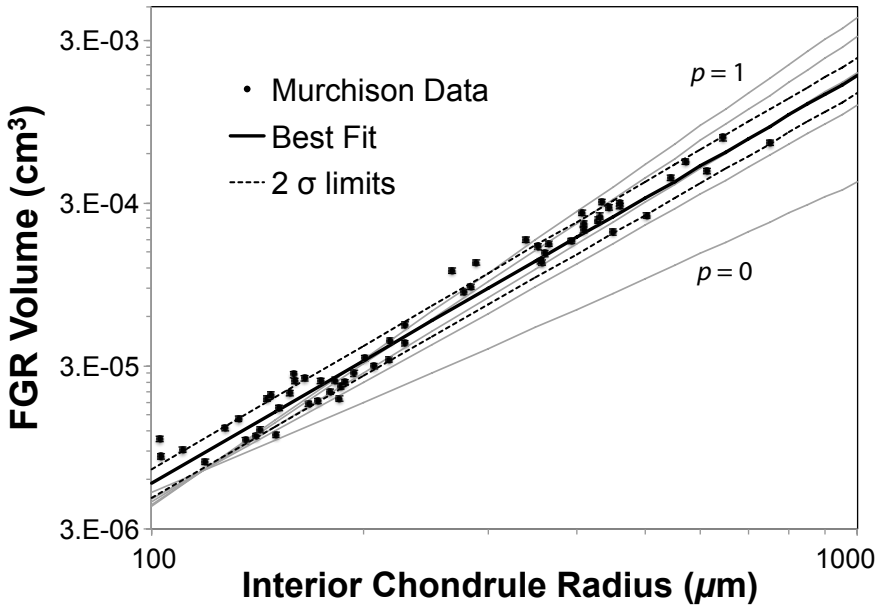

Fig. 3.12 Murchison data with rim volume predictions from Cuzzi (2004). *Rim volume predictions for p = 0.0, 0.5, 0.7, 0.9, and 1.0 using Equation (11) from Cuzzi (2004) (thin grey lines) and the data for the Murchison samples (circles) with measurement uncertainty in rim volume (4.1%). Interior chondrule radius measurement uncertainty (1.3%) is about the size of the symbol. The thick solid line is the best fit through the Murchison data (same fit is shown Fig. 3.6B) and the dotted lines represent the 2-sigma uncertainties in the best fit.*

turbulent or laminar and the size of the rimmed chondrules relative to the Kolmogorov scale, which changes based on the particular turbulence conditions of the nebula (Fig. 3.12).

The exact value of *p* that the Murchison data mostly closely corresponds to is difficult to determine visually from the graph as the best fit line and its 2-sigma uncertainties cross all lines (p = 0.0 to 1.0) at some point. Among the various *p* cases (Fig. 3.12), the slope (i.e., power law exponent) of the line is what most uniquely determines each case as the vertical axis intercept represents the absolute rim volume that depends on other parameters such as the local dust density and rimming timescale (Cuzzi, *personal communication, 2016*). Therefore, we determined a best-fit linear relationship

using linear regression (R^2=0.998) to the *p* parameter versus its power law exponent from Equation (11) of Cuzzi (2004)

$$y = 1.08p + 1.90 \quad (4)$$

where *y* is the power law exponent. Using this relationship, the best-fit line to the Murchison data with 2-sigma uncertainty corresponds to a *p* value of 0.56 ± 0.02. This indicates that the nebula was turbulent, and also that the rimmed particles were larger than Kolmogorov-stopping-time particles. This is a different result than that found with the limited data previously collected for CV Allende, which was found to be a best fit with *p* = 0.7-0.9 (Cuzzi, 2004). However, in that work the small number of data points (n=14) and their larger scatter made it impossible to completely rule out smaller and larger values of *p* (from 0.5 to 1.0) (Cuzzi, 2004). Therefore, the different values of *p* found for CM Murchison could represent either a real difference for rimmed particles compared to CV Allende (which perhaps could vary among the different chondrite classes) or simply reflect the more statistically significant data set. More data will be collected in the future for other chondrite classes to determine whether similar values of *p* are indicated.

One simplifying assumption in the Cuzzi (2004) model is that the particles are perfectly spherical. However, our shape analysis results show that the shape of the interior chondrules can be quite irregular (Figs. 3.6-3.8). We quantify shape irregularity separately as ellipticity and roughness, where the ellipticity is the ellipsoidal shape of the chondrule that is thought to have originated during deformation on the CM parent body and thus not present when the chondrules were in the nebula. Therefore, only the surface roughness of the chondrules is relevant when considering how the chondrules accumulated dust to form fine-grained rims. To determine whether this surface roughness influenced dust accumulation and therefore the rim volume to chondrule radius relationship (and thus the estimate of *p*), we split the data into 2 groups based on their interior chondrule roughness value (Fig. 3.13). A frequency histogram indicates that there are two natural values for splitting the data (Fig. 3.13A). The interior chondrule

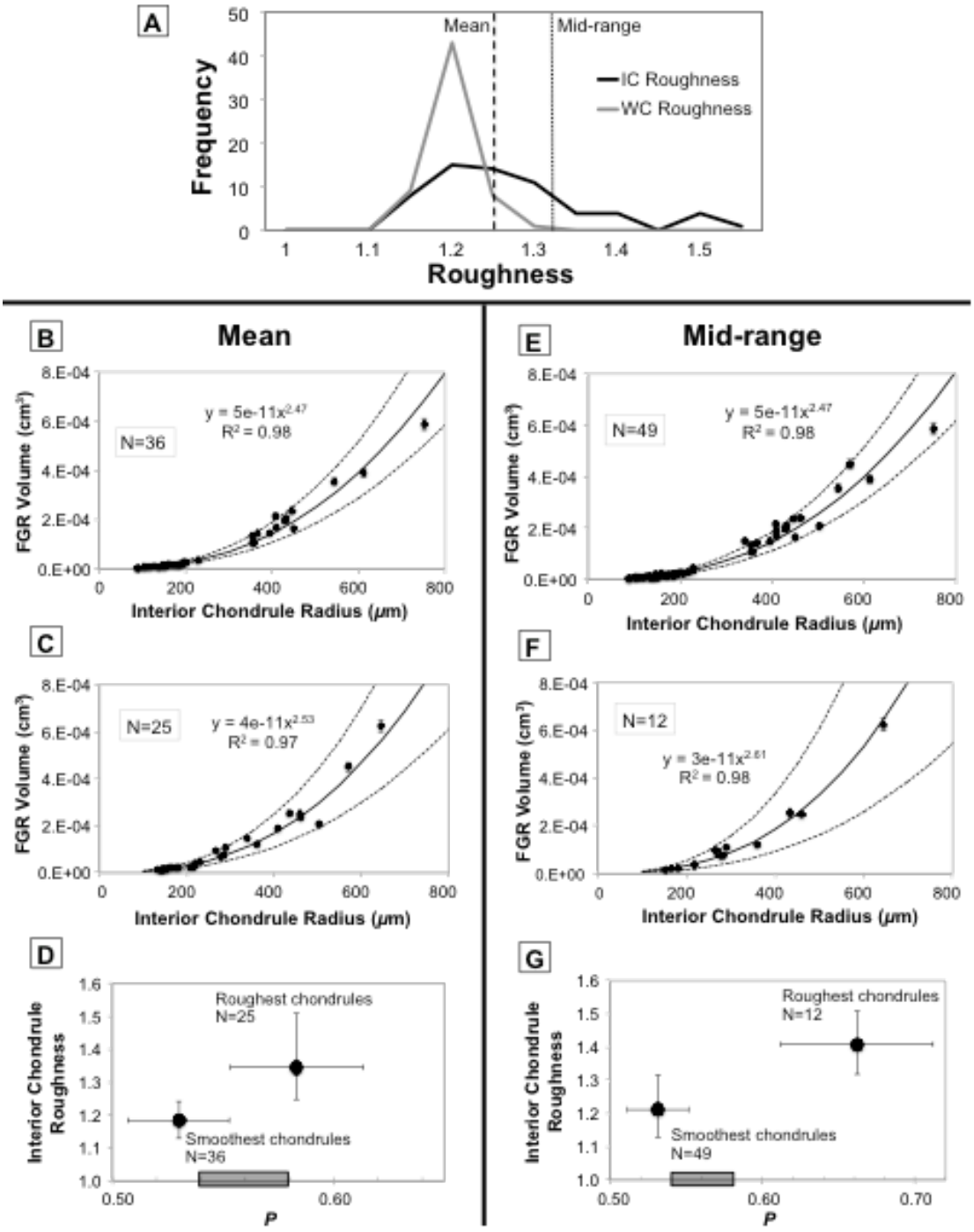

Fig. 3.13 Murchison data split into 2 groups based on their interior chondrule roughness indices.

Fig. 3.13, cont.
(A) Frequency histogram of roughness values for interior chondrules (IC) and whole chondrules (WC). Dashed line shows the mean IC roughness value (1.25) and dotted line shows the mid-range IC roughness value (1.32). The IC roughness distribution is asymmetric and the mean value overlaps with the main peak, as well as a portion of the WC roughness values. The Murchison data is split into 2 groups based on the mean (Figs. 3.13B-D) and mid-range values (Figs. 3.13E-G). (B) Best-fit power law (solid line) with 2-sigma uncertainties (dotted lines) to group (N=36) with smoothest IC values below mean value of 1.25. Vertical error bars are 4.1% measurement uncertainty on the rim volume. (C) Best-fit power law (solid line) with 2-sigma uncertainties (dotted lines) to group (N=25) with roughest IC values above mean value of 1.25. Vertical error bars are 4.1% measurement uncertainty on the rim volume. (D) Graph of P values of each group shown in Fig. 3.13B-C calculated with Equation (4) with 2-sigma uncertainties. Groups are barely separated in P space, with rougher chondrules corresponding to a higher P value. The gray bar indicates the calculated P values using the full Murchison dataset (0.54-0.58; see text). (E) Best-fit power law (solid line) with 2-sigma uncertainties (dotted lines) to group (N=49) with smoothest IC values below mid-range value of 1.32. Vertical error bars are 4.1% measurement uncertainty on the rim volume. (F) Best-fit power law (solid line) with 2-sigma uncertainties (dotted lines) to group (N=12) with roughest IC values above mean value of 1.32. Vertical error bars are 4.1% measurement uncertainty on the rim volume. (G) Graph of P values of each group shown in Fig. 3.13B-C calculated with Equation (4) with 2-sigma uncertainties. Groups are very well separate separated in P space, with rougher chondrules corresponding to a higher P value. The gray bar indicates the calculated P values using the full Murchison dataset (0.54-0.58; see text).

roughness distribution is asymmetric and thus the mean value (1.25) overlaps with the main peak, as well as a portion of the whole chondrule roughness values. Therefore a mid-range value (of interior chondrules; 1.32) is also defined, which appears to better separate the interior chondrules into smoother particles (main peak) and relatively rougher particles (asymmetric tail).

The Murchison data was split into two groups based on the mean (Figs. 13.3B-D) and mid-range (Figs. 3.13E-G) interior chondrule roughness values. When splitting by mean roughness (1.25), the smoother chondrule group (n=36) has a best-fit power law exponent of 2.47, and converting this to p using Equation (4) with the 2-sigma uncertainties results in $p = 0.52 \pm 0.02$. The rougher particle group (n=25) has a best-fit power law exponent of 2.53 and $p = 0.58 \pm 0.03$. Therefore, the 2 groups are just barely separated in p space with the rougher chondrules having a relative higher p value. When the data is split using the mid-range roughness (1.32) instead, the groups are better separated (Fig. 3.13E-G). The best-fit power law relationship of the smoother chondrule group (n=49) is essentially unchanged with a best-fit power law exponent of 2.47 and $p = 0.52 \pm 0.02$. The rougher particle group (n=12) now has a higher best-fit power law exponent of 2.61, and converting this to p using Equation (4) with the 2-sigma uncertainties results in $p = 0.66 \pm 0.05$.

In both situations the rougher chondrules have a relatively higher p value compared to the smoother chondrules. According to the Cuzzi (2004) model this indicates that the relatively rougher particles are behaving like they are slightly smaller relative to Kolmogorov-stopping-time particles than the smoother particle group (both are relatively larger than Kolmogorov-stopping-time particles in general, however). This requires either that the two groups of particles acquired rims in different turbulent conditions (with different Kolmogorov-scale turbulence) or that the surface roughness is somehow influencing the volume of rim that is accreted in the same nebular turbulence conditions. It is possible that the FGRs formed in separate areas of the nebula with different degrees of turbulence and were then mixed together to accrete on the CM parent

body. Some compositional and chemical variation is seen among FGRs in CMs, including Murchison (Brearley and Geiger, 1993; Brearley and Geiger, 1991; Metzler et al., 1992) suggesting different nebular reservoirs, but it is yet unknown if these chemical differences are correlated with surface roughness or if the variations are possibly the result of parent body alteration. We did compare the grayscales of the XCT data (which are a function of composition) of the FGRs to interior chondrule roughness and did not find any systematic correlations. We therefore think it more likely that the chondrule surface roughness is influencing the accretion behavior of dust in the nebula and we discuss this further in Section 3.4.3. Regardless, this finding lends further support to the formation of FGRs by accretion in a turbulent nebular setting, as such a particle-roughness dependence of the rim volume to interior radius relationship would not be expected in a parent-body setting.

The other FGR formation mechanism that has been considered in the past is impact-generated accretionary lapilli (King and King, 1981) and while it has not been investigated recently as an FGR-formation process, the formation of chondrules as an impact-related process has recently been revived (e.g., Dullemond et al., 2016; Johnson et al., 2015; Sanders and Scott, 2012; Villeneuve et al., 2015). The general texture of dust-rimmed chondrules does closely resemble that of both volcanic and impact accretionary lapilli where a coarse-grained core, often angular or irregular in shape, is surrounded by fine dust which has a smooth outer morphology (e.g., Carracedo Sánchez et al., 2015). And modeling and field observations have confirmed that accretionary lapilli are generated in terrestrial and lunar impacts (e.g., Branney and Brown, 2011; Graup, 1981; Johnson and Melosh, 2014; McKay and Morrison, 1971) and most likely form in turbulent flows (Branney and Brown, 2011; Johnson and Melosh, 2014). However, it is unknown if the chondrules would experience the same size-dependent velocity in impact generated turbulence as that modeled for nebular turbulence by Cuzzi and Hogan (2003). In addition, the current chondrule impact formation models either do not include dust production in their model (Johnson et al., 2015) or do not provide details on the physical

nature of the plume of dust generated by such an impact (Sanders and Scott, 2012). Therefore, while it is possible that FGRs can be produced in a dusty, turbulent plume from a parent body impact, much more work is needed to determine if this would manifest in the same rim volume/interior chondrule radius relationship as that proposed by Cuzzi (2004) for a turbulent nebula.

3.4.2 Subsequent deformation on the parent body

Because the rims were consistently deformed (Fig. 3.10) during the impact event which foliated and aqueously altered Murchison (Hanna et al., 2015), they were clearly already formed and in place at the time of the deformation. Further, because the rims are thicker in the foliation plane we can use this difference between the thicker portion of the rims (in the foliation plane) and the thinner portion of the rims (perpendicular to this plane) to estimate how much strain is recorded by the FGRs (i.e., resulting in thinner rims in the maximum strain direction y and elongation in x; Fig. 3.11). Figure 3.10 expresses the thickness of the FGRs normalized to the maximum chondrule radius and shows that the thickest portion of the rims is between 7.8-9.2% compared to 6.4-7.8% for the thinner portion of the rims. If we take the average relative rim thickness, 7.8%, as the thickness of the FGRs if they were an equant thickness around the chondrule (i.e., no differential deformational strain recorded within the FGRs), this means that maximum change (in either x or y) in relative rim thickness is 1.4%. This translates to a strain (shortening in y and lengthening in x) of 17.9% within the FGRs (i.e., 1.4%/7.8% = 17.9%). This strain within the FGRs is also consistent with the ellipticity and aspect ratio differences between the inner and whole chondrules (Fig. 3.6F-G), which are less than expected for equal FGR thickness around the deformed chondrules (Appendix F).

To compare this to the shortening (flattening) experienced by the interior chondrules, we use the average aspect ratio of the interior chondrules, 1.53 (Table 3.3), and the uniaxial shortening equations (6) and (10) of Hanna et al. (2015) for initially spherical chondrules. The inner chondrule average aspect ratio of 1.53 therefore

corresponds to uniaxial shortening of the inner chondrules by 25-35% where the lower limit is for incompressible chondrules and the upper limit is for completely compressible chondrules (Hanna et al., 2015). Therefore, we find that the FGRs around the chondrules have experienced less strain (17.9%) than the interior chondrules (25-35%).

The fact that the FGRs experienced a different degree of strain to the interior chondrules is not surprising as the mineralogy and textures differ significantly between them and therefore their rheological response should also be different. Type I chondrules in Murchison are porphyritic and composed primarily of forsterite and clinoenstatite with lesser amounts of low-Ca pyroxene, serpentine, and sulfides (Fuchs et al., 1973; Hanna et al., 2015). Individual grain sizes within the porphyritic chondrules vary widely from 5 to ~300 microns, with the largest grains most commonly forsterite (Hanna et al., 2015). The FGRs in contrast are a very uniform fine-grained mixture of olivine, sulfides (primarily pentlandite and pyrrhotite), serpentine, cronstedtite, tochilinite, and amorphous material with grain sizes on the order of nanometers up to a few microns (Brearley and Geiger, 1993; Brearley and Geiger, 1991; Brearley et al., 1999; Zolensky et al., 1993). It is expected that these grain size and mineralogy differences between the interior chondrule and FGR would result in differing rheological responses to stress, which we observe. Hanna et al. (2015) found that the interior chondrules deformed primarily by brittle mechanisms such as cataclasis, pore collapse, and grain boundary sliding, so it is assumed that similar processes are happening to accommodate the strain in the rims as well.

Beitz et al. (2013a) measured a porosity of ~10% in two FGRs in Murchison but it is unknown if these rims were deformed or not. Regardless, it is highly probable that a portion the original FGR porosity was removed during the deformation in Murchison. If we assume that all of the deformation was accommodated by this porosity loss, and that 10% represents the post-deformation porosity, this translates to a maximum pre-deformation porosity of 26% using the porosity loss equation (9) of Hanna et al. (2015). While this represents an upper limit, it implies that the original porosity of FGRs when

accreted on the CM parent body may be closer to the theoretically and experimentally modeled 60-70% rim porosity estimated for dust accreting around chondrules in the nebula (e.g., Beitz et al., 2013a; Blum and Schräpler, 2004; Blum et al., 2006; Ormel et al., 2008). This would help remove some of the need for post-accretional, nebular compaction that is required for FGRs before they accrete to a parent body, which current models are at a loss to adequately explain (e.g., Beitz et al., 2013a; Blum et al., 2006; Ormel et al., 2008; Trigo-Rodriguez et al., 2006). Finally, we note that although portions of the rims show evidence for volume reduction (i.e., compression by up to 17.9% in the plane of maximum stress), this does not alter any of our results based on the rim volume/interior chondrule radius relationship (Figs. 3.6, 3.12-3.13) because all volumes are decreased by the same proportional amount and thus the power law exponent will remain the same.

3.4.3 Irregular chondrule shape

It is often assumed that chondrules were originally approximately spherical because they represent crystallized melt that was freely floating in the nebula. Despite the deformed shape of chondrules in CM Murchison, ellipticity analysis has shown that they were most likely nearly, but not perfectly, spherical prior to the deformation (Hanna et al., 2015). However, numerous workers have observed that interior chondrules in CMs have irregular outlines that are effectively smoothed out by the FGRs which infill embayed areas resulting in a smoother outer surface that does not reflect the irregular interior morphology of the chondrules (Cuzzi, 2004; Hua et al., 2002; Kinnunen and Saikkonen, 1983; Lauretta et al., 2000; Metzler et al., 1992; Tomeoka et al., 1991; Zega and Buseck, 2003). Our shape analysis confirms these observations, indicating that the whole chondrule exteriors are much smoother (lower roughness) than their interiors (Figs. 3.6H and 3.7).

The origin of the irregular shapes of the interior chondrules is not known, but the 2D expression of highly irregular chondrules (e.g., Fig. 3.7B) is reminiscent of

embayment such as might occur through alteration of the interior chondrule edges along favorable pathways. If the irregular shape is indeed the result of alteration, we would expect that these portions of the FGR were formed from alteration of the interior chondrule, as suggested by Sears et al. (1993) and Takayama and Tomeoka (2012) for Murchison and Tagish Lake, respectively. If FGR volumes are actually growing via alteration of the interior chondrule, we would also expect that higher degrees of alteration would lead to higher surface roughness for the interior chondrule and larger relative FGR volumes (normalized to the whole chondrule volume, as FGR volume is positively correlated with the chondrule size; Fig. 3.6A-B). Figure 3.6J shows that this relationship clearly does not exist. There is no correlation ($R^2 = 0.00$) between the relative FGR volume and the interior chondrule roughness. This is a strong argument against the formation of the FGR, as well as interior chondrule roughness, through aqueous alteration of the interior chondrule.

In addition to this evidence against a parent body alteration origin for the interior chondrule roughness, we also see evidence that the surface roughness of some chondrules may have influenced their dust accumulation behavior relative to their size in the nebula (Fig. 3.13 and Section 3.4.1). Taken together, this evidence suggests that the irregular shape (surface roughness) of the chondrules is a primary feature, and predates both FGR accretion and chondrule accretion to the CM parent body. The exact origin of this irregular chondrule shape is beyond the scope of this study but should be considered in chondrule formation models.

Finally, we consider how the primary, irregular shape of chondrules could influence the relationship between rim volume and interior chondrule size as suggested by Fig. 3.13. Specifically, we find that rougher particles show a rim volume/particle radius relationship that is consistent with higher values of p. Examination of Fig. 3.12 reveals that higher values of p are indicative of a larger rim volume on with larger interior chondrule radius (i.e., for the same interior chondrule radius, curves with higher p values have a relatively larger rim volume). Therefore, chondrules with rougher surfaces show

relatively larger FGR volumes at relatively larger interior chondrule radii. It is important to note that this is a more subtle behavior than rougher particles simply accreting a larger volume of dust regardless of their size. If this were the case, there would be a positive correlation of relative FGR volume with chondrule roughness (similar to what might occur with FGR formation through alteration), which was not found (Fig. 3.6J). In addition, the rim volume would increase proportionally for all sizes of rough particles, which would not change the power law exponent of the best-fit line, compared to smoother particles. The fact that the power law exponent (and thus *p*) changes for rougher particles indicate rather that for these particles, there is a *relatively greater rim volume accreted for relatively larger particles*.

Reasons for this greater rim volume for increased chondrule radius *r* for more irregular (rougher) particles are merely speculative at this point but we propose here a possible explanation. First, it has been shown, largely in the volcanic aerodynamic modeling literature, that particles with an irregular shape have higher surface to volume ratios and thus higher surface roughness and curvature which can increase their adsorption and geometrical interlocking capabilities (e.g., Vonlanthen et al., 2015). Particle shape has been also considered a factor in nebular dust aggregation models that show an increase in dust growth with irregular particle (dust) shapes due to an increase in sticking probability (Torsten et al., 2000). Because surface area increases proportional to the particle radius as r^2, larger particles provide exponentially more surface area for this effect to operate, thereby increasing the relative amount of rim volume that can be accreted more efficiently due to this irregular surface effect. This would result in larger irregular particles having a relatively larger FGR volume and therefore the power law fit to the rim volume/chondrule radius would have a higher exponent (and therefore *p*; Fig. 3.13). In addition, Cuzzi (2004) noted that FGRs infill hollows and have rounded exteriors which indicate that some erosion must taking place in the nebula to create the smooth exteriors that are observed. He proposed that the portion of FGRs in these protected hollows will preferentially survive the erosion process, and again since larger

chondrules provide relatively more surface area, a larger portion of the rim could be preserved in this manner. This erosional process may also help explain why the outer, rimmed surface of chondrules have a much more limited range in surface roughness than the interior chondrules (Fig. 3.6H). We note that another documented consequence of irregular particle shape in turbulent flow is an increase in drag force which causes a relative decrease in velocity (Dellino et al., 2005). This would actually cause a decrease in the dust accumulation rate leading to smaller-than-expected rim volumes for irregular particles. However, the magnitude of this effect is *independent* of particle size (Dellino et al., 2005) and therefore would not change the power law relationship of FGR volume to chondrule size, nor the resulting p.

3.5 Conclusions

We have found strong morphological evidence based on 3D XCT data that FGRs in CM Murchison were formed in a weakly turbulent nebula. The relationship between FGR volume and interior chondrule interior radius is extremely well described by a power law relationship as proposed for a weakly turbulent nebula setting by Cuzzi (2004). The power law exponent of the best-fit power law including its 2-sigma uncertainty suggests that the rimmed chondrules were slightly larger than Kolmogorov-stopping-time nebular particles. In addition, we rule out parent-body aqueous alteration as an origin for significant FGR formation based on several data: the lack of correlation between interior chondrule shape irregularity (a proxy for degree of alteration) and FGR volume, the presence of a positive correlation between rim thickness and chondrule size, and evidence that FGRs are a similar composition despite their interior chondrule compositions or types. We find that the FGRs were deformed along with the interior chondrules during the impact(s) that foliated and lineated the chondrules in CM Murchison (2015). This provides additional evidence against parent body formation of the FGRs, as this latest deformation event (i.e. regolith compaction) and the aqueous alteration that accompanied it would have modified the FGRs, erasing the distinctive

power law relationship between FGR volume and interior chondrule radius imparted by the nebular accretion process. Finally, we propose that the highly irregular shape of some chondrules in CM Murchison are a primary feature resulting from chondrule formation, and that highly irregular particles with larger particle radii accreted a relatively larger amount of nebular dust.

Summary

The Murchison CM chondrite, which contains primitive nebular material, has undergone significant secondary processing on its asteroid parent body. We have found that foliated and lineated chondrules, including their fine-grained rims, were deformed by impact and that primarily brittle, rather than plastic, mechanisms accommodated their deformation. Due to the lack of plastic deformation within chondrules Murchison is commonly classified as shock stage S1 (i.e. the lowest shock stage) even though the impact strain it experienced was substantial. Pyroxene and chondrule mesostasis were the primary phases accommodating the strain within chondrules, and there is evidence to suggest that the chondrules were not completely incompressible and that some pore collapse occurred within them in addition to in the surrounding microporous matrix during impact. Some aqueous alteration post-dated, or was perhaps contemporaneous with the deformation, and there were multiple episodes of fracturing and mineralization. We estimate that the strain experienced by our Murchison sample was 17-43% and likely the upper limit of this as the chondrules were compressible along with the matrix. This allows us to make the first estimate of pre-deformation bulk porosity for a chondrite, 32.2 – 53.4%, perhaps providing a glimpse of primary, accretionary porosity for chondrite parent bodies.

Most importantly, our findings suggest that significant impact-derived deformation and compaction can occur on chondrite parent bodies whose samples may record only a low level of shock, and that significant chondrule deformation resulting in a chondrite foliation fabric can occur primarily through brittle processes and does not require plastic deformation of grains. While it is impossible to know the impact force required to form such a petrofabric from solely brittle processes, this work in combination with Bland et al.'s (2014) impact modeling into matrix/chondrule mixtures suggest that the carbonaceous chondrite impact shock pressures currently derived from

shock stage assessment of chondrule olivine may not be valid in all cases (Scott et al., 1992). Further, the impact deformation caused significant porosity loss in Murchison, highlighting that the microporosity of CMs prior to impact deformation is likely closer to the hypothesized 60-75% accretional porosity (Beitz et al., 2013a; Ormel et al., 2008). If our chondrite collection is indeed biased towards compacted, low porosity chondrites that can survive delivery to Earth, this raises the possibility that some asteroids may be significantly more microporous than our current chondrite meteorite collection implies. This has significant implications for a variety of asteroidal modeling that take porosity into account (e.g., Bland et al., 2009; Davison et al., 2012).

Despite the impact-induced deformation of the fine-grained rims, we find that we are still able to test formation theories for FGRs within CM Murchison. The relationship between FGR volume and interior chondrule radius is extremely well described by a power law relationship as proposed for a weakly turbulent nebula setting by Cuzzi (2004). The power law exponent of the best-fit power law including its 2-sigma uncertainty suggests that the rimmed chondrules were slightly larger than Kolmogorov-stopping-time nebular particles. Evidence against parent body FGR formation includes a positive correlation between rim thickness and chondrule size and no correlation between interior chondrule roughness (used as a proxy for degree of aqueous alteration) and FGR volume. We confirm that the FGRs were deformed along with the interior chondrules during the impact(s) resulting in rims that are thickest in the plane of foliation, indicating that they were already formed and in place at the time of the impact deformation as well as the aqueous alteration that accompanied it. Finally, we propose that the highly irregular shape of some chondrules in CM Murchison are a primary feature resulting from chondrule formation, and that highly irregular particles with larger particle radii accreted a relatively larger amount of nebular dust.

Thus, in the case of CM Murchison the morphology and size of the fine-grained rims in relation to their underlying chondrules definitively proves that the rims were formed via accretion of dust in the nebula and are not the result of parent body processes.

Further, this data also sheds light on early nebular conditions, indicating that the solar nebula, at least at the time and location of CM FGR formation, was weakly turbulent and that the scale of the Kolmogorov eddy was sized such that the stopping times of the Murchison chondrules were larger than this eddy scale. These turbulence parameters should be taken into account when modeling early nebula dynamical conditions. Future work will investigate whether these same nebular conditions are indicated by FGR morphology and size relationships in other CMs as well as other meteorite classes (CV, CR, CO).

X-ray computed tomography was a critical element in the observations and results presented in this work and as such is proving to be an essential analytical technique in meteoritic and astrophysical research. Some observations, such as the discovery of a foliated petrofabric defined by chondrules, may have been possible using carefully prepared orthogonal thin sections cut from the sample, however the fabric strength and orientation differences among different sub volume regions of Murchison would have gone unnoticed. Likewise the observation of the 3D spatial variation in the FGR thicknesses around the chondrules was only possible using an in-situ 3D imaging technique such as X-ray CT. And the accurate measurement of the FGR volumes and interior chondrule sizes possible with XCT allowed confirmation of a nebular formation origin of the FGRs. In summary, XCT has enabled a significant leap forward in the understanding of early nebular and asteroidal processes and is quickly earning its place among the standard analytical techniques available today to study planetary materials.

Appendices

Appendix A: MuCalc

MuCalc is a Microsoft Excel workbook that can be used to compare the X-ray attenuation of various minerals. A mineral's X-ray attenuation is primarily determined by its chemical formula and density, and the key to distinguishing between different minerals in a rock using XCT is to scan at an energy where each mineral has a different X-ray attenuation (if possible). This workbook allows a user to determine if the various minerals in their sample will be distinguishable in the scan data, and if there is an optimal energy at which to scan in order to maximize their relative differences in attenuation. Within the workbook, the user selects the constituent minerals from a drop-down list and their X-ray attenuation versus energy (up to 500 keV) are plotted together on a graph (see Fig. 3 for an example). The mass X-ray attenuation coefficients for the minerals in the workbook were retrieved using the NIST XCOM database at http://physics.nist.gov/PhysRefData/Xcom/Text/XCOM.html, and the coefficients are multiplied by the mineral's common density to obtain the final X-ray attenuation values.

The workbook currently contains a list of ~250 common terrestrial and extraterrestrial minerals and native elements but detailed instructions are included on how to add a new mineral or element. In addition, there is a solid solution tool that can be used to define a new solid solution mineral out of existing minerals in the workbook and to add this to the permanent mineral list. MuCalc can be downloaded at http://www.ctlab.geo.utexas.edu/software/.

Appendix B: XCT data orientation transformations

Because the orientation of the sample was different for each of the three scans (Chapter 2), it was necessary to rotate the orientation results of the two sub-volume scans to match the full-volume scan to facilitate fabric orientation comparisons. There are various ways to solve this problem but the method described here is specific to Avizo™ 8.0 and the Blob3D program (Ketcham, 2005a; Ketcham, 2005b). First, relative transformations between volumes are determined in Avizo™ using manual feature alignment. For our study we created exterior isosurfaces for the three datasets and manually translated and rotated the two sub-volumes to match the orientation of the full-volume scan using the Transform Editor. The resulting transformation vectors and angles can be accessed in Avizo™ via the Transformation Editor Dialog (Absolute tab). Although the sub-volumes were translated to match the full-volume, only the rotation part of the transformation is needed to properly adjust the orientation data and therefore only the rotation vector and angle (θ) are recorded for each sub-volume. With the rotation vector normalized to a unit vector u,v,w the rotation-only transformation matrix is calculated as

$$T = \begin{bmatrix} u^2 + (v^2 + w^2)\cos\theta & uv(1-\cos\theta) - w\sin\theta & uw(1-\cos\theta) + v\sin\theta \\ uv(1-\cos\theta) + w\sin\theta & v^2 + (u^2 + w^2)\cos\theta & vw(1-\cos\theta) - u\sin\theta \\ uw(1-\cos\theta) - v\sin\theta & uw(1-\cos\theta) + u\sin\theta & w^2 + (u^2 + v^2)\cos\theta \end{bmatrix} \quad \text{(A.1)}$$

where θ is in radians. This matrix is then used to transform a set of orientation direction cosine vectors $\boldsymbol{a}$ to the new coordinate system $\boldsymbol{b}$ with

$$\boldsymbol{b} = T\boldsymbol{a} \quad \text{(A.2)}$$

However, because Blob3D and Avizo™ place the origin at different locations within a TIFF image (Avizo™ places the origin at the top left of the image and Blob3D places it at the bottom left) the y axis between their coordinate systems is flipped, and therefore the y direction cosines from Blob3D are negated before and after the transform to assure that

the transform is applied in the Avizo™ coordinate system. This algorithm has been implemented in IDL in the ROTATE_VECTORS.PRO program shown below.

```
; ROTATE_VECTORS.PRO is used to transform the direction cosines of one dataset (#2)
;     to the local coordinate system of another dataset (#1),
;     where the vector and angle to transform #2 to #1 is expressed as (l,m,n) and
;     theta angle in Avizo, and the direction cosines are out of Blob3D.
;
;  Note that since the Y direction between Blob and Avizo are switched, this
;     transformation negates the Y direction cosine prior to and
;     after applying the transformation.
;
;  After running this program on a set of direction cosines (saved as a CSV file),
;     the resulting direction cosines can be changed to trend/plunge notation for import
;     and viewing into Stereo32 progrm.  Then the two data sets will be in the
;     same global coordinate system and can be directly compared.
;
; INPUTS:
;   infile : path to direction cosine CSV file, no header (via Excel -
;              cut and paste the X1,Y1,Z1 (or X3) values to a new sheet and Save As...)
;   theta, l, m, n : Rotation angle and vector (from Avizo transformation dialog)
;
; OUTPUT:
;   <infile>_Rotated.txt tab-deliminated file with rotated direction cosines
;
FUNCTION RotationMatrix, a,b,c,uUn,vUn,wUn,theta

        l = sqrt(uUn*uUn + vUn*vUn + wUn*wUn)

        ; In this instance we normalize the direction vector.
        u = uUn/l;
        v = vUn/l;
        w = wUn/l;

        ; Set some intermediate values.
        u2 = u*u;
        v2 = v*v;
        w2 = w*w;
        theta = theta*(!PI/180)
        cosT = cos(theta);
        oneMinusCosT = 1-cosT;
        sinT = sin(theta);

        ; Build the matrix entries element by element.
        m11 = u2 + (v2 + w2) * cosT;
        m12 = u*v * oneMinusCosT - w*sinT;
        m13 = u*w * oneMinusCosT + v*sinT;
        m14 = (a*(v2 + w2) - u*(b*v + c*w))*oneMinusCosT + (b*w - c*v)*sinT;

        m21 = u*v * oneMinusCosT + w*sinT;
        m22 = v2 + (u2 + w2) * cosT;
        m23 = v*w * oneMinusCosT - u*sinT;
```

```
        m24 = (b*(u2 + w2) - v*(a*u + c*w))*oneMinusCosT + (c*u - a*w)*sinT;

        m31 = u*w * oneMinusCosT - v*sinT;
        m32 = v*w * oneMinusCosT + u*sinT;
        m33 = w2 + (u2 + v2) * cosT;
        m34 = (c*(u2 + v2) - w*(a*u + b*v))*oneMinusCosT + (a*v - b*u)*sinT;

        return, [[m11, m12, m13, m14], $
                 [m21, m22, m23, m24], $
                 [m31, m32, m33, m34], $
                 [0,0,0,1]]
END



PRO RotateVectors, infile, theta, l, m, n

   dat = read_csv(infile, COUNT=num)

    pts = [[dat.field1],[dat.field2],[dat.field3]]
    pts = double(transpose(pts))
    results = pts
    if num EQ 1 then begin
        pts = reform(pts, 3, 1)
        results = reform(results, 3, 1)
    endif

    rot_matrix = RotationMatrix(0,0,0,l,m,n,theta)

    for i=0, num-1 do begin
        x = pts[0,i]
        y = -1.0*pts[1,i]  ; negate Y coordinate for transform
        z = pts[2,i]
        results[0, i] = rot_matrix[0,0]*x + rot_matrix[1,0]*y + rot_matrix[2,0]*z + $
               rot_matrix[3,0]
        results[1, i] = rot_matrix[0,1]*x + rot_matrix[1,1]*y + rot_matrix[2,1]*z + $
               rot_matrix[3,1]
        results[2, i] = rot_matrix[0,2]*x + rot_matrix[1,2]*y + rot_matrix[2,2]*z + $
               rot_matrix[3,2]
        len = sqrt(results[0,i]^2 + results[1,i]^2 + results[2,i]^2)
        results[*,i] = results[*,i]/len
        results[1,i] = -1.0*results[1,i]  ; negate Y coordinate again
    endfor

    ; write csv file
    base = strpos(infile, '.', /REVERSE_SEARCH)
    outfile = strmid(infile, 0, base) + '_ROTATED.csv'
    write_csv, outfile, results
END
```

Appendix C: XCT Object measurement comparisons among scan volumes

To verify that the differences in fabric strength or orientation were not the result of systematic bias due to the different scanners and settings used, we examined five dark-toned XCT objects in each sub-volume that were also segmented in the full-volume (the two sub-volumes do not overlap so it is not possible to compare them directly). We compared the shape and orientation of each of the ten objects among the three different scan volumes. Size and shape results are presented in Tables C.1-C.2. For all ellipsoid axis lengths, the average measurement departures between the full-volume and sub-volume scans were much less than a single voxel size and the percent difference was at most 4.1%. For the shape parameters (aspect ratio, elongation, and flatness) the percent differences were even smaller at a maximum of 3%. Objects were consistently, slightly larger when measured in the sub-volume scans but this is unsurprising as the data resolution is higher in these scans leading to a more accurate measurement of the actual object size. For a lower resolution scan, the partial volume effect (blur) will lead to a higher-than-expected greyscale value in the outer margin voxels of a low-attenuation object as the surrounding bright matrix is incorporated in these voxels. Therefore, the outermost edge of the object will not be included in the measurement of the object and lead to small, albeit measureable, differences in the length scale. This propagates to the volume calculation where object volumes are on average 7-9% smaller in the lower resolution, full-volume scan. More importantly however these differences are essentially erased when calculating the shape parameters based on relative axis lengths and therefore these match within 3% between the different datasets.

Tables C.1 and C.2 also list the angular separation between the best-fit ellipsoid orientations and these are visualized in Figure C.1. Individual axis orientation

Table C.1 Five dark-toned XCT object best-fit ellipsoid measurement comparisons between full-volume and sub-volume #1

	Object #1		Object #2		Object #3		Object #4		Object #5		All Objects		
	Diff[1]	% Diff	Diff[1]	% Diff	Diff[1]	% Diff	Diff[1]	% Diff	Diff[1]	% Diff	Mean Diff	Median Diff	Mean % Diff
Primary Axis Length (μm)	-10	-2.0 %	-12	-2.9 %	20	2.9 %	-19	-1.7 %	-14	-2.0 %	-7	-12	-1.1 %
Secondary Axis Length (μm)	-6	-1.3 %	-10	-2.9 %	-5	-0.9 %	-23	-2.5 %	-26	-4.2 %	-14	-10	-2.3 %
Tertiary Axis Length (μm)	-14	-3.6 %	1	0.5 %	-40	-7.7 %	-9	-1.2 %	-25	-5.0 %	-17	-14	-3.4 %
Aspect Ratio[2]	0.02	1.6 %	-0.04	-3.3 %	0.13	9.9 %	-0.01	-0.5 %	0.04	2.8 %	0.03	0.02	2.1 %
Elongation[3]	-0.01	-0.7 %	0.00	0.1 %	0.04	3.8 %	0.01	0.7 %	0.02	2.1 %	0.01	0.01	1.2 %
Flatness[4]	0.03	2.3 %	-0.04	-3.4 %	0.07	6.3 %	-0.02	-1.3 %	0.01	0.8 %	0.01	0.01	0.9 %
Volume (mm^3)	-0.026	-7.0 %	-0.011	-5.4 %	-0.050	-5.6 %	-0.180	-5.5 %	-0.111	-11.6 %	-0.076	-0.050	-7.0 %
Primary Axis Separation	7.8°		11.2°		22.1°		4.4°		3.0°		9.7°	7.8°	
Tertiary Axis Separation	10.6°		21.8°		16.1°		6.9°		9.5°		13.0°	10.6°	

[1]Difference calculated as full-volume measurement - sub-volume measurement [2]Primary axis length/Tertiary axis length
[3]Primary axis length/Secondary axis length [4]Secondary axis length/Tertiary axis length

Table C.2 Five dark-toned XCT object best-fit ellipsoid measurement comparisons between full-volume and sub-volume #2

	Object #1		Object #2		Object #3		Object #4		Object #5		All Objects		
	Diff[1]	% Diff	Diff[1]	% Diff	Diff[1]	% Diff	Diff[1]	% Diff	Diff[1]	% Diff	Mean Diff	Median Diff	Mean % Diff
Primary Axis Length (µm)	-22	-2.4 %	-38	-7.0 %	-19	-4.2 %	23	-1.7 %	-30	-4.5 %	-17	-22	-3.0 %
Secondary Axis Length (µm)	4	0.6 %	-29	-7.5 %	1	-0.4 %	32	-2.5 %	-23	-4.4 %	-3	-1	-1.0 %
Tertiary Axis Length (µm)	-12	-2.1 %	-18	-5.2 %	-14	-4.7 %	0	0.0 %	-33	-8.6 %	-15	-14	-4.1 %
Aspect Ratio[2]	0.00	-0.3 %	-0.03	-1.7 %	0.01	0.5 %	0.06	3.2 %	0.07	3.8 %	0.02	0.01	1.1 %
Elongation[3]	-0.04	-2.9 %	0.01	0.5 %	-0.06	-4.6 %	-0.04	-2.9 %	0.00	-0.1 %	-0.03	-0.04	-2.0 %
Flatness[4]	0.04	2.6 %	-0.03	-2.2 %	0.06	4.9 %	0.09	6.0 %	0.05	3.9 %	0.04	0.05	3.0 %
Volume (mm^3)	-0.066	-3.9 %	-0.063	-21.0 %	-0.019	-8.7 %	0.056	9.0%	-0.102	-18.5 %	-0.039	-0.063	-8.6 %
Primary Axis Separation	26.6°		14.2°		25.1°		3.8°		13.4°		16.6°	14.2°	
Tertiary Axis Separation	4.6°		22.7°		5.6°		3.8°		1.8°		7.7°	4.6°	

[1]Difference (Diff) calculated as full-volume measurement - sub-volume measurement [2]Primary axis length/Tertiary axis length [3]Primary axis length/Secondary axis length [4]Secondary axis length/Tertiary axis length

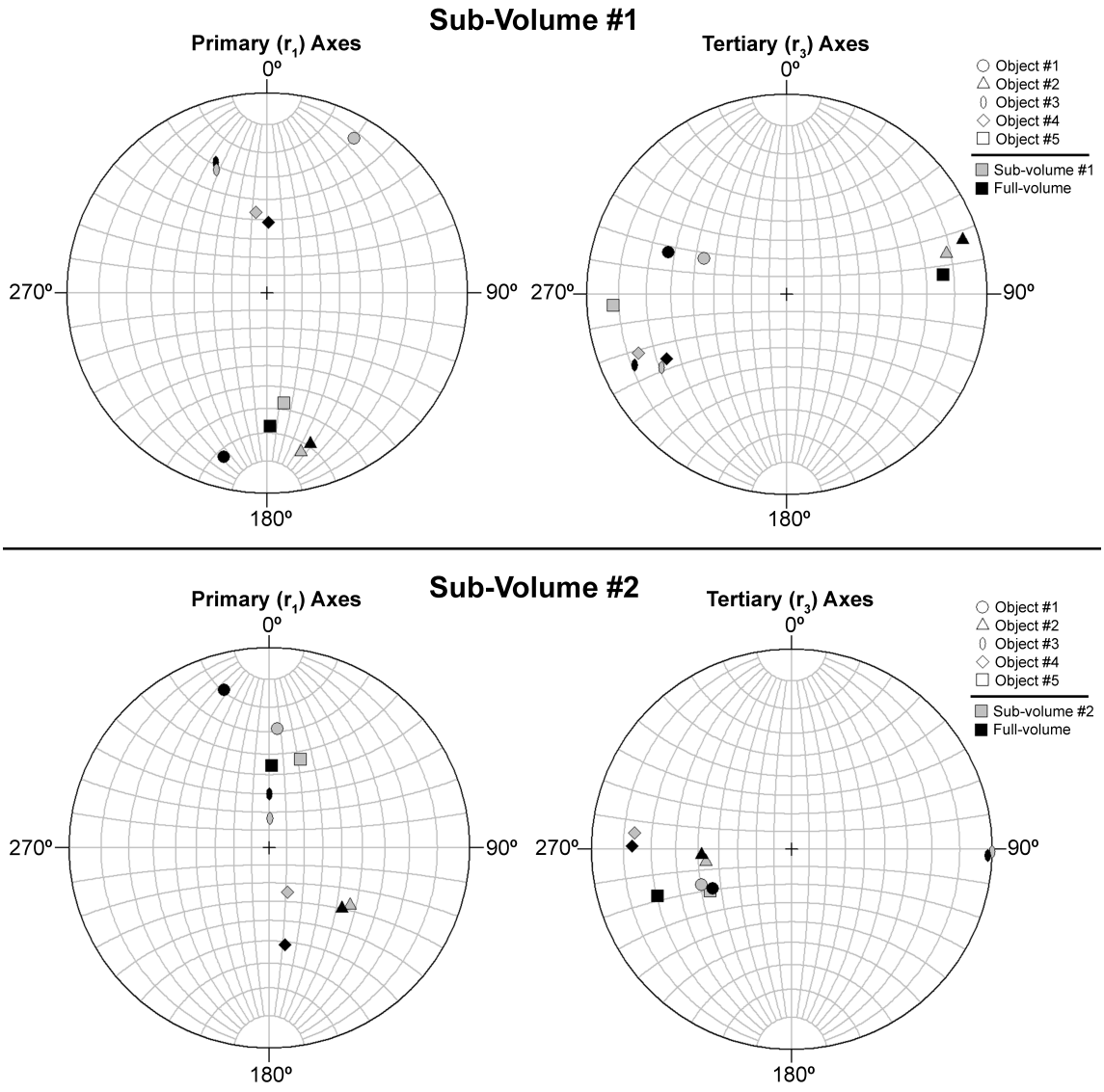

Fig. C.1 Orientations of five dark-toned XCT objects in each sub-volume to matching objects in full-volume.
Orientations from best-fit ellipsoids. Directions of angular departure of orientations are random.

differences can be up to 26.6° but the median departures between the different scans are a maximum of 14.2°. This is only slightly above the estimated measurement error (9-12°) for object orientation using the orthogonal plane segmentation method. More

significantly, the direction of the angular departures are random in nature (Figure C.1) and are therefore likely the result of the departures in general object measurement outlined above rather than different scanner geometries or settings. In summary, we do not find any systematic differences in the derived size or orientation of dark-toned XCT objects between the various scans and therefore interpret any fabric strength or orientation differences (above the measurement error) among the scan volumes to be real.

Appendix D: Chondrule and FGR XCT measurement error

Measurement errors for various reported parameters derived from or directly measured with the XCT data were estimated by having 3 analysts (author R.D.H and two additional users familiar with XCT data measurement) segment and measure the same 8 chondrules. Six chondrules (#1-6 in Tables D.1-D.16) were from the 5.5 μm resolution Chip A dataset and two chondrules (#7-8 in Tables D.1-D.16) were from the 9.99 μm resolution Chip 3-5 dataset (Table 3.1). Chondrules from both scans had similar relative errors among all reported parameters, indicating that the influence of scan resolution on the relative error was negligible. Tables D.1 – D.16 list for each chondrule the average value calculated among all analysts and the absolute and relative differences from this average value for each analyst. The minimum, maximum, average, and standard deviation of the relative differences among all 8 chondrules and all 3 users are shown (so for each table n=24). The standard deviation is used as the relative measurement error for each parameter and reported in Table 3.2. Measurement or derivation of each parameter in the Appendix D tables are the same as that described in the main text, apart from the FGR % thickness (Table D.8). This measurement error was estimated by using the average FGR thickness (Table D.7) normalized by the primary (long) axis length of the best-fit ellipsoid to the whole chondrule (including the rim). This differs from the parameter calculation reported in the main text and Figure 3.10 only in that the average FGR thickness was used instead of the actual FGR thickness (which varies in 3D across hundreds of calculated orientations for each chondrule). This therefore represents a simplified, and likely conservative, error estimate on this parameter.

Table D.1 Interior chondrule volume

	All Users	User #1		User #2		User #3	
	Avg. Volume (mm^3)	Diff (mm^3)	% Diff	Diff (mm^3)	% Diff	Diff (mm^3)	% Diff
Chondrule #1	0.00474	-0.00012	2.4%	-0.00008	1.8%	0.00003	0.7%
Chondrule #2	0.02637	0.00008	0.3%	-0.00019	0.7%	-0.00027	1.0%
Chondrule #3	0.18960	0.00656	3.5%	-0.00070	0.4%	-0.00726	3.8%
Chondrule #4	0.00298	0.00006	2.1%	0.00013	4.5%	0.00007	2.4%
Chondrule #5	0.01126	0.00180	16.0%	0.00156	13.9%	-0.00024	2.1%
Chondrule #6	0.04141	0.00127	3.1%	0.00203	4.9%	0.00075	1.8%
Chondrule #7	1.77512	0.00495	0.3%	-0.02049	1.2%	-0.02543	1.4%
Chondrule #8	0.31862	0.01329	4.2%	0.00082	0.3%	-0.01248	3.9%
Min % Diff	0.3%						
Max % Diff	16.0%						
Avg. % Diff	3.2%						
Std. Dev. % Diff	3.9%						

Table D.2 Whole chondrule volume

	All Users	User #1		User #2		User #3	
	Avg. Volume (mm^3)	Diff (mm^3)	% Diff	Diff (mm^3)	% Diff	Diff (mm^3)	% Diff
Chondrule #1	0.01118	0.00040	3.5%	0.00054	4.8%	0.00014	1.3%
Chondrule #2	0.04128	0.00098	2.4%	0.00008	0.2%	-0.00089	2.2%
Chondrule #3	0.32538	-0.00735	2.3%	-0.00068	0.2%	0.00667	2.1%
Chondrule #4	0.00768	-0.00041	5.4%	0.00006	0.8%	0.00047	6.1%
Chondrule #5	0.02772	0.00104	3.8%	-0.00015	0.5%	-0.00119	4.3%

Chondrule #6	0.07224	-0.00224	3.1%	-0.00079	1.1%	0.00145	2.0%
Chondrule #7	2.37501	-0.00730	0.3%	-0.04672	2.0%	-0.03941	1.7%
Chondrule #8	0.53881	-0.01119	2.1%	-0.01360	2.5%	-0.00241	0.4%
Min % Diff	0.2%						
Max % Diff	6.1%						
Avg. % Diff	2.3%						
Std. Dev. % Diff	1.7%						

Table D.3 FGR volume[a]

	All Users	User #1		User #2		User #3	
	Avg. Volume (mm^3)	Diff (mm^3)	% Diff	Diff (mm^3)	% Diff	Diff (mm^3)	% Diff
Chondrule #1	0.00051	0.00051	8.0%	0.00062	9.7%	0.00011	0.1%
Chondrule #2	0.00090	0.00090	6.0%	0.00027	1.8%	-0.00062	0.3%
Chondrule #3	-0.01391	-0.01391	10.2%	0.00002	0.0%	0.01393	3.9%
Chondrule #4	-0.00047	-0.00047	10.1%	-0.00007	1.6%	0.00040	0.4%
Chondrule #5	-0.00076	-0.00076	4.6%	-0.00171	10.4%	-0.00095	0.7%
Chondrule #6	-0.00352	-0.00352	11.4%	-0.00282	9.1%	0.00070	0.3%
Chondrule #7	-0.01225	-0.01225	2.0%	-0.02623	4.4%	-0.01398	1.9%
Chondrule #8	-0.02448	-0.02448	11.1%	-0.01441	6.5%	0.01007	2.4%
Min % Diff	0.0%						
Max % Diff	11.4%						
Avg. % Diff	4.9%						
Std. Dev. % Diff	4.1%						

[a]FGR Volume = Whole chondrule volume – interior chondrule volume

Table D.4 FGR % volume[a]

	All Users	User #1		User #2		User #3	
	Avg. Volume (mm^3)	Diff (mm^3)	% Diff	Diff (mm^3)	% Diff	Diff (mm^3)	% Diff
Chondrule #1	0.57500	0.02530	4.4%	0.02857	5.0%	0.00328	0.6%
Chondrule #2	0.36099	0.01299	3.6%	0.00575	1.6%	-0.00725	2.0%
Chondrule #3	0.41680	-0.03362	8.1%	0.00044	0.1%	0.03406	8.2%
Chondrule #4	0.61145	-0.02971	4.9%	-0.01528	2.5%	0.01443	2.4%
Chondrule #5	0.59428	-0.04817	8.1%	-0.05776	9.7%	-0.00959	1.6%
Chondrule #6	0.42627	-0.03604	8.5%	-0.03445	8.1%	0.00159	0.4%
Chondrule #7	0.25253	-0.00434	1.7%	-0.00601	2.4%	-0.00167	0.7%
Chondrule #8	0.40829	-0.03737	9.2%	-0.01640	4.0%	0.02097	5.1%
Min % Diff	0.1%						
Max % Diff	9.7%						
Avg. % Diff	4.3%						
Std. Dev. % Diff	3.1%						

[a]FGR volume normalized by whole chondrule volume

Table D.5 Interior Chondrule Radius[a]

	All Users	User #1		User #2		User #3	
	Avg. Radius (mm)	Diff (mm)	% Diff	Diff (mm)	% Diff	Diff (mm)	% Diff
Chondrule #1	0.10424	-0.00085	0.8%	-0.00062	0.6%	0.00023	0.2%
Chondrule #2	0.18465	0.00019	0.1%	-0.00044	0.2%	-0.00064	0.3%
Chondrule #3	0.35635	0.00410	1.2%	-0.00047	0.1%	-0.00457	1.3%
Chondrule #4	0.08925	0.00063	0.7%	0.00134	1.5%	0.00072	0.8%

Chondrule #5	0.13880	0.00727	5.2%	0.00652	4.7%	-0.00075	0.5%
Chondrule #6	0.21459	0.00221	1.0%	0.00353	1.6%	0.00132	0.6%
Chondrule #7	0.75112	0.00071	0.1%	-0.00289	0.4%	-0.00359	0.5%
Chondrule #8	0.42365	0.00586	1.4%	0.00031	0.1%	-0.00555	1.3%
Min % Diff	0.1%						
Max % Diff	5.2%						
Avg. % Diff	1.1%						
Std. Dev. % Diff	1.3%						

[a]Equivalent volume spherical radius

Table D.6 Whole Chondrule Radius[a]

	All Users	User #1		User #2		User #3	
	Avg. Radius (mm)	Diff (mm)	% Diff	Diff (mm)	% Diff	Diff (mm)	% Diff
Chondrule #1	0.13871	0.00164	1.2%	0.00224	1.6%	0.00060	0.4%
Chondrule #2	0.21439	0.00169	0.8%	0.00014	0.1%	-0.00155	0.7%
Chondrule #3	0.42666	-0.00322	0.8%	-0.00031	0.1%	0.00291	0.7%
Chondrule #4	0.12238	-0.00220	1.8%	0.00028	0.2%	0.00248	2.0%
Chondrule #5	0.18772	0.00234	1.2%	-0.00035	0.2%	-0.00269	1.4%
Chondrule #6	0.25835	-0.00269	1.0%	-0.00095	0.4%	0.00173	0.7%
Chondrule #7	0.82765	-0.00083	0.1%	-0.00541	0.7%	-0.00458	0.6%
Chondrule #8	0.50477	-0.00350	0.7%	-0.00423	0.8%	-0.00073	0.1%
Min % Diff	0.1%						
Max % Diff	2.0%						
Avg. % Diff	0.8%						
Std. Dev. % Diff	0.6%						

[a]Equivalent volume spherical radius

Table D.7 Average FGR Thickness[a]

	All Users	User #1		User #2		User #3	
	Avg. Thickness (mm)	Diff (mm)	% Diff	Diff (mm)	% Diff	Diff (mm)	% Diff
Chondrule #1	0.03447	0.00249	7.2%	0.00286	8.3%	0.00037	1.1%
Chondrule #2	0.02974	0.00149	5.0%	0.00058	1.9%	-0.00091	3.1%
Chondrule #3	0.07031	-0.00732	10.4%	0.00016	0.2%	0.00748	10.6%
Chondrule #4	0.03313	-0.00282	8.5%	-0.00106	3.2%	0.00176	5.3%
Chondrule #5	0.04892	-0.00493	10.1%	-0.00687	14.0%	-0.00194	4.0%
Chondrule #6	0.04376	-0.00489	11.2%	-0.00448	10.2%	0.00041	0.9%
Chondrule #7	0.07654	-0.00154	2.0%	-0.00252	3.3%	-0.00099	1.3%
Chondrule #8	0.08112	-0.00936	11.5%	-0.00454	5.6%	0.00482	5.9%
Min % Diff	0.2%						
Max % Diff	14.0%						
Avg. % Diff	6.0%						
Std. Dev. % Diff	4.1%						

[a]Avg. FGR thickness = Whole chondrule equivalent spherical radius – interior chondrule equivalent spherical radius

Table D.8 FGR % Thickness[a]

	All Users	User #1		User #2		User #3	
	Avg. Fractional Thickness	Diff	% Diff	Diff	% Diff	Diff	% Diff
Chondrule #1	0.20640	0.02021	9.8%	0.01581	7.7%	-0.00439	2.1%

Chondrule #2	0.12628	0.00578	4.6%	0.00379	3.0%	-0.00199	1.6%
Chondrule #3	0.12389	-0.01218	9.8%	0.00070	0.6%	0.01288	10.4%
Chondrule #4	0.23896	-0.01580	6.6%	-0.01178	4.9%	0.00403	1.7%
Chondrule #5	0.22381	-0.02561	11.4%	-0.02709	12.1%	-0.00148	0.7%
Chondrule #6	0.13080	-0.01273	9.7%	-0.01272	9.7%	0.00001	0.0%
Chondrule #7	0.07368	-0.00139	1.9%	-0.00192	2.6%	-0.00053	0.7%
Chondrule #8	0.13370	-0.01414	10.6%	-0.00626	4.7%	0.00788	5.9%
Min % Diff	0.0%						
Max % Diff	12.1%						
Avg. % Diff	5.5%						
Std. Dev. % Diff	4.1%						

[a]Average FGR thickness normalized by primary axis length of best-fit ellipsoid to whole chondrule

Table D.9 Interior Chondrule Aspect Ratio[a]

	All Users	User #1		User #2		User #3	
	Avg. Aspect Ratio	Diff	% Diff	Diff	% Diff	Diff	% Diff
Chondrule #1	1.53830	0.01346	0.9%	-0.00534	0.3%	-0.01881	1.2%
Chondrule #2	1.17521	-0.00795	0.7%	0.00297	0.3%	0.01092	0.9%
Chondrule #3	1.93066	-0.00863	0.4%	-0.01574	0.8%	-0.00712	0.4%
Chondrule #4	1.38053	0.01081	0.8%	0.02072	1.5%	0.00991	0.7%
Chondrule #5	1.39907	0.01204	0.9%	-0.01413	1.0%	-0.02617	1.9%
Chondrule #6	1.54214	0.00992	0.6%	-0.00158	0.1%	-0.01150	0.7%
Chondrule #7	1.56411	-0.00666	0.4%	0.00816	0.5%	0.01482	0.9%
Chondrule #8	1.51139	-0.02222	1.5%	-0.02252	1.5%	-0.00030	0.0%
Min % Diff	0.0%						

Max % Diff	1.9%
Avg. % Diff	0.8%
Std. Dev. % Diff	0.5%

[a]Aspect ratio = primary axis length/tertiary axis length of best-fit ellipsoid to interior chondrule

Table D.10 Whole Chondrule Aspect Ratio[a]

	All Users	User #1		User #2		User #3	
	Avg. Aspect Ratio	Diff	% Diff	Diff	% Diff	Diff	% Diff
Chondrule #1	1.37050	-0.05573	3.9%	-0.00956	0.7%	0.04617	3.2%
Chondrule #2	1.17474	-0.00266	0.2%	-0.03035	2.6%	-0.02769	2.4%
Chondrule #3	1.70576	-0.01855	1.1%	-0.00804	0.5%	0.01051	0.6%
Chondrule #4	1.36176	-0.01081	0.8%	0.04016	2.9%	0.05097	3.7%
Chondrule #5	1.41613	-0.01688	1.2%	-0.07069	4.9%	-0.05381	3.8%
Chondrule #6	1.47821	-0.01943	1.3%	-0.00063	0.0%	0.01880	1.3%
Chondrule #7	1.53254	0.01253	0.8%	-0.01162	0.8%	-0.02415	1.6%
Chondrule #8	1.36741	0.00386	0.3%	-0.00472	0.3%	-0.00858	0.6%
Min % Diff	0.0%						
Max % Diff	4.9%						
Avg. % Diff	1.6%						
Std. Dev. % Diff	1.4%						

[a]Aspect ratio = primary axis length/tertiary axis length of best-fit ellipsoid to whole chondrule

Table D.11 Interior Chondrule CVI

	All Users	User #1		User #2		User #3	
	Avg. CVI	Diff	% Diff	Diff	% Diff	Diff	% Diff
Chondrule #1	1.25014	-0.00570	0.5%	0.01465	1.2%	0.02035	1.6%
Chondrule #2	1.16900	0.00801	0.7%	0.01101	0.9%	0.00300	0.3%
Chondrule #3	1.42949	-0.00908	0.6%	0.04267	3.0%	0.05174	3.6%
Chondrule #4	1.13729	0.01011	0.9%	0.00651	0.6%	-0.00360	0.3%
Chondrule #5	1.37046	-0.05775	4.2%	-0.07254	5.3%	-0.01479	1.1%
Chondrule #6	1.30522	-0.02360	1.8%	-0.03951	3.0%	-0.01591	1.2%
Chondrule #7	1.20659	-0.00399	0.3%	0.01456	1.2%	0.01855	1.5%
Chondrule #8	1.25466	0.00789	0.6%	0.01410	1.1%	0.00621	0.5%
Min % Diff	0.3%						
Max % Diff	5.3%						
Avg. % Diff	1.5%						
Std. Dev. % Diff	1.3%						

Table D.12 Whole Chondrule CVI

	All Users	User #1		User #2		User #3	
	Avg. CVI	Diff	% Diff	Diff	% Diff	Diff	% Diff
Chondrule #1	1.16769	0.00505	0.4%	0.00276	0.2%	-0.00229	0.2%
Chondrule #2	1.15493	0.00598	0.5%	-0.00602	0.5%	-0.01200	1.0%
Chondrule #3	1.26028	-0.01903	1.5%	0.03580	2.8%	0.05483	4.4%
Chondrule #4	1.16200	0.01869	1.6%	0.00983	0.8%	-0.00886	0.8%
Chondrule #5	1.21881	-0.01976	1.6%	0.00034	0.0%	0.02011	1.6%

Chondrule #6	1.22331	0.00424	0.3%	0.02652	2.2%	0.02228	1.8%
Chondrule #7	1.17824	-0.00107	0.1%	0.01647	1.4%	0.01754	1.5%
Chondrule #8	1.17012	0.01360	1.2%	0.01286	1.1%	-0.00075	0.1%
Min % Diff	0.0%						
Max % Diff	4.4%						
Avg. % Diff	1.2%						
Std. Dev. % Diff	1.0%						

Table D.13 Interior Chondrule Ellipticity

	All Users	User #1		User #2		User #3	
	Avg. Ellipticity	Diff	% Diff	Diff	% Diff	Diff	% Diff
Chondrule #1	1.02682	-0.00121	0.1%	-0.00021	0.0%	0.00142	0.1%
Chondrule #2	1.00362	0.00029	0.0%	0.00009	0.0%	-0.00038	0.0%
Chondrule #3	1.05904	0.00110	0.1%	-0.00149	0.1%	0.00040	0.0%
Chondrule #4	1.01578	-0.00090	0.1%	0.00026	0.0%	0.00063	0.1%
Chondrule #5	1.01755	-0.00157	0.2%	-0.00111	0.1%	0.00268	0.3%
Chondrule #6	1.02745	-0.00092	0.1%	-0.00004	0.0%	0.00096	0.1%
Chondrule #7	1.02662	0.00050	0.0%	0.00061	0.1%	-0.00111	0.1%
Chondrule #8	1.02735	0.00177	0.2%	-0.00127	0.1%	-0.00050	0.0%
Min % Diff	0.0%						
Max % Diff	0.3%						
Avg. % Diff	0.1%						
Std. Dev. % Diff	0.1%						

Table D.14 Whole Chondrule Ellipticity

	All Users	User #1		User #2		User #3	
	Avg. Ellipticity	Diff	% Diff	Diff	% Diff	Diff	% Diff
Chondrule #1	1.01726	0.00310	0.3%	-0.00027	0.0%	-0.00283	0.3%
Chondrule #2	1.00363	0.00016	0.0%	-0.00114	0.1%	0.00099	0.1%
Chondrule #3	1.03963	0.00181	0.2%	-0.00057	0.1%	-0.00123	0.1%
Chondrule #4	1.01722	0.00066	0.1%	0.00295	0.3%	-0.00361	0.4%
Chondrule #5	1.02098	0.00253	0.2%	-0.00633	0.6%	0.00380	0.4%
Chondrule #6	1.02374	0.00106	0.1%	-0.00042	0.0%	-0.00064	0.1%
Chondrule #7	1.02338	-0.00088	0.1%	-0.00080	0.1%	0.00167	0.2%
Chondrule #8	1.01334	0.00006	0.0%	-0.00018	0.0%	0.00012	0.0%
Min % Diff	0.0%						
Max % Diff	0.6%						
Avg. % Diff	0.2%						
Std. Dev. % Diff	0.2%						

Table D.15 Interior Chondrule Roughness

	All Users	User #1		User #2		User #3	
	Avg. Roughness	Diff	% Diff	Diff	% Diff	Diff	% Diff
Chondrule #1	1.21750	0.00700	0.6%	0.01452	1.2%	-0.02152	1.8%
Chondrule #2	1.16478	-0.00833	0.7%	0.01087	0.9%	-0.00255	0.2%
Chondrule #3	1.34982	0.00721	0.5%	0.04215	3.1%	-0.04936	3.7%
Chondrule #4	1.11962	-0.00896	0.8%	0.00612	0.5%	0.00284	0.3%
Chondrule #5	1.34681	0.05873	4.4%	-0.06974	5.2%	0.01102	0.8%
Chondrule #6	1.27035	0.02409	1.9%	-0.03840	3.0%	0.01431	1.1%

Chondrule #7	1.17530	0.00331	0.3%	0.01349	1.1%	-0.01679	1.4%
Chondrule #8	1.22127	-0.00979	0.8%	0.01523	1.2%	-0.00544	0.4%
Min % Diff	0.2%						
Max % Diff	5.2%						
Avg. % Diff	1.5%						
Std. Dev. % Diff	1.4%						

Table D.16 Whole Chondrule Roughness

	All Users	User #1		User #2		User #3	
	Avg. Roughness	Diff	% Diff	Diff	% Diff	Diff	% Diff
Chondrule #1	1.14789	-0.00848	0.7%	0.00303	0.3%	0.00545	0.5%
Chondrule #2	1.15075	-0.00615	0.5%	-0.00469	0.4%	0.01083	0.9%
Chondrule #3	1.21222	0.01620	1.3%	0.03506	2.9%	-0.05126	4.2%
Chondrule #4	1.14234	-0.01912	1.7%	0.00639	0.6%	0.01273	1.1%
Chondrule #5	1.19459	0.01726	1.4%	0.00850	0.7%	-0.02577	2.2%
Chondrule #6	1.19495	-0.00538	0.5%	0.02638	2.2%	-0.02100	1.8%
Chondrule #7	1.15134	0.00205	0.2%	0.01699	1.5%	-0.01904	1.7%
Chondrule #8	1.15472	-0.01350	1.2%	0.01289	1.1%	0.00060	0.1%
Min % Diff	0.1%						
Max % Diff	4.2%						
Avg. % Diff	1.2%						
Std. Dev. % Diff	1.0%						

Appendix E: 3D FGR Thickness IDL code

The algorithm to measure 3D FGR thickness around each chondrule was inserted into the Blob3D program. The main algorithm and code is shown below (CalcRimThickness). All of the objects and other functions within the code are defined in the larger Blob3D program and not reproduced here. The core of the function was written by Rich Ketcham (using existing Quant3D code) with subsequent modifications and updates by Romy Hanna.

```
;=============================================================
; METHODNAME:
; B3D_ExtObject::CalcRimThickness
;
; PURPOSE:
;   Calculate Rim Thickness in various directions from a specified center
;
; CALLING SEQUENCE:
;   [B3D_ExtObject::] CalcRimThickness
;
; INPUTS:
;   max_length: max length of blob (in mm), used to calcuated rim thickness
;               percentage (of full object)
;   SYM: use averaged symmetrical (upper/lower projection) vectors to
;        calculate rim thickness
;
; KEYWORD PARAMETERS:
;
; MODIFICATION HISTORY:
;   Written by:  Rich Ketcham, 1/5/16
;       Some code pilfered from Quant3D
;   RDH 4/2016: Modified/improved and added SYM keyword
; =============================================================

Function B3D_ExtObject::CalcRimThickness, max_axis, SYM

  ; Make sure we have current isosurface
  self->MakeSurface, 127B
  self.surf->GetProperty,DATA=verts,POLYGONS=polys

  ; Find central point.
  ; Possibilities are center of mass, center of fitted ellipsoid
  ;     (see CalcEllipsoidStats for code), average isosurface vertex, ...?
  center = Round(Mean(verts, DIMENSION=2))  ; Average isosurface vertex
  ; *** RAK NOTE, this is not necessarily the best answer
  ; RDH - This is actually nearly the best solution, better would be center of
  ;       interior blob only but doubt it would make much of a difference

  ; Get directions.
```

```
;  RDH- Although ROTATE randomly spins the sphere, the directions are still
;     symmetrically distributed across sphere so to get a truly random set
;     of directions, generate 5 sets of directions and collate
if not Obj_Valid(self.sph) then begin
   self.sph = Obj_New('B3D_SphereIsoGen',RESOLUTION=2, /ROTATE)
   ; call 5 more times to generate additional nonsymmetric vertices
   for i=0,6 do self.sph->Collate, RESOLUTION=2, /ROTATE
endif
latLong = self.sph->GetLatLong()*!RADEG
numOrient = (Size(latLong))[2]

; Generate the vectors
; vectorLength: How long to make the vectors.
; They need to reach from roughly the center to the edge of the volume.
vectorLength = CEIL(Max(self.upperCoord-self.lowerCoord)/1.9)
; RAK - Define an array for saving them all.
if (SYM EQ 1) then begin
  thickness = FltArr(numOrient/2)
  thicknessPerc = FltArr(numOrient/2)
endif else begin
  thickness = FltArr(numOrient)
  thicknessPerc = FltArr(numOrient)
endelse
vol = *self.vol

; calculate length in max_axis direction (POS)
latlongMax = CV_Coord(FROM_RECT=max_axis,/TO_SPHERE,/DEGREES)
disp = self->GenerateDisplacementVector(latLongMax[0], latLongMax[1],vectorLength)

; Translate vector to begin at center point
for j=0,2 do disp[j,*] += center[j]
trav = FltArr(vectorLength)

; Figure out where the traverse goes negative, if ever, as no error is thrown
;     for negative indices anymore
lastInd = vectorLength
negInds = Where(disp LT 0, count)
if (count GT 0) then lastInd = negInds[0]/3
; Check for positive
normdisp = Float(disp)
szVol = Size(vol,/DIMENSIONS)-1.0
for k=0,2 do normDisp[k,*] = disp[k,*]/szVol[k]
posInds = Where(normDisp GT 1.0,count)
if (count GT 0) then lastInd = lastInd < posInds[0]/3

; get max trav values from volume
trav = vol[B3D_ArrayIndices(Size(vol),disp[*,0:lastInd-1],/REVERSE)] EQ 255B
dirAdj = Sqrt(Total(((disp[*,0]-disp[*,vectorLength-1])* $
      [self.dataParams.pixelSpacing,self.dataParams.pixelSpacing,$
      self.dataParams.sliceSpacing])^2))/(vectorLength-1.0)
; double the max length along this vector
rimLoc = where(trav EQ 1, count)
voxel_lenth_to_blob_edgePOS = rimLoc[count-1] + 1

; calculate length in max_axis direction NEG
```

```
latlongMax = CV_Coord(FROM_RECT=(-1*max_axis),/TO_SPHERE,/DEGREES)
disp = self->GenerateDisplacementVector(latLongMax[0], latLongMax[1],vectorLength)
for j=0,2 do disp[j,*] += center[j]
trav = FltArr(vectorLength)
; Figure out where the traverse goes negative, if ever, as no error is thrown
;     for negative indices anymore
lastInd = vectorLength
negInds = Where(disp LT 0, count)
if (count GT 0) then lastInd = negInds[0]/3
; Check for positive
normdisp = Float(disp)
szVol = Size(vol,/DIMENSIONS)-1.0
for k=0,2 do normDisp[k,*] = disp[k,*]/szVol[k]
posInds = Where(normDisp GT 1.0,count)
if (count GT 0) then lastInd = lastInd < posInds[0]/3

; get max trav values from volume
trav = vol[B3D_ArrayIndices(Size(vol),disp[*,0:lastInd-1],/REVERSE)] EQ 255B
dirAdj = Sqrt(Total(((disp[*,0]-disp[*,vectorLength-1])*$
      [self.dataParams.pixelSpacing,self.dataParams.pixelSpacing,$
      self.dataParams.sliceSpacing])^2))/(vectorLength-1.0)
; double the max length along this vector
rimLoc = where(trav EQ 1, count)
voxel_lenth_to_blob_edgeNEG = rimLoc[count-1] + 1
max_length = (voxel_lenth_to_blob_edgePOS+voxel_lenth_to_blob_edgeNEG)*dirAdj

; RDH- for orient vector, 1st and 2nd (and so on) are symmetric pair.
;     If symmetric option selected it averages the thickness for each symmetric pair
;     of orientations, instead of returning every single orientation
for i=0,numOrient-1 do begin
  disp = self->GenerateDisplacementVector(latLong[0,i], latLong[1,i],vectorLength)
  if (SYM EQ 1) then disp2 = self->GenerateDisplacementVector(latLong[0,i+1], $
      latLong[1,i+1],vectorLength)

  ; Calculate directional adjustment; can also do this from angles,
  ;     but this is easier...
  dirAdj = Sqrt(Total(((disp[*,0]-disp[*,vectorLength-1])*$
      [self.dataParams.pixelSpacing,self.dataParams.pixelSpacing,$
      self.dataParams.sliceSpacing])^2))/(vectorLength-1.0)

  ; Translate vector to begin at center point
  for j=0,2 do disp[j,*] += center[j]
  if (SYM EQ 1) then for j=0,2 do disp2[j,*] += center[j]

  ; Extract values from blob volume along vector
  ;    use error catching to see when we exit
  trav = FltArr(vectorLength)
  if (SYM EQ 1) then trav2 = FltArr(vectorLength)

  ; Figure out where the traverse goes negative, if ever, as no error is thrown for
  ;     negative indices anymore
  lastInd = vectorLength
  negInds = Where(disp LT 0, count)
  if (count GT 0) then lastInd = negInds[0]/3
  ; Check for positive
```

```
    normdisp = Float(disp)
    szVol = Size(vol,/DIMENSIONS)-1.0
    for k=0,2 do normDisp[k,*] = disp[k,*]/szVol[k]
    posInds = Where(normDisp GT 1.0,count)
    if (count GT 0) then lastInd = lastInd < posInds[0]/3

    if (SYM EQ 1) then begin
      lastInd2 = vectorLength
      negInds2 = Where(disp2 LT 0, count)
      if (count GT 0) then lastInd2 = negInds2[0]/3
      ; Check for positive
      normdisp= Float(disp2)
      szVol = Size(vol,/DIMENSIONS)-1.0
      for k=0,2 do normDisp[k,*] = disp2[k,*]/szVol[k]
      posInds2 = Where(normDisp GT 1.0,count)
      if (count GT 0) then lastInd2 = lastInd2 < posInds2[0]/3
    endif

    trav = vol[B3D_ArrayIndices(Size(vol),disp[*,0:lastInd-1],/REVERSE)] EQ 255B
    if (SYM EQ 1) then trav2 = vol[B3D_ArrayIndices(Size(vol),disp2[*,0:lastInd2-1],$
          /REVERSE)] EQ 255B

    ; thickness in this direction should be number of set voxels,
    ;     times non-orthogonal directional adjustment (with pixel scale).
    if (SYM EQ 1) then begin
      thickness[(i/2)] = ((Total(trav)+ Total(trav2))*dirAdj)/2
      thicknessPerc[(i/2)] = thickness[(i/2)]/max_length
    endif else begin
      thickness[i] = Total(trav)*dirAdj
      thicknessPerc[i] = thickness[i]/max_length
    endelse

    ; increment i artificially if we already have next one
    if (SYM EQ 1) then if (i EQ numOrient-2) then i+=2 else i+=1
  endfor

  if Ptr_Valid(self.rimThickData) then Ptr_Free, self.rimThickData
  self.rimThickData = Ptr_New(thickness)
  if Ptr_Valid(self.rimThickPercData) then Ptr_Free, self.rimThickPercData
  self.rimThickPercData = Ptr_New(thicknessPerc)

  return, self.UniqueNum
End
```

Appendix F: Chondrule and FGR ellipticity and aspect ratio analysis

In this study we measured and quantified the shapes of the inner and whole (including FGR) chondrules separately. We found that the ellipticity and aspect ratio between the inner and whole chondrule varies in a systematic way where the inner chondrules have a consistently higher ellipticity and aspect ratio than the whole chondrules (Figs. 3.6F-G and Table F.1). In an effort to understand these differences, we examine how the aspect ratio varies between the inner and whole chondrules for 2 idealized cases (Fig. F.1). Because ellipticity and aspect ratio are related (the former takes into account all 3 axes of the ellipsoid while the latter includes only the longest and shortest axes), for simplicity we examine only the aspect ratio here although results for ellipticity will be similar. For the illustrated examples in Figure F.1 we are using the measured average primary (longest) radius of whole chondrules (408 μm; Table F.1), the average aspect ratio of whole chondrules (1.46; Table F.1), and the average uniform FGR thickness relative to the primary axis of the whole chondrule (7.8% or 63 μm; Fig. 3.10 and Section 3.4.2).

We first consider the case where the FGR thickness around the deformed chondrules is a uniform thickness (Fig. F.1 left). In this case the inner chondrule aspect is larger than the whole chondrule aspect ratio and the ratio of the two aspect ratios is 1.10 (i.e., the aspect ratio of the inner chondrule is 10% larger than the aspect ratio of the whole chondrule). This is a larger difference than the observed average difference of inner to whole chondrule aspect ratios, which is 5% (1.05; Table F.1). However, we find that the thickness of the FGR is not uniform around the chondrule but is instead consistently thicker in the plane of foliation (Fig. 3.10). If we increase the thickness of the FGR in the whole chondrule long axis direction and decrease it in the short axis direction by the observed difference in thickness (1.4%; Fig. 3.10 and Section 3.4.2), the aspect ratio of the whole chondrule is increased, which decreases the relative difference between it and the inner chondrule aspect ratio (Fig. F.1 right). In this idealized case, the

ratio between the inner and whole chondrule aspect ratios is decreased to 1.03, which is closer to our observed average difference (5% or 1.05; Table F.1). This further confirms our observation that FGR thicknesses are larger in the plane of foliation (i.e., the plane of elongation of deformed chondrules) and explains why the aspect ratios, as well as the ellipticities, of the inner chondrules are consistently, slightly larger than the whole chondrules (Figs. 3.6F-G).

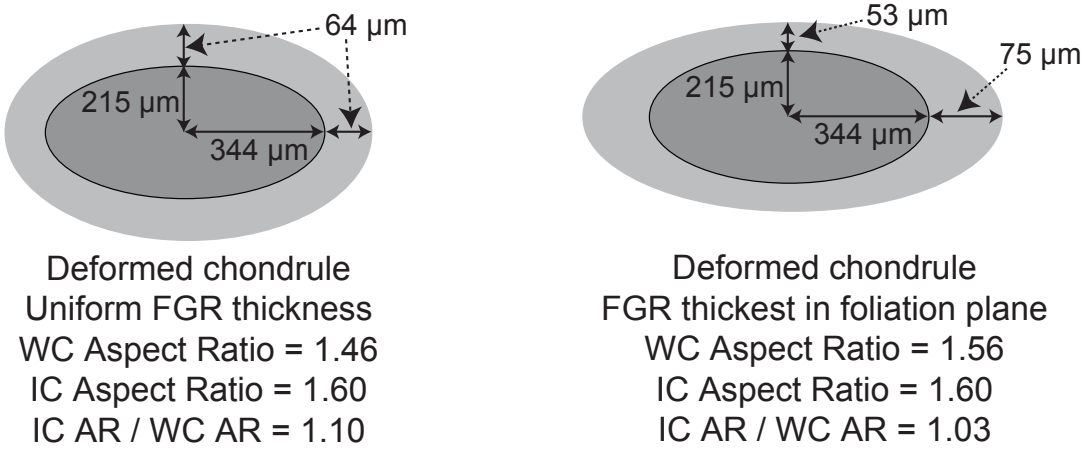

Fig. F.1 Differences in aspect ratios for inner and whole chondrules for two idealized cases.
Uniform FGR thickness is depicted on left and thicker FGR in foliation plane shown on right. Numbers are derived from the measured average primary radius of whole chondrules, average aspect ratio for whole chondrules, and average relative FGR thickness around deformed chondrules (see text). WC refers to whole chondrule, IC refers to inner chondrule, and AR is aspect ratio. For both cases the aspect ratio of the whole chondrule is smaller than for the inner chondrule, but in the deformed FGR case (right) the larger FGR thickness in the plane of elongation of the chondrule results in less of a difference between the inner and whole chondrule aspect ratios. Figure not to scale.

Table F.1. XCT shape measurements of 61 chondrules with FGR among 6 samples.

	Num.	Whole Chondrule Primary Radius[a] (mm)	Interior Chondrule Aspect Ratio	Whole Chondrule Aspect Ratio	Interior Chondrule Ellipticity	Whole Chondrule Ellipticity	IC Ellipticity/ WC Ellipticity	IC Aspect Ratio/ WC Aspect Ratio
Chip A	1	0.253	1.43	1.38	1.02	1.02	1.00	1.03
	2	0.262	1.76	1.54	1.05	1.03	1.02	1.14
	3	0.401	1.42	1.31	1.02	1.01	1.01	1.09
	4	0.255	1.71	1.51	1.04	1.02	1.02	1.13
	5	0.259	1.78	1.68	1.04	1.04	1.01	1.06
	6	0.163	1.55	1.37	1.03	1.01	1.01	1.13
	7	0.229	2.02	1.70	1.07	1.04	1.03	1.19
	8	0.237	1.17	1.17	1.00	1.00	1.00	0.99
	9	0.449	1.89	1.58	1.05	1.03	1.03	1.20
	10	0.262	1.65	1.46	1.03	1.02	1.01	1.13
	11	0.564	1.92	1.71	1.06	1.04	1.02	1.13
	12	0.183	1.12	1.23	1.00	1.01	1.00	0.91
	13	0.297	1.42	1.37	1.02	1.01	1.00	1.04
	14	0.236	1.23	1.32	1.01	1.01	1.00	0.93
	15	0.249	1.33	1.29	1.01	1.01	1.00	1.04
	16	0.300	1.49	1.57	1.02	1.03	0.99	0.95

17	0.261	1.23	1.25	1.01	1.01	1.00	0.99
18	0.182	1.35	1.27	1.01	1.01	1.00	1.07
19	0.136	1.39	1.36	1.02	1.02	1.00	1.02
20	0.336	1.64	1.49	1.03	1.02	1.01	1.10
21	0.274	1.85	1.66	1.05	1.04	1.02	1.12
22	0.222	1.41	1.42	1.02	1.02	1.00	1.00
23	0.406	1.43	1.32	1.02	1.01	1.01	1.08
24	0.161	1.36	1.24	1.02	1.01	1.01	1.09
25	0.298	1.90	1.64	1.05	1.03	1.02	1.15
26	0.178	1.35	1.36	1.01	1.01	1.00	0.99
27	0.329	1.55	1.48	1.03	1.02	1.01	1.05
28	0.206	1.58	1.45	1.03	1.02	1.01	1.09
29	0.155	1.16	1.11	1.00	1.00	1.00	1.05
30	0.258	1.71	1.50	1.04	1.02	1.02	1.14
31	0.264	1.44	1.47	1.02	1.02	1.00	0.98
32	0.244	1.56	1.48	1.03	1.02	1.01	1.06
33	0.363	2.01	1.75	1.07	1.05	1.02	1.15
34	0.274	1.55	1.40	1.03	1.02	1.01	1.10
35	0.290	1.20	1.20	1.00	1.01	1.00	1.00
36	0.135	1.14	1.21	1.00	1.01	1.00	0.94
37	0.463	1.73	1.55	1.04	1.03	1.01	1.11
38	0.198	1.22	1.23	1.01	1.01	1.00	1.00

	39	0.492	1.39	1.38	1.02	1.01	1.00	1.01
	40	0.222	1.32	1.40	1.01	1.02	0.99	0.94
Chip 1	1	0.770	2.29	2.14	1.10	1.08	1.02	1.07
	2	0.824	1.51	1.53	1.02	1.03	1.00	0.98
Chip 3-1	1	0.625	2.12	1.97	1.08	1.06	1.01	1.07
	2	0.668	2.18	2.01	1.10	1.08	1.02	1.09
	3	0.734	1.65	1.56	1.03	1.03	1.01	1.06
	4	0.544	1.62	1.57	1.04	1.04	1.00	1.04
	5	0.462	1.26	1.17	1.01	1.00	1.00	1.08
Chip 3-3	1	0.942	1.57	1.42	1.03	1.02	1.01	1.10
	2	0.810	1.50	1.49	1.02	1.02	1.00	1.01
	3	0.535	1.20	1.25	1.00	1.01	1.00	0.96
	4	0.580	1.44	1.42	1.02	1.02	1.00	1.01
	5	0.517	1.49	1.45	1.02	1.02	1.00	1.03
	6	0.609	1.53	1.52	1.02	1.02	1.00	1.00
Chip 3-5	1	1.037	1.56	1.53	1.03	1.02	1.00	1.02
	2	0.600	1.49	1.37	1.03	1.01	1.01	1.09
	3	0.700	1.79	1.77	1.05	1.05	1.00	1.01
	4	0.584	1.42	1.35	1.02	1.01	1.00	1.05
Chip 3-6	1	0.702	1.19	1.25	1.00	1.01	1.00	0.95
	2	0.569	1.19	1.23	1.01	1.01	1.00	0.97
	3	0.452	1.19	1.19	1.00	1.00	1.00	1.00

4	0.669	1.89	1.74	1.07	1.05	1.02	1.08
Minimum	0.135	1.12	1.11	1.00	1.00	0.99	0.91
Maximum	1.037	2.29	2.14	1.10	1.08	1.03	1.20
Mean (*n*=61)	0.408	1.53	1.46	1.03	1.02	1.01	1.05

[a] Of best-fit ellipsoid to whole chondrule

References

Alexander C. M. O. D., Howard K. T., Bowden R., and Fogel M. L. (2013) The classification of CM and CR chondrites using bulk H, C and N abundances and isotopic compositions. *Geochimica et Cosmochimica Acta* **123**, 244-260.

Almeida N. V., Smith C. L., Sykes D., Downes H., Ahmed F., and Russell S. S. (2015) Quantifying the deformation of Leoville chondrules in 3D: Implications for the post-accretional history of the CV3 parent body. In *78th Annual Meeting of the Meteoritical Society*, pp. 5112, Berkeley, CA.

Als-Nielson J. and McMorrow D. (2011) *Elements of Modern X-ray Physics*. John Wiley & Sons Ltd, Singapore.

Alves H., Lima I., and Lopes R. T. (2014) Methodology for attainment of density and effective atomic number through dual energy technique using microtomographic images. *Applied Radiation and Isotopes* **89**, 6-12.

Alwmark C., Schmitz B., Holm S., Marone F., and Stampanoni M. (2011) A 3-D study of mineral inclusions in chromite from ordinary chondrites using synchrotron radiation X-ray tomographic microscopy—Method and applications. *Meteoritics & Planetary Science* **46**(8), 1071-1081.

Armstrong R. T., Georgiadis A., Ott H., Klemin D., and Berg S. (2014) Critical capillary number: Desaturation studied with fast X-ray computed microtomography. *Geophysical Research Letters* **41**(1), 2013GL058075.

Arnold J. R., Testa J. P., Friedman P. J., and Kambic G. X. (1983) Computed tomographic analysis of meteorite inclusions. *Science* **219**(4583), 383-384.

ASTM E1441-11 (2011) Standard Guide for Computed Tomography (CT) Imaging. ASTM International, West Conshohocken, PA.

Baldwin B. and Sheaffer Y. (1971) Ablation and breakup of large meteoroids during atmospheric entry. *Journal of Geophysical Research* **76**(19), 4653–4668.

Batenburg K. J. and Sijbers J. (2011) DART: A practical reconstruction algorithm for discrete tomography. *IEEE Transactions on Image Processing* **20**(9), 2542-2553.

Bechtel H. A., Flynn G. J., Allen C., Anderson D., Ansari A., Bajt S., Bastien R. K., Bassim N., Borg J., Brenker F. E., Bridges J., Brownlee D. E., Burchell M., Burghammer M., Butterworth A. L., Changela H., Cloetens P., Davis A. M., Doll R., Floss C., Frank D. R., Gainsforth Z., Grün E., Heck P. R., Hillier J. K., Hoppe P., Hudson B., Huth J., Hvide B., Kearsley A., King A. J., Lai B., Leitner J., Lemelle L., Leroux H., Leonard A., Lettieri R., Marchant W., Nittler L. R., Ogliore R., Ong W. J., Postberg F., Price M. C., Sandford S. A., Tresseras J.-A. S., Schmitz S., Schoonjans T., Silversmit G., Simionovici A. S., Solé V. A., Srama R., Stadermann F. J., Stephan T., Sterken V. J., Stodolna J., Stroud R. M., Sutton S., Trieloff M., Tsou P., Tsuchiyama A., Tyliszczak T., Vekemans B., Vincze L., Von Korff J., Westphal A. J., Wordsworth N., Zevin D., Zolensky M. E., and >30000 Stardust@home dusters (2014a) Stardust Interstellar Preliminary Examination III: Infrared spectroscopic analysis of interstellar dust candidates. *Meteoritics & Planetary Science* **49**(9), 1548-1561.

Bechtel H. A., Flynn G. J., Allen C., Anderson D., Ansari A., Bajt S., Bastien R. K., Bassim N., Borg J., Brenker F. E., Bridges J., Brownlee D. E., Burchell M., Burghammer M., Butterworth A. L., Changela H., Cloetens P., Davis A. M., Doll R., Floss C., Frank D. R., Gainsforth Z., Grün E., Heck P. R., Hillier J. K., Hoppe P., Hudson B., Huth J., Hvide B., Kearsley A., King A. J., Lai B., Leitner J., Lemelle L., Leroux H., Leonard A., Lettieri R., Marchant W., Nittler L. R., Ogliore R., Ong W. J., Postberg F., Price M. C., Sandford S. A., Tresseras J.-A. S., Schmitz S., Schoonjans T., Silversmit G., Simionovici A. S., Solé V. A., Srama R., Stadermann F. J., Stephan T., Sterken V. J., Stodolna J., Stroud R. M., Sutton S., Trieloff M., Tsou P., Tsuchiyama A., Tyliszczak T., Vekemans B., Vincze L., Von Korff J., Westphal A. J., Wordsworth N., Zevin D., Zolensky M. E., and dusters S. h. (2014b) Stardust Interstellar Preliminary Examination III: Infrared spectroscopic analysis of interstellar dust candidates. *Meteoritics & Planetary Science* **49**(9), 1548-1561.

Beister M., Kolditz D., and Kalender W. A. (2012) Iterative reconstruction methods in X-ray CT. *Physica Medica* **28**(2), 94-108.

Beitz E., Blum J., Mathieu R., Pack A., and Hezel D. C. (2013a) Experimental investigation of the nebular formation of chondrule rims and the formation of chondite parent bodies. *Geochimica et Cosmochimica Acta* **116**, 41-51.

Beitz E., Güttler C., Nakamura A. M., Tsuchiyama A., and Blum J. (2013b) Experiments on the consolidation of chondrites and the formation of dense rims around chondrules. *Icarus* **225**(1), 558-569.

Benedix G. K., Ketcham R. A., Wilson L., McCoy T. J., Bogard D. D., Garrison D. H., Herzog G. F., Xue S., Klein J., and Middleton R. (2008) The formation and

chronology of the PAT 91501 impact-melt L chondrite with vesicle-metal-sulfide assemblages. *Geochimica et Cosmochimica Acta* **72**(9), 2417-2428.

Berger M. J., Hubbell J. H., Seltzer S. M., Chang J., Coursey J. S., Sukumar R., Zucker D. S., and Olsen K. (2010) XCOM: Photon Cross Section Database (version 1.5). National Institute of Standards and Technology, [Online] http://physics.nist.gov/xcomw.

Bertrand L., Schöeder S., Anglos D., Breese M. B. H., Janssens K., Moini M., and Simon A. (2015) Mitigation strategies for radiation damage in the analysis of ancient materials. *TrAC Trends in Analytical Chemistry* **66**, 128-145.

Bischoff A., Scott E. R. D., Metzler K., and Goodrich C. A. (2006) Nature and Origins of Meteoritic Breccias. In *Meteorites and the Early Solar System II* (eds. D. Lauretta and H. Y. J. McSween), pp. 679-712. University of Arizona Press, Tucson.

Biscoff A., Scott E. R. D., Metzler K., and Goodrich C. A. (2006) Nature and Origins of Meteoritic Breccias. In *Meteorites and the Early Solar System II* (eds. D. Lauretta and H. Y. J. McSween), pp. 679-712. University of Arizona Press, Tucson.

Bland P. A., Collins G. S., Davison T. M., Abreu N. M., Ciesla F. J., Muxworthy A. R., and Moore J. (2014) Pressure-temperature evolution of primordial solar system solids during impact-induced compaction. *Nature Communications* **5**, 5451.

Bland P. A., Jackson M. D., Coker R. F., Cohen B. A., Webber J. B. W., Lee M. R., Duffy C. M., Chater R. J., Ardakani M. G., McPhail D. S., McComb D. W., and Benedix G. K. (2009) Why aqueous alteration in asteroids was isochemical: High porosity /= high permeability. *Earth and Planetary Science Letters* **287**, 559-568.

Bleuet P., Gergaud P., Lemelle L., Bleuet P., Tucoulou R., Cloetens P., Susini J., Delette G., and Simionovici A. (2010) 3D chemical imaging based on a third-generation synchrotron source. *TrAC Trends in Analytical Chemistry* **29**(6), 518-527.

Blott S. J. and Pye K. (2008) Particle shape: a review and new methods of characterization and classification. *Sedimentology* **55**(1), 31-63.

Blum J. and Schräpler R. (2004) Structure and Mechanical Properties of High-Porosity Macroscopic Agglomerates Formed by Random Ballistic Deposition. *Physical Review Letters* **93**(11), 115503.

Blum J., Schräpler R., Davidsson B. J., and Trigo-Rodríguez J. M. (2006) The physics of protoplanetesimal dust agglomerates. I. Mechanical properties and relations to primitive bodies in the solar system. *The Astrophysical Journal* **652**(2), 1768.

Blumenfeld E. J., Evans C. A., Oshel E. R., Liddle D. A., Beaulieu K., Zeigler R., Hanna R. D., and Ketcham R. A. (2015) Comprehensive non-destructive conservation documentation of lunar samples using high-resolution 3D reconstructions and X-ray CT data. In *Lunar and Planetary Science Conference XLVI*, pp. 2740, Houston, TX.

Boone M. N., Garrevoet J., Tack P., Scharf O., Cormode D. P., Van Loo D., Pauwels E., Dierick M., Vincze L., and Van Hoorebeke L. (2014) High spectral and spatial resolution X-ray transmission radiography and tomography using a Color X-ray Camera. *Nuclear Instruments and Methods in Physics Research Section A: Accelerators, Spectrometers, Detectors and Associated Equipment* **735**, 644-648.

Branney M. J. and Brown R. J. (2011) Impactoclastic Density Current Emplacement of Terrestrial Meteorite-Impact Ejecta and the Formation of Dust Pellets and Accretionary Lapilli: Evidence from Stac Fada, Scotland. *The Journal of Geology* **119**(3), 275-292.

Brearley A. and Geiger T. (1993) Fine-grained chondrule rims in the Murchison CM2 chondrite: Compositional and mineralogical systematics. *Meteoritics* **28**, 328-329.

Brearley A. J. (2006) The Action of Water. In *Meteorites and the Early Solar System II* (eds. D. Lauretta and H. Y. J. McSween), pp. 584-624. University of Arizona Press, Tucson.

Brearley A. J. and Geiger T. (1991) Mineralogical and chemical studies bearing on the origin of accretionary rims in the Murchison CM2 carbonaceous chondrite. *Meteoritics* **26**, 33.

Brearley A. J., Hanowski N. P., and Whalen J. F. (1999) Fine-grained rims in CM carbonaceous chondrites: A comparison of rims in Murchison and ALH 81002. In *Lunar and Planetary Science Conference*, pp. 1460.

Brewer L. N., Field D. P., and Merriman C. C. (2009) Mapping and Assessing Plastic Deformation using EBSD. In *Electron Backscatter Diffraction in Materials Science* (eds. A. J. Schwartz, M. Kumar, B. L. Adams, and D. P. Field), pp. 251-262. Springer Science+Business Media, LLC, New York.

Britt D. T. and Consolmagno G. (2000) The Porosity of Dark Meteorites and the Structure of Low-Albedo Asteroids. *Icarus* **146**(1), 213-219.

Britt D. T., Yeomans D., Housen K., and Consolmagno G. (2002) Asteroid Density, Porosity, and Structure. In *Asteroids III* (eds. W. F. J. Bottke, A. Cellino, P. Paolicchi, and R. P. Binzel), pp. 785. The University of Arizona Press, Tucson.

Broennimann C., Eikenberry E. F., Henrich B., Horisberger R., Huelsen G., Pohl E., Schmitt B., Schulze-Briese C., Suzuki M., Tomizaki T., Toyokawa H., and Wagner A. (2006) The PILATUS 1M detector. *Journal of Synchrotron Radiation* **13**(2), 120-130.

Brownlow L., Mayo S., Miller P. R., and Sheffield-Parker J. (2006) Towards 50-nanometre resolution with an SEM-hosted X-ray microscope. *Microscopy and Analysis* **20**(2), 13-15.

Bunch T. and Chang S. (1984) CAI rims and CM2 dustballs: Products of gas-grain interactions, mass transport, grain aggregation and accretion in the nebula? In *Lunar and Planetary Science Conference*, pp. 100-101.

Bunch T. E. and Chang S. (1980) Carbonaceous chondrites. II - Carbonaceous chondrite phyllosilicates and light element geochemistry as indicators of parent body processes and surface conditions. *Geochimica et Cosmochimica Acta* **44**, 1543-1577.

Buseck P. R., Nord G. L., and Veblen D. R. (1980) Subsolidus phenomena in pyroxenes. In *Reviews in Mineralogy 7: Pyroxenes* (ed. C. T. Prewitt), pp. 117-221. Mineralogical Society of America, Washington D.C.

Buzug T. M. (2008) *Computed Tomography: From Photon Statistics to Modern Cone-Beam CT*. Springer-Verlag, Berlin Heidelberg. pp. 531.

Byrne P. K., Klimczak C., Celal Sengor A. M., Solomon S. C., Watters T. R., and Hauck I. I. S. A. (2014) Mercury's global contraction much greater than earlier estimates. *Nature Geosci* **7**(4), 301-307.

Cain P. M., McSween H. Y., and Woodward N. B. (1986) Structural deformation of the Leoville chondrite. *Earth and Planetary Science Letters* **77**, 165-175.

Carracedo Sánchez M., Sarrionandia F., Arostegui J., and Gil Ibarguchi J. I. (2015) Silicate glass micro and nanospherules generated in explosive eruptions of ultrabasic magmas: Implications for the origin of pelletal lapilli. *Journal of Volcanology and Geothermal Research* **293**, 13-24.

Chapman C. R. (1999) Asteroids. In *The New Solar System* (eds. J. K. Beatty, C. C. Peterson, and A. Chaikin), pp. 337-350. Sky Publishing Corporation, Cambridge.

Chen G.-H., Tang J., and Leng S. (2008) Prior image constrained compressed sensing (PICCS): A method to accurately reconstruct dynamic CT images from highly undersampled projection data sets. *Medical physics* **35**(2), 660-663.

Clark B. E., Binzel R. P., Howell E. S., Cloutis E. A., Ockert-Bell M., Christensen P., Barucci M. A., DeMeo F., Lauretta D. S., Connolly H., Soderberg A., Hergenrother C., Lim L., Emery J., and Mueller M. (2011) Asteroid (101955) 1999 RQ36: Spectroscopy from 0.4 to 2.4 *u*m and meteorite analogs. *Icarus* **216**, 462-475.

Cloetens P., Ludwig W., Boller E., Peyrin F., Chlenker M., and Baruchel J. (2002) 3D Imaging using coherent synchrotron radiation. *Image Analysis & Stereology* **21**(4), S75-S85.

Cnudde V. and Boone M. N. (2013) High-resolution X-ray computed tomography in geosciences: A review of the current technology and applications. *Earth-Science Reviews* **123**, 1-17.

Coe R. S. and Kirby S. H. (1975) The orthoenstatite to clinoenstatite transformation by shearing and reversion by annealing: mechanism and potential applications. *Contributions to Mineralogy and Petrology* **52**, 29-55.

Connolly H. C., Huss G. R., and Wasserburg G. J. (2001) On the formation of Fe-Ni metal in Renazzo-like carbonaceous chondrites. *Geochimica et Cosmochimica Acta* **65**(24), 4567-4588.

Consolmagno G., Britt D., and Macke R. (2008) The significance of meteorite density and porosity. *Chemie der Erde / Geochemistry* **68**, 1-29.

Cuzzi J. N. (2004) Blowing in the wind: III. Accretion of dust rims by chondrule-sized particles in a turbulent protoplanetary nebula. *Icarus* **168**(2), 484-497.

Cuzzi J. N., Dobrovolskis A. R., and Hogan R. C. (1996) Turbulence, chondrules, and planetesimals. In *Chondrules and the protoplanetary disk* (eds. R. H. Hewins, R. H. Jones, and E. R. D. Scott), pp. 35-43. Cambridge University Press, Cambridge.

Cuzzi J. N. and Hogan R. C. (2003) Blowing in the wind: I. Velocities of chondrule-sized particles in a turbulent protoplanetary nebula. *Icarus* **164**(1), 127-138.

Cuzzi J. N., Hogan R. C., Paque J. M., and Dobrovolskis A. R. (2001) Size-selective concentration of chondrules and other small particles in protoplanetary nebula turbulence. *The Astrophysical Journal* **546**, 496-508.

Cuzzi J. N., Hogan R. C., and Shariff K. (2008) Toward Planetesimals: Dense Chondrule Clumps in the Protoplanetary Nebula. *The Astrophysical Journal* **687**(2), 1432.

Cuzzi J. N. and Weidenschilling S. J. (2006) Particle-gas dynamics and primary accretion. In *Meteorites and the Early Solar System II* (eds. D. Lauretta and H. Y. J. McSween), pp. 353-381. University of Arizona Press, Tuscon.

Davison T. M., Ciesla F. J., and Collins G. S. (2012) Post-impact thermal evolution of porous planetesimals. *Geochimica et Cosmochimica Acta* **95**, 252-269.

De Man B., Nuyts J., Dupont P., Marchal G., and Suetens P. (1999) Metal streak artifacts in X-ray computed tomography: a simulation study. *Nuclear Science, IEEE Transactions on* **46**(3), 691-696.

De Witte Y., Vlassenbroeck J., and Van Hoorebeke L. (2010) A multiresolution approach to iterative reconstruction algorithms in X-ray computed tomography. *Image Processing, IEEE Transactions on* **19**(9), 2419-2427.

DeCarli P. S., Bowden E., and Seaman L. (2001) Shock-induced compaction and porosity in meteorites. In *64th Annual Meteoritical Society Meeting*, pp. 5171, Vatican City.

Dellino P., Mele D., Bonasia R., Braia G., La Volpe L., and Sulpizio R. (2005) The analysis of the influence of pumice shape on its terminal velocity. *Geophysical Research Letters* **32**(21), L21306.

Deng H., Fitts J. P., and Peters C. A. (2016) Quantifying fracture geometry with X-ray tomography: Technique of Iterative Local Thresholding (TILT) for 3D image segmentation. *Computational Geosciences* **20**(1), 231-244.

Dodd R. T., Jr. (1965) Preferred orientation of chondrules in chondrites. *Icarus* **4**, 308-316.

Dullemond C. P., Harsono D., Stammler S. M., and Johansson A. (2016) Forming chondrules in impact splashes - II Volatile retention. *Astrophysical Journal* **in press**.

Eastwood D. S., Bradley R. S., Tariq F., Cooper S. J., Taiwo O. O., Gelb J., Merkle A., Brett D. J. L., Brandon N. P., Withers P. J., Lee P. D., and Shearing P. R. (2014) The application of phase contrast X-ray techniques for imaging Li-ion battery electrodes. *Nuclear Instruments and Methods in Physics Research Section B: Beam Interactions with Materials and Atoms* **324**, 118-123.

Ebel D. S., Greenberg M., Rivers M. L., and Newville M. (2009) Three-dimensional textural and compositional analysis of particle tracks and fragmentation history in aerogel. *Meteoritics & Planetary Science* **44**(10), 1445-1463.

Ebel D. S. and Rivers M. L. (2007) Meteorite 3-D synchrotron microtomography: Methods and applications. *Meteoritics and Planetary Science* **42**(9), 1627-1646.

Ebel D. S., Weisberg M. K., Hertz J., and Campbell A. J. (2008) Shape, metal abundance, chemistry, and origin of chondrules in the Renazzo (CR) chondrite. *Meteoritics & Planetary Science* **43**(10), 1725-1740.

Ebihara M., Shirai N., Sekimoto S., Nakamura T., Tsuchiyama A., Matsuno J., Matsumoto T., Tanaka M., Abe M., Fujimura A., Ishibashi Y., Karouji Y., Mukai T., Okada T., Uesugi M., and Yada T. (2015) Chemical and mineralogical compositions of two grains recovered from asteroid Itokawa. *Meteoritics & Planetary Science* **50**(2), 243-254.

Edey D. R., McCausland P. J. A., Holdsworth D. W., and Flemming R. L. (2013) Extended dynamic range micro-computed tomography of meteorites using a biomedical scanner. In *Lunar and Planetary Science Conference XLIV*, pp. 2693, The Woodlands, TX.

Egan C. K., Jacques S. D. M., Wilson M. D., Veale M. C., Seller P., Beale A. M., Pattrick R. A. D., Withers P. J., and Cernik R. J. (2015) 3D chemical imaging in the laboratory by hyperspectral X-ray computed tomography. *Scientific Reports* **5**, 15979.

Eggl E., Schleede S., Bech M., Achterhold K., Loewen R., Ruth R. D., and Pfeiffer F. (2015) X-ray phase-contrast tomography with a compact laser-driven synchrotron source. *Proceedings of the National Academy of Sciences* **112**(18), 5567-5572.

Elangovan P., Hezel D. C., Howard L., Armstrong R., and Abel R. L. (2012) PhaseQuant: A tool for quantifying tomographic data sets of geological specimens. *Computers & Geosciences* **48**, 323-329.

Elkins-Tanton L. T. (2015) Personal Communication.

Elkins-Tanton L. T., Weiss B. P., and Zuber M. T. (2011) Chondrites as samples of differentiated planetesimals. *Earth and Planetary Science Letters* **305**(1-2), 1-10.

Espes E., Andersson T., Björnsson F., Gratorp C., Hansson B. A. M., Hemberg O., Johansson G., Kronstedt J., Otendal M., Tuohimaa T., and Takman P. (2014) Liquid-metal-jet x-ray tube technology and tomography applications. In *Proc. SPIE 9212, Developments in X-ray Tomography IX*, pp. 92120J, San Diego, CA.

Etheridge M. A. and Oertel G. (1979) Strain measurements from phyllosilicate preferred orientation - A precautionary note. *Tectonophysics* **60**, 170-120.

Fang X. and Klaus M. (2007) Real-time 3D computed tomographic reconstruction using commodity graphics hardware. *Physics in Medicine and Biology* **52**(12), 3405.

Feser M., Holzner C., and Lauridsen E. M. (2015) Laboratory x-ray micro-tomography system with crystallographic grain orientation mapping capabilities. Google Patents.

Flynn G. J., Rivers M. L., Sutton S. R., Eng P., and Klock W. (2000) X-ray computed microtomography (CMT): A non-invasive screening tool for characterization of returned rock cores from mars and other solar system bodies. In *Lunar and Planetary Science XXXI*, pp. 1893, Houston, TX.

Folco L. and Mellini M. (2000) Enstatite chemical composition and microstructures in the La Villa H4 chondrite. *Meteoritics and Planetary Science* **35**, 733-742.

Friedrich J. M. (2008) Quantitative methods for three-dimensional comparison and petrographic description of chondrites. *Computers & Geosciences* **34**(12), 1926-1935.

Friedrich J. M., Glavin D. P., Rivers M. L., and Dworkin J. P. (2016) Effect of a synchrotron X-ray microtomography imaging experiment on the amino acid content of a CM chondrite. *Meteoritics and Planetary Science* **51**(2), 429-437.

Friedrich J. M., Macke R. J., Wignarajah D. P., Rivers M. L., Britt D. T., and Ebel D. S. (2008a) Pore size distribution in an uncompacted equilibrated ordinary chondrite. *Planetary and Space Science* **56**, 895-900.

Friedrich J. M. and Rivers M. L. (2013) Three-dimensional imaging of ordinary chondrite microporosity at 2.6 μ m resolution. *Geochimica et Cosmochimica Acta* **116**, 63-70.

Friedrich J. M., Rubin A. E., Beard S. P., Swindle T. D., Isachsen C. E., Rivers M. L., and Macke R. J. (2014a) Ancient porosity preserved in ordinary chondrites: Examining shock and compaction on young asteroids. *Meteoritics & Planetary Science* **49**(7), 1214-1231.

Friedrich J. M., Ruzicka A., Rivers M. L., Ebel D. S., Thostenson J. O., and Rudolph R. A. (2013) Metal veins in the Kernouve (H6 S1) chondrite: Evidence for pre- or syn-metamorphic shear deformation. *Geochimica et Cosmochimica Acta* **116**, 71-83.

Friedrich J. M., Weisberg M. K., and Rivers M. L. (2014b) Multiple impact events recorded in the NWA 7298 H chondrite breccia and the dynamical evolution of an ordinary chondrite asteroid. *Earth and Planetary Science Letters* **394**(0), 13-19.

Friedrich J. M., Wignarajah D. P., Chaudhary S., Rivers M. L., Nehru C. E., and Ebel D. S. (2008b) Three-dimensional petrography of metal phases in equilibrated L chondrites-Effects of shock loading and dynamic compaction. *Earth and Planetary Science Letters* **275**(1,Äì2), 172-180.

Fuchs L. H., Olsen E., and Jensen K. J. (1973) Mineralogy, mineral-chemistry, and composition of the Murchison (C2) meteorite. *Smithsonian Contributions to Earth Sciences* **10**, 39.

Fujimura A., Kato M., and Kumazawa M. (1983) Preferred orientation of phyllosilicate (001) in matrix of Murchison meteorite and possible mechanisms of generating the oriented texture in chondrites. *Earth and Planetary Science Letters* **66**, 25-32.

Fusseis F., Xiao X., Schrank C., and De Carlo F. (2014) A brief guide to synchrotron radiation-based microtomography in (structural) geology and rock mechanics. *Journal of Structural Geology* **65**, 1-16.

Gattacceca J., Rochette P., Denise M., Consolmagno G., and Folco L. (2005) An impact origin for the foliation of chondrites [rapid communication]. *Earth and Planetary Science Letters* **234**, 351-368.

Gattacceca J., Suavet C., Rochette P., Weiss B. P., Winklhofer M., Uehara M., and Friedrich J. M. (2014) Metal phases in ordinary chondrites: Magnetic hysteresis properties and implications for thermal history. *Meteoritics & Planetary Science* **49**(4), 652-676.

Gnos E., Hofmann B., Franchi I. A., Al-Kathiri A., Huser M., and Moser L. (2002) Sayh al Uhaymir 094: A new martian meteorite from the Oman desert. *Meteoritics & Planetary Science* **37**(6), 835-854.

Graham D. J. and Midgley N. G. (2000) Graphical representation of particle shape using triangular diagrams: an Excel spreadsheet method. *Earth Surface Processes and Landforms* **25**(13), 1473-1477.

Grant J. A., Davis J. R., Wells P., and Morgan M. J. (1994) X-ray diffraction tomography at the Australian National Beamline Facility. *Optical Engineering* **33**(8), 2803-2807.

Graup G. (1981) Terrestrial chondrules, glass spherules and accretionary lapilli from the suevite, Ries Crater, Germany. *Earth and Planetary Science Letters* **55**(3), 407-418.

Greshake A., Krot A. N., Flynn G. J., and Keil K. (2005) Fine-grained dust rims in the Tagish Lake carbonaceous chondrite: Evidence for parent body alteration. *Meteoritics & Planetary Science* **40**(9-10), 1413-1431.

Griffin L. D., Elangovan P., Mundell A., and Hezel D. C. (2012) Improved segmentation of meteorite micro-CT images using local histograms. *Computers & Geosciences* **39**, 129-134.

Hanna R. D. and Ketcham R. A. (2015) 3D Measurement of fine-grained rims in CM Murchison using XCT. In *Met. Soc. Meeting LXXVIII*, pp. 5350, Berkeley, California.

Hanna R. D. and Ketcham R. A. (in review) X-ray computed tomography of planetary materials: A primer and review of recent studies. *Chemie der Erde - Geochemistry*.

Hanna R. D., Ketcham R. A., and Hamilton V. E. (2012) Inclusion foliation in Murchison as revealed by high resolution X-ray CT. In *Lunar Planet. Sci. XLIII*, pp. 1242, Lunar Planet. Inst., Houston.

Hanna R. D., Ketcham R. A., Zolensky M., and Behr W. (2015) Impact-induced brittle deformation, porosity loss, and aqueous alteration in the Murchison CM chondrite. *Geochimica et Cosmochimica Acta* **171**, 256-282.

Hanowski N. P. and Brearley A. J. (2001) Aqueous alteration of chondrules in the CM carbonaceous chondrite, Allan Hills 81002: implications for parent body alteration. *Geochimica et Cosmochimica Acta* **65**, 495-518.

Hansen C. D. and Johnson C. R. (2005) *The Visualization Handbook*. Academic Press, Burlington, MA.

Hemberg O., Otendal M., and Hertz H. M. (2003) Liquid-metal-jet anode electron-impact x-ray source. *Applied Physics Letters* **83**(7), 1483-1485.

Herbig M., King A., Reischig P., Proudhon H., Lauridsen E. M., Marrow J., Buffière J.-Y., and Ludwig W. (2011) 3-D growth of a short fatigue crack within a polycrystalline microstructure studied using combined diffraction and phase-contrast X-ray tomography. *Acta Materialia* **59**(2), 590-601.

Herman G. T. (1979) Correction for beam hardening in computed tomography. *Physics in Medicine and Biology* **24**(1), 81-106.

Hertz J., Ebel D. S., and Weisberg M. K. (2003) Tomographic study of shapes and metal abundances of Renazzo chondrules. In *Lunar and Planetary Science Conference XXXIV*, pp. 1959, Houston, TX.

Hezel D. C., Elangovan P., Viehmann S., Howard L., Abel R. L., and Armstrong R. (2013a) Visualisation and quantification of CV chondrite petrography using micro-tomography. *Geochimica et Cosmochimica Acta* **116**, 33-40.

Hezel D. C., Friedrich J. M., and Uesugi M. (2013b) Looking inside: 3D structures of meteorites. *Geochimica et Cosmochimica Acta* **116**(0), 1-4.

Hildebrand A. R., McCausland P. J. A., Brown P. G., Longstaffe F. J., Russell S. D. J., Tagliaferri E., Wacker J. F., and Mazur M. J. (2006) The fall and recovery of the Tagish Lake meteorite. *Meteoritics and Planetary Science* **41**, 407-431.

Hippertt J. F. M. (1993) 'V'-pull-apart microstructures: a new shear-sense indicator. *Journal of Structural Geology* **15**(12), 1393-1403.

Hirano T., Minoru F., Nagata T., Taguchi I., Hamada H., Usami K., and Hayakawa K. (1990) Observation of Allende and Antarctic meteorites by monochromatic X-ray CT based on synchrotron radiation. In *Fourteenth Symposium on Antarctic Meteorites* (ed. K. Yanai), pp. 270-281, Tokyo.

Horz F. and Quaide W. L. (1973) Debye-Scherrer investigations of experimentally shocked silicates. *The Moon* **6**, 45-82.

Hounsfield G. N. (1973) Computerized transverse axial scanning (tomography). *British Journal of Radiology* **46**, 1016-1022.

Hounsfield G. N. (1976) Apparatus for examining a body by radiation such as X or gamma radiation. British Patent No 1.283.915, London.

Hsieh J. (2009) *Computed Tomography: Principles, Design, Artifacts, and Recent Advances*. SPIE John Wiley & Sons Inc., Bellingham, Washington
Hooken, New Jersey. pp. 556.

Hua X., Wang J., and Buseck P. R. (2002) Fine-grained rims in the Allan Hills 81002 and Lewis Cliff 90500 CM2 meteorites: Their origin and modification. *Meteoritics & Planetary Science* **37**(2), 229-244.

Humphreys F. J. (2001) Grain and subgrain characterisation by electron backscatter diffraction. *Journal of Materials Science* **36**(16), 3833-3854.

Huss G. R., Rubin A. E., and Grossman J. N. (2006) Shock Effects in Meteorites. In *Meteorites and the Early Solar System II* (eds. D. S. Lauretta and H. Y. McSween Jr), pp. 567-586. University of Arizona Press, Tuscon.

Ikeda S., Nakano T., Tsuchiyama A., Uesugi K., Suzuki Y., Nakamura K., Nakashima Y., and Yoshida H. (2004) Nondestructive three-dimensional element-concentration mapping of a Cs-doped partially molten granite by X-ray computed tomography using synchrotron radiation. *American Mineralogist* **89**(8-9), 1304-1313.

Jaffray D. A., Siewerdsen J. H., and Drake D. G. (1999) Performance of a volumetric CT scanner based upon a flat-panel imager. In *Proc. SPIE 3659, Medical Imaging 1999: Physics of Medical Imaging*, pp. 204-214, San Diego, CA.

Jenniskens P., Rubin A. E., Yin Q.-Z., Sears D. W. G., Sandford S. A., Zolensky M. E., Krot A. N., Blair L., Kane D., Utas J., Verish R., Friedrich J. M., Wimpenny J., Eppich G. R., Ziegler K., Verosub K. L., Rowland D. J., Albers J., Gural P. S., Grigsby B., Fries M. D., Matson R., Johnston M., Silber E., Brown P., Yamakawa A., Sanborn M. E., Laubenstein M., Welten K. C., Nishiizumi K., Meier M. M. M., Busemann H., Clay P., Caffee M. W., Schmitt-Kopplin P., Hertkorn N., Glavin D. P., Callahan M. P., Dworkin J. P., Wu Q., Zare R. N., Grady M., Verchovsky S., Emel'Yanenko V., Naroenkov S., Clark D. L., Girten B., and Worden P. S. (2014) Fall, recovery, and characterization of the Novato L6 chondrite breccia. *Meteoritics & Planetary Science* **49**(8), 1388-1425.

Jerram D. A. and Higgins M. D. (2007) 3D analysis of rock textures: Quantifying igneous microstructures. *Elements* **3**(4), 239-245.

Johnson B. C. and Melosh H. J. (2014) Formation of melt droplets, melt fragments, and accretionary impact lapilli during a hypervelocity impact. *Icarus* **228**, 347-363.

Johnson B. C., Minton D. A., Melosh H. J., and Zuber M. T. (2015) Impact jetting as the origin of chondrules. *Nature* **517**(7534), 339-341.

Johnson G., King A., Honnicke M. G., Marrow J., and Ludwig W. (2008) X-ray diffraction contrast tomography: A novel technique for three-dimensional grain mapping of polycrystals. II. The combined case. *Journal of Applied Crystallography* **41**(2), 310-318.

Ketcham R. A. (2005a) Computational methods for quantitative analysis of three-dimensional features in geological specimens. *Geosphere* **1**(1), 32-41.

Ketcham R. A. (2005b) Three-dimensional grain fabric measurements using high-resolution X-ray computed tomography. *Journal of Structural Geology* **27**(7), 1217-1228.

Ketcham R. A. (2006a) Accurate Three-dimensional Measurements of Features in Geological Materials from X-ray Computed Tomography Data. In *Advances in X-ray Tomography for Geomaterials* (eds. J. Desrues, G. Viggiani, and P. Bésuelle), pp. 143-148. ISTE, London.

Ketcham R. A. (2006b) New algorithms for ring artifact removal. In *Proc. SPIE 6318, Developments in X-Ray Tomography V* (ed. U. Bonse), San Diego, CA.

Ketcham R. A. and Carlson W. D. (2001) Acquisition, optimization and interpretation of X-ray computed tomographic imagery; Applications to the geosciences. *Comp. & Geosci.* **27**(4), 381-400.

Ketcham R. A. and Hanna R. D. (2014) Beam hardening correction for X-ray computed tomography of heterogeneous natural materials. *Computers & Geosciences* **67**, 49-61.

Ketcham R. A. and Hildebrandt J. (2014) Characterizing, measuring, and utilizing the resolution of CT imagery for improved quantification of fine-scale features. *Nuclear Instruments and Methods in Physics Research Section B: Beam Interactions with Materials and Atoms* **324**, 80-87.

Ketcham R. A. and Koeberl C. (2013) New textural evidence on the origin of carbonado diamond: An example of 3-D petrography using X-ray computed tomography. *Geosphere* **9**(5), 1336-1347.

Ketcham R. A. and Ryan T. M. (2004) Quantification and visualization of anisotropy in trabecular bone. *Journal of Microscopy* **213**(2), 158-171.

King A., Reischig P., Adrien J., and Ludwig W. (2013) First laboratory X-ray diffraction contrast tomography for grain mapping of polycrystals. *Journal of Applied Crystallography* **46**(6), 1734-1740.

King A., Reischig P., Adrien J., Peetermans S., and Ludwig W. (2014) Polychromatic diffraction contrast tomography. *Materials Characterization* **97**, 1-10.

King T. V. V. and King E. A. (1981) Accretionary dark rims in unequilibrated chondrites. *Icarus* **48**(3), 460-472.

Kinnunen K. A. and Saikkonen R. (1983) Kivesvaara C2 chondrite: Silicate petrography and chemical composition. *Bulletin of the Geological Survey of Finland* **55**, 35-49.

Kondo M., Tsuchiyama A., Hirai H., and Koishikawa A. (1997) High resolution X-ray computed tomographic (CT) images of chondrites and a chondrule. *Antarctic Meteorite Research* **10**, 437-447.

Krot A. N., Hutcheon I. D., Brearley A. J., Pravdivtseva O. V., Petaev M., and Hohenberg C. M. (2006) Timescales and Settings for Alteration of Chondritic Meteorites. In *Meteorites and the Early Solar System II* (eds. D. Lauretta and H. Y. J. McSween), pp. 525-553. The Univeristy of Arizona Press, Tucson.

Krumm M., Kasperl S., and Franz M. (2008) Reducing non-linear artifacts of multi-material objects in industrial 3D computed tomography. *NDT & E International* **41**(4), 242-251.

Krzesińska A. (2011) High resolution X-ray tomography as a tool for analysis of internal textures in meteorites. *Meteorites* **1**(1), 3-12.

Krzesińska A., Gattacceca J., Friedrich J. M., and Rochette P. (2015) Impact-related noncoaxial deformation in the Pułtusk H chondrite inferred from petrofabric analysis. *Meteoritics & Planetary Science* **50**(3), 401-417.

Kuebler K. E., McSween Jr H. Y., Carlson W. D., and Hirsch D. (1999) Sizes and masses of chondrules and metal-troilite grains in ordinary chondrites: Possible implications for nebular sorting. *Icarus* **141**(1), 96-106.

Kyle J. R. and Ketcham R. A. (2015) Application of high resolution X-ray computed tomography to mineral deposit origin, evaluation, and processing. *Ore Geology Reviews* **65, Part 4**, 821-839.

Kyriakou Y., Meyer E., Prell D., and Kachelrieß M. (2010) Empirical beam hardening correction (EBHC) for CT. *Medical Physics* **37**(10), 5179-5187.

LaRoque S. J., Sidky E. Y., and Pan X. (2008) Accurate image reconstruction from few-view and limited-angle data in diffraction tomography. *Journal of the Optical Society of America. A, Optics, Image Science, and Vision* **25**(7), 1772-1782.

Larsson D. H., Takman P. A. C., Lundström U., Burvall A., and Hertz H. M. (2011) A 24 keV liquid-metal-jet x-ray source for biomedical applications. *Review of Scientific Instruments* **82**(12), 123701.

Lauretta D. S., Bartels A. E., Barucci M. A., Bierhaus E. B., Binzel R. P., Bottke W. F., Campins H., Chesley S. R., Clark B. C., Clark B. E., Cloutis E. A., Connolly H. C., Crombie M. K., Delbó M., Dworkin J. P., Emery J. P., Glavin D. P., Hamilton V. E., Hergenrother C. W., Johnson C. L., Keller L. P., Michel P., Nolan M. C., Sandford S. A., Scheeres D. J., Simon A. A., Sutter B. M., Vokrouhlický D., and Walsh K. J. (2015) The OSIRIS-REx target asteroid (101955) Bennu: Constraints on its physical, geological, and dynamical nature from astronomical observations. *Meteoritics & Planetary Science* **50**(4), 834-849.

Lauretta D. S., Hua X., and Buseck P. R. (2000) Mineralogy of fine-grained rims in the alh 81002 cm chondrite. *Geochimica et Cosmochimica Acta* **64**(19), 3263-3273.

Lauretta D. S., Nagahara H., and Alexander C. (2006) Petrology and origin of ferromagnesian silicate chondrules. In *Meteorites and the early solar system II* (eds. D. Lauretta and H. Y. McSween Jr), pp. 431-459. University of Arizona Press, Tucson.

Leitner C., Hofmann P., and Marschallinger R. (2014) 3D-modeling of deformed halite hopper crystals by Object Based Image Analysis. *Computers & Geosciences* **73**, 61-70.

Lemelle L., Simionovici A., Truche R., Rau C., Chukalina M., and Gillet P. (2004) A new nondestructive X-ray method for the determination of the 3D mineralogy at the micrometer scale. In *American Mineralogist*, pp. 547.

Leroux H. (2001) Microstructural shock signatures of major minerals in meteorites. *European Journal of Mineralogy* **13**(2), 253-272.

Lindgren P., Hanna R. D., Dobson K. J., Tomkinson T., and Lee M. R. (2015) The paradox between low shock-stage and evidence for compaction in CM carbonaceous chondrites explained by multiple low-intensity impacts. *Geochimica et Cosmochimica Acta* **148**, 159-178.

Lindgren P. and Lee M. R. (2015) Tracking the earliest stages of aqueous alteration in the mildly altered CM chondrite EET 96029. In *Lunar Planet. Sci. XLVI*, pp. 1760.

Liu J., Regenauer‐Lieb K., Hines C., Liu K., Gaede O., and Squelch A. (2009) Improved estimates of percolation and anisotropic permeability from 3D X‐ray

microtomography using stochastic analyses and visualization. *Geochemistry, Geophysics, Geosystems* **10**(5), Q05010.

Ludwig W., Lauridsen E. M., Schmidt S., Poulsen H. F., and Baruchel J. (2007) High-resolution three-dimensional mapping of individual grains in polycrystals by topotomography. *Journal of Applied Crystallography* **40**(5), 905-911.

Macke R. J., Consolmagno G. J., and Britt D. T. (2011) Density, porosity, and magnetic susceptibility of carbonaceous chondrites. *Meteoritics and Planetary Science* **46**, 1842-1862.

Maire E. and Withers P. J. (2014) Quantitative X-ray tomography. *International Materials Reviews* **59**(1), 1-43.

Martin L. and Lindgren P. (in review) Serpentinization of chondrules from the Murchison CM2 carbonaceous chondrite: replacement, cementation, and the genesis of polyhedral phyllosilicate crystals. *Meteoritics and Planetary Science* **Ms. ID MAPS-2374**.

Martin P. M. and Mills A. A. (1980) Preferred chondrule orientations in meteorites. *Earth and Planetary Science Letters* **51**(1), 18-25.

Martin P. M., Mills A. A., and Walker E. (1975) Preferential orientation in four C3 chondritic meteorites. *Nature* **257**, 37.

Masuda A., Taguchi I., and Tanaka K. (1986) Non-destructive analysis of meteorites by using a high-energy X-ray CT scanner. In *Symposium on Antarctic Meteorites XI* (ed. K. Yanai), pp. 148-149, Tokyo.

Matsumoto T., Tsuchiyama A., Nakamura-Messenger K., Nakano T., Uesugi K., Takeuchi A., and Zolensky M. E. (2013) Three-dimensional observation and morphological analysis of organic nanoglobules in a carbonaceous chondrite using X-ray micro-tomography. *Geochimica et Cosmochimica Acta* **116**, 84-95.

Mayo S., Josh M., Nesterets Y., Esteban L., Pervukhina M., Clennell M. B., Maksimenko A., and Hall C. (2015) Quantitative micro-porosity characterization using synchrotron micro-CT and xenon K-edge subtraction in sandstones, carbonates, shales and coal. *Fuel* **154**, 167-173.

Mayo S., Miller P., Gao D., and Sheffield-Parker J. (2007) Software image alignment for X-ray microtomography with submicrometre resolution using a SEM-based X-ray microscope. *Journal of Microscopy* **228**(3), 257-263.

Mayo S. C., Miller P. R., Sheffield-Parker J., Gureyev T. E., and Wilkins S. W. (2005) Attainment of <60 nm resolution in phase-contrast X-ray microscopy using an add-on to an SEM. In *Proc. 8th Int. Conf. X-ray Microscopy*, Himeji, Japan.

McDonald S. A., Reischig P., Holzner C., Lauridsen E. M., Withers P. J., Merkle A. P., and Feser M. (2015) Non-destructive mapping of grain orientations in 3D by laboratory X-ray microscopy. *Scientific Reports* **5**, 14665.

McKay D. S. and Morrison D. A. (1971) Lunar breccias. *Journal of Geophysical Research* **76**(23), 5658-5669.

McSween H. Y. (1999) Meteorites. In *The New Solar System* (eds. J. K. Beatty, C. C. Peterson, and A. Chaikin), pp. 351-363. Sky Publishing Corporation, Cambridge.

Melosh H. J. (1989) *Impact Cratering: A geologic process*. Oxford University Press, New York. pp. 245.

Meng L. J., Li N., and La Riviere P. J. (2011) X-ray fluorescence emission tomography (XFET) with novel imaging geometries – A Monte Carlo study. *IEEE Transactions on Nuclear Science* **58**(6), 3359-3369.

Metzler K. and Bischoff A. (1996) Constraints on Chondrite Agglomeration from Fine-Grained Chondrule Rims. In *Chondrules and the protoplanetary disk* (eds. R. H. Hewins, R. H. Jones, and E. R. D. Scott), pp. 153-162. Cambridge University Press, Cambridge.

Metzler K., Bischoff A., and Stoeffler D. (1992) Accretionary dust mantles in CM chondrites - Evidence for solar nebula processes. *Geochimica et Cosmochimica Acta* **56**, 2873-2897.

Milan S., Hlavac V., and Boyle R. (2014) *Image Processing, Analysis, and Machine Vision*. Cengage Learning, Stamford, CT.

Mittlefehldt D. W. and Lindstrom M. M. (2001) Petrology and geochemistry of Patuxent Range 91501, a clast-poor impact melt from the L-chondrite parent body and Lewis Cliff 88663, an L7 chondrite. *Meteoritics & Planetary Science* **36**(3), 439-457.

Moini M., Rollman C. M., and Bertrand L. (2014) Assessing the impact of synchrotron X-ray irradiation on proteinaceous specimens at macro and molecular levels. *Analytical Chemistry* **86**(19), 9417-9422.

Mokso R., Marone F., Haberthür D., Schittny J. C., Mikuljan G., Isenegger A., and Stampanoni M. (2011) Following Dynamic Processes by X‐ray Tomographic Microscopy with Sub‐second Temporal Resolution. *AIP Conference Proceedings* **1365**(1), 38-41.

Morfill G. E., Durisen R. H., and Turner G. W. (1998) An Accretion Rim Constraint on Chondrule Formation Theories. *Icarus* **134**(1), 180-184.

Mori H. and Takeda H. (1988) Stress induced transformation of pigeonites from achondritic meteorites. *Physics and Chemistry of Minerals* **15**(3), 252-259.

Myers G. R., Kingston A. M., Varslot T. K., Turner M. L., and Sheppard A. P. (2011) Dynamic tomography with a priori information. *Applied Optics* **50**(20), 3685-3690.

Nakamura T. and Nakamuta Y. (1996) X-ray study of PCP from the Murchison CM carbonaceous chondrite. *Antarctic Meteorite Research* **9**, 37.

Nakamura T., Noguchi T., Tanaka M., Zolensky M. E., Kimura M., Tsuchiyama A., Nakato A., Ogami T., Ishida H., Uesugi M., Yada T., Shirai K., Fujimura A., Okazaki R., Sandford S. A., Ishibashi Y., Abe M., Okada T., Ueno M., Mukai T., Yoshikawa M., and Kawaguchi J. (2011) Itokawa dust particles: A direct link between S-type asteroids and ordinary chondrites. *Science* **333**(6046), 1113-1116.

Nakamura T., Noguchi T., Tsuchiyama A., Ushikubo T., Kita N. T., Valley J. W., Zolensky M. E., Kakazu Y., Sakamoto K., Mashio E., Uesugi K., and Nakano T. (2008a) Chondrulelike objects in short-period comet 81P/Wild 2. *Science* **321**(5896), 1664-1667.

Nakamura T., Tomeoka K., Sekine T., and Takeda H. (1995) Impact-induced chondrule flattening in the Allende CV3 carbonaceous chondrite: Shock experiments. *Meteoritics* **30**, 344.

Nakamura T., Tomeoka K., Takaoka N., Sekine T., and Takeda H. (2000) Impact-Induced Textural Changes of CV Carbonaceous Chondrites: Experimental Reproduction. *Icarus* **146**, 289-300.

Nakamura T., Tomeoka K., and Takeda H. (1992) Shock effects of the Leoville CV carbonaceous chondrite - A transmission electron microscope study. *Earth and Planetary Science Letters* **114**, 159-170.

Nakamura T., Tsuchiyama A., Akaki T., Uesugi K., Nakano T., Takeuchi A., Suzuki Y., and Noguchi T. (2008b) Bulk mineralogy and three-dimensional structures of

individual Stardust particles deduced from synchrotron X-ray diffraction and microtomography analysis. *Meteoritics & Planetary Science* **43**(1-2), 247-259.

Nakano T., Tsuchiyama A., Uesugi K., Uesugi M., and Shinohara K. (2006) Slice - Softwares for basic 3-D analysis. Japan Synchrotron Radiation Research Institute (JASRI), Slice Home Page (web), http://www-bl20.spring8.or.jp/slice/.

Needham A. W., Abel R. L., Tomkinson T., and Grady M. M. (2013) Martian subsurface fluid pathways and 3D mineralogy of the Nakhla meteorite. *Geochimica et Cosmochimica Acta* **116**, 96-110.

Nettles J. W., Lofgren G. E., Carlson W. D., and McSween H. Y. (2006) Extent of chondrule melting: Evaluation of experimental textures, nominal grain size, and convolution index. *Meteoritics & Planetary Science* **41**(7), 1059-1071.

Nichols R. H. J. (2006) Chronological Constraints on Planetary Accretion. In *Meteorites and the Early Solar System II* (eds. D. Lauretta and H. Y. McSween Jr), pp. 463-472. University of Arizona Press, Tucson.

Oertel G. (1983) The relationship of strain and preferred orientation of phyllosilicate grains in rocks - A review. *Tectonophysics* **100**, 413-447.

Ormel C. W., Cuzzi J. N., and Tielens A. G. G. M. (2008) Co-accretion of chondrules and dust in the solar nebula. *The Astrophysical Journal* **679**, 1588-1610.

Passchier C. W. and Trouw R. A. J. (2005) *Microtectonics*. Springer, Berlin. pp. 366.

Petrou M. and Garcia Sevilla P. (2006) *Image Processing: Dealing with Texture*. Wiley, New York. pp. 618.

Pham D. L., Xu C., and Prince J. L. (2000) Current methods in medical image segmentation. *Annual Review of Biomedical Engineering* **2**(1), 315-337.

Poludniowski G., Landry G., DeBlois F., Evans P. M., and Verhaegen F. (2009) SpekCalc: A program to calculate photon spectra from tungsten anode X-ray tubes. *Physics in Medicine and Biology* **54**(19), N433.

Popova O. P., Jenniskens P., Emel,Äôyanenko V., Kartashova A., Biryukov E., Khaibrakhmanov S., Shuvalov V., Rybnov Y., Dudorov A., Grokhovsky V. I., Badyukov D. D., Yin Q.-Z., Gural P. S., Albers J., Granvik M., Evers S. G., Kuiper J., Kharlamov V., Solovyov A., Rusakov Y. S., Korotkiy S., Serdyuk I., Korochantsev A. V., Larionov M. Y., Glazachev D., Mayer A. E., Gisler G., Gladkovsky S. V., Wimpenny J., Sanborn M. E., Yamakawa A., Verosub K. L.,

Rowland D. J., Roeske S., Botto N. W., Friedrich J. M., Zolensky M. E., Le L., Ross D., Ziegler K., Nakamura T., Ahn I., Lee J. I., Zhou Q., Li X.-H., Li Q.-L., Liu Y., Tang G.-Q., Hiroi T., Sears D., Weinstein I. A., Vokhmintsev A. S., Ishchenko A. V., Schmitt-Kopplin P., Hertkorn N., Nagao K., Haba M. K., Komatsu M., and Mikouchi T. (2013) Chelyabinsk airburst, damage assessment, meteorite recovery, and characterization. *Science* **342**(6162), 1069-1073.

Poulsen H. F. (2004) *Three-dimensional X-ray diffraction microscopy. Mapping polycrystals and their dynamics*. Springer, Berlin.

Press W. H. (2007) *Numerical recipes 3rd edition: The art of scientific computing*. Cambridge university press.

Prior D. J. (1999) Problems in determining the misorientation axes, for small misorientations, using electron backscatter diffraction in the SEM. *Journal of Microscopy* **195**(3), 217-225.

Raleigh C. B. and Talbot J. L. (1967) Mechanical twinning in naturally and experimentally deformed diopside. *American Journal of Science* **265**, 151-165.

Ramsey J. G. and Huber M. I. (1983) *Techniques of Modern Structural Geology*. Academic Press, London. pp. 307.

Rasband W. S. (1997-2015) ImageJ. U.S. National Institutes of Health, Bethesda, Maryland, USA, http://imagej.nih.gov/ij/.

Raterron P. and Jaoul O. (1991) High-temperature deformation of diopside single crystal: 1. Mechanical data. *Journal of Geophysical Research: Solid Earth* **96**(B9), 14277-14286.

Reed S. J. B. (2005) *Electron Microprobe Analysis and Scanning Electron Microscopy in Geology*. Cambridge University Press, Cambridge. pp. 192.

Remeysen K. and Swennen R. (2008) Application of microfocus computed tomography in carbonate reservoir characterization: Possibilities and limitations. *Marine and Petroleum Geology* **25**(6), 486-499.

Roeller K. and Trepmann C. (2010) Stereo32.

Rubin A. E. (2012) Collisional facilitation of aqueous alteration of CM and CV carbonaceous chondrites. *Geochimica et Cosmochimica Acta* **90**, 181-194.

Rubin A. E., Scott E. R. D., and Keil K. (1997) Shock metamorphism of enstatite chondrites. *Geochimica et Cosmochimica Acta* **61**(4), 847-858.

Rubin A. E. and Swindle T. D. (2011) Flattened chondrules in the LAP 04581 LL5 chondrite: Evidence for an oblique impact into LL3 material and subsequent collisional heating. *Meteoritics & Planetary Science* **46**(4), 587-600.

Rubin A. E., Trigo-Rodriguez J. M., Huber H., and Wasson J. T. (2007) Progressive aqueous alteration of CM carbonaceous chondrites. *Geochimica et Cosmochimica Acta* **71**, 2361-2382.

Rubin A. E., Ulff-Moller F., Wasson J. T., and Carlson W. D. (2001) The Portales Valley meteorite breccia: evidence for impact-induced melting and metamorphism of an ordinary chondrite. *Geochimica et Cosmochimica Acta* **65**(2), 323-342.

Russell S. S., Hartmann L., Cuzzi J., Krot A. N., Gounelle M., and Weidenschilling S. (2006) Timescales of the solar protoplanetary disk. In *Meteorites and the Early Solar System II* (eds. D. Lauretta and H. Y. McSween Jr), pp. 233-251. University of Arizona Press, Tucson.

Russell S. S. and Howard L. (2013) The texture of a fine-grained calcium-aluminium-rich inclusion (CAI) in three dimensions and implications for early solar system condensation. *Geochimica et Cosmochimica Acta* **116**, 52-62.

Ruzicka A. (1990) Deformation and thermal histories of chondrules in the Chainpur (LL3.4) chondrite. *Meteoritics* **25**(2), 101-113.

Ruzicka A., Brown R., Friedrich J., Hutson M., Hugo R., and Rivers M. (2015) Shock-induced mobilization of metal and sulfide in planetesimals: Evidence from the Buck Mountains 005 (L6 S4) dike-bearing chondrite. *American Mineralogist* **100**, 2725-2738.

Sahagian D. L. and Proussevitch A. A. (1998) 3D particle size distributions from 2D observations: stereology for natural applications. *Journal of Volcanology and Geothermal Research* **84**(3), 173-196.

Sakdinawat A. and Attwood D. (2010) Nanoscale X-ray imaging. *Nat Photon* **4**(12), 840-848.

Sanders I. S. and Scott E. R. D. (2012) The origin of chondrules and chondrites: Debris from low-velocity impacts between molten planetesimals? *Meteoritics & Planetary Science* **47**(12), 2170-2192.

Sasso M. R., Macke R. J., Boesenberg J. S., Britt D. T., Rivers M. L., Ebel D. S., and Friedrich J. M. (2009) Incompletely compacted equilibrated ordinary chondrites. *Meteoritics & Planetary Science* **44**(11), 1743-1753.

Scott E. R. D. (2007) Chondrites and the Protoplanetary Disk. *Annual Review of Earth and Planetary Sciences* **35**(1), 577-620.

Scott E. R. D., Keil K., and Stoeffler D. (1992) Shock metamorphism of carbonaceous chondrites. *Geochimica et Cosmochimica Acta* **56**, 4281-4293.

Sears D., Ebel D. S., Wallace S. W., and Friedrich J. M. (2015) X-ray computed tomography and the radiation history of meteorites. In *78th Annual Meeting of the Meteoritical Society*, pp. 5156, Berkeley, CA.

Sears D., Sears H., Ebel D. S., Wallace S. W., and Friedrich J. M. (2016) X-ray computed tomography imaging: A not-so-nondestructive technique. *Meteoritics and Planetary Science* **51**(4), 833-838.

Sears D. W. G., Benoit P. H., and Jie L. (1993) Two chondrule groups each with distinctive rims in Murchison recognized by cathodoluminescence. *Meteoritics* **28**(5), 669-675.

Sears D. W. G., Ninagawa K., and Singhvi A. K. (2013) Luminescence studies of extraterrestrial materials: Insights into their recent radiation and thermal histories and into their metamorphic history. *Chemie der Erde - Geochemistry* **73**(1), 1-37.

Seibert J. A. (2006) Flat-panel detectors: how much better are they? *Pediatric Radiology* **36**(Suppl 2), 173-181.

Sham T. K. and Rivers M. L. (2002) A brief overview of synchrotron radiation. *Reviews in Mineralogy and Geochemistry* **49**(1), 117-147.

Sharp T. G., de Carli P. S., and McSween H. Y. (2006) Shock Effects in Meteorites. In *Meteorites and the Early Solar System II* (eds. D. S. Lauretta and H. Y. McSween Jr), pp. 653-677. University of Arizona Press, Tuscon.

Sidky E. Y., Kao C.-M., and Pan X. (2006) Accurate image reconstruction from few-views and limited-angle data in divergent-beam CT. *Journal of X-Ray Science and Technology* **14**(2), 119-139.

Simionovici A., Allen C., Bajt S., Bastien R., Bechtel H., Borg J., Brenker F. E., Bridges J. C., Brownlee D. E., Cloetens P., Davis A. M., Floss C., Flynn G. J., Frank D., Gainsforth Z., Grun E., Heck P. R., Hillier J., Hoppe P., Howard L., Huss G. R., Huth J., Kearsley A. T., King A. J., Lai B., Leitner J., Lemelle L., Leroux H., Lettieri R., Marchant W., Nittler L. R., Ogliore R., Postberg F., Sandford S., Sans Tresseras J. A., Schoonjans T., Schmitz S., Silvermit G., Sole V. A., Srama R., Stephan T., Stodolna J., Stroud R. M., Sutton S. R., Trieloff M., Tsou P.,

Tsuchiyama A., Tyliczszak T., Vekemans B., Vincze L., Westphal A. J., Zevin D., and Zolensky M. (2011) Synchrotron X-ray irradiation of Stardust interstellar candidates: From "No" to "Low" damage effects. In *74th Annual Meteoritical Society Meeting*, pp. 5517, London.

Smith D. L., Ernst R. E., Samson C., and Herd R. (2006) Stony meteorite characterization by non-destructive measurement of magnetic properties. *Meteoritics and Planetary Science* **41**(3), 355-373.

Sneyd D. S., McSween H. Y., Jr., Sugiura N., Strangway D. W., and Nord G. L., Jr. (1988) Origin of petrofabrics and magnetic anisotropy in ordinary chondrites. *Meteoritics* **23**, 139-149.

Stoffler D., Bischoff A., Buchwald V., and Rubin A. E. (1988) Shock effects in meteorites. In *Meteorites and the Early Solar System* (eds. J. F. Kerridge and M. S. Matthews), pp. 165-202. University of Arizona Press, Tucscon.

Sugiura N. and Strangway D. W. (1983) Magnetic anisotropy and porosity of chondrites. *Geophysical Research Letters* **10**(1), 83-86.

Tait A. W., Tomkins A. G., Godel B. M., Wilson S. A., and Hasalova P. (2014) Investigation of the H7 ordinary chondrite, Watson 012: Implications for recognition and classification of Type 7 meteorites. *Geochimica et Cosmochimica Acta* **134**, 175-196.

Takayama A. and Tomeoka K. (2012) Fine-grained rims surrounding chondrules in the Tagish Lake carbonaceous chondrite: Verification of their formation through parent-body processes. *Geochimica et Cosmochimica Acta* **98**, 1-18.

Tkachuk A., Duewer F., Cui H., Feser M., Wang S., and Yun W. (2007) X-ray computed tomography in Zernike phase contrast mode at 8 keV with 50-nm resolution using Cu rotating anode X-ray source. *Zeitschrift für Kristallographie - Crystalline Materials* **222**(11/2007), 650-655.

Tomeoka K., Hatakeyama K., Nakamura T., and Takeda H. (1991) Evidence for pre-accretionary aqueous alteration in the Yamato-793321 CM carbonaceous chondrite. In *16th Symposium on Antarctic Meteorites*, pp. 37-39. NIPR, Tokyo, Japan.

Tomeoka K., Yamahana Y., and Sekine T. (1999) Experimental shock metamorphism of the Murchison CM carbonaceous chondrite. *Geochimica et Cosmochimica Acta* **63**(21), 3683-3703.

Tomioka N., Tomeoka K., Nakamura-Messenger K., and Sekine T. (2007) Heating effects of the matrix of experimentally shocked Murchison CM chondrite: Comparison with micrometeorites. *Meteoritics and Planetary Science* **42**(1), 19-30.

Tomkinson T., Lee M. R., Mark D. F., Dobson K. J., and Franchi I. A. (2015) The Northwest Africa (NWA) 5790 meteorite: A mesostasis-rich nakhlite with little or no Martian aqueous alteration. *Meteoritics & Planetary Science* **50**(2), 287-304.

Tonui E., Zolensky M., Hiroi T., Nakamura T., Lipschutz M. E., Wang M.-S., and Okudaira K. (2014) Petrographic, chemical and spectroscopic evidence for thermal metamorphism in carbonaceous chondrites I: CI and CM chondrites. *Geochimica et Cosmochimica Acta* **126**, 284-306.

Torsten P., Jürgen B., and Thomas H. (2000) Analogous Experiments on the Stickiness of Micron-sized Preplanetary Dust. *The Astrophysical Journal* **533**(1), 454.

Trepmann C. A. (2008) Shock effects in quartz: Compression versus shear deformation, An example from the Rochechouart impact structure, France. *Earth and Planetary Science Letters* **267**, 322-332.

Trigo-Rodriguez J. M., Rubin A. E., and Wasson J. T. (2006) Non-nebular origin of dark mantles around chondrules and inclusions in CM chondrites. *Geochimica et Cosmochimica Acta* **70**, 1271-1290.

Tsuchiyama A., Kawabata T., Kondo M., Uesugi M., Nakano T., Suzuki Y., Yagi N., Umetani K., and Shirono S. (2000) Spinning chondrules deduced from their three-dimensional structures by X-ray CT method. In *Lunar and Planetary Science Conference XXXI*, pp. 1566, Houston, TX.

Tsuchiyama A., Nakamura T., Nakano T., and Nakamura N. (2002) Three-dimensional description of the Kobe meteorite by micro X-ray CT method: Possibility of three-dimensional curation of meteorite samples. *Geochemical Journal* **36**(4), 369-390.

Tsuchiyama A., Nakano T., Uesugi K., Uesugi M., Takeuchi A., Suzuki Y., Noguchi R., Matsumoto T., Matsuno J., Nagano T., Imai Y., Nakamura T., Ogami T., Noguchi T., Abe M., Yada T., and Fujimura A. (2013) Analytical dual-energy microtomography: A new method for obtaining three-dimensional mineral phase images and its application to Hayabusa samples. *Geochimica et Cosmochimica Acta* **116**, 5-16.

Tsuchiyama A., Uesugi K., Nakano T., and Ikeda S. (2005) Quantitative evaluation of attenuation contrast of X-ray computed tomography images using monochromatized beams. *American Mineralogist* **90**(1), 132-142.

Tsuchiyama A., Uesugi M., Matsushima T., Michikami T., Kadono T., Nakamura T., Uesugi K., Nakano T., Sandford S. A., Noguchi R., Matsumoto T., Matsuno J., Nagano T., Imai Y., Takeuchi A., Suzuki Y., Ogami T., Katagiri J., Ebihara M., Ireland T. R., Kitajima F., Nagao K., Naraoka H., Noguchi T., Okazaki R., Yurimoto H., Zolensky M. E., Mukai T., Abe M., Yada T., Fujimura A., Yoshikawa M., and Kawaguchi J. (2011) Three-dimensional structure of hayabusa samples: origin and evolution of Itokawa regolith. *Science* **333**(6046), 1125-1128.

Turner F. J. and Weiss L. E. (1963) *Structural analysis of metamorphic tectonites*. McGraw-Hill. pp. 545.

Uesugi K., Takeuchi A., and Suzuki Y. (2006) Development of micro-tomography system with Fresnel zone plate optics at SPring-8. In *Proc. SPIE 6318, Developments in X-ray Tomography V*, pp. 63181F, San Diego, CA.

Uesugi M., Uesugi K., and Oka M. (2010) Non-destructive observation of meteorite chips using quantitative analysis of optimized X-ray micro-computed tomography. *Earth and Planetary Science Letters* **299**(3,Äì4), 359-367.

Uesugi M., Uesugi K., Takeuchi A., Suzuki Y., Hoshino M., and Tsuchiyama A. (2013) Three-dimensional observation of carbonaceous chondrites by synchrotron radiation X-ray CT - Quantitative analysis and developments for the future sample return missions. *Geochimica et Cosmochimica Acta* **116**, 17-32.

Van Geet M., Swennen R., and Wevers M. (2000) Quantitative analysis of reservoir rocks by microfocus X-ray computerised tomography. *Sedimentary Geology* **132**(1–2), 25-36.

Van Gompel G., Van Slambrouck K., Defrise M., Batenburg K. J., de Mey J., Sijbers J., and Nuyts J. (2011) Iterative correction of beam hardening artifacts in CT. *Medical Physics* **38**(S1), S36-S49.

Varslot T., Kingston A., Myers G., and Sheppard A. (2011) High-resolution helical cone-beam micro-CT with theoretically-exact reconstruction from experimental data. *Medical Physics* **38**(10), 5459.

Villeneuve J., Libourel G., and Soulié C. (2015) Relationships between type I and type II chondrules: Implications on chondrule formation processes. *Geochimica et Cosmochimica Acta* **160**, 277-305.

Vonlanthen P., Rausch J., Ketcham R. A., Putlitz B., Baumgartner L. P., and Grobéty B. (2015) High-resolution 3D analyses of the shape and internal constituents of small volcanic ash particles: The contribution of SEM micro-computed tomography (SEM micro-CT). *Journal of Volcanology and Geothermal Research* **293**, 1-12.

Wadhwa M., Srinivasan G., and Carlson R. W. (2006) Timescales of Planetary Differentiation in the Early Solar System. In *Meteorites and the Early Solar System II* (eds. D. Lauretta and H. Y. McSween Jr), pp. 715-731. University of Arizona Press, Tucson.

Weiss B. P. and Elkins-Tanton L. T. (2013) Differentiated Planetesimals and the Parent Bodies of Chondrites. *Annual Review of Earth and Planetary Sciences* **41**(1), 529-560.

Wildenschild D. and Sheppard A. P. (2013) X-ray imaging and analysis techniques for quantifying pore-scale structure and processes in subsurface porous medium systems. *Advances in Water Resources* **51**, 217-246.

Wilkins S. W., Gureyev T. E., Gao D., Pogany A., and Stevenson A. W. (1996) Phase-contrast imaging using polychromatic hard X-rays. *Nature* **384**(6607), 335-338.

Willmott P. (2011) *An Introduction to Synchrotron Radiation*. John Wiley and Sons, Ltd, Singapore. pp. 352.

Withers P. J. (2007) X-ray nanotomography. *Materials Today* **10**(12), 26-34.

Woodcock N. H. (1977) Specification of fabric shapes using an eigenvalue method. *Geological Society of America Bulletin* **88**(9), 1231-1236.

Woodcock N. H. and Naylor M. A. (1983) Randomness testing in three-dimensional orientation data. *Journal of Structural Geology* **5**(5), 539-548.

Yasuda M., Kitamura M., and Morimoto N. (1983) Electron microscopy of clinoenstatite from a boninite and a chondrite. *Physics and Chemistry of Minerals* **9**(5), 192-196.

Yu Z. and Xiaochuan P. (2004) Exact image reconstruction on PI-lines from minimum data in helical cone-beam CT. *Physics in Medicine and Biology* **49**(6), 941-959.

Zanda B., Bourot-Denise M., Hewins R. H., Cohen B. A., Delaney J. S., Humayun M., and Campbell A. J. (2002) Accretion textures, iron evaporation, and re-condensation in Renazzo chondrules. In *Lunary and Planetary Science XXXIII*, pp. 1852, Houston, TX.

Zega T. J. and Buseck P. R. (2003) Fine-grained-rim mineralogy of the Cold Bokkeveld CM chondrite. *Geochimica et Cosmochimica Acta* **67**(9), 1711-1721.

Zeigler R., Almeida N. V., Sykes D., and Smith C. L. (2014) X-ray micro-computed tomography of Apollo samples as a curation technique enabling better research. In *77th Annual Meteoritical Society Meeting*, pp. 5436, Casablanca.

Zimbelman J. R. (1986) The role of porosity in thermal inertia variations on basaltic lavas. *Icarus* **68**(2), 366-369.

Zolensky M., Barrett R., and Browning L. (1993) Mineralogy and composition of matrix and chondrule rims in carbonaceous chondrites. *Geochimica et Cosmochimica Acta* **57**, 3123-3148.

Zolensky M., Herrin J., Mikouchi T., Ohsumi K., Friedrich J., Steele A., Rumble D., Fries M., Sandford S., Milam S., Hagiya K., Takeda H., Satake W., Kurihara T., Colbert M., Hanna R., Maisano J., Ketcham R., Goodrich C., Le L., Robinson G., Martinez J., Ross K., Jenniskens P., and Shaddad M. H. (2010) Mineralogy and petrography of the Almahata Sitta ureilite. *Meteoritics & Planetary Science* **45**(10-11), 1618-1637.

Zolensky M., Mikouchi T., Fries M., Bodnar R., Jenniskens P., Yin Q.-z., Hagiya K., Ohsumi K., Komatsu M., Colbert M., Hanna R., Maisano J., Ketcham R., Kebukawa Y., Nakamura T., Matsuoka M., Sasaki S., Tsuchiyama A., Gounelle M., Le L., Martinez J., Ross K., and Rahman Z. (2014) Mineralogy and petrography of C asteroid regolith: The Sutter's Mill CM meteorite. *Meteoritics & Planetary Science* **49**(11), 1997-2016.

Zolensky M. E., Mittlefehldt D. W., Lipschutz M. E., Wang M.-S., Clayton R. N., Mayeda T. K., Grady M. M., Pillinger C., and Barber D. (1997) CM chondrites exhibit the complete petrologic range from type 2 to 1. *Geochimica et Cosmochimica Acta* **61**, 5099.